



Poznan University of Technology
Faculty of Chemical Technology
Institute of Chemistry and Technical Electrochemistry
Field of study: Chemical Technology



Barbara Górską

Development of electrochemical capacitors based on protic ionic liquids

Badania nad kondensatorami elektrochemicznymi z wykorzystaniem
protonowych cieczy jonowych jako elektrolitów

DOCTORAL DISSERTATION

Promoter:

prof. François Béguin

Poznań 2017



**INNOWACYJNA
GOSPODARKA**
NARODOWA STRATEGIA SPÓJNOŚCI



Fundacja na rzecz Nauki Polskiej

UNIA EUROPEJSKA
EUROPEJSKI FUNDUSZ
ROZWOJU REGIONALNEGO



This thesis' research was supported by the ECOLCAP project funded in the frame of the Welcome Programme implemented by the Foundation for Polish Science (FNP) within the Measure 1.2. 'Strengthening the human resources potential of science', of the Innovative Economy Operational Programme supported by European Union.

Project leader: Professor François Béguin

Badania do niniejszej pracy prowadzone były przy wsparciu projektu ECOLCAP realizowanego w ramach Programu Welcome, finansowanego przez Fundację Nauki Polskiej (FNP) zgodnie z Działaniem 1.2. „Wzmocnienie potencjału kadrowego nauki”, Programu Operacyjnego Innowacyjna Gospodarka wspieranego przez Unię Europejską.

Kierownik projektu: Profesor François Béguin

Acknowledgements

“Ce qui n'est pas clair, n'est pas français.”

Antoine Rivaroly

I would like to express my sincere gratitude to my supervisor Prof. François Béguin for the continuous support of my PhD study and related research.

„Duża część postępu w nauce była możliwa dzięki ludziom niezależnym lub myślącym nieco inaczej.”

Chris Darimont

I am sincerely grateful to my advisor Prof. Juliusz Pernak for his scientific guidance and support since my master project.

“Dans les champs de l'observation le hasard ne favorise que les esprits préparés.”

Louis Pasteur

My sincere thanks also go to Prof. Mérièm Anouti, who provided me an opportunity to join her team for an internship helping me to develop my skills and knowledge, and who has been constant source of encouragement and enthusiasm.

“Anybody who has been seriously engaged in scientific work of any kind realizes that over the entrance to the gates of the temple of science are written the words: Ye must have faith. It is a quality which the scientist cannot dispense with.”

Max Planck

I wish to express my sincere gratitude to Prof. Elżbieta Frąckowiak for her help and support.

***“A foolish consistency is the hobgoblin of little minds,
adored by little statesmen and philosophers and divines”***

Ralph Waldo Emerson

Table of Contents

General Introduction	9
Chapter I Literature review	14
1. Introduction	15
2. Electrochemical Capacitors.....	15
2.1. Principles and properties of electrochemical capacitors	17
2.1.1. The electrical double-layer	17
2.1.2. Construction of an electrochemical capacitor.....	19
2.1.3. Energy and power of electrochemical capacitors	20
2.1.4. Electrochemical pseudocapacitance	22
2.2. Carbon based electrodes.....	24
2.2.1. Variety of carbon materials structures and forms.....	25
2.2.2. Porous texture of carbon materials	30
2.2.3. Effect of carbon porous texture on EDLC performance.....	33
2.2.3.1. Dependence between capacitance and measured SSA of ACs.....	33
2.2.3.2. Impact of ions/pore matching on capacitance	34
2.2.3.3. Desolvation effect.....	35
2.2.3.4. Saturation of electrode porosity.....	37
2.2.4. Surface functionality of carbon materials and faradaic contributions	38
2.3. Conventional electrolytes.....	39
2.3.1. Aqueous electrolytes.....	40
2.3.2. Organic electrolytes	43
2.4. Ionic liquids as non-conventional electrolytes.....	44
2.4.1. General introduction on ionic liquids (ILs)	44
2.4.2. Physicochemical and electrochemical properties of ILs	48
2.4.3. State-of-the-art on AILs based ECs.....	52
2.4.4. Approach toward lowering the melting point of AILs	55
2.4.5. The subclass of Protic Ionic Liquids (PILs)	57
2.4.6. PILs as electrolytes for ECs.....	59
3. Conclusion and perspectives	63
Chapter II Performance enhancement of PIL-based ECs through the optimization of electrodes.....	65
1. Introduction	66

2.	Effect of binder on the performance of PIL-based ECs	67
2.1.	Assessment of electrodes wettability by PIL	68
2.2.	Porous texture characterization of electrodes	69
2.3.	Electrochemical performance of symmetric carbon/carbon capacitors using PVDF and PTFE bound electrodes in [HN ₂₂₂][TFSI] electrolyte	72
3.	In search of ACs with porous texture tuned for PIL electrolytes	74
4.	Conclusion.....	83
Chapter III Effect of low water content in protic ionic liquid on ions electrosorption in carbon porosity.....		84
1.	Introduction	85
2.	Effect of water traces on the thermal and transport properties of [HN ₂₂₂][TFSI].....	86
3.	How does various amount of incorporated water in PIL affect the operation of AC electrodes and AC-based ECs?	88
3.1.	Characterization of the electrolyte species by computational methods	88
3.2.	Cathodic behavior of AC in [HN ₂₂₂][TFSI] with various water contents.....	90
3.3.	Cyclic voltammograms of AC-based ECs in [HN ₂₂₂][TFSI] with various water contents.....	92
3.4.	Capacitance of AC-based ECs in [HN ₂₂₂][TFSI] with various water contents.....	95
3.5.	Impact of current collectors on the performance of AC-based ECs in [HN ₂₂₂][TFSI] with high water content.....	100
4.	Conclusion.....	104
Chapter IV Development of a novel family of protic ionic liquids.....		106
1.	Introduction	108
2.	Synthesis and characterization of PILs with N-chloroalkyl functionalized cations... ..	109
2.2.	Structural characterization of the PILs by NMR	110
2.3.	Computational evaluation of the ions properties	111
2.4.	Thermal properties of the PILs	113
2.4.2.	Thermal stability	116
2.5.	Physicochemical properties.....	117
2.5.1.	Density.....	117
2.5.2.	Refractive index and molar refractivity	119
2.5.3.	Air-liquid surface tension	121
2.6.	Transport properties of PILs	121
2.6.2.	Conductivity	124
2.6.3.	Ionicity.....	127

3. Conclusion.....	128
Chapter V Evaluation of protic ionic liquids with N-chloroalkyl functionalized cations as electrolytes for ECs	130
1. Introduction	131
2. Electrochemical potential window of the PILs	131
2.1. Evaluation of the PILs electrochemical stability by computational methods	131
2.2. Practical electrochemical stability of the PILs evaluated on glassy carbon	133
3. Electrochemical behavior of aluminum and stainless steel current collectors in the tested PILs	134
3.1. Electrochemical stability of N-chloroalkyl functionalized PILs on stainless steel 316L	134
3.2. Electrochemical behavior of aluminum in N-chloroalkyl functionalized PILs	136
3.3. Conclusions on current collector applicability.....	140
4. Stability limits of N-chloroalkyl functionalized PILs on AC electrode.....	140
4.1. Literature background	140
4.2. Potential limits of N-chloroalkyl functionalized PILs on AC electrode.....	143
5. Symmetric AC/AC electrochemical capacitors based on N-chloroalkyl functionalized PILs	150
6. Conclusion.....	155
General conclusion	157
Annex	161
1. Abbreviations and symbols	162
1.1. Abbreviations	162
1.2. Abbreviations and Symbols in Equations	165
2. Reagents, chemicals and carbons	170
3. Preparation of PILs.....	171
4. Characterization of PILs.....	171
4.1. Nuclear magnetic resonance spectroscopy (NMR).....	171
4.2. Karl-Fischer titration.....	172
4.3. Physicochemical properties.....	172
4.4. Computational methods	173
5. Electrochemical characterizations	180
5.1. Electrodes preparation.....	180
5.2. Porous texture characterization of carbons and electrodes	180

5.3. Silver wire quasi reference electrode	181
5.4. Cells construction.....	181
5.4.1. Electrochemical stability of PILs on GC	181
5.4.2. Electrochemical behavior of PILs on Al	181
5.4.3. Electrochemical behavior of PILs on stainless steel	181
5.4.4. Manufacturing of three- and two-electrode cells with AC electrodes.....	182
5.5. Electrochemical measurements.....	182
References	184
Scientific Achievements.....	196
Abstract	203
Streszczenie	208

General Introduction

The great technological advances we are witnessing nowadays challenge energy production and management in terms of increasing its efficiency simultaneously with reducing fossil fuels consumption and CO₂ emissions. The enormous release of this principal greenhouse gas, originated from the domination of coal, natural gas and oil combustion for energy, transportation and industrial processes, has become a serious threat to our planet contributing to global warming. Taking heed of the fact that “*We do not inherit the earth from our ancestors; we borrow it from our children*” the idea of sustainable development has emerged and proclaims balance between the development of human civilization with its goals and environment conservation. As we cannot imagine life without electricity, cars, smart technology devices and other obvious facilities and comforts of modern society, the processes of obtaining and using energy have to be modified. Therefore, the world has focused on generating safe and waste-free energy from renewables such as sunlight, wind, tides, waves and geothermal heat. In parallel, great interest has been paid to the support of energy distribution by smart grids adjusting consumption to production. In terms of transportation, *green vehicles* including cars, buses, tramways, trains etc., are employed as tools to decrease fuel consumption and limit air pollution. Yet, all this recent energy policy can be effectively supported by devices for electrochemical energy conversion and storage such as fuel cells, batteries and electrochemical capacitors (ECs).

Undoubtedly, the application of batteries is the most widespread and reflected in their established market position in contrast to the niche usage of fuel cells, while the utilization of electrochemical capacitors has recently significantly grown. The ECs’ technology has been developed for over fifty years, and today’s blooming of their commercial employment ranks them as mature and mainstream electrical storage systems which have conquered the market. Essentially, the charge storage mechanism in ECs involves a simple ions separation in the electrical double-layer (EDL) formed at the electrode/electrolyte interface (charges are stored physically). The advantageous EC operation characteristics are short charge and discharge times, high power output and long cycle life. It means that they are addressed to applications requiring repeated power pulses during short periods. As a result, ECs are broadly employed in hybrid and electric vehicles to recover energy during braking (regenerative braking) and to provide quick bursts of energy during acceleration. ECs effectively support energy management of power grids, stabilizing the fluctuations by storing the production surplus. ECs are also intended for application in small portable devices like laptops and cell phones in order to reduce charging time.

Since the energy density of ECs is strongly dependent on the operating voltage U , as expressed by the equation of energy $E = \frac{1}{2} \cdot C \cdot U^2$, commercial ECs are mostly based on organic electrolytes. However, they incorporate molecular solvents such as acetonitrile, which are classified as flammable, hazardous and ecologically unfriendly. Currently, in search for safer and more environment-friendly solutions, two main alternative electrolytes are considered: ionic liquids (ILs) and aqueous electrolytes. ILs are solvent-free electrolytes, which are widely recognized as *green* compounds owing to their great thermal stability and negligible vapor pressure. They can provide high operational voltage (3.0-4.0 V), thus high energy density, but the power of ECs based on ILs is limited due to their relatively poor transport properties. By contrast, ECs based on aqueous electrolytes display good output power, as a result of high conductivity and low viscosity of these electrolytes, but restricted voltage (0.8-1.6 V) due to electrochemical decomposition of water. However, the energy density can be enhanced in this case through reversible faradaic contributions involving simultaneous electrons and protons transfers.

Recently, in aim to combine advantages of large voltage window together with faradaic behavior related with the presence of protons in the medium, the attention has been drawn to the application of protic ionic liquids (PILs). This unique subclass of ILs is characterized by a labile hydrogen atom attached to the central atom of the cation, in contrast to only non-proton substituents in the cation of classical aprotic ionic liquids (AILs). Hence, PILs are expected to serve as anhydrous protic medium and, if the transferable proton plays the same role as the hydronium ion in aqueous electrolytes, to participate in proton-coupled electron transfer resulting in faradaic current impact. Simultaneously, PILs are considered to provide advantages of ILs in terms of high operational voltage and wide temperature range. However, despite careful drying, PILs are generally obtained with some amount of residual water, which may impact their potential electrochemical performance.

Therefore, fundamental investigations leading to the understanding of PILs properties and operating principles in activated carbon (AC) based ECs are required, especially in terms of transferable-proton impact. For this reason, in-depth multifaceted study is required and should include: i) determining the favorable composition of electrodes for performance enhancement of PILs-based ECs as well as establishing the effective amount of water in PILs to obtain faradaic contributions from a reversible proton coupled electron transfer; 2/ designing PILs which display properties tuned toward applications in ECs while focusing

on bis[(trifluoromethyl)sulfonyl]imide, [TFSI]⁻, known to be the most beneficial anion incorporated in PILs for electrochemical applications.

Based on the foreword, the dissertation is divided into five chapters.

The first chapter presents a literature review of the state-of-the-art on AC-based ECs. It includes a short description of ECs operation principles and targeted applications. The typical electrode materials are presented with a special attention to ACs. The three main types of electrolytes are introduced: the so-called conventional ones, namely aqueous and organic electrolytes, and the performance of ECs based on these electrolytes, as well as the non-conventional ones, namely ionic liquids, paying attention to their general properties and implementation in ECs. Finally, a significant part of the chapter is dedicated to the particular physicochemical properties of PILs and recent advances on their application in ECs.

The second chapter focuses on the effect of electrode composition, i.e. binder type and texture of porous carbon, on the performance of ECs. The evaluation is carried out using the PIL already firmly established in EC applications, namely triethylammonium bis[(trifluoromethyl)sulfonyl]imide, [HN₂₂₂][TFSI]. Electrodes were manufactured with the most currently used binders, e.g., polyvinylidene fluoride (PVDF) or polytetrafluoroethylene (PTFE), and their wettability by the PIL was estimated by measuring the contact angle. Then, the accessible surface area of electrodes is assessed as the fraction enabling the [TFSI]⁻ anion to penetrate in the porosity, i.e. corresponding to pores larger than its width. Taking into account the relatively bulky dimensions of ions in the PIL, the electrodes consist of three carbon materials differing significantly by the micropore/mesopore volume ratio and the type of mesoporosity. The role of mesopores in determining the performance of PIL-based ECs is established by cyclic voltammetry (CV) and galvanostatic charge/discharge (GC/GD) carried out on 2-electrode cells, with and without reference electrode.

The third chapter discusses the effect of low water content in [HN₂₂₂][TFSI] (ranging from less than 20 ppm to 1%) on the physicochemical properties of the PIL and electrochemical performance of three- or two-electrode cells in this PIL. The impact of water in the PIL on phase transitions, viscosity and conductivity is determined. Hydrogen electrosorption onto AC in dependence of water content in PIL is evaluated under negative polarization of the activated carbon electrode. Afterwards, AC-based ECs equipped with aluminum or stainless steel current collectors are examined by CV, GC/GD and

electrochemical impedance spectroscopy (EIS) to determine the resulting capacitance and to comprehend water-dependent changes in electrodes operation.

The fourth chapter presents the development of novel PILs, their synthesis and physicochemical characterization. The study includes a range of PILs based on the aforementioned [TFSI]⁻ anion, combined with N-chloroalkyl functionalized ammonium cations such as morpholinium, piperidinium, pyrrolidinium and three alkylammonium with various length of chains. The functionalization of the PILs is intended for melting temperature decrease. As all the six synthesized PILs are liquid at least at room temperature, their physicochemical properties such as density, refractive index, surface tension, viscosity, and conductivity are investigated and interpreted. The measurements carried out on the series allow the effect of cation structure on PIL physicochemical properties to be distinguished, and especially their applicability for ECs to be predetermined by considering transport properties.

The fifth chapter investigates the electrochemical stability window of the N-chloroalkyl functionalized PILs themselves on glassy carbon, as well as their compatibility with components of ECs (current collectors and electrode materials). Regarding the current collectors, the main requisite is a good electrochemical stability with limited corrosion, while keeping good conductivity, reasonable cost and low weight of the material. For these studies, stainless steel and aluminum are explored. The electrochemical stability window of AC electrodes in the PILs is determined by means of potential window opening measurements. Finally, the detailed electrochemical performance of 2-electrode and 2-electrode cells with reference based on N-chloroalkyl functionalized PILs is presented and compared to the operation of ECs based on [HN₂₂₂][TFSI].

The manuscript ends by a general conclusion, underlying the main results and information from this work and suggesting possible opportunities for further developments.

Chapter I

Literature review

1. Introduction

Electrochemical capacitors (ECs) are energy storage devices operating through a simple separation of charges at the electrode/electrolyte interface upon polarization of electrodes. Owing to the physical charge accumulation, they display exceptionally fast charging/discharging time, while providing high power output and excellent cyclic stability. It is believed that ECs fill the gap between conventional capacitors and batteries, performing with higher energy density than the former and higher power density than the latter [1, 2].

The first ECs utilizing electrical double-layer charging were developed by Becker with porous carbon electrodes in aqueous electrolyte; the invention patented in 1957 by General Electric [3] was not commercialized. A few years later, research conducted under the aegis of the SOHIO company resulted in two patents (1962 [4] and 1970 [5]) laying the foundation for many subsequent patents of ECs technology, and in 1978 the Nippon Electric Company (NEC), licensed by SOHIO, introduced a commercial device called NEC's SuperCapacitor. This trademark name spread becoming the commonly used term for ECs. Later on, over the years, other companies like Panasonic, ELNA, Nippon Chemi-Con (Japan), Maxwell (U.S.), CAP-XX (Australia), NESSCap (South Korea), Blue Solutions (formerly Batscap, France), Yunasko (Ukraine) and recently Skeleton Technology (Estonia) offering various technologies and constructions entered the market [6, 7]. The fast improvement in ECs performance placed them as a meaningful energy storage technology, while according to some forecasts the market value of ECs will amount to \$3.5 billion in 2020 [8].

2. Electrochemical Capacitors

Generally, ECs operate by two main mechanisms: i) electrostatic charge accumulation in an electrical double-layer (EDL) formed at the electrode-electrolyte interface or ii) quick faradaic reactions providing so-called pseudocapacitance [9]. ECs are also named supercapacitors or ultracapacitors, where the prefixes *super-* or *ultra-* originate from their huge capacitance values measured in farads in comparison to electrostatic capacitors whose capacitance values range from picofarads (pF) to few microfarads (μ F) or electrolytic capacitors displaying capacitance values in the range of microfarads (μ F). Another commonly accepted name of ECs is electrical double-layer capacitors (EDLCs) in reference to the elementary charge storage mechanism; however, this name is very often non-appropriately applied and should be essentially limited to systems employing organic electrolytes or aprotic

ionic liquids. Therefore, taking into account that other phenomena can be associated to EDL charging, the use of the name electrochemical capacitors is the most accurate [10, 11].

Presently, ECs are viewed as one of the most attractive devices for electrochemical energy storage due to their extremely fast charging time, measured in few seconds, and their relatively high energy density. The performance of ECs among other energy storage and conversion devices is illustrated in figure 1 by the *Ragone plot* correlating the specific power and specific energy. ECs are superior in terms of power density to most energy storage or conversion electrochemical devices such as batteries (referred to as accumulators, e.g. lead–acid battery) and fuel cells operating at ambient temperature, yet they display inferior energy density. Therefore, they are commonly hybridized with these devices to deliver high power and energy. Importantly, owing to the electrostatic charge storage without exchange of electrons, ECs exhibit a great cycle life, in contrast to accumulators where chemical changes lead to progressive degradation of electrodes.

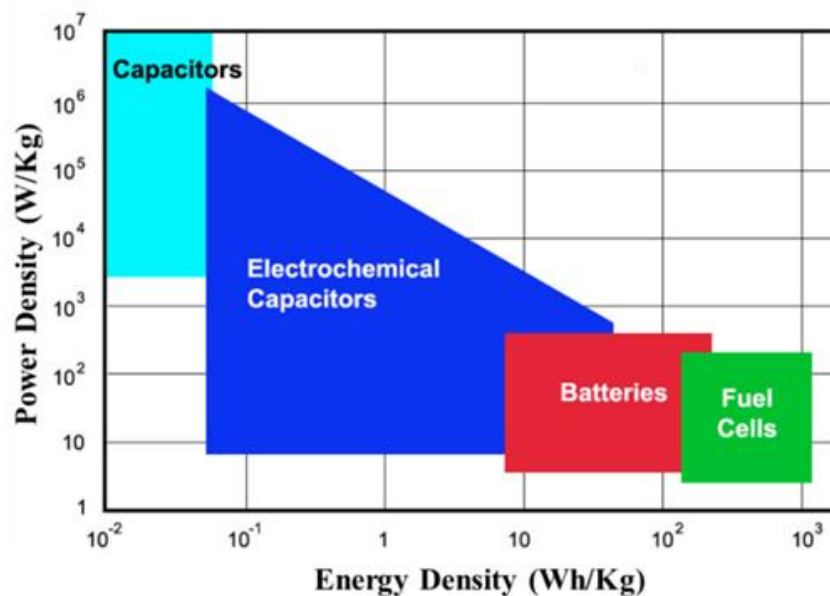


Fig. 1 Ragone plot characterizing energy and power available for a load from energy storage and/or conversion devices (from [12]).

So where are ECs applicable? Currently, the main demand comes from the automotive sector, where ECs can be coupled with accumulators as interconnected devices in electric vehicles (EVs) and hybrid electric vehicles (HEVs), including cars, buses, trucks, trams and trains. Conceptually, the short-term, high-power output of ECs supports harvesting energy from regenerative braking, which can then be re-utilized when high power is demanded.

As a result of such combination with ECs in a power supply system, the life of batteries can be extended. Since ECs are capable of storing “surge of energy”, they can also effectively support the stabilization of power grids affected by day-night fluctuations of the production/consumption ratio, as well as renewable energy engineering influenced by changeable weather conditions. Electrochemical capacitors can also serve in various back-up systems in a wide spectrum of portable devices like laptops, phones, cameras. Finally, a significant “space” for ECs application is located in space industry, which development requires devices for energy management and storage, as ECs perform with high power and durability over a wide temperature range from -40 °C to 70 °C (in contrast to e.g., batteries).

2.1. Principles and properties of electrochemical capacitors

2.1.1. The electrical double-layer

Fundamentally, the charge in electrochemical capacitors is stored in the EDL formed once a potential is applied and electrodes polarized. In the early concept of EDL proposed by Helmholtz in 1853, when an electrode (conducting material) is polarized, a charge separation occurs at the electrode/electrolyte interface, with ions of opposite sign diffusing from the bulk of the electrolyte and compensating the charge on the electrode surface (Fig. 2a). The model resembles a two-plate conventional capacitor of capacitance (C_H) as expressed in equation (1):

eq. 1

$$C_H = \frac{\varepsilon_0 \varepsilon_r S}{d}$$

where ε_0 is the vacuum permittivity ($\varepsilon_0 = 8.854 \cdot 10^{-12} \text{ F} \cdot \text{m}^{-1}$), ε_r the dielectric constant of the electrolyte, S the electrochemically accessible surface area and d the effective thickness of the double-layer. Since this simple EDL model was considered as rigid layers of opposite charges, and does not take into account the diffusion of ions in the solution and the interactions between the dipole moments of the solvent and the electrode, modifications were proposed by Gouy and Chapman who took into consideration the continuous distribution of electrolyte ions in the electrolyte solution driven by electrical and thermal fields. The Gouy-Chapman model is also known as diffuse model of the EDL in reference to the potential decreasing exponentially from the electrode surface to the fluid bulk (Fig. 2b [13]). However, the later model overestimates the EDL capacitance due to charged ions close to the electrode surface. Therefore, a combination of Helmholtz and Gouy-Chapman models was suggested by

Stern, who distinguished the inner region called the compact layer (named also Stern layer) and the diffuse layer (already defined in the Gouy–Chapman model) (Fig. 2c [13]). The two layers are equivalent to two capacitors in series, and the EDL capacitance C_{dl} can be expressed by equation 2:

eq. 2

$$\frac{1}{C_{dl}} = \frac{1}{C_H} + \frac{1}{C_{diff}}$$

where C_H is the Helmholtz (compact) double-layer capacitance and C_{diff} represents the diffusion region capacitance [13-15].

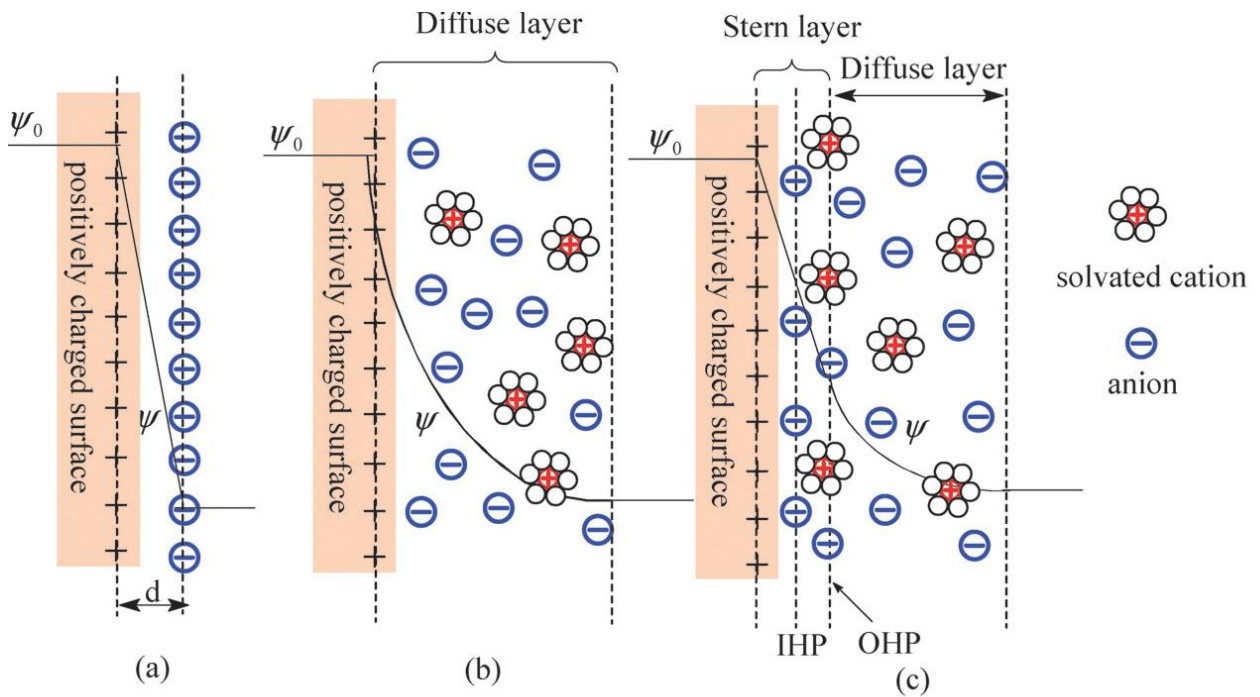


Fig. 2 Scheme of the electrical double-layer: (a) Helmholtz model, (b) Gouy-Chapman model, (c) Stern model. d stands for the DL distance in the Helmholtz model (a), whereas IHP and OHP stand for the inner Helmholtz plane and outer Helmholtz plane, accordingly, Ψ_0 and Ψ represent the potentials at the electrode surface and the electrode/electrolyte interface, respectively (from [13]).

Further, a Triple-Layer Model, taking into account that ions can be dehydrated in the vicinity of the electrode and specifically adsorbed onto it, was proposed by three groups: Esin and Markov [16], Grahame [17], Devanathan [18]. In consequence, the ions create a strongly attached “inner layer” (determined by their gravity centers) between the electrode surface and the Helmholtz layer. The specific adsorption of ions is explained by different types of electrical interactions between the electrode and ions: electric field forces, image forces,

dispersion forces, and electronic or repulsive forces [15]. Another model, nowadays commonly acknowledged and considering a greater effect of the solvent, was proposed by Bockris, Devanathan and Müller (also called water-dipole model in reference to the predominance of water as a solvent for electrochemical reactions) [19]. It states that polar solvents (such as water) interact with the electrode leading to the orientation of their dipoles creating a molecular layer of polarized solvent on the electrode surface. This layer remains on the surface and, due to competitive adsorption, includes specifically adsorbed ions and non-specifically adsorbed counterions. The differentiation arising from the two types of adsorbed ions leads to the division into inner Helmholtz plane (IHP) passing through the centers of gravity of specifically adsorbed ions (possibly partially desolvated) and outer Helmholtz plane (OHP) determined by the centers of gravity of electrostatically adsorbed counterions (Fig. 3) [15].

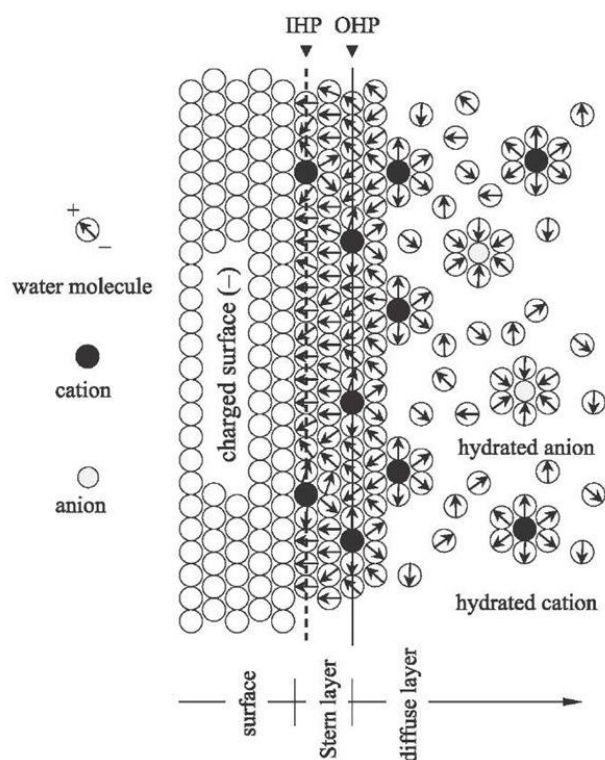


Fig. 3 The Bockris, Devanathan and Müller EDL model (from [20]).

2.1.2. Construction of an electrochemical capacitor

Generally, the most typical EC system involves a symmetric configuration of two equal, commonly activated carbon (AC) based electrodes at the interface with metallic current collectors and separated by an ion-conductive but electronically insulating film soaked with

an electrolyte (Fig. 4). Accordingly, when an electric potential difference is applied between the electrodes (or when an electric current is passed), the system is charged, inducing the attraction of anions on the positive electrode and cations on the negative one, and forming the EDL interfacial region. The simplest equivalent circuit of this construction is represented in figure 4 by two capacitors in series, where R_s stays for resistors in series and R_f for charge transfer resistance, i.e. the resistance to faradaic currents at the electrode surface. Hence, the overall capacitance (C) of the system is given by equation 3:

eq. 3

$$\frac{1}{C} = \frac{1}{C_+} + \frac{1}{C_-}$$

where C_+ and C_- represent the capacitance of the positive and negative electrodes, respectively. According to equation 3, the capacitance of the system is essentially controlled by the electrode with the smallest capacitance [14].

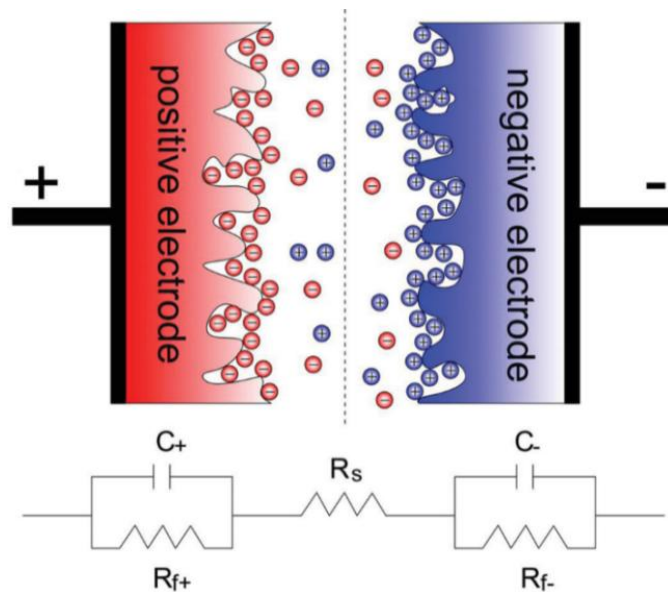


Fig. 4 Scheme of the charged state of an AC-based symmetric EDLC and representation of the corresponding equivalent circuit (R_s stays for resistors in series, R_f for the resistance to faradaic current at the electrode surface and C for capacitors) (from [14]).

2.1.3. Energy and power of electrochemical capacitors

The above introduced *Ragone plot* (Fig. 1) characterizes energy and power available for a load from energy storage or conversion devices; these two parameters will be discussed with respect to ECs. The stored specific energy E ($\text{Wh}\cdot\text{kg}^{-1}$), is expressed in equation (eq. 4):

eq. 4

$$E = \frac{1}{2} \cdot C \cdot U^2$$

where C (F) is capacitance and U (V) the maximum cell voltage. As indicated in equation 1, the capacitance depends on the properties of electrodes and electrolyte. A significant increase of the surface area of the electrode/electrolyte interface is generally realized by applying high surface area activated carbons (ACs) with specific surface area (SSA) ranging from 1000 to 2500 $\text{m}^2 \cdot \text{g}^{-1}$. At the same time, owing to the small size of ions, the distance between charges is very short, thus the effective thickness of the double-layer small and estimated to be around 1 nm. Hence, capacitance values of approximately 100 $\text{F} \cdot \text{g}^{-1}$ can be easily displayed [14]. In turn, the maximum voltage is mainly controlled by the stability potential window of the applied electrolyte. The cyclic voltammograms (CVs) of AC/AC symmetric capacitors in figure 5 show that the maximum voltage in aqueous acidic electrolyte is around 0.6-0.8 V, and it increases in organic electrolyte (tetraethylammonium tetrafluoroborate, $[\text{N}_{2222}][\text{BF}_4]$ later abbreviated as $[\text{TEA}][\text{BF}_4]$), to reach its highest value exceeding even 3 V in aprotic ionic liquid, here trihexyldodecylphosphonium bis[(trifluoromethyl)sulfonyl]imide, $[\text{P}_{666,14}][\text{TFSI}]$ [21]. Therefore, the application of ionic liquids (ILs) is claimed to be an attractive way of increasing the specific energy of ECs, yet their inferior transport properties may restrict power of the system in comparison to aqueous and organic electrolytes.

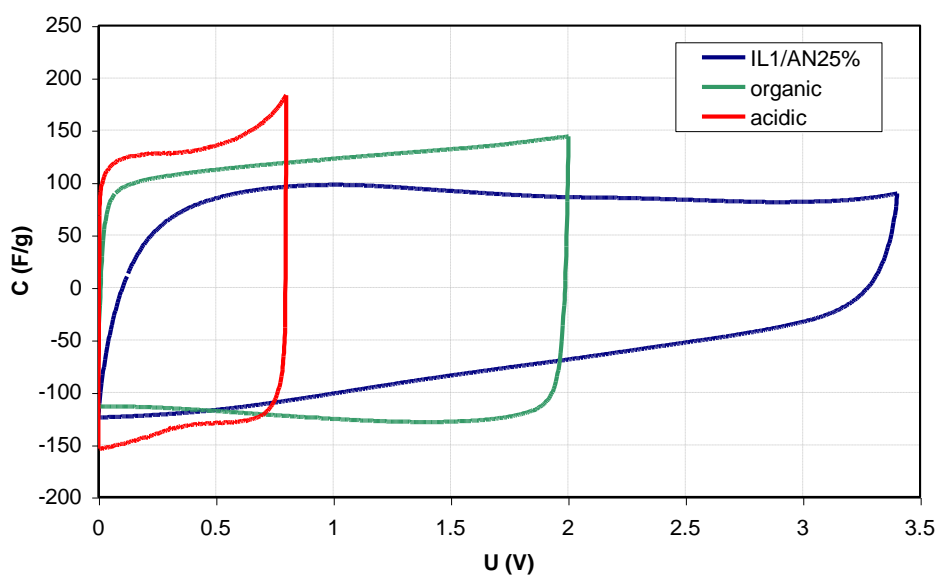


Fig. 5 Cyclic voltammograms ($5 \text{ mV} \cdot \text{s}^{-1}$) of AC-based symmetric ECs operating in three different electrolytes: $1 \text{ mol} \cdot \text{L}^{-1} \text{H}_2\text{SO}_4$, $1 \text{ mol} \cdot \text{L}^{-1} [\text{TEA}][\text{BF}_4]/\text{ACN}$ and $[\text{P}_{666,14}][\text{TFSI}]/\text{ACN}$ (25% wt.) (from [21]).

The maximum specific power P of ECs is indicated in equation (5):

eq. 5

$$P = \frac{U^2}{4R_S}$$

where U (V) is the maximum cell voltage and R_S (Ω) represents the equivalent series resistance (ESR) of the cell. The influence of maximum voltage is the same as for energy, whereas the ESR value is the sum of few factors including: the electrolyte resistance, the electronic resistance of the electrode material, the interface resistance between the electrode and the current collector, the ionic resistance resulting from ions moving in small pores (micropores) of the electrode - called the diffusion resistance [2].

2.1.4. Electrochemical pseudocapacitance

Pseudocapacitance refers to electric energy stored electrochemically through fast reversible faradaic reactions, while the system presents the characteristics of a capacitor, for example a rectangular cyclic voltammogram; it is generally related with an electron charge transfer between the electrode material and the electrolyte. Yet, the term “pseudocapacitance” is very often misused, especially in hybrid ECs employing one battery-like electrode. Recently, this issue has been widely discussed in few papers, indicating a clear division between “pseudocapacitance” and battery-like storage and imposing an appropriate nomenclature [22-26]. Accordingly, the following classification was suggested:

- *non-faradaic, capacitive storage*: typical EDL charging involving electrostatic and non-faradic processes, where no electron transfer occurs across the electrode/electrolyte interface and no chemical and physical changes inside the solid phase of the electrode are observed; in experimental terms such processes are characterized by rectangular cyclic voltammograms (CVs) and linear (or triangular) galvanostatic charge and discharge (GC/GD) profiles;
- *faradaic, capacitive-like storage (pseudocapacitance)*: charge storage attributed to phenomena involving the electrosorption of ions accompanied by surface redox reactions and electron transfer (reduction or oxidation changes in the electrode materials); just like EDL charging, it is characterized by rectangular CVs and linear/triangular GC/GD profiles, therefore it is called pseudo-capacitance. It is characterized by a constant current flow as a result of redox active sites mutual interactions, due to the short separation

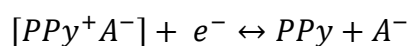
between them and/or good electronic conductivity. In the case of metal oxides, it refers to the merger of energy states into a broad band with negligible differences between the neighboring states. In the case of electrically conducting polymers (ECPs) it is realized by the electron delocalization of conjugated chemical bonds, whose electron orbitals (between neighboring atoms) overlap, causing continuous electron transfer over a wide range of potential;

- *non-capacitive faradaic storage* is observed with redox active materials undergoing a reversible or quasi-reversible electron transfer reaction employing well separated or isolated sites and is reflected in non-linear potential (or voltage) changes. As a result, current peaks are formed on the CVs and non-linear GC/GD profiles are displayed. This kind of electrochemical performance resembles the operating characteristics of rechargeable batteries, and capacitance values should not be calculated from such data [24]. However, the coupling of a battery-like electrode with an EDL type one is a common strategy and acknowledged as hybrid capacitor.

The pseudocapacitive phenomena contribute to enhance capacitance and in turn the specific energy of ECs. Pseudocapacitance itself may vary depending on its origin. The most typical pseudocapacitive electrode materials are classified and described below.

- **Electrically conducting polymers (ECPs)** – are mainly represented by polyaniline (PANI), polypyrrole (PPy), polythiophene (PT), poly[3-methylthiophene] (PMT) and poly[3,4-ethylenedioxythiophene] (PEDOT). The charge storage involving electrodes based on ECPs occurs through redox reactions related with the π -conjugated polymer chains. This oxidation/reduction process in fact is ascribed as insertion/extraction or doping/dedoping, while counter ions of the electrolyte are reversibly transported to the polymer chain according to equation (6) shown in the example of PPy:

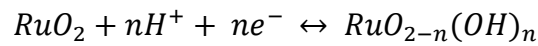
eq. 6



Importantly, the charging - doping process occurs in the electrode bulk, providing high values of specific capacitance [27, 28]. However, the counter ions transfer during cycling provokes volumetric changes of the polymer structure and may lead to mechanical degradation of the electrode material. Therefore, attention has been directed to conducting polymer/carbon composites (carbon black, carbon fibers, carbon nanotubes or graphene) in order to improve the resiliency and conductivity of ECPs based electrodes [27, 29-33].

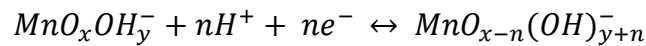
- **Transition metal oxides** predominantly include ruthenium oxide (RuO₂) [23, 34, 35] and manganese oxides (MnO₂) [23, 36]. The most remarkable values of gravimetric capacitance are reported for RuO₂ electrodes (practically 750 F·g⁻¹ for electrodeposited RuO₂ and 800-1200 F·g⁻¹ for hydrous RuO₂/carbon composite compared to the theoretical value of 1358 F·g⁻¹ [37]), which combine great electrical conductivity (3·10² S·cm⁻¹ [37]) and high cyclic stability owing to the excellent reversibility of the faradaic processes. The reaction takes place according to equation (7):

eq. 7



indicating the necessity of employing a protic medium to obtain the desired faradaic contribution. Yet, the high price of ruthenium oxide limits its commercial usage. Significantly cheaper manganese oxide (MnO₂) has been widely recognized and tested [36-38]. It can be found in many forms, therein diverse crystallographic structures like α , β , γ , λ -MnO₂. In the case of the amorphous form (a-MnO₂·nH₂O), the faradaic reaction is described in equation (8):

eq. 8



where $MnO_xOH_y^-$ and $MnO_{x-n}(OH)_{y+n}^-$ correspond to high and low oxidation states of manganese. Apart from MnO₂ a few other low cost materials such as Fe₃O₄ and V₂O₅ were examined [36, 37]. Due to the low electrical conductivity of most oxides, composites with carbon conductive backbones (carbon nanotubes, graphene) must be prepared to improve the capacitance properties of these materials [39].

- **Carbons enriched in heteroatoms** like oxygen, nitrogen also display a pseudocapacitive effect in protic electrolytes enhancing the total capacitance. This will be discussed in detail in section 2.2.4.

2.2. Carbon based electrodes

Carbon based electrodes have been extensively tailored and harnessed for their use in ECs technology owing to the diversity of carbon dimensionalities as well as the versatility of its structures/nanotextures and morphologies. Carbons continuously dominate other electrode materials for ECs, since they have been coined to this application in the early patent from the late 50's of the previous century. Their advantages include high electronic conductivity

combined with well-developed specific surface area as well as good chemical and thermal stability. Simultaneously they are ecofriendly, lightweight and cost effective materials.

2.2.1. Variety of carbon materials structures and forms

Carbon is one of the most common elements on Earth occurring itself in four crystalline allotropic forms: carbyne, fullerenes (made of fullenene molecules), graphite and diamond, characterized by sp^1 , 'distorted' sp^2 , sp^2 , and sp^3 hybridization of carbon, respectively. The first two representatives are manmade, whereas the other two occur naturally or maybe also manmade. Apart from inorganic carbon materials, this element is abundant in the form of organic compounds – hydrocarbons, both aliphatic and aromatic ones [2, 40]. The above introduced representation of organic and inorganic families in reference to their bonding is shown below in figure 6.

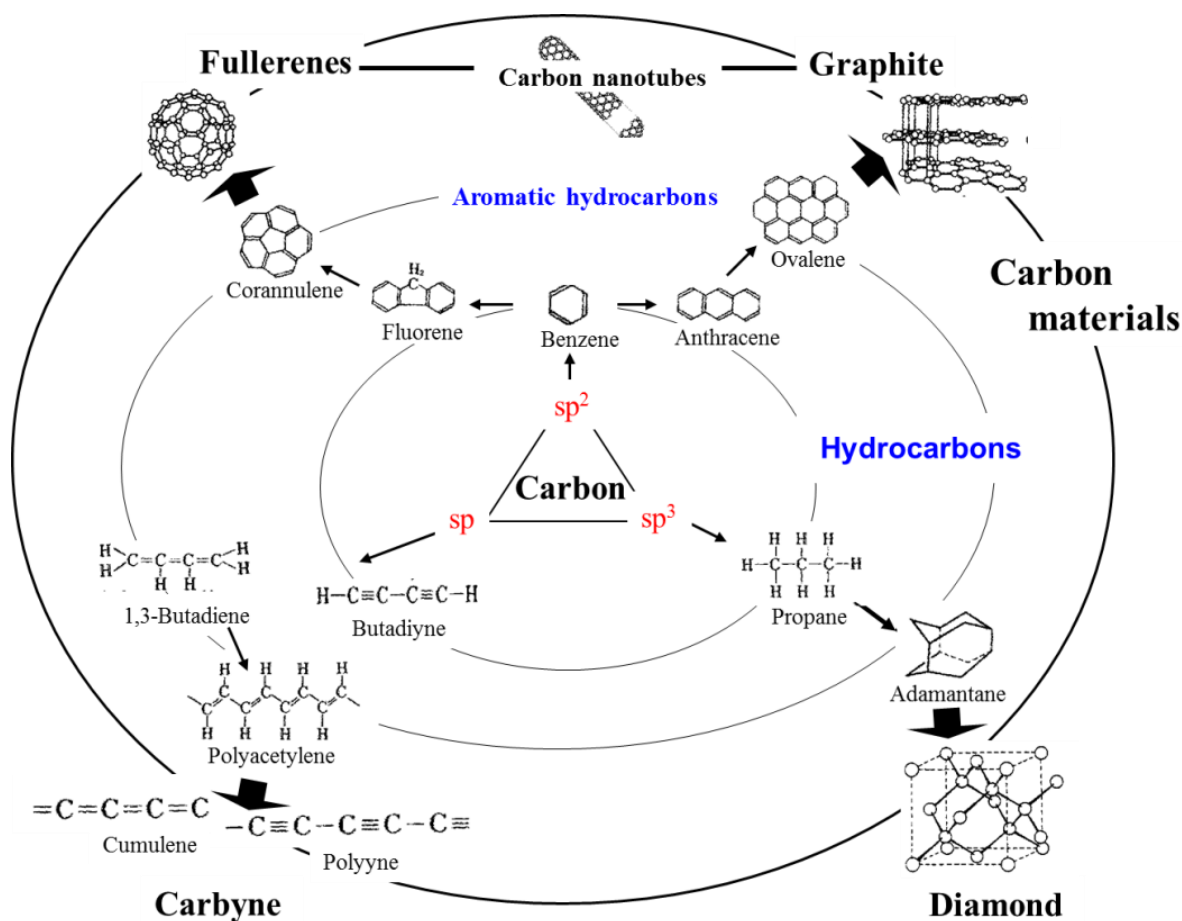
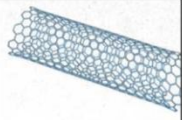
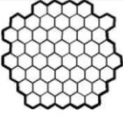
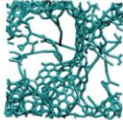
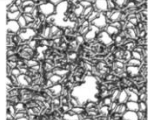


Fig. 6 Scheme of organic and inorganic families of carbon materials in dependence on carbon hybridization (from [40]).

In terms of dimensionality, the carbon materials applied in electrochemical capacitors vary from 0D to 3D, as shown in table 1.

Table 1 Representation of different carbon electrode materials used in electrochemical capacitors (from [41]).

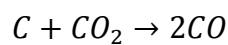
Material	Carbon onions	Carbon nanotubes	Graphene	Activated carbon	Carbide derived carbon	Templated carbon
Dimensionality	0-D	1-D	2-D	3-D	3-D	3-D
Conductivity	High	High	High	Low	Moderate	Low
Volumetric Capacitance	Low	Low	Moderate	High	High	Low
Cost	High	High	Moderate	Low	Moderate	High
Structure						

- **Carbon onions** also known as onion-like carbons (OLCs) represent 0-dimensional carbons. They consist of concentric layered and spherically closed carbon shells looking like an onion structure. One of the most known methods of carbon onions synthesis is the annealing of nanodiamond (1300-1800 °C) resulting in an external specific surface area (SSA) ranging from 400 to 600 m²·g⁻¹ depending on the treatment temperature or up to 820 m²·g⁻¹ after activation with KOH [42]. Carbon onions were tested for ECs in aqueous and organic electrolytes, and their excellent properties were reflected in great power capabilities combined with remarkable capacitance retention at high current densities, even at the level of 200 mA·cm⁻² (15 A·g⁻¹) [43, 44]. Such good electrochemical properties are related to the fact that only the outer-surface between carbon onion particles is involved in EDL formation.
- **Carbon nanotubes (CNTs)** are 1-D materials which owe their name from their extremely high length-to-diameter ratio, where their diameter varies from 2 to 50 nm. CNTs walls are formed from sp² bonded carbons, whereas their graphene cylinder structure occurs in a form of individual Single-Wall Nano Tubes (SWNTs) or Multi-Walled Nano Tubes (MWNTs) comprising several concentric layers. Typically, CNTs may be synthesized by carbon-arc discharge, laser ablation of carbon or chemical vapor deposition (mostly on catalytic particles) [45, 46]. Nevertheless, the capacitance values for electrodes of untreated CNTs are rather low, i.e., from 5 to 40 F·g⁻¹ [47].
- **Graphene** represents a 2D structure consisting of sp²-bonded carbon atoms in planar monolayers (ideally one atom-thick). It is characterized by a high conductivity (owing to enhanced electron mobility), great mechanical strength and chemical stability as well as

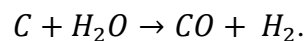
high and entirely accessible surface, with theoretical specific surface area value of $2670 \text{ m}^2 \cdot \text{g}^{-1}$ [48]. In practice, the preparation method is based on chemical exfoliation of graphite with strong oxidants, giving graphite oxide which is further reduced giving so-called graphene, which in fact contains relatively high amount of residual oxygen and has tendency to restack [49]. Consequently, a huge variety of materials, with more or less oxygen amount and number of stacked layers have been described in the literature and investigated for ECs application in various electrolytes, giving extremely scarce values of capacitance [50]. For example, a capacitance of $100 \text{ F} \cdot \text{g}^{-1}$ has been claimed in non-aqueous electrolyte [51], which actually is not higher than the values found for ACs. Nonetheless, pure graphene is actually never synthesized and it additionally exhibits a very low density which leads in turn to low values of volumetric capacitance.

- **Activated carbons (ACs)** are the most dominating and extensively investigated materials in the ECs application thanks to their high SSA and low cost. They are classified as 3D structures consisting of sp^2 and some sp^3 carbon atoms [2, 40]. ACs can be found in a few widespread forms like powders, carbon fabrics (cloth), felts and monoliths. ACs powders are produced by solid phase carbonization, where carbon-rich precursors are heat treated in inert atmosphere, and further physically or chemically activated to develop the surface area by creating a porous network in the bulk of the carbon particles. The most widely used natural precursors include cokes, pitches, wood, fruit shells (e.g. coconut shells), whereas synthetic precursors are polymers. In physical activation, the carbonized precursor is oxidized with CO_2 or steam according to equations (9) and (10) [40, 52, 53]:

eq. 9



eq. 10



Chemical activation is accomplished by hot acids (H_3PO_4), alkaline (KOH) or inorganic salts (ZnCl_2) [40, 53]. Activation may result in SSA as high as $3000 \text{ m}^2 \cdot \text{g}^{-1}$, but in practice the useful SSA for EDL formation is in the range from 1000 to $2000 \text{ m}^2 \cdot \text{g}^{-1}$, because only a part of the pores are accessible to ions. It is due to a limited pore size control in the activation process causing not optimal pore size distribution. Activated carbon fabrics (ACFs) are more convenient to handle in comparison to powders as they do not require

binder to form electrodes. ACFs are usually obtained from thermosetting organic materials such as rayon, phenolic resin and poly(acrylonitrile) (PAN). They combine SSA in the range from 1000 to 2000 $\text{m}^2\cdot\text{g}^{-1}$ similarly to AC powders with higher conductivity (200-1000 $\text{S}\cdot\text{cm}^{-1}$); however, the price and low volumetric density [54] of ACFs restrict their wider application in ECs [52]. It is worth also to mention that, with some materials from the biomass rich in group I and II elements, such as tobacco wastes, carbonization and self-activation can be realized simultaneously during the thermal treatment, giving rise to nanoporous carbons displaying remarkable values of capacitance of 167 $\text{F}\cdot\text{g}^{-1}$ and 141 $\text{F}\cdot\text{g}^{-1}$ in aqueous ($1\text{ mol}\cdot\text{L}^{-1}$ Li_2SO_4) and organic ($1\text{ mol}\cdot\text{L}^{-1}$ $[\text{TEA}][\text{BF}_4]$ in ACN) electrolytes, respectively [55].

- **Carbide derived carbons (CDCs)** are 3D carbon materials, very comparable to activated carbons, which can be obtained with slightly better controlled pore size distribution. They are generally synthesized from carbide precursors, e.g., SiC, TiC, Mo_2C , VC, from which the metal or metalloid is extracted by chlorine treatment at high temperature. The pore size can be finely tuned by controlling the temperature, giving rise to electrode materials with optimized capacitance (see also section 2.2.3) [56].
- **Templated carbons** are another type of tailorable carbons with well-controlled pore size. The template technique can be divided in hard- and soft-templating. The former synthesis is based on the carbonization of an organic compound in the confined nanospace of an inorganic template, followed by removal of the template framework by dissolution, e.g., in HF, in order to extract the created carbon. The latter method involves a self-assembly process accomplished by co-condensation and carbonization of the soft template, yet without issue of the template removal [57].
- **Carbon xerogels** are classified as materials with designable mesopore size. They are formed from the sol-gel route just like carbon aerogels or carbon cryogels. As shown in figure 7, the method involves the poly-condensation reaction of resorcinol and formaldehyde, where the formation of a three-dimensional polymer in solvent (gelation step) is followed by the crosslinking of formerly formed polymer clusters (curing). Finally, the drying step determines the characteristics of the final product - subcritical drying (conventional) in xerogels, supercritical in aerogels and freezing in cryogels. Overall, the synthesis of xerogels is a relatively simple, fast, economical and environmentally friendly method of obtaining materials characterized by large mesopores

(between 2 and 50 nm) and high SSA (in range of 1500-2200 m²·g⁻¹). Nevertheless, this preparation process leads to the presence of capillary forces destroying a part of their initial porosity. Another drawback is their low density values resulting in low volumetric capacitance [58].

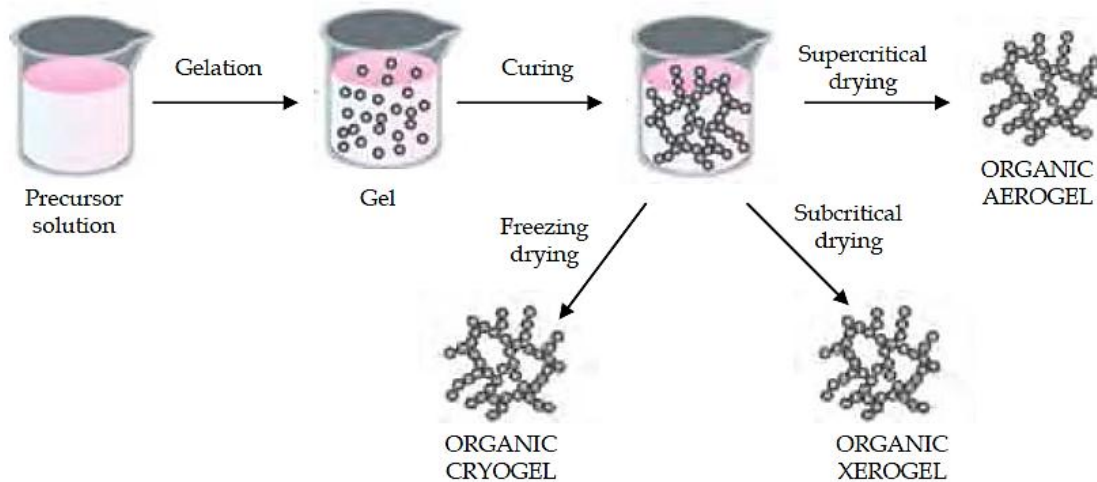


Fig. 7 Schematic representation of the steps involved in the synthesis of organic gels (from [58]).

- Apart from the above introduced representatives of various dimensionality, great interest has been attracted by **carbon blacks (CBs)** having nearly spherical carbon particles of small size, which makes them a completely different structure from ACs. CBs have a chemically clean (oxygen free) surface and display high conductivity (typically in the range from 10⁻¹ to 10² S·cm⁻¹). They are obtained by partial combustion or thermal decomposition of hydrocarbons (usually gases, oils or distillates from petroleum sources). During the initial stage of carbon black formation, primary particles are developed followed by their fusion into three-dimensional branched clusters called aggregates. If the number of primary particles per aggregate is high, CB is classified as a high structure, whereas a low structure CB has only weak aggregation. CBs display a low density compared to activated carbons, and they are mainly used as conductive additives in electrodes [2]. CBs have been also used as active material of ECs, and similarly to CNTs, only the outer surface is utilized for EDL formation. As a result, CB-based ECs can operate at frequencies higher than systems based on ACs where micropores are essentially involved [59].

A wide range of carbon materials of sundry kinds – porous, planar, exohedral – categorized by their structural/textural properties has been presented above. However, to meet the requirements of application in ECs, these properties must be well established and correlated with the electrolyte characteristics, including ions/pores size matching, in order to gain the best performance of the device, understood as high capacitance, energy and power.

2.2.2. Porous texture of carbon materials

The first models of carbon structure/nanotexture were coined by Franklin [60], based on X-ray diffraction data, and led to assume that carbon consists of cross-linked graphene structural units, either oriented randomly (non-graphitizing carbon) or well-ordered (graphitizing carbon), as shown in figure 8. However, the X-ray diffraction technique does not account for individual graphene layers, and consequently these models present only the organized part of the material made of stacks of few graphene layers [61].

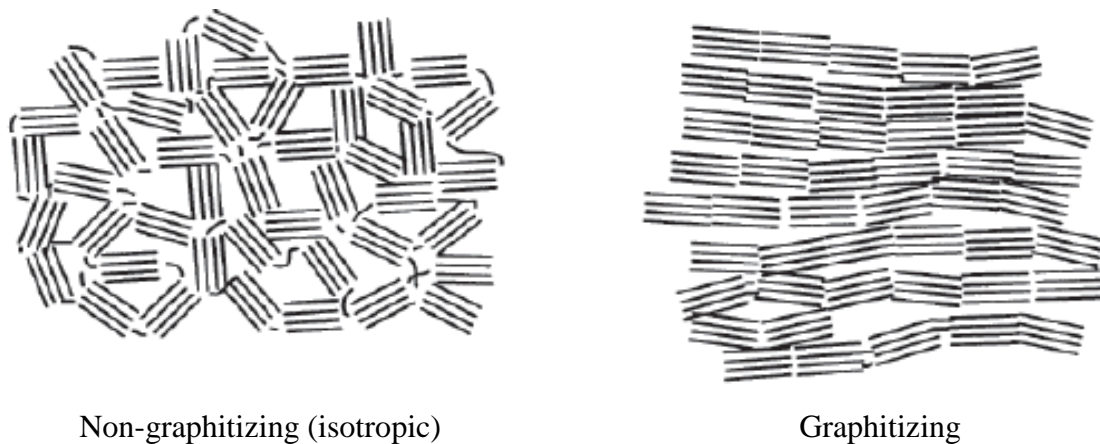


Fig. 8 Franklin's representations of non-graphitizing, partially graphitizing and graphitizing carbon (from [61]).

Afterwards, the first transmission electron microscopy imaging on a non-graphitizing carbon prepared from polyvinylidene chloride (PVDC) by Ban et al. suggested a model of entangled-ribbon like structure/texture (Fig. 9) [14]. Later on, to explain the structure and textural entanglement of units it has been proposed that some atoms in the graphene structure are sp^3 -hybridized, and that ACs have fullerene-like fragments including pentagons and/or other non-hexagonal rings [14, 52], giving rise to curvature as shown in figure 10.

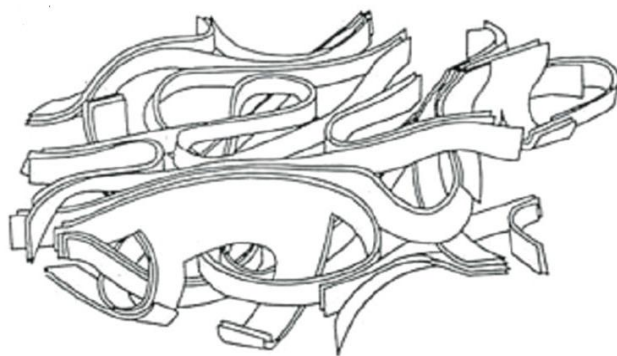


Fig. 9 Nanotextural model of a PVDC derived non-graphitizable AC according to Ban et al. (from [14]).

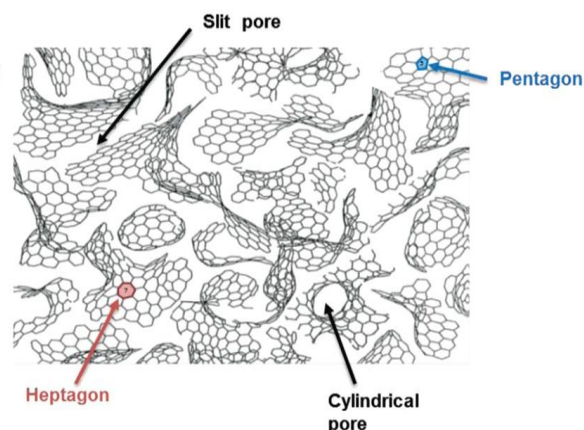


Fig. 10 Nanotextural and structural model of a non-graphitizable carbon proposed by Harris et al. (from [14]).

Basically, depending on the preparation process, ACs may include a wide range of pores, which are defined and divided accordingly to IUPAC recommendations in macropores which are larger than 50 nm, mesopores in the range between 2 and 50 nm, and micropores smaller than 2 nm [62]. A schematic representation of the various types of pores in a granule is given in figure 11.

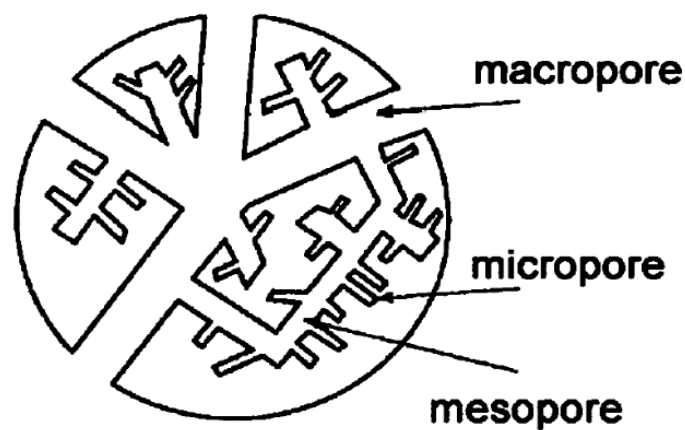


Fig. 11 Scheme of pores in an activated carbon granule (from [63]).

The main technique used for determining the porous texture of ACs (Specific surface area –SSA, pore volume, pore size distribution –PSD) is nitrogen adsorption at 77 K, enabling to get so-called nitrogen adsorption isotherms. The most common calculation procedure of the SSA from the adsorption isotherm is based on the BET method (Brunauer-Emmett-Teller). According to IUPAC, six types of isotherms may be distinguished as presented in figure 12 [62].

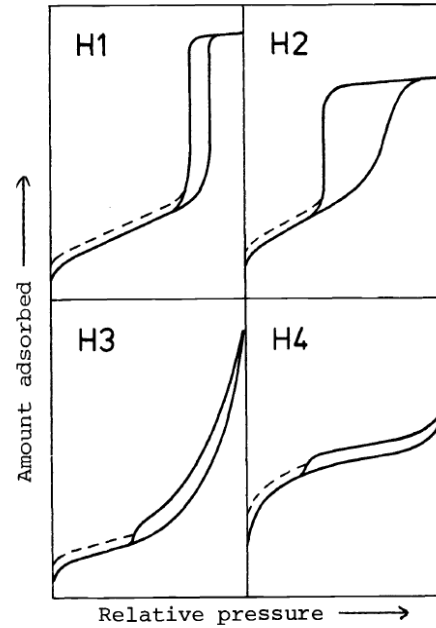
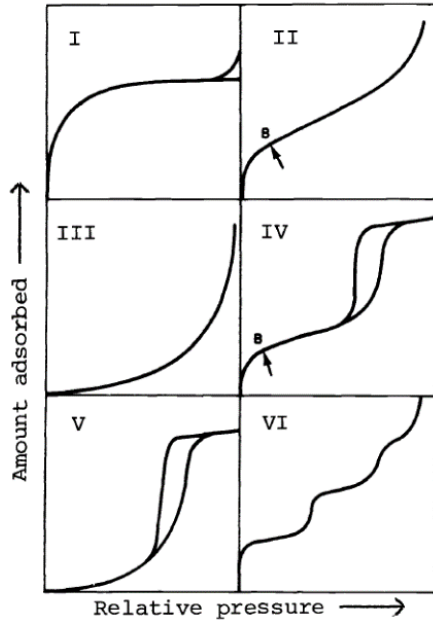


Fig. 12 Types of adsorption/desorption isotherms Fig. 13 Different types of hysteresis (from [62]).
(from [62]).

The type I isotherm is assigned to porous materials having only micropores, where the maximum amount of gas adsorbed is reached without any inflection and the shape indicates the formation of only a monolayer. The type II isotherm is assigned to non-porous or macroporous materials; it depicts an unrestricted monolayer-multilayer formation in the adsorption process, where the point B indicates the completeness of monolayer formation and beginning of multilayer adsorption at high relative pressure (shown as the linear middle section of the isotherm). The type III isotherm is associated with both non-porous and microporous adsorbents, however having weaker adsorbate-adsorbent interactions unlike adsorbate molecules in the liquid state. Overall, the isotherms I, II and III show a full reversibility during the desorption step, which is attributed to materials without mesopores. In turn, in presence of mesopores, a hysteresis loop between adsorption and desorption is clearly visible and is characteristic for type IV and V isotherms. This phenomenon can be explained by a different mechanism of mesopores filling and emptying, so-called capillary condensation. Consequently, the type IV isotherm is a variation of the type II one presenting the adsorption of a monolayer at low pressure, followed by the formation of a multilayer in mesopores at high pressure. Similarly, the type V isotherm merges the characteristics of type III isotherm at low pressure with capillary condensation occurring in mesopores. The type VI isotherm is a particular case, where the step-like shape represents the gradual formation of individual adsorbate layers [62].

In addition, important information about the pore structure is provided by the kind of hysteresis in type IV and V isotherms, and is classified into 4 types by IUPAC as presented in figure 13. The type H1 represents porous materials with a narrow distribution of regular, well-defined cylindrical-like pores. H2 hysteresis is associated with ill-defined shape pores and wide pore size distribution resulting in the effect of pore blocking and/or percolation phenomena. H3 hysteresis suggests the presence of slit-shaped pores; however, a reliable evaluation of pore size distribution or total pore volume is restricted. H4 hysteresis corresponds to narrow slit pores within the micropore region of the material combining micropores and mesopores [64].

2.2.3. Effect of carbon porous texture on EDLC performance

Throughout the years of ECs development, a great attention has been paid to the understanding of their capacitive properties in dependence on porous texture characteristics, especially considering the relationship presented in eq. 1. The main findings, trends and correlations, are introduced below.

2.2.3.1. Dependence between capacitance and measured SSA of ACs

One might expect (in accordance with eq. 1) some proportionality between the specific surface area measured by gas adsorption and the surface area of the electrode/electrolyte interface, hence that capacitance should increase proportionally to the SSA. Attempts to link the gravimetric capacitance with the calculated SSA have been widely reported, however, no straightforward linear correlation was established as shown in figure 14 [65]. It turned out that capacitance is proportional to S_{BET} for low values, and that it becomes almost constant for S_{BET} higher than 1200-1500 $\text{m}^2\cdot\text{g}^{-1}$. In fact, it has been demonstrated that S_{BET} is representative only for slit-shaped pores with width of 0.9 nm, whereas it underestimates the actual surface area for pores of lower size and overestimates it for pores of higher size [66], justifying the constant value of capacitance at high value of S_{BET} . As an alternative, capacitance was also plotted versus the specific surface area estimated by the density functional theory (DFT) and it resulted in slightly more accurate correlation, although a plateau of capacitance is maintained for S_{DFT} higher than 1500 $\text{m}^2\cdot\text{g}^{-1}$ [67].

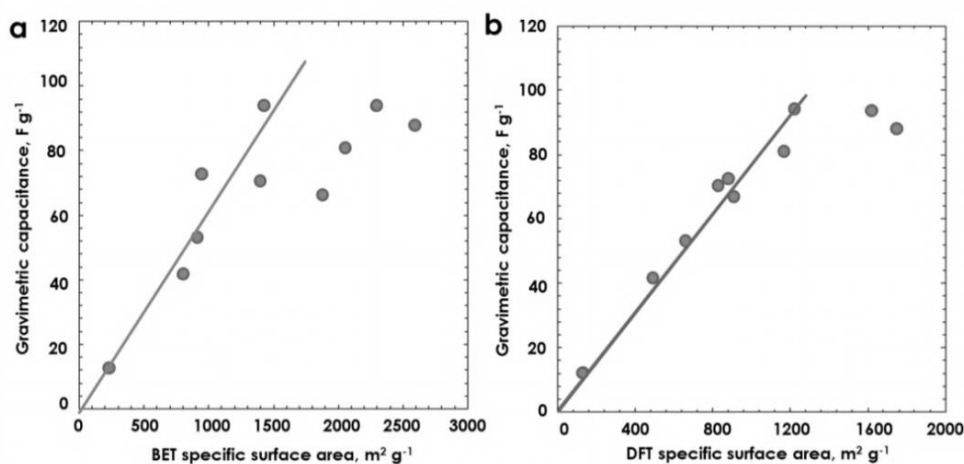


Fig. 14 Gravimetric capacitance plotted versus (a) S_{BET} and (b) S_{DFT} of a series of ACs (from [65]).

2.2.3.2. Impact of ions/pore matching on capacitance

Importantly, a part of SSA detected for ACs is inaccessible for electrolyte ions when the pore size is smaller than the ion size. As a consequence, ions are electrosorbed selectively and the phenomenon is called ion sieving. Nevertheless, it is difficult to figure out the ideal dimensions of both partners participating in EDL formation due to the fact that activated carbons are characterized by a broad pore size distribution, whereas the size of ions adsorbed in the EDL is speculative, depending whether they are solvated or not.

Therefore, for the considered purpose, solvent-free electrolytes consisting solely of ions, such as ionic liquids (ILs), were examined to ensure a more accurate interpretation. For a series of ILs coupling alkoxymethyltriethylphosphonium $[P_{666,R-O-1}]^+$ cations with bis[(trifluoromethyl)sulfonyl]imide $[TFSI]^-$ anion, it was reported that the capacitance decreases with increasing length of alkyl substituents in the phosphonium cation (R =propyl, butyl, heptyl and dodecyl), demonstrating the significance of the relationship between the cation size and accessible volume in dependence on pore size [68]. Such observations were confirmed in a subsequent study with a series of imidazolium-based ILs varying by the substituent length (ethyl, butyl, hexyl) on the cation [69].

The pore to ion size dependence was also tested by Largeot et al. using the same ionic liquid, namely 1-ethyl-3-methylimidazolium bis[(trifluoromethyl)sulfonyl]imide, $[C_2C_1Im][TFSI]$, with a series of Ti-CDCs of various average pore sizes (L_0) at 60 °C [70, 71]. A maximum of gravimetric capacitance ($F \cdot g^{-1}$) was observed for L_0 of 0.72 nm (Fig. 15a) which is close to the size of both ions (Fig. 15b), with minimal free space available

left. In reference to eq. 1, the good fitting of ions and pores size enables to minimize the distance between the pore wall and the center of the ion (d) and in turn to increase the capacitance. For pore size from 1.1 to 0.72 nm, there is only space for one ion, and capacitance increases as d decreases. For pores smaller than 0.72 nm, the sieving effect occurs and the capacitance decreases; however, since an average value is determined by gas adsorption, for L_0 lower than 0.72 nm, there is still a fraction of pores larger than this value which can accommodate ions, and consequently the capacitance does not drop immediately to zero.

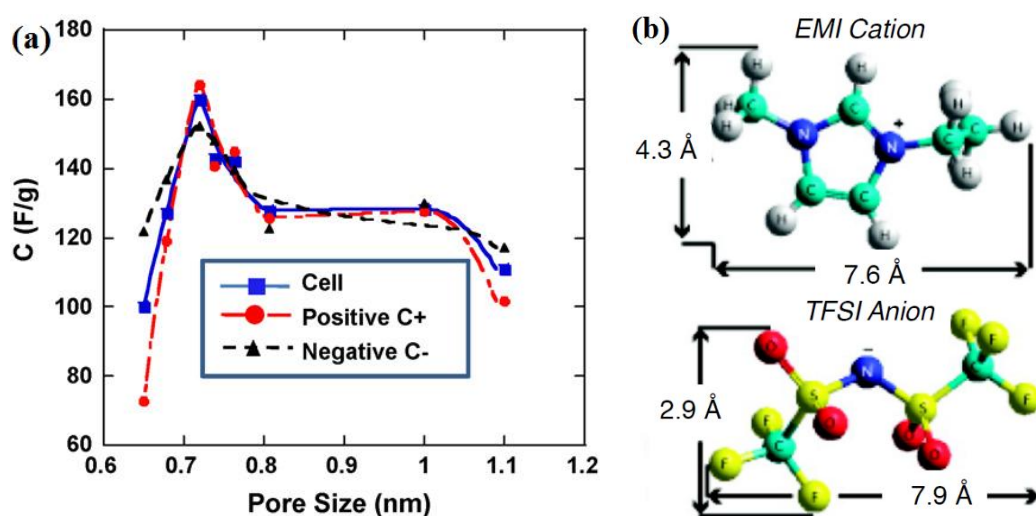


Fig. 15 (a) Gravimetric capacitance ($F \cdot g^{-1}$) versus average pore size of CDCs tested in neat $[C_2C_1Im][TFSI]$ electrolyte at 60 °C (from [71]); (b) structural representation and size of $[C_2C_1Im]^+$ and $[TFSI]^-$ (from [70]).

2.2.3.3. Desolvation effect

In the aftermath, a number of experimental data obtained with classical aqueous or organic electrolytes demonstrated different size of ions in the bulk electrolyte and in the pores of carbon. A linear relationship between the specific capacitance and the ultra-micropore volume (pores smaller than 0.7 – 0.8 nm, from CO_2 adsorption) of templated carbons was established for aqueous and organic electrolytes. Since ultramicropores are smaller than the size of solvated ions, this trend lead to postulate that ions must be at least partly desolvated to penetrate in such pores [72]. Such interpretation was further supported by data obtained with activated carbons and carbide derived carbons (CDCs) showing high capacitance values for pores smaller than 1 nm [73, 74].

Further tests on the pore size - ion size correlation accounting for the desolvation effect were carried out in a 2-electrode cell with RE in order to detect eventual differences

between electrodes [75]. Analogously, a substantial increase of system capacitance was observed for electrode materials with L_0 of 0.7-0.8 nm, yet different contribution from positive and negative electrode was revealed. Since the size of solvated $[\text{TEA}]^+$ cation of 1.30 nm is too big for pores of 0.7-0.8 nm and the size of bare (desolvated) $[\text{TEA}]^+$ cation of 0.67 nm is close to this range, the occurrence of desolvation was reasoned.

The above suggestion of ions desolvation, occurring when ions are confined in small micropores, has been directly confirmed by nuclear magnetic resonance (NMR) on electrodes extracted from AC/AC capacitors in organic electrolyte after charging at various voltage values. The molar proportion of each electrolyte component ($[\text{TEA}]^+$, $[\text{BF}_4]^-$ and ACN) was plotted vs. the applied voltage for the positive and negative electrodes (Fig. 16). Initially, in uncharged state, the electrolyte components are adsorbed in carbon porosity. With the increase of cell voltage, the molar proportion of $[\text{TEA}]^+$ increases in the negative electrode, whereas the ACN amount decreases to become negligible at ~ 2.3 V, proving the desolvation of cations. In turn, during electrosorption of $[\text{BF}_4]^-$ anions in the positive electrode, no significant change of ACN amount is observed. This almost constant amount of ACN is explained by the desorption of bulky $[\text{TEA}]^+$ cations leaving enough space to accommodate the less bulky $[\text{BF}_4]^-$ anions and ACN molecules [76]. A recent study on charge storage mechanism in microporous electrodes using *in-situ* NMR spectroscopy and electrochemical quartz crystal microbalance (EQCM) confirms ion desolvation, and also shows that, under positive polarization, cations are exchanged for anions, whereas for negative polarization, cations adsorption dominates [77].

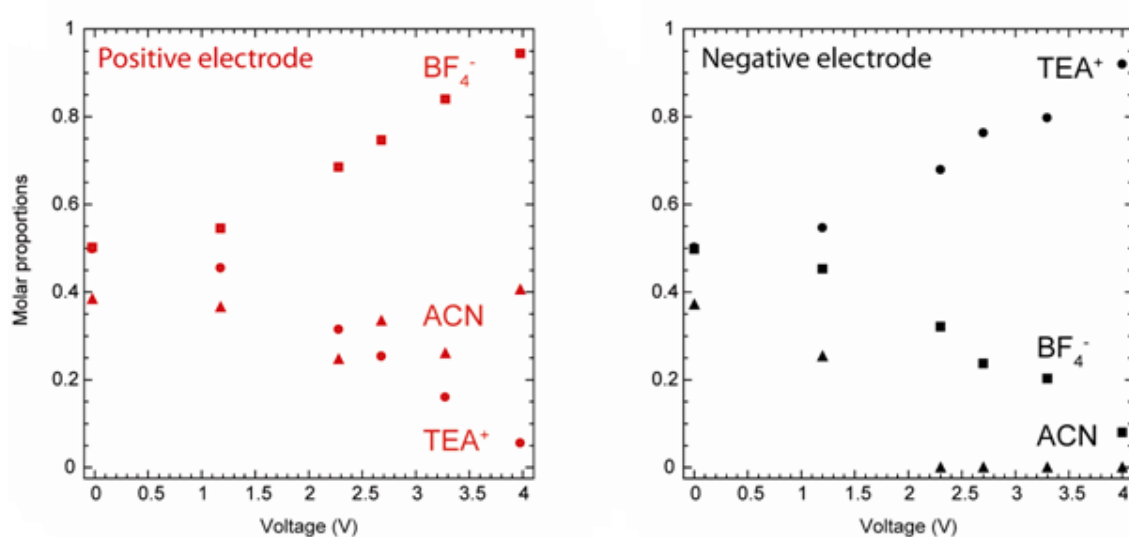


Fig. 16 Molar proportions of $[\text{TEA}]^+$, $[\text{BF}_4]^-$ and ACN in the positive and negative electrodes of an electrochemical capacitor in $1 \text{ mol}\cdot\text{L}^{-1}$ $[\text{TEA}][\text{BF}_4]/\text{ACN}$ after polarization at various voltage values (from [76]).

2.2.3.4. Saturation of electrode porosity

Since an increase of capacitance can be effectively realized by matching the size of pores to the size of desolvated ions, ACs with strongly controlled PSD have been widely tested. However, as proven by Mysyk et al. [78, 79], if at the same time the SSA is not developed sufficiently, the available active surface becomes fully saturated with ions before reaching the maximum voltage, thus capacitance decays. For example, two-electrode cells were realized with a pitch-derived activated carbon PC ($S_{\text{DFT}} = 1434 \text{ m}^2 \cdot \text{g}^{-1}$) of average pore size close to the size of desolvated cations ($L_0 = 0.7 \text{ nm}$) and a viscose-derived activated carbon VC ($S_{\text{DFT}} = 2160 \text{ m}^2 \cdot \text{g}^{-1}$ and $L_0 = 1.4 \text{ nm}$) using 1.5 mol L^{-1} $[\text{TEA}][\text{BF}_4]$ in ACN as electrolyte. In case of the PC-based EC, the cyclic voltammograms show a decay of capacitive current at voltage higher than ca 1.2 V, whereas such decay does not occur with the VC carbon where the CV characterizes a typical EDL charging (Fig. 17). The tendency was confirmed by non-linear galvanostatic profiles with the carbon PC despite low current applied [78]. It has been proved that, when the voltage reaches ca. 1.2 V with PC, there is almost no more room left available to accommodate additional ions. Such difference of performance between the two carbons can be easily explained by considering the specific surface area which corresponds to pores larger than the diameter of the $[\text{TEA}]^+$ cation (0.67 nm), i.e. $S_{\text{DFT} > 0.67} = 198 \text{ m}^2 \cdot \text{g}^{-1}$ and $964 \text{ m}^2 \cdot \text{g}^{-1}$ for PC and VC, respectively. Similar results were observed when organic electrolytes ($[\text{N}_{\text{RRRR}}][\text{TFSI}]$ in ACN) with increasing length of alkyl substituent (R) in the $[\text{N}_{\text{RRRR}}]^+$ cations were harnessed [79]. Hence, beside optimal adjustment of pores to ions size, sufficiently high pore volume is an additional criterion to ensure the capacitor performance.

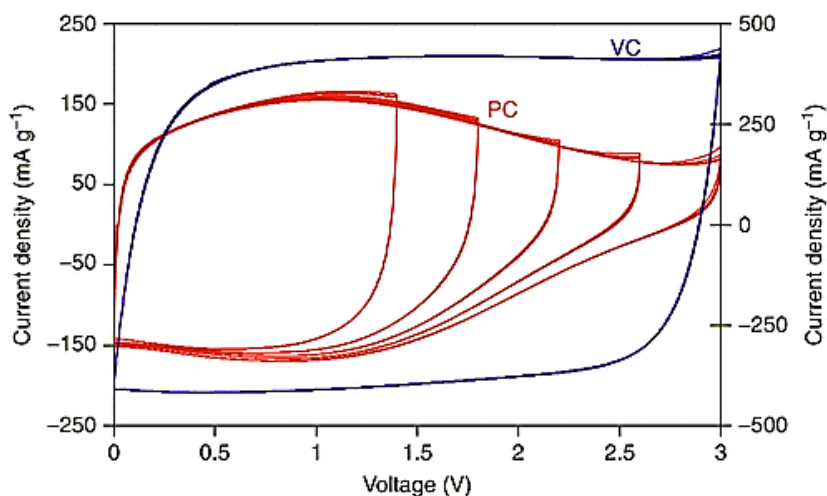


Fig. 17 Cyclic voltammograms of ECs based on PC and VC carbons (left- Y-axis or right- Y-axis for current, respectively) (from [78]).

2.2.4. Surface functionality of carbon materials and faradaic contributions

Carbon materials do not only consist of elemental carbon, and they also incorporate heteroatoms, mainly oxygen and hydrogen, followed by nitrogen, sulfur or some halogens. These heteroatoms are mostly bound to carbon at edges of aromatic sheets or at defect positions [2]. Figure 18 shows the oxygenated and nitrogenated functionalities generally identified at the surface of nanoporous carbons [80]. The presence of heteroatoms in porous carbons is linked to their occurrence in the starting materials and partial remaining in the structure after carbonization. They can be also incorporated by post-treatment of the materials or, in case of oxygen, simply during their exposure to air [2].

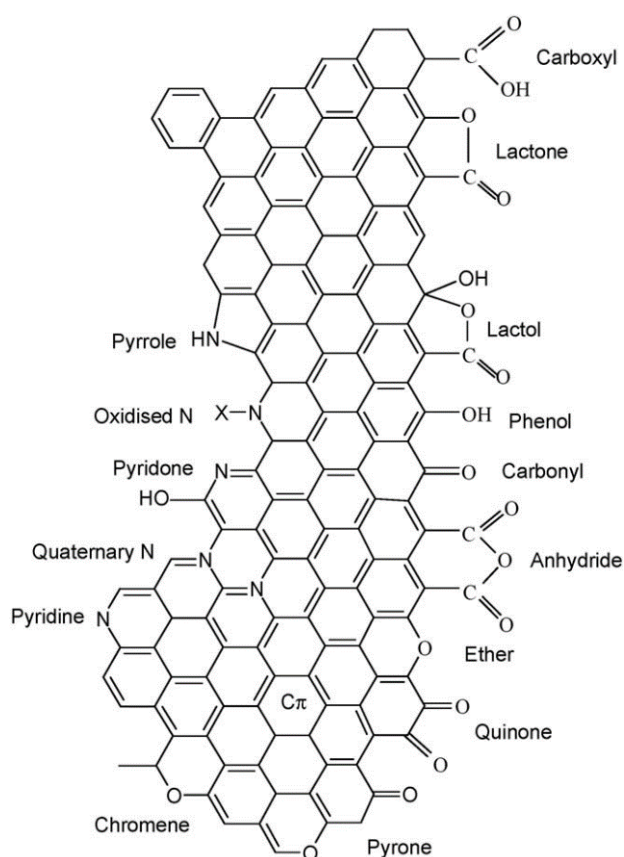


Fig. 18 Most common nitrogen- and oxygen-based surface groups occurring on ACs (from [80]).

In general, it is widely accepted that the elimination of oxygen from the carbon electrodes used in organic electrolyte improves their stability and cycle life [81]. However, when using aqueous electrolytes, the occurrence of oxygenated groups might be beneficial as the presence of hydrophilic surface groups improves the wettability and capacitance. Particular oxygenated or/and nitrogenated functionalities on the activated carbon surface may also have a positive effect on ECs performance owing to their participation in reversible redox

reactions, as for example the quinone/hydroquinone redox couple [82-85]. When oxygenated groups are created on carbon nanofibers in a controlled oxidation process, hydroxyl groups also contribute to reversible faradaic reactions [86].

Many types of ACs with nitrogenated and oxygenated surface groups have been extensively investigated to enhance the capacitance performance in aqueous electrolyte [27]. The effects of nitrogen to carbon ratio and nitrogen to oxygen ratio, specific chemical arrangement, strength of surface functional groups, their acidity/basicity and their location on the carbon surface have been examined [87]. ACs with comparable porous texture but with increasing nitrogen content demonstrate a proportional increase of capacitance in aqueous medium, in contrast to almost constant capacitance values in an organic aprotic electrolyte, which was attributed to redox reactions of the nitrogenated functionality with available protons [88]. However, if nitrogen incorporation causes a decrease of SSA, capacitance may not increase [89, 90].

Besides, the capacitance of carbons can be enhanced by developing the electroactive surface area, i.e. the amount of porosity filled with the electrolyte [81]. In case of organic electrolytes, this can be done through the creation of hydrophobic surface functionality by physical methods like elevated temperature treatment in inert atmosphere to eliminate hydrophilic functional groups, or chemical methods such as the addition of surfactants enriching carbon in hydrophobic functional groups or gas phase fluorination [91]. For example, carbon aerogels were treated with vinyltrimethoxysilane in order to enrich them with hydrophobic functional groups, without significant effect on SSA. As a result, capacitance increased by $10 \text{ F}\cdot\text{g}^{-1}$ with no faradaic contribution, ESR decreased, and the cyclic stability did not deteriorate in comparison to the non-functionalized analogue [92].

2.3. Conventional electrolytes

In general, the classification of electrolytes for ECs includes aqueous electrolytes, organic electrolytes and more recently ionic liquids. The first two, organic and aqueous, are known as conventional electrolytes in reference to their well-established status and common application in commercial ECs.

The requirements for electrolytes are governed by factors involved in the equations of specific energy (eq. 4) and power (eq. 5), e.g., operating voltage, resistance and capacitance. Therefore, the following electrolyte properties are desired: a wide electrochemical stability window, high conductivity, a good ionic adsorption into carbon porosity to provide higher

capacitance and all together to maximize energy and power with good cyclability. Importantly, an operation temperature range at least between -40/+60 °C is required, while the safety under these conditions should be maintained. Finally, economic and environmental considerations like reasonable cost and low toxicity, respectively, should be taken into account.

2.3.1. Aqueous electrolytes

Aqueous electrolytes are generally solutions of acids, bases and neutral salts with limited operational voltage originating from water decomposition – 1.23 V [93]. In practice, these stability limits are different, from strictly narrower for H₂SO₄ and KOH aqueous electrolytes with less than 1.0 V [94] to wider limits of neutral aqueous electrolytes where the voltage was reported to be enlarged to 1.6 V in 0.5 mol·L⁻¹ Na₂SO₄ [95, 96] or even to 2.0 V in 1 mol·L⁻¹ Li₂SO₄ on gold current collectors [97, 98]. Nonetheless, when using cheaper stainless steel current collectors, the system could operate with high cycle life at 1.5 V in 1 mol·L⁻¹ Li₂SO₄ [99]. Despite voltage limitations as compared to organic electrolytes, the advantages of aqueous electrolyte application include high ionic conductivity (e.g., 409 mS·cm⁻¹ for 1 mol·L⁻¹ H₂SO₄, 508 mS·cm⁻¹ for 6 mol·L⁻¹ KOH and 91 mS·cm⁻¹ for 1 mol·L⁻¹ Na₂SO₄ [100]) contributing to lower ESR values as well as very low cost induced by manufacturing conditions under air atmosphere. The capacitance values in aqueous electrolytes may significantly vary from 135 F·g⁻¹ (0.2 A·g⁻¹) in 0.5 mol·L⁻¹ Na₂SO₄ with commercial AC [95] to 180 F·g⁻¹ in 1 mol·L⁻¹ Li₂SO₄ once AC with adjusted porosity is applied [97]. However, the possible corrosion of current collectors may restrict the application of cheap metals, such as stainless steel or nickel, and/or affect the cycle life of the devices.

It is worth also reminding, as described in sections 2.1.4. and 2.2.4, that aqueous electrolytes serve as proton source for pseudocapacitive processes based on transition metal oxides and conducting polymers as well as for faradaic contribution of heteroatom-doped ACs.

A particular aspect of using aqueous electrolyte is hydrogen electrosorption also called hydrogen storage. It is an electrochemical reversible reaction with nascent hydrogen chemisorption [101] in the nanopores of AC, whereas its mechanism strongly depends on the electrolyte acidity/basicity.

Hydrogen electroadsorption may be characterized by cyclic voltammetry with progressive shifting of negative vertex potential, as shown in Fig. 19 for experiments conducted in 3 mol·L⁻¹ H₂SO₄ (Fig. 19b) and 3 mol·L⁻¹ KOH (Fig. 19a) aqueous solutions [102]. For high values of vertex potential, regardless of the electrolyte type, only EDL charging reflected in the *quasi*-rectangular shape of CV loops is observed; hydrated potassium cations in 3 mol·L⁻¹ KOH or solvated hydronium cations, H₃O⁺, in 3 mol·L⁻¹ H₂SO₄ are adsorbed/desorbed. Further decreasing the vertex potential leads to water electrodecomposition and hydrogen generation followed by its immediate electroadsorption, which is proven by the increase of cathodic current demonstrated by a leap in the CV profiles. Once polarization is reversed, hydrogen is desorbed resulting in its oxidation and recombination into water as indicated by a corresponding “hump” in CVs during the positive scan.

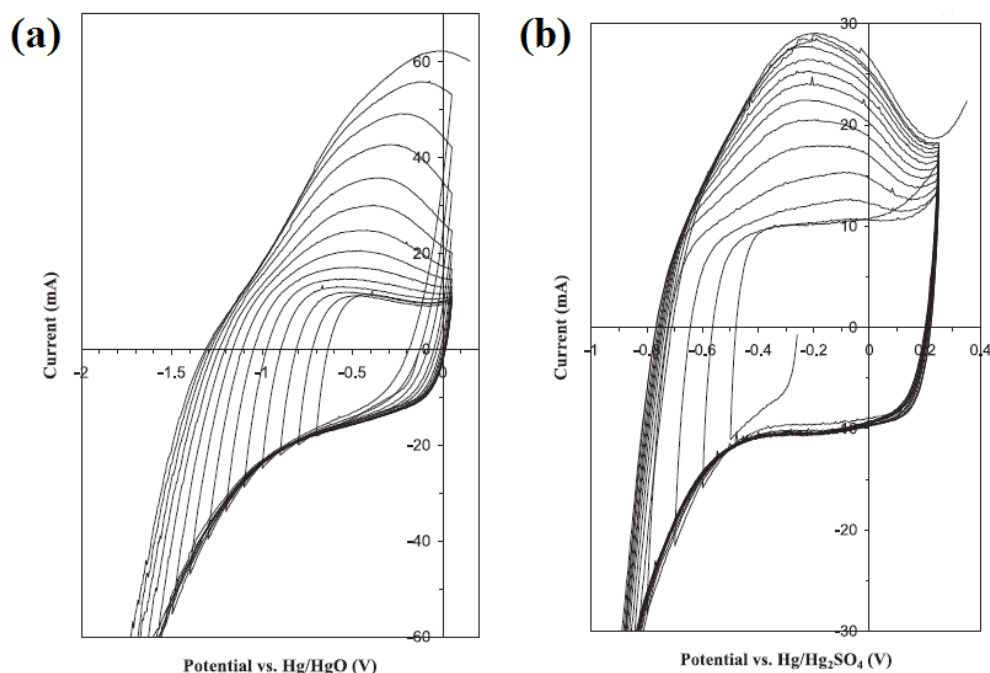
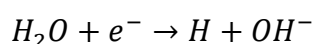


Fig. 19 Dependence of the voltammetry characteristics of AC on electrolyte acidity/basicity: (a) electroadsorption from 3 mol·L⁻¹ KOH; (b) electroadsorption from 3 mol·L⁻¹ H₂SO₄ (from [102]).

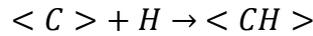
The comparison of the plots in figure 19 reveals a marked contrast between the two electrolytic media which is associated with the particular pathways of hydrogen generation and differences in energy of the C-H bond. The proton source in alkaline solution is water itself as indicated in equation 11 (Volmer reaction):

eq. 11



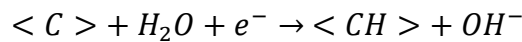
and the released nascent hydrogen is chemisorbed in the active carbon material represented by $\langle C \rangle$:

eq. 12



where $\langle CH \rangle$ stands for hydrogen chemisorbed on the AC surface. All the process is summarized by equation (13):

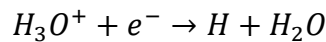
eq. 13



and, in turn, anodic oxidation leads to reversible hydrogen desorption.

In acidic medium protons are supplied from hydronium cations in accordance with eq. 14:

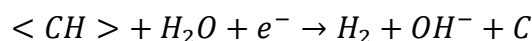
eq. 14



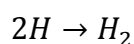
and then nascent hydrogen is electrosorbed on carbon as described in eq. 12. In alkaline solution, one must also observe that the desorption peak shifts toward more positive values when the vertex potential decreases, indicating stronger hydrogen bonding to carbon (Fig. 19a). It means that the electrosorbed hydrogen diffuses further into the bulk of carbon occupying sites with higher energy. In the case of acidic electrolyte, the position of the desorption hump is constant (Fig. 19b), which indicates that protons are directly available in the electrode/electrolyte interface for the redox processes [102]; it facilitates hydrogen oxidation if scanning is reversed.

If hydrogen adsorption energy is not sufficiently high, the competitive reactions of its recombination to molecular hydrogen occur. Di-hydrogen can evolve by electrochemical or chemical way in accordance with Heyrovski (eq. 15) or Tafel (eq. 16) reactions, respectively.

eq. 15



eq. 16



Overall, the experimental data pointed out that the efficiency of the sorption process depends on the electrolyte type, and that higher amounts of stored hydrogen were measured

for KOH based solutions owing to higher overpotential of $\langle H_{ad} \rangle$ recombination to di-hydrogen than in H_2SO_4 [102].

The effect of electrolyte pH on the local retention of electrochemically sorbed hydrogen was later studied by Chun and Whitacre [103]. They utilized electrolytes based on $0.5 \text{ mol}\cdot\text{L}^{-1} \text{ Na}_2\text{SO}_4$ with variably adjusted pH (by addition of $1 \text{ mol}\cdot\text{L}^{-1} \text{ H}_2\text{SO}_4$ or $1 \text{ mol}\cdot\text{L}^{-1} \text{ NaOH}$) ranging from 1.89 to 10.48. It turned out that intermediate pH solutions (3.95, 6.06 and 7.99) displayed the lowest hydrogen evolution potentials, as opposed to the electrolytes with extreme pHs (1.89 and 10.48). During charging, the *in-situ* measured pH of the almost neutral solutions approached 11 due to OH^- evolution according to eq. 11, whereas it remained unchanged in the most alkali and acidic solutions which are self-buffered. The pH increase in case of neutral electrolytes promotes hydrogen adsorption and its diffusion into the bulk of carbon in preference to the hydrogen evolution; as a result, greater hydrogen amount is stored [103].

Using KOH solution, the activation energy of hydrogen desorption is $110 \text{ kJ}\cdot\text{mol}^{-1}$, suggesting a weak chemisorption [101]. Accordingly, the sorption/desorption kinetics is accelerated at elevated temperature ($60 \text{ }^\circ\text{C}$), and the amount of reversibly stored hydrogen is greater than at room temperature [101, 104]. Additionally, such parameters as porous carbon texture and its surface chemistry were examined pointing out to the preference of microporous ACs with pores width of $\sim 0.6 \text{ nm}$ [105] as well as the advantage of surface-clean ACs over materials with functional groups participating to side reactions, thus limiting the effectiveness of hydrogen storage [106].

2.3.2. Organic electrolytes

Organic electrolytes are solutions of quaternary ammonium salts, usually tetraethylammonium tetrafluoroborate [TEA][BF_4], in organic solvents such as anhydrous acetonitrile (ACN) or propylene carbonate (PC). Symmetric ECs in these electrolytes display higher operating voltages of 2.2-3.0 V [93], mostly 2.5-2.8 V [107], but lower specific capacitance ($100\text{-}150 \text{ F}\cdot\text{g}^{-1}$) in comparison to aqueous electrolytes. Owing to this high voltage and stored energy, commercial devices are essentially based on organic electrolyte [14], although such ECs are expensive and may display safety issues because of solvent volatility and flammability. For these reasons, as well as considering enlargement of operating voltage, alternative electrolytes using various solvents (sulfone, alkylated cyclic carbonates and adiponitrile) were investigated (Fig. 20). However, their transport properties, like conductivity

and viscosity, are relatively low causing power limitations. The application of lithium-ion battery (LIB) organic electrolytes was another examined substitute (Fig. 20). They contain a lithium salt, e.g., LiPF_6 , admixed with a combination of solvents typically employed in LIBs: ethylene carbonate (EC) providing high dielectric constant and dimethyl carbonate (DMC) ensuring low viscosity [108]. However, these electrolytes present some disadvantages, namely moisture sensitivity, and more importantly, reduction in safety. In search of overcoming the limitations originating from the solvent, ionic liquids are proposed as green and safe electrolytes for high voltage ECs [14].

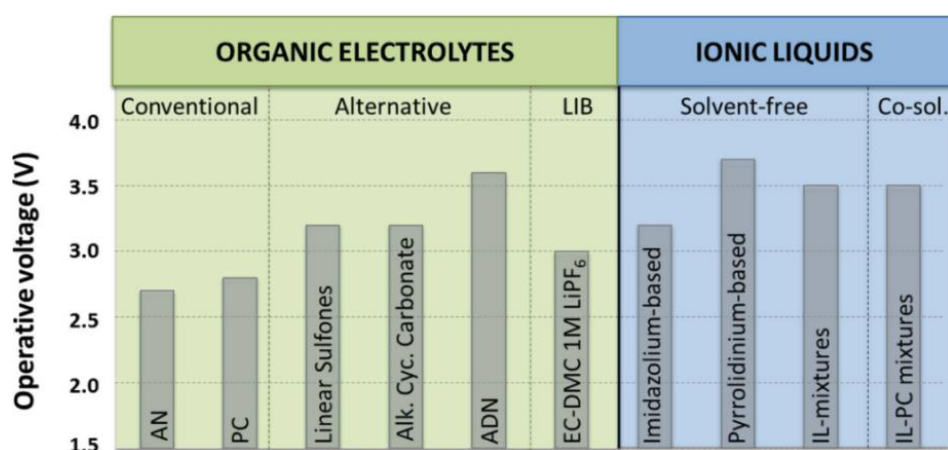


Fig. 20 Comparison of organic electrolytes (left) and ionic liquids (right) in reference to the maximum operational voltage of ECs (from [14]).

2.4. Ionic liquids as non-conventional electrolytes

Ionic Liquids (ILs) are defined as compounds consisting entirely and solely of ions (an organic cation and organic or inorganic anion) with melting point arbitrary limited to 100 °C. They possess a very wide liquid range and display the characteristic utility of molecular solvents [109-113]. ILs have been proposed as electrolytes for ECs because they have an ionic character, thereby conducting electric charges, while being liquid without any solvent causing safety issues and reducing the operational voltage.

2.4.1. General introduction on ionic liquids (ILs)

Ethylammonium nitrate with melting point of 12 °C, reported by Paul Walden in 1914, is generally accepted to be the first ionic liquid [114]. Nevertheless, most of the currently known ionic liquids originate directly from studies conducted at the U.S. Air Force Academy in the 60s of last century to replace the LiCl/KCl molten salt electrolyte used in thermal

batteries [109, 115]. The idea evolved gradually, starting from NaCl/AlCl₃ mixture and its eutectic composition with a melting point of 107 °C. The next step involved binary mixtures of chlorides of various ammonium cations (aliphatic and alicyclic) with aluminum chloride. As shown by the phase diagram of 1-ethyl-3-methylimidazolium chloride [C₂C₁Im][Cl] (abbreviated as [MeEtIm][Cl] in figure 21) mixed with AlCl₃, a freezing point below room temperature is observed for AlCl₃ molar fraction between 0.33 and 0.67 [115].

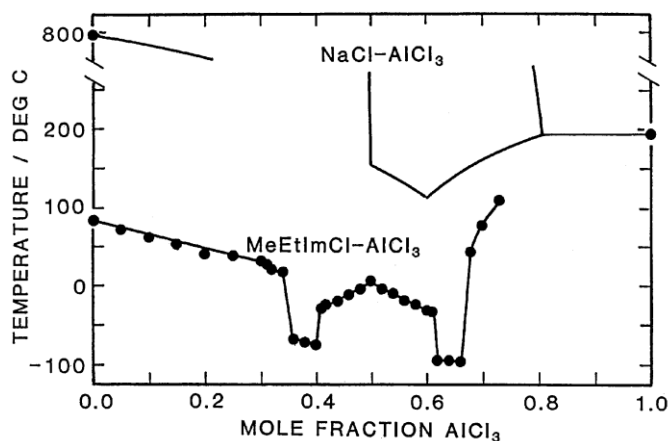


Fig. 21 Phase diagrams of the 1-ethyl-3-methylimidazolium chloride–aluminum chloride and sodium chloride–aluminum chloride mixtures (from [115]).

However, these chloroaluminate ionic liquids are sensitive to moisture, releasing corrosive HCl. The invention of water stable ionic liquids [116], also called non-chloroaluminate ILs [115], proved to be a milestone in this field. These ILs were obtained in a simple metathesis reaction (outside of a glove box) between dialkylimidazolium chlorides and salts containing the following anions: tetrafluoroborate [BF₄]⁻, hexafluorophosphate [PF₆]⁻, nitrate [NO₃]⁻, sulfate [SO₄]²⁻ and acetate [CH₃COO]⁻. Subsequently, other cation-anion couples were tested and described, where their matrix included the already introduced dialkylimidazolium cations as well as series of mono- and trialkylimidazolium cations combined with the above mentioned anions plus other ones like bromide [Br]⁻, dicyanamide [N(CN)₂]⁻, hydrogen sulfate [HSO₄]⁻, iodate [IO₃]⁻, trifluoromethanesulfonate [CF₃SO₃]⁻, bis[(trifluoromethyl)sulfonyl]amide [N(CF₃SO₂)₂]⁻ with acronym [TFSI]⁻ [111, 115]. The abundance of chemical structures serving as cation and anion leads to almost unlimited possibilities of adjusting the physicochemical parameters of ILs. Roughly, the number of possible cation-anion combinations is estimated to be 10¹⁸. Currently, the main suppliers of commercial ILs are: Merck, BASF, Cytec, Scionix, Solvent Innovation, IoLiTec, Solvionic and Sigma-Aldrich.

Apart from the historical division between chloroaluminate and non-chloroaluminate, ILs can be classified into three broad categories: aprotic ionic liquids (AILs), protic ionic liquids (PILs) and zwitterionic liquids (ZILs) as illustrated figure 22 [117].

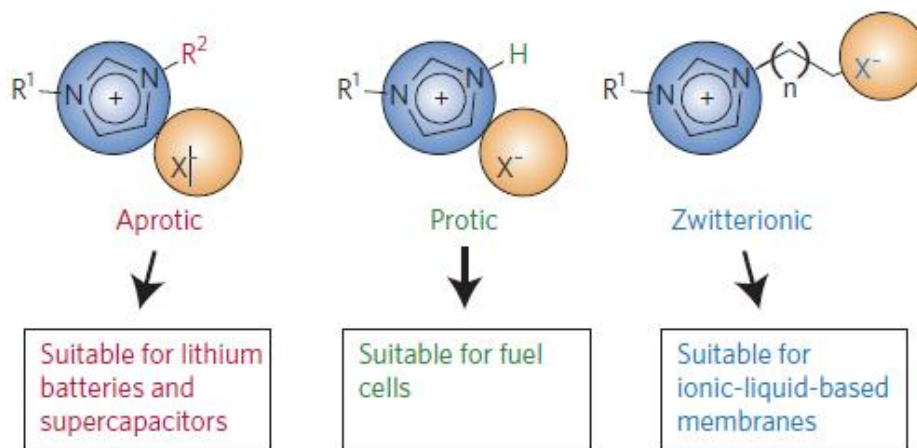


Fig. 22 Classes of ionic liquids (aprotic ionic liquids, protic ionic liquids and zwitterionic liquids) and their preferential electrochemical energy applications (from [117]).

- AILs consist of a positively charged cation and negatively charged counterion, where depending on the type of central atom the cations may be ammonium [118, 119], phosphonium [21, 120] or sulphonium [121-123] (with four or three alkyl substituents, respectively) (See Fig. 23).

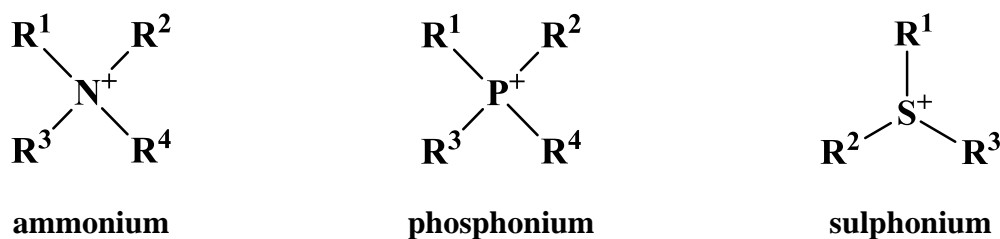


Fig. 23 The three common cation types used in ILs differing by their central heteroatom. R^1 , R^2 , R^3 and R^4 stand for substituents, which may be various alkyl $CH_3(CH_2)_n$ (where $n=0,1,2,3..$) or aryl groups.

Considering that ammonium ILs are the most commonly investigated ones, a further classification includes ILs with sp^3 -hybridized nitrogen like tetraalkylammonium [124], N-dialkylpiperidinium [125], N-dialkylpyrrolidinium [126-127], N-dialkylmorpholinium [128] or sp^2 -hybridized nitrogen like N-alkylpyridinium, N,N-dialkylimidazolium and triazolium [129] presented in figure 24.

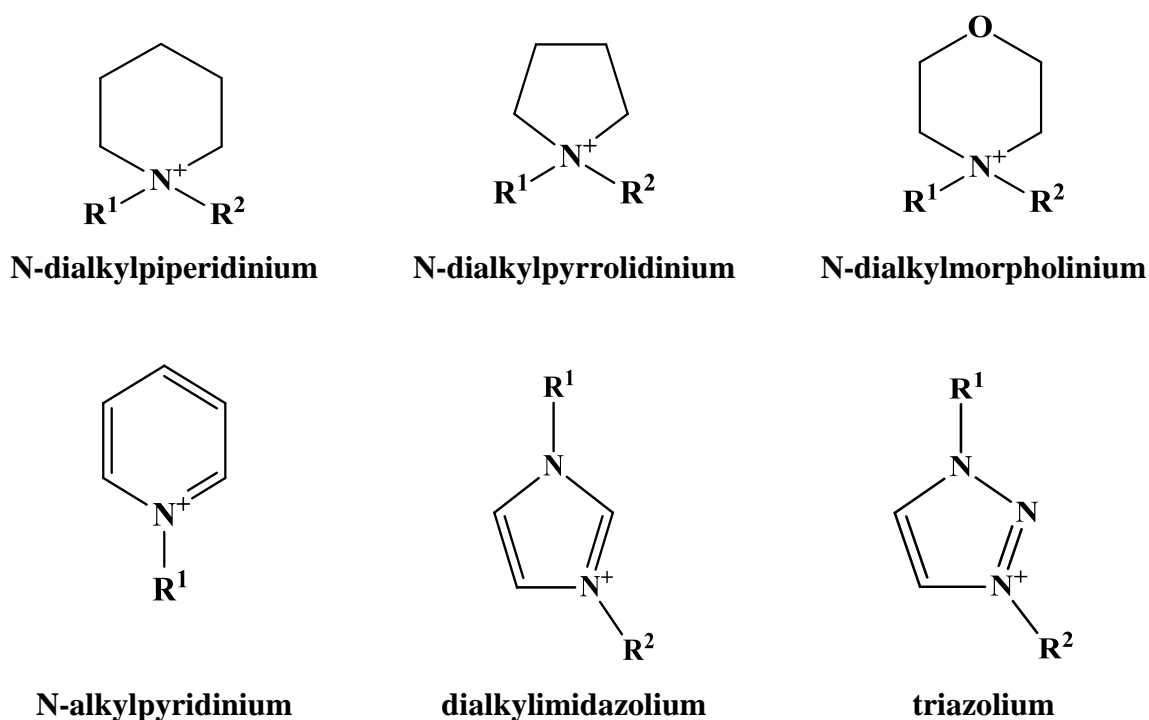


Fig. 24 The most common cations with central nitrogen atom. R¹ and R² stand for substituents, which may be various alkyl CH₃(CH₂)_n (where n=0,1,2,3..) or aryl groups.

AILs are characterized by the widest spectrum of applications. They can be utilized as solvents and catalysts or employed in engineering, physical chemistry, analytical chemistry, biological uses and electrochemistry (including metal plating, solar panels, fuel cells and electro-optics) [111]. According to ref [117], AILs may be also used as electrolytes dedicated to electrochemical capacitors and lithium ion batteries.

- PILs (in comparison to AILs) are distinguished by at least one hydrogen atom attached to the positively charged central atom of the cation (N or P). This labile, acidic and weakly bonded hydrogen is considered to be a source of “dry proton”, thus PILs were proposed as proton conductors for fuel cells operating in a wide temperature range [130]. (See more in 2.4.5).
- Zwitterionic ILs (ZILs) consist of molecules with the positive and negative charges tethered in one structure, which is expected not to migrate even under a potential gradient. Though the ZILs are isolators, this property can be improved by adding alkali metal salts, resulting in ionic conductivity of only 10⁵-10⁷ S·cm⁻¹ at room temperature. This approach is desired in applications such as fuel cells, where the mobility of ions is considered as a drawback [131].

2.4.2. Physicochemical and electrochemical properties of ILs

The founding fathers of ionic liquids, King and Wilkes from U.S. Air Force Academy, claimed that *“if a new material is to be accepted as a technically useful material, the chemists must present reliable data on the chemical and physical properties needed by engineers to design processes and devices”* [109]. Therefore, determining and collecting data on ILs properties is broadly performed since the very beginning and it is still valid today.

The most important property of ILs is their liquidus range. As the above definition indicates, melting temperature lower than 100 °C is the key requirement to classify these materials as ILs. Ideally, for many applications, the solid–liquid transition is expected to occur below room temperature. Some ILs may even solidify much below RT or not at all within an attainable low temperature range, e.g., N-methyl-N-propylpyrrolidinium fluorosulfonyl-(trifluoromethanesulfonyl)imide [C₁C₃Pyrr][FTFSI], which does not solidify down to -150 °C and exhibits only a glass transition at -107 °C upon heating, owing to its highly asymmetric anion [132]. In turn, the upper limit of the liquidus range of ILs is determined by their total decomposition temperature, which generally occurs between 350-450 °C, if no other lower temperature decomposition pathway occurs. For example, Grimmitt et al. reported the E2 elimination of the N-substituent of imidazolium halides as the reverse reaction of the S_N2 substitution under ionic liquid formation [109]. In summary, for some ILs the upper limit of the liquidus range may be greater than even 400 °C.

Since the physicochemical properties of ILs depend on the selected cation-anion pair, only general trends will be presented here, mainly focusing on well-reviewed ILs designed for electrochemistry. The most often reported properties of ILs are density (ρ), viscosity (η) and specific conductivity (σ).

The density of ILs ranges generally between 1.2 and 1.6 g·cm⁻³ at RT. Considering ILs composed of the same cation and various anions, the density increases as follows: [CH₃SO₃]⁻ ≈ [BF₄]⁻ < [CF₃CO₂]⁻ < [CF₃SO₃]⁻ < [C₃F₇CO₂]⁻ < [TFSI]⁻. Yet, ILs with densities lower than 1.0 g·cm⁻³ have been reported with the [N(CN)₂]⁻ anion. Besides, for alkylammonium or alkylimidazolium cations, it has been extensively reported that the density slightly decreases when the length of the alkyl chain increases [109].

In general, the reported viscosity values of ILs are in the range from 10 to 500 mPa·s, hence considerably higher than the ones of molecular solvents. In the majority, ILs are

reported to be Newtonian fluids [133, 134], demonstrating constant shear stress/shear rate ratio, unlike non-Newtonian fluids which do not exhibit such constant ratio. However, examples of non-Newtonian ILs, both aprotic and protic, have been published recently [135, 137], e.g., S-butyl-3-methylmethimidazolium hexafluorophosphate (AIL) and diethanoloammonium acetate (PIL) [136]. Separovic et al. [136] correlated the non-Newtonian behavior of ILs, namely the viscous shear thinning, with the presence of a considerable amount of hydrogen bonds participating to liquid-phase ordering or aggregation, consequently affecting their viscous flow. Typically the viscosity of ILs increases when temperature decreases and can be described either by an Arrhenius equation:

eq. 17

$$\eta = \eta_0 \exp \left[\frac{E_a}{RT} \right]$$

(where E_a - activation energy for the viscous flow ($\text{kJ}\cdot\text{mol}^{-1}$), η_0 - maximum viscosity (at infinite temperature), T - temperature (K), R - gas constant ($8.314 \text{ J}\cdot\text{K}\cdot\text{mol}^{-1}$)) or by the Vogel–Tammann–Fulcher (VTF) equation when the plot of $\ln \eta$ versus $1/T$ deviates from linearity at sub-ambient temperatures:

eq. 18

$$\eta = \eta_0 \exp \left[\frac{B'_\eta}{T - T_0} \right]$$

(where B'_η - constant, T_0 - temperature at which the viscosity goes to zero ideal or glass transition temperature (usually T_0 is 30-50 K lower than the T_g obtained by DSC measurement)).

The specific conductivity of ILs at RT ranges from 0.1 to 18 $\text{mS}\cdot\text{cm}^{-1}$ [138]. Based on the various cation-anion combinations which were examined, depending on the cation, the conductivity increases in the following order: pyridinium < ammonium < sulphonium < imidazolium [139]. The highest values were reported for ILs with $[\text{C}_2\text{C}_1\text{Im}]^+$ cations. Besides, the correlation between the anion type or size and conductivity of ILs is ambiguous. Usually, smaller anions like $[\text{BF}_4]^-$ provide higher conductivity. However, ILs consisting of $[\text{TFSI}]^-$ often display higher conductivity than those consisting of smaller anions like $[\text{CH}_3\text{COO}]^-$. [109]. Above room temperature, the conductivity of ILs follows the classical linear Arrhenius behavior expressed in equation 19:

eq. 19

$$\sigma = \sigma_0 \exp \left[-\frac{E_a}{RT} \right]$$

(where E_a - activation energy for electrical conduction ($\text{kJ}\cdot\text{mol}^{-1}$), σ_0 - maximum electrical conductivity (at infinite temperature), T - temperature (K), R - gas constant ($8.314 \text{ J}\cdot\text{K}\cdot\text{mol}^{-1}$)), whereas below room temperature, when approaching the glass transition temperatures (T_g), the conductivity negatively deviates from linear behavior. The observed temperature dependence of conductivity complies with glass-forming liquids, and it is better described by the empirical VTF equation:

eq. 20

$$\sigma = \sigma_0 \exp \left[-\frac{B'_\sigma}{T - T_0} \right]$$

(where B'_σ - constant, T_0 - temperature at which the conductivity goes to zero ideal or glass transition temperature (usually T_0 is 30-50 K lower than the T_g obtained by DSC measurement)).

The conductivity and viscosity of ILs can be correlated in the Walden rule:

eq. 21

$$\Lambda\eta = \text{constant}$$

where Λ is the molar conductivity of the ionic liquid, according to equation (22):

eq. 22

$$\Lambda = \frac{\sigma \cdot M_w}{\rho}$$

with M_w the molecular weight of the ionic liquid and ρ its density. For good electrolytes, the Walden product ($\Lambda\eta$) is expected to remain constant independently of temperature, yet it was shown that for ILs this product varies inversely with ion size [109]. The qualitative approach to the Walden rule and its applicability for ILs was extensively investigated by Angell et al. [140-142]. However, aiming at better indicating the number of mobile charge carriers in an IL, the relationship between conductivity and viscosity was assessed by the so-called Walden Plot ($\log \Lambda$ vs. $\log \eta^{-1}$). The plot includes the “ideal” Walden line representing the situation where ions are fully dissociated and have equal mobility (usually based on a calibration point obtained with 0.1 M KCl in water). Considering the regions described in the Walden plot

(Fig. 25), and depending on their transport properties, ILs may be classified into: superionic glasses, superionic liquids, good ionic liquids, poor ionic liquids and non-ionic liquids.

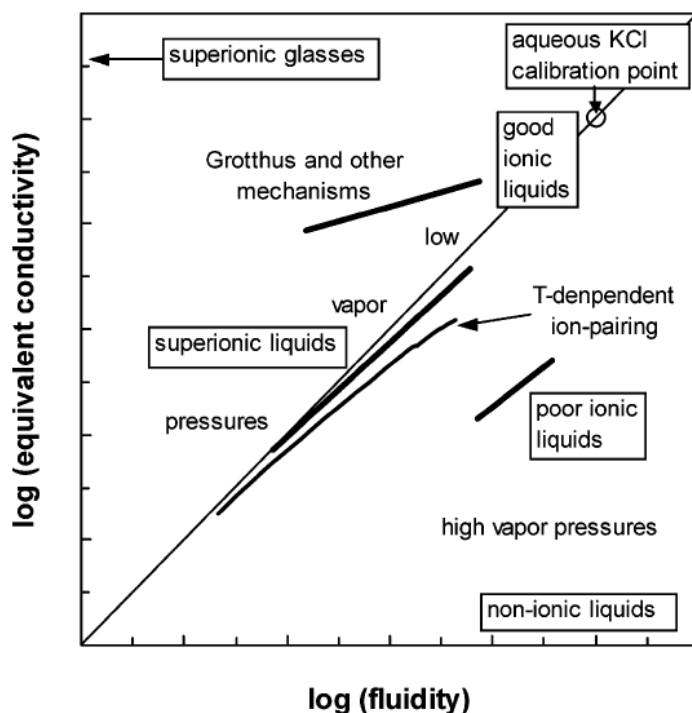


Fig. 25 Classification diagram of ionic liquids based on the Walden rule (from [142]).

Moreover, the conductivity is related to the available charge carriers and their mobility. Due to the fact that ILs consist entirely of ions, good conductivity is expected, however, not all ions from IL appear to be available to participate in the conduction processes, yet, smaller measured conductivity values are attributed to the reduction of available charge carriers caused by ion pairing and/or ion aggregation, and to the decrease of ion mobility mostly resulting from the large size of ILs cations. Although the “degree of ionicity” of ILs was extensively investigated, the concept of ionicity does not necessarily relate with chemical availability of individual ions and may depend more strongly on the associated nature of the ionic liquid [143].

Finally, a key feature of ILs for the purpose of this manuscript is their electrochemical stability, namely the potential range over which they are electrochemically inert. The electrochemical window (EW) reflects the stability of the compound toward oxidation (E_{AL}) and reduction (E_{CL}) versus a certain reference electrode (RE) and is measured in a three-electrode cell. In case of ILs, it reflects the resistance of the cation to reduction and of the anion to oxidation. Usually, $EW = E_{AL} - E_{CL}$ of ILs is obtained by linear sweep voltammetry

performed on an inert electrode, e.g., glassy carbon (GC) or platinum, where the threshold values of E_{AL} and E_{CL} are determined by a dramatic rise of background current due to oxidation and reduction, respectively (Fig. 26) [109, 144].

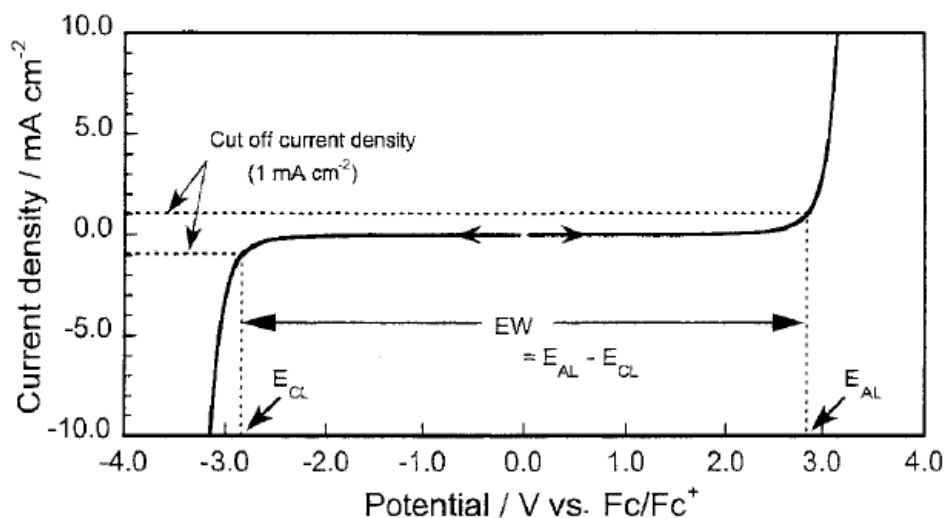


Fig. 26 Typical linear sweep voltammogram of ILs (from [144]).

The general trend in electrochemical stability depending on the type of cation is as follows: pyridinium < pyrazolium < imidazolium < sulphonium < ammonium and for anions: halides ($[Cl]^-$, $[F]^-$, $[Br]^-$) < chloroaluminates ($[AlCl_4]^-$, $[Al_2Cl_7]^-$) \leq fluorinated ions ($[BF_4]^-$, $[PF_6]^-$, $[AsF_6]^-$) \leq triflate/triflyl ions ($[CF_3SO_3]^-$, $[TFSI]^-$, $[(C_2F_5SO_2)_2N]^-$, $[(CF_3SO_2)_3C]^-$) [109]. The exemplar values of EW measured on GC are as follows: N-methyl-N-butylpyrrolidinium bis[(trifluoromethyl)sulfonyl]imide, $[C_1C_4Pyr][TFSI]$, with 5.5 V, 1-ethyl-3-methylimidazolium tetrafluoroborate, $[C_1C_2Im][BF_4]$, with 4.3 V or $[C_1C_2Im][TFSI]$ with 4.1 V. As already suggested by Wilkes et al. in the late 70's of the 20th century, the electrochemical oxidation and reduction potentials are determined by the energy (given in eV) of the highest occupied molecular orbital (HOMO) and lowest unoccupied molecular orbital (LUMO), respectively [115]. Recent computational methods including HOMO/LUMO values calculation showed fairly good agreement with existing experimental data [145].

2.4.3. State-of-the-art on AILs based ECs

As announced above, owing to their non-volatile and non-flammable characteristics as well as great electrochemical stability, ILs are considered as potential electrolytes for ECs. The earliest documented use of ILs as electrolytes in ECs was with activated carbon cloth (ACC) electrodes and $[C_2C_1Im][TFSI]$ [146, 147]. Due to the moderate conductivity and

viscosity values of ILs, subsequent reports concerned their application in AC based ECs at elevated temperature (60 °C). Using a microporous AC (SSA = 1428 m²·g⁻¹) and [C₁C₄Pyrr][TFSI] as electrolyte, a specific capacitance of 60 F·g⁻¹ was determined by CV at 20 mV·s⁻¹, and remained stable for several thousand galvanostatic cycles up to 3.5 V [148]. A supplementary test, also at elevated temperature (60 °C), comparing two ILs with five-membered cyclic cations (imidazolium and pyrrolidinium) coupled with the same anion, showed that higher capacitance is displayed by [C₂C₁Im][TFSI] than [C₁C₄Pyrr][TFSI]. It was attributed to two factors: the cation polarizability which affects the dielectric constant in the double-layer and the double-layer thickness which depends on the cation preferential orientation under the applied electric field [149, 150]. Moreover, it was pointed out that capacitance follows the already introduced trend stating that only pores wider than the IL ions size are easily accessible and effectively participate in the double-layer charging process [150]. Apart from the dependence of capacitance on cation properties, it was demonstrated that the maximal operational voltage is strongly dependent on cation, hence higher operational voltage of 3.7 V was reported for [C₁C₄Pyrr][TFSI] as compared to 3.4 V for [C₂C₁Im][TFSI] [151]. Generally, it is established that 1,3-dialkylimidazolium cations display limited cathodic stability unlike other common cations. It is explained by the electron deficiency of the C2 carbon with attached acidic hydrogen recognized as a reduction site [152]. Importantly, the higher voltage while using [C₁C₄Pyrr][TFSI] was realized in an asymmetric configuration utilizing carbon electrodes with different masses allowing to adjust their potential range [151].

To generalize, the most often investigated ILs for ECs combine [TFSI]⁻, [BF₄]⁻ or [PF₆]⁻ anions, together with two main groups of cations, namely imidazolium- or pyrrolidinium-type. The former group provides ILs with relatively high ionic conductivity and low viscosity, but restricted safe operational voltage of EC, 3.0–3.2 V, whereas the latter gives low ionic conductivity and high viscosity but safe operation of EC up to 3.5–3.7 V [14]. For these reasons, researchers aimed their efforts at improving ILs properties through:

- adding small amount of organic solvent, e.g., acetonitrile [153] or propylene carbonate [154, 155] to enhance the ILs transport properties without significant decrease of voltage. The solutions thereby obtained resemble the classical organic electrolytes used in ECs, and although literature claims are generally optimistic, it is difficult to assimilate such mixtures to pure ILs;
- investigating different anions like:

- the bis(fluorosulfonyl)imide $[\text{FSI}]^-$ anion, which applied in 1-ethyl-3-methylimidazolium bis(fluorosulfonyl)imide, $[\text{C}_2\text{C}_1\text{Im}][\text{FSI}]$, gives a conductivity of $15.5 \text{ mS}\cdot\text{cm}^{-1}$ similar to the value of $15.3 \text{ mS}\cdot\text{cm}^{-1}$ displayed by the triethylmethylammonium tetrafluoroborate, $[\text{N}_{1222}][\text{BF}_4]$,/PC solution [156]; however, in the presence of residual chlorine impurities, N-methyl-N-butylpyrrolidinium bis(fluorosulfonyl)imide, $[\text{C}_1\text{C}_4\text{Pyrr}][\text{FSI}]$, demonstrated inferior anodic stability to its analogue $[\text{C}_1\text{C}_4\text{Pyrr}][\text{TFSI}]$, [157];
 - perfluoroalkyltrifluoroborate, e.g., $[\text{BF}_3\text{C}_2\text{F}_5]^-$ which combined in $[\text{C}_2\text{C}_1\text{Im}][\text{BF}_3\text{C}_2\text{F}_5]$ provides a higher capacitance than $[\text{C}_1\text{C}_2\text{Im}][\text{BF}_4]$, but the cell did not show a good cycle life [158];
 - tetracyanoborate $[\text{B}(\text{CN})_4]^-$, e.g., once coupled with $[\text{C}_2\text{C}_1\text{Im}]^+$, the IL displays similar transport properties and operational voltage as its analogue $[\text{C}_2\text{C}_1\text{Im}][\text{BF}_4]$, yet $[\text{C}_2\text{C}_1\text{Im}][\text{B}(\text{CN})_4]$ is not susceptible to undergo hydrolysis and HF release with residual water present, as opposed to $[\text{C}_2\text{C}_1\text{Im}][\text{BF}_4]$, [159, 160].
- examining different cations:
- methoxy-functionalized cations coupled in ILs with common anions such as $[\text{BF}_4]^-$ and $[\text{TFSI}]^-$. N,N-diethyl-N-methyl-N-(2-methoxyethyl)ammonium tetrafluoroborate, $[\text{N}_{122,2-0-1}][\text{BF}_4]$, applied as electrolyte for EC exhibits comparable performance to $1 \text{ mol}\cdot\text{L}^{-1}$ $[\text{TEA}][\text{BF}_4]$ in PC at 2.5 V [161]. N-methoxyethyl-N-methylpyrrolidinium bis[(trifluoromethyl)sulfonyl]imide, $[\text{C}_1\text{C}_{2-0-1}\text{Pyrr}][\text{TFSI}]$, displays higher conductivity (3.8 and $8.4 \text{ mS}\cdot\text{cm}^{-1}$ at RT and $60 \text{ }^\circ\text{C}$, respectively) than $[\text{C}_1\text{C}_4\text{Pyrr}][\text{TFSI}]$ (2.6 and $6.0 \text{ mS}\cdot\text{cm}^{-1}$ at RT and $60 \text{ }^\circ\text{C}$, respectively), thus providing higher practical energy and power values at both temperatures despite narrower voltage (3.7 vs. 4.0 V) [162];
 - azepanium-based ionic liquids including N-butyl-N-methylazepanium $[\text{C}_1\text{C}_4\text{Azep}]$ and N-hexyl-N-methylazepanium $[\text{C}_1\text{C}_6\text{Azep}]$ combined with $[\text{TFSI}]^-$ anion were tested as low-cost alternatives to well-established $[\text{C}_1\text{C}_4\text{Pyrr}][\text{TFSI}]$ demonstrating similar operative potential window but inferior transport properties [163].

In conclusion, improving one parameter generally leads to the deterioration of the other, resulting in a very limited optimization of IL electrolytes parameters.

Essentially, most of the important voltage values claimed in the above mentioned papers were established from cyclic voltammetry experiments and should be confirmed by prolonged galvanostatic cycling or potentiostatic floating. A reliable method for determining the stability limits of ECs operating in organic and IL electrolytes was introduced by

Kötz et al. [164]. The method combines the determination of safe working potentials of each electrode in respect to the individual cathodic and anodic stability limits of IL on a selected carbon material, whereas the feasibility of the defined voltage extent (in asymmetric configuration to adjust the potential range of each electrode in the IL stability limits) is confirmed by floating. The values of potential window given in table 2 for a carbon electrode with IL electrolytes are believed to be realistic only in such conditions. This approach will be discussed in details in chapter V section 4.1.

Table 2 Positive and negative safe potential limits (PL) and corresponding potential window obtained in various IL electrolytes by the method developed in reference [164].

	[C ₂ C ₁ Im] [BF ₄]	[C ₂ C ₁ Im] [FAP]	[C ₄ C ₁ Im] [BF ₄]	[C ₂ C ₁ Im] [B(CN) ₄]	[C ₂ C ₁ Im] [TFSI]	[C ₃ C ₁ Pyrr] [TFSI]	[C ₄ Pyrr] [TFSI]	[C ₄ C ₁ Pyrr] [BF ₄]
PL _{pos} vs. AC (V)	1.6	1.5	1.6	1.6	1.5	1.4	1.4	1.5
PL _{neg} vs. AC (V)	-1.9	-1.9	-2	-1.8	-1.9	-1.7	-1.0	-1.1
Potential window (V)	3.5	3.4	3.6	3.4	3.4	3.1	2.4	2.6

* [FAP]⁻ - tris(pentafluoroethyl)trifluorophosphate; [C₄Pyrr]⁺ - N-butylpyridinium.

2.4.4. Approach toward lowering the melting point of AILs

The research on melting point reduction and liquidus range increase of AILs was started by Wilkes et al. for their early application as battery electrolytes [165]. The strategy generally involves to changing both the anion and cation size, including their symmetry, or more precisely asymmetry, by adjusting the substituents length and applied functionality [109].

Generally, the increase of size and asymmetry of the anion generates a reduction of the melting point by decreasing the Coulombic attraction contributing to the lattice energy of the crystal. For the common [C₂C₁Im]⁺ cation and various anions, T_m decreases as follows: [Cl]⁻ 87 °C > [Br]⁻ 81 °C > [I]⁻ 79-81 °C > [PF₆]⁻ 62 °C > [NO₂]⁻ 55 °C > [NO₃]⁻ 38 °C > [BF₄]⁻ 15 °C > [TFSI]⁻ -3 °C > [CF₃SO₃]⁻ -9 °C > [CF₃CO₂]⁻ -14 °C > [N(CN)₄]⁻ -21 °C [109]. Enhanced asymmetry was achieved by applying the [FTFSI]⁻ anion, and lack of crystallization was observed down to -150 °C for ILs with [C₁C₃Pyrr]⁺, [C₁C₄Pyrr]⁺ and [C₁C₂₋₀₋₁Pyrr]⁺ cations showing only T_g at -107, -104 and -103 °C, respectively [132].

Similarly, larger cation size and greater asymmetry supports decreasing of melting point via weakening ion–ion packing in the crystal. The effect of increasing cation size is confirmed by decreasing the melting point of the following series of alkylammonium bromides: $[N_{1111}]^+$ over 300 °C > $[N_{2222}]^+$ 284 °C > $[N_{4444}]^+$ 124-128 °C > $[N_{6666}]^+$ 98-100 °C > $[N_{8888}]^+$ 95-98 °C. Their analogues with asymmetric substituent display even lower melting point: $[N_{4448}]^+$ 67.3 °C > $[N_{2666}]^+$ 46.5 °C. In turn, the example of a series of 1-alkyl-3-methylimidazolium tetrafluoroborates showed that the maximum reduction of melting point is achieved for substituents between butyl and decyl, whereas a further extension of the alkyl chain length leads to an increase of melting point [109]. A similar trend with respect to the length of the cation aliphatic side chain is followed by ILs formed of a series of N-alkyl-N-alkyl-piperidinium cations and $[TFSI]^-$ anion [125].

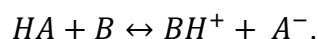
Another way of manipulating with melting point of ILs is to introduce some functionality in the cation substituent. The most commonly applied functionalities are alkoxy or hydroxyl groups. The methoxyethyl substituent is relatively flexible and, once applied in a cation with sp^3 - hybridized nitrogen, like linear quaternary ammonium, pyrrolidinium, piperidinium and morpholinium, (usually) provides lower melting point and decrease of T_g , as well as contributes to lower viscosity and higher conductivity [166]. Importantly, methoxy- or hydroxylfunctionalized alkylammonium ILs have been considered as alternative to imidazolium based ILs electrolytes displaying limited cathodic stability [167]. As already mentioned above, using quaternary ammonium salt with methoxyethyl functionality resulted in the improved performance of the RTILs applied in ECs [161, 162].

Overall, the melting point of the most commonly used ILs for application in ECs is in the range of –20 to 15 °C. Therefore, in respect to low temperature applications, the decrease of T_m was reached by the usage of ILs binary mixtures. The analyzes of binary mixtures with various mole fractions of $[C_2C_1Im][CF_3SO_3]$ and $[C_2C_1Im][TFSI]$ revealed only a glass transition in comparison to pure ILs displaying glass and melting transition [168]. Later, reduced melting transitions and enhanced liquidus range were detected on a series of binary mixtures prepared from $[C_1C_4Pyrr][FSI]$, $[C_1C_3Pyrr][FSI]$, $[C_1C_4Pyrr][TFSI]$, $[C_1C_3Pyrr][TFSI]$. In addition, it was observed that the crystallization process of the mixtures is mainly influenced by the anion [169]. Hence, ECs based on activated graphene and the binary 1:1 (by mol) mixture of $[C_1C_4Pyrr][TFSI]$ and N-methyl-N-propylpiperidinium bis[(trifluoromethyl)sulfonyl]imide, $[C_1C_3Pip][TFSI]$, were capable to operate from -50 to 80 °C [170].

2.4.5. The subclass of Protic Ionic Liquids (PILs)

Protic Ionic Liquids (PILs) are a subclass of ILs featured by at least one hydrogen atom attached to a positively charged central atom in the cation. They are formed by a proton transfer from a Brønsted acid to a Brønsted base, similarly to AILs where the cation is created by ionization of a starting amine via accepting any other group than proton. The formation of the protonated amine involves a proton attraction from the acid to the lone electron pair of the amine according to equation 23 [19, 171, 172]:

eq. 23



PILs are the most often prepared by the reaction of amines with oxoacides like HNO₃, H₂SO₄, H₃PO₄, CH₃SO₃H [173, 174, 175] or carboxylic acids [175, 176] or imide-acids like H-TFSI [174, 177]. They can be also synthesized in a simple metathesis reaction (utilizing a halogenated precursor) which mainly applies to PILs with fluorinated anions, e.g., [TFSI]⁻, [FSI]⁻ [178, 179]. Similarly to AILs, compounds consisting of phosphonium [180] cations were also reported.

PILs display some general properties of AILs, such as ionicity, hence capability of ionic conductance, as well as liquid state over a wide temperature range or at least below 100 °C. However, due to the cation acting as a proton-carrier in the liquid, PILs exhibit special characteristics attributed to this labile or mobile hydrogen and its variable activity.

One way of assessing the degree of proton transfer is to employ the aqueous pK_a difference between acid and base, where ΔpK_a^{aq} greater than 10 is considered as required for full protonation [142]. This assumption was confirmed by studies of the potential gap between the onset of hydrogen oxidation and proton reduction, where ΔpK_a extracted from electrochemical measurements showed good correlation with ΔpK_a^{aq} [181]. The pK_a theory was also discussed by MacFarlane et al. in terms of acidity-basicity of PILs, categorizing the component ions into acidic, neutral and basic [182]. Moreover, the authors show the difference of ionicity degree of PILs consisting of primary and tertiary amines with similar pK_a^{aq} values coupled with acetic acid. The former PIL displays a “close-to-ideal” behavior, whereas the later one forms mixtures with low degree of proton transfer. It means that simple primary amines give rise to highly ionized PILs, facilitating a proton transfer owing to the predominance of ionic species. In contrast, tertiary amines tend to form mixtures with a low

degree of proton transfer, revealing the presence of neutral non-conducting species, possibly the acid and base precursor, as well as pairing of ions and aggregates formation [183].

Importantly, the characteristics of proton conduction in PILs have been studied and debated without any straightforward verification. In general, two proton-transport mechanisms can be distinguished (Fig. 27) [184]:

- Grotthuss mechanism also called proton hopping which owes its name to proton transfer along hydrogen bonds from one site to another through the formation and breaking of hydrogen bonds between hydrogen-bonded molecules and hydronium ions (proton hopping);
- Vehicle mechanism which is based on simple protons migration (diffusion) through the medium along with a “vehicle” such as H_3O^+ , H_5O_2^+ , and H_9O_4^+ .

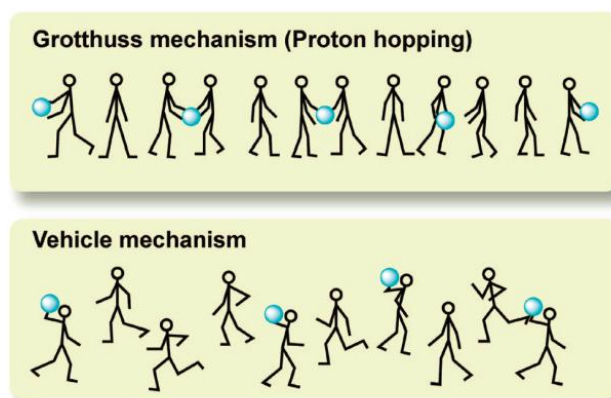


Fig. 27 Conceptual illustration of two proton transport mechanisms: Grotthuss (top) and vehicle (bottom) (from [184]).

The first investigation on proton conduction in PILs was reported by Watanabe et. al. who tested mixtures of imidazole (Brønsted base) and H-TFSI (Brønsted acid) with various concentrations and indicated the combination of a Grotthuss “hopping” mechanism and a “vehicle” mechanism [185]. Later, a test on the same base-acid couple, forming a conventional PIL with equimolar concentration of substrates, imidazolium bis[(trifluoromethyl)sulfonyl]imide, $[\text{Im}][\text{TFSI}]$, corroborated a protonic conduction [177]. Furthermore, a comparative study on anhydrous PILs (<100 ppm H_2O) and regular ones (~ 1000 ppm H_2O) consisting of triethylammonium, $[\text{HN}_{222}]^+$, with $[\text{CH}_3\text{SO}_3]^-$, $[\text{TFSI}]^-$, $[\text{AlCl}_4]^-$ or $[\text{BETI}]^-$ anions showed no proton decoupled (Grotthuss mechanism) mobility in the anhydrous PILs, whereas the presence of a moderate amounts of water (~ 1000 ppm) has a considerable influence on the self-diffusion coefficient of the acidic proton [186]. In addition, the investigations of 8 PILs consisting of diethylmethylammonium - $[\text{HN}_{122}]^+$,

[HN₂₂₂]⁺, ethylimidazolium - [C₂Im]⁺, butylimidazolium - [C₄Im]⁺ cations and [CF₃SO₃]⁻ or [CH₃SO₃]⁻ anions indicated proton transport by a vehicle mechanism except for [C₄Im][CH₃SO₃] displaying a Grotthus mechanism of proton transport due to restricted mobility [187]. Accordingly, the vehicle type of mechanism was confirmed for [C₂Im][TFSI] [188]. Studies on water - PILs (pyrrolidinium hydrogen sulfate, [Pyr][HSO₄], and pyrrolidinium trifluoroacetate, [Pyr][CF₃COO]) binary mixtures by Anouti et al. indicated a combination of Grotthus- and vehicle type mechanisms related to water increase [189].

2.4.6. PILs as electrolytes for ECs

As introduced above, predominantly aqueous electrolytic solutions were investigated to utilize the beneficial effects of pseudocapacitance owing to redox reactions involving available protons. However, the application of aqueous solutions and especially the acidic ones is restricted because of the limited operational voltage and corrosive character of these media. An interesting alternative to overcome water limitations, e.g., voltage and temperature range extending, in applications where a protic medium is required, was proposed by Rochefort et al. applying PILs as non-aqueous electrolytes with available acidic hydrogen. The investigations utilized RuO₂ electrodes known to undergo the reaction indicated in eq. 7, in acidic protic medium, as typically observed in aqueous solution of sulfuric acid in the form of enhanced current on the cyclic voltammograms. The experiments involving RuO₂ electrodes in PILs (conventional 1:1 and acid-enriched 1:2 ratios consisting of 3-methylpyridazine and [CF₃CO₂]⁻, Fig. 28) demonstrated also a high current attributed to faradaic reactions, especially in the case of acid enriched-PIL (Fig. 28a) displaying more pronounced redox waves (indicated by arrows). It is explained by shifting the proton transfer equilibrium towards the formation of ionic species leading to higher conductivity and by the increased number of H⁺ available for the proton-coupled reactions at the RuO₂ electrode. The participation of acid hydrogen originating from PILs was confirmed by the comparison with H₂SO₄ and an AIL ([C₄C₁Im][PF₆] dotted line) as shown in Fig. 28b. As anticipated, the RuO₂ electrode exhibited a wider electrochemical window with PIL than with sulfuric acid, yet narrower than with AIL due to H₂ evolution. Overall, this experiment proves that the protonated amine acts similarly to the hydronium cation in aqueous electrolytes. The detected capacitance values, for PILs with various amines and [CF₃CO₂]⁻ anion, were in the range of 28-40 F·g⁻¹ [190-192].

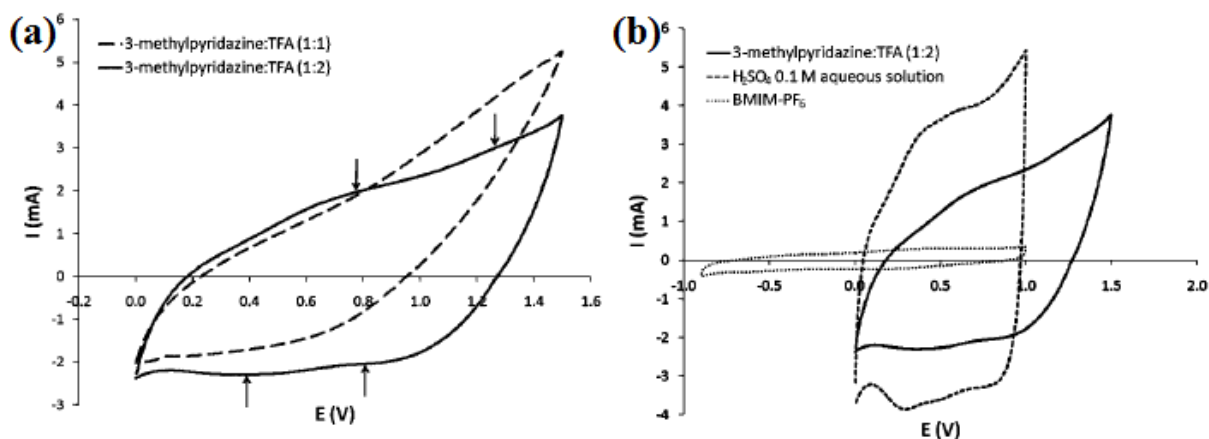


Fig. 28 Pseudocapacitive properties of RuO_2 in: (a) conventional 1:1 and acid-enriched 1:2 ratio PILs of 3-methylpyridazine and $[\text{CF}_3\text{CO}_2]^-$; (b) PILs and H_2SO_4 (aq) as compared to the low current observed in the case of an AIL (scan rate $10 \text{ mV}\cdot\text{s}^{-1}$) (from [191]).

Additionally, another PIL, $[\text{HN}_{122}][\text{CF}_3\text{SO}_3]$, pure and in mixture with ACN, was tested with RuO_2 electrodes showing a slight increase of the specific capacitance for the mixture in comparison to the pure PIL (e.g. ~ 50 vs. $\sim 35 \text{ F}\cdot\text{g}^{-1}$ at $50 \text{ mV}\cdot\text{s}^{-1}$), except for slow scan rates (~ 235 vs. $\sim 135 \text{ F}\cdot\text{g}^{-1}$ at $2 \text{ mV}\cdot\text{s}^{-1}$) pointing out to the limitation of proton transfers in pure PIL [193]. This assumption was supported by the results obtained in high-temperature tests (40 - $120 \text{ }^\circ\text{C}$, every $20 \text{ }^\circ\text{C}$) demonstrating the feasibility of PIL safe operation, even up to $120 \text{ }^\circ\text{C}$, with excellent capacitance of $338 \text{ F}\cdot\text{g}^{-1}$ ($2 \text{ mV}\cdot\text{s}^{-1}$) owing to enhanced conductivity and proton mobility [193]. Furthermore, tests on ECs utilizing transition metal oxides electrodes with PILs were conducted on less expensive MnO_2 , using 2-methoxypyridine and $\text{CF}_3\text{CO}_2\text{H}$ in 1:1 and 1:2 ratios, and the 1:2 formulation demonstrated a capacitance value of $397 \text{ F}\cdot\text{g}^{-1}$ at $5 \text{ mV}\cdot\text{s}^{-1}$, comparable to the values obtained in an aqueous solution of $0.1 \text{ mol}\cdot\text{L}^{-1}$ Na_2SO_4 [194]. However, it should be emphasized that the maximum voltage reached in all these experiments was still relatively low – in a range of only 1.0 - 1.5 V .

Similarly, PILs, e.g., pyrrolidinium nitrate, $[\text{Pyrr}][\text{NO}_3]$, and pyrrolidinium formate, $[\text{Pyrr}][\text{HCOO}]$, were tested on activated carbon electrodes. For an activated carbon containing a considerable amount of oxygenated functionalities, 3-electrode cell investigations demonstrated the occurrence of reversible redox peaks [195]. However, common nitrates [196-199]), formates [195] or the above described trifluoroacetates and trifluoromethanesulfonates display narrow potential range in comparison to AILs such as $[\text{C}_1\text{C}_2\text{Im}][\text{TFSI}]$ or $[\text{C}_1\text{C}_4\text{Pyrr}][\text{TFSI}]$.

Bearing in mind that ILs properties depend on the coupled cation-anion, the investigations were further directed to the employment of PILs with the $[\text{TFSI}]^-$ anion promoting a liquid state at ambient conditions and providing higher anodic stability than other anions. In a short time, $[\text{HN}_{222}][\text{TFSI}]$ has become the most commonly used PIL in ECs [178, 197, 198], owing to the combination of its relatively good conductivity ($5 \text{ mS}\cdot\text{cm}^{-1}$ at $25 \text{ }^\circ\text{C}$ [178]), reasonable viscosity ($39 \text{ mPa}\cdot\text{s}$ at $25 \text{ }^\circ\text{C}$ [178]) and promising potential window of 3.8 V detected on platinum WE [198].

Figure 29 shows the three-electrode voltammograms of an activated carbon electrode in $[\text{HN}_{222}][\text{TFSI}]$, while shifting the negative vertex potential at each loop. Reversible redox contributions attributed to hydrogen chemisorption/desorption appear when this vertex potential becomes lower than the reduction potential of the protonated cation [197]. It suggests that processes comparable to those described in section 2.3.1 for the aqueous media might be at the origin of the observed redox peaks. As clearly visible in figure 29 from the comparison of CVs obtained with a PIL containing 200 and 5000 ppm of water, the effectiveness of the process increases with the water content.

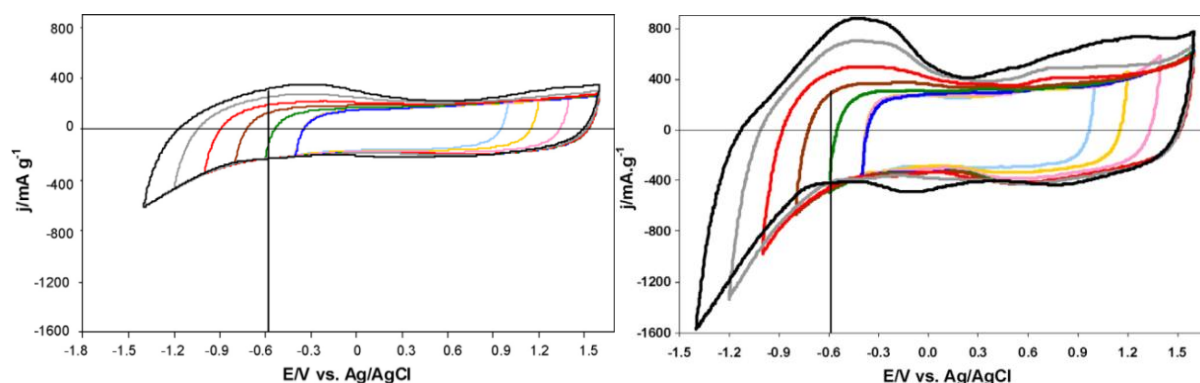


Fig. 29 Three-electrode cyclic voltammograms of AC in $[\text{HN}_{222}][\text{TFSI}]$ with 200 ppm (left) and 5000 ppm (right) of water; scan rate $2 \text{ mV}\cdot\text{s}^{-1}$ (from [197]).

Correlatively, it was demonstrated (in 2-electrode cell experiments) that increasing the amount of water incorporated in PIL entails the voltage limitations and capacitance changes. The comparison of the same materials - samples of $[\text{HN}_{222}][\text{TFSI}]$ with 200 and 5000 ppm of H_2O and AC - pointed to the more stable cell operation in the drier PIL reaching 3.0 V (with efficiency $\eta \geq 95\%$) in contrast to the more hydrated one with 2.5 V ($\eta \geq 95\%$). However, the latter exhibited higher capacitance (by around $15 \text{ F}\cdot\text{g}^{-1}$) up to 2.0 V , in the region corresponding to EDL charging. Above this voltage, the capacitance values became distinct due to various impact of hydrogen electrosorption [197].

In other reports ([178, 198]) where $[\text{HN}_{222}][\text{TFSI}]$ with ≤ 10 ppm H_2O (Fig. 30a and b) or 200 ppm H_2O (Fig. 30c) was implemented, the authors claimed about a typical capacitive behavior of the electrodes in three-electrode cell configuration (Fig. 30a) [198], and almost rectangular shape of CVs in asymmetric (Fig. 30b) [198] or symmetric two-electrode cell (Fig. 30c) [178]. However, we can notice that the CV shapes seem to be affected by some faradaic current, e.g., some humps or leaps are observed between around 1.7 V and 2 V during charge and discharge (Fig. 30b and c), whereas in three-electrode cell a slight contribution of hydrogen sorption can be observed below -0.7 V vs. Ag. Nevertheless, tests performed using various water contents in PIL, different current collectors (gold [197] or aluminium ([178, 198]) and sundry carbon electrodes do not allow for straightforward comparison of water-dependent EC operation.

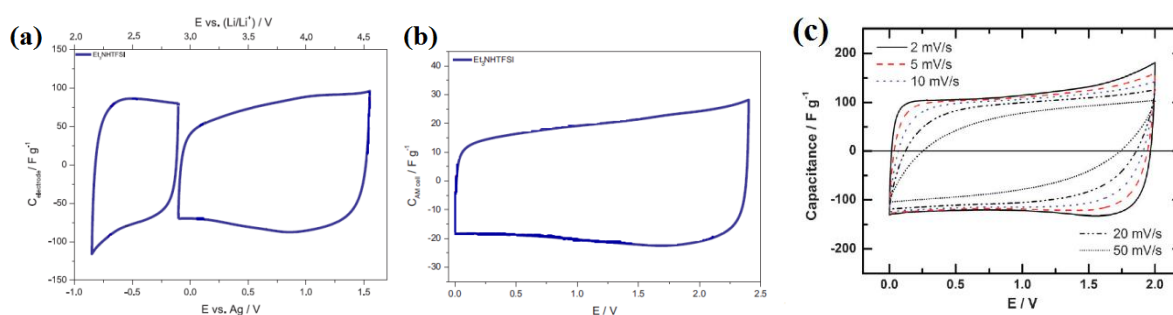


Fig. 30 (a) Three-electrodes CVs and (b) CVs of AC/AC cell in $[\text{HN}_{222}][\text{TFSI}]$ with ≤ 10 ppm H_2O (scan rate $5 \text{ mV} \cdot \text{s}^{-1}$) (from [198]); (c) CVs for a two-electrode cell in $[\text{HN}_{222}][\text{TFSI}]$ with 200 ppm of H_2O at different scan rates (from [178]).

Later, a comparative study of activated carbon electrodes in $[\text{Pyrr}][\text{TFSI}]$ and diisopropylethylammonium bis[(trifluoromethyl)sulfonyl]imide, $[\text{DIPEA}][\text{TFSI}]$, showed that the cation structure has an impact on the hydrogen reduction potential, which is lower in $[\text{DIPEA}][\text{TFSI}]$ with -1.1 V vs. NHE than in $[\text{Pyrr}][\text{TFSI}]$ with -0.8 V vs. NHE. Accordingly, as depicted in figure 31, a significantly higher cathodic current was observed for $[\text{Pyrr}][\text{TFSI}]$ with more available hydrogen than in $[\text{DIPEA}][\text{TFSI}]$, where branched alkyl substituents with higher degree of rotational freedom shield the attached hydrogen [200].

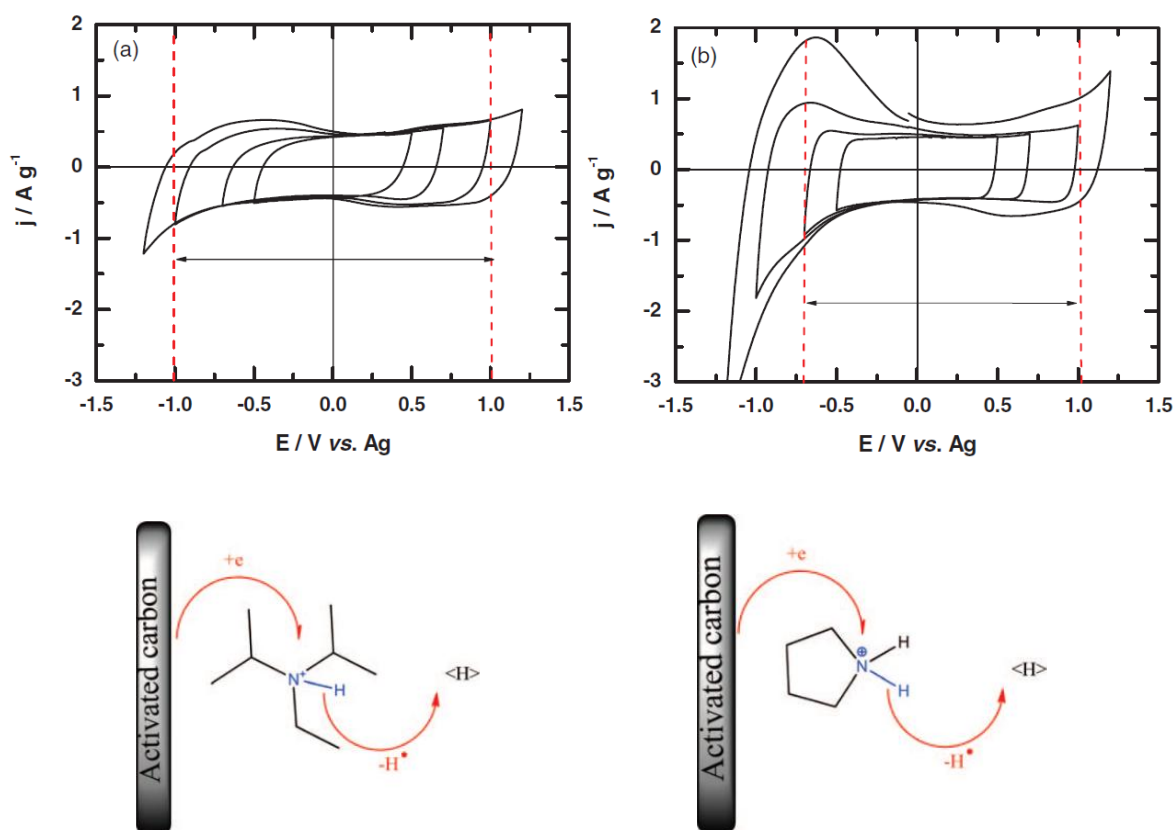


Fig. 31 3-electrode CVs of a PVDF-AC electrode in [DIPEA][TFSI] (a) and [Pyrr][TFSI] (b) vs. AgQRE (scan rate $5 \text{ mV}\cdot\text{s}^{-1}$, at $30 \text{ }^\circ\text{C}$); explanatory figure of the steric effect of an alkyl substituent on hydrogen reduction (from [200]).

Similarly to the case of AILs, the dissolution of PILs, including [HN₂₂₂][TFSI] [178], trimethylammonium bis[(trifluoromethyl)sulfonyl]imide, [HN₁₁₁][TFSI], [198, 201] and tributylphosphonium tetrafluoroborate, [HP₄₄₄][BF₄], [180], in organic solvents (ACN, PC), showed a possible improvement of their transport properties or overcoming limitations arising from their solid state, however at the expense of voltage and stability, as well as an effective utilization of hydrogen.

3. Conclusion and perspectives

This chapter summarized the most important aspects of electrochemical capacitor technology such as: the operation principles of ECs and the mechanisms of charge storage (capacitive non-faradaic, capacitive faradaic and non-capacitive faradaic), the characteristics of electrode active materials and their design toward desired improvement of EC performance, as well as the characteristics of electrolytes and their selection toward enhancement in capacitance and voltage, thus energy and power. Keeping in mind some of these requirements, the chapter then focuses on ionic liquids, referred to as unconventional

electrolytes, introducing their advantages and disadvantages, especially for application in ECs. Finally, the unique subclass of protic ionic liquids (PILs) is broadly described, including selected issues of proton conductance playing a requisite role in further discussing their electrochemical behavior, and finally presenting the state-of-the art of their implementation in ECs.

Based on this literature review, it is believed that the incorporation of the [TFSI]⁻ anion in PILs leads to the formation of electrochemically stable compounds in preference to other widely reported anions. The use of [TFSI]⁻ in AC/AC capacitors makes it possible to reach an operational voltage exceeding the one typical of systems based on PILs with oxoacid anions. However, most of the tests on PIL-based ECs are dominated by almost one PIL, [HN₂₂₂][TFSI], with a very few exceptions, and among these exceptions, the PILs are not adapted for ECs due to their high melting point. Although, the study by Balducci et al, using strictly dehydrated sample on high-purity commercial AC, provided reliable data on utilization of the most popular PIL in EC, namely [HN₂₂₂][TFSI], the effect of hydrogen sorption was rather neglected due to limiting negative polarization to too high value. Hence, advantages of hydrogen related capacitance enhancement, e.g., aforementioned reversible hydrogen electrosorption were not explored. Therefore, in search for effective PILs utilization in AC-based ECs, a complex and comparative study of the factors governing the protonated cation reduction, including water content, of the cation properties such as its structure and acidity (pK_a values), as well as of the effect of EC components like electrode material and current collectors is required.

From the foregoing, the work presented in this manuscript will aim at designing a family of novel protic ionic liquids (PILs) exhibiting valuable physico- and electrochemical properties, especially faradaic contribution, for application in electrochemical capacitors (ECs). Firstly, the electrodes composition, binder type and porous carbon texture, will be adjusted to the bulky ions of PILs, especially the large [TFSI]⁻ anion, using the model PIL, [HN₂₂₂][TFSI]. Next, the same compound will be harnessed for testing the crucial issue of PIL water content effect on EC operation, especially considering hydrogen electrosorption. Then, new PILs will be tailored by manipulating the cation structure, while keeping the common [TFSI]⁻ anion. The compatibility of these novel PILs with EC components (current collectors and activated porous carbons electrodes) will be evaluated, and finally the performance of the resulting ECs will be measured.

Chapter II
Performance enhancement of PIL-based ECs
through the optimization of electrodes

1. Introduction

The adjustment of AC based electrodes to the properties of the electrolyte plays a key role in the advantageous performance of ECs, especially in terms of the obtained capacitance. It has been extensively expound in chapter I, section 2.2.3, that capacitance is enhanced when the size of carbon nanopores fits with the dimensions of ions. Besides, as stated in chapter I, section 2.2.4, the capacitance of carbon electrodes can be enhanced by enlarging the electroactive surface area, understood as the amount of porosity filled with the electrolyte, which depends on the compatibility between the surface chemistry of carbon electrodes and the electrolyte. Once the electrolyte itself is selected, here PIL, such objectives can be reached by an appropriate formulation of electrodes.

Since chapter I, section 2.4.6, clearly indicated that the most propitious PILs for their application in AC-based ECs comprise the $[\text{TFSI}]^-$ anion, compounds with the latter anion will be the interest of this dissertation. Besides, taking into account that among all the previously presented PILs, only triethylammonium bis[(trifluoromethyl)sulfonyl]imide, $[\text{HN}_{222}][\text{TFSI}]$, is really liquid at room temperature as well as it displays relatively good transport properties and high electrochemical stability on porous electrodes, it has been selected for the tests on performance enhancement of PILs-based ECs through electrodes optimization.

Accordingly, this chapter presents the effective routes for optimizing the capacitance through tailoring self-standing electrodes toward the PIL-electrolyte. The first section describes the selection of a suitable binder which involves: i) examining the electrodes wettability by the electrolyte, having in mind that the better wettability, the better distribution of the electrolyte within the accessible porous network; ii) investigating the available DFT specific surface area of the electrodes for PIL ions, which depends on the type of binder; iii) interpreting the electrochemical performance of symmetric AC/AC cells in PIL-electrolyte based on the analysis of the aforementioned factors. The second section focuses on the choice of the most beneficial porous structure for the active material to enhance the capacitance of PIL-based ECs. This discussion is illustrated by the use of three significantly different active materials (bound in electrodes), which differ by their SSA and micro/mesopores volume ratio. The electrochemical study enables to determine an advantageous composition of electrodes and to develop guidelines for the selection of active material texture.

2. Effect of binder on the performance of PIL-based ECs

As mentioned in chapter I, section 2.2.1, a binder is required to make electrodes from activated carbon powder. The effect of binder type on the wetting of electrodes in PILs has been already reported for [DIPEA][TFSI], and the following binders: polyvinylidene fluoride (PVDF) or carboxymethyl cellulose (CMC) with addition of styrene-butadiene rubber (SBR) [200]. Better wettability, manifested by a fast contact angle decrease of the PIL drop, was observed for the electrodes with the PVDF binder as opposed to the ones with CMC/SBR (Fig. 32). Accordingly, higher capacitance, $100 \text{ F}\cdot\text{g}^{-1}$ vs. $55 \text{ F}\cdot\text{g}^{-1}$ (at 2 V and $0.2 \text{ A}\cdot\text{g}^{-1}$, $30 \text{ }^\circ\text{C}$), was achieved for PVDF-based ECs [200] proving the superiority of the PVDF over CMC/SBR. Yet, it is worth noticing that wettability deterioration may likely originate from the presence of SBR in the electrodes.

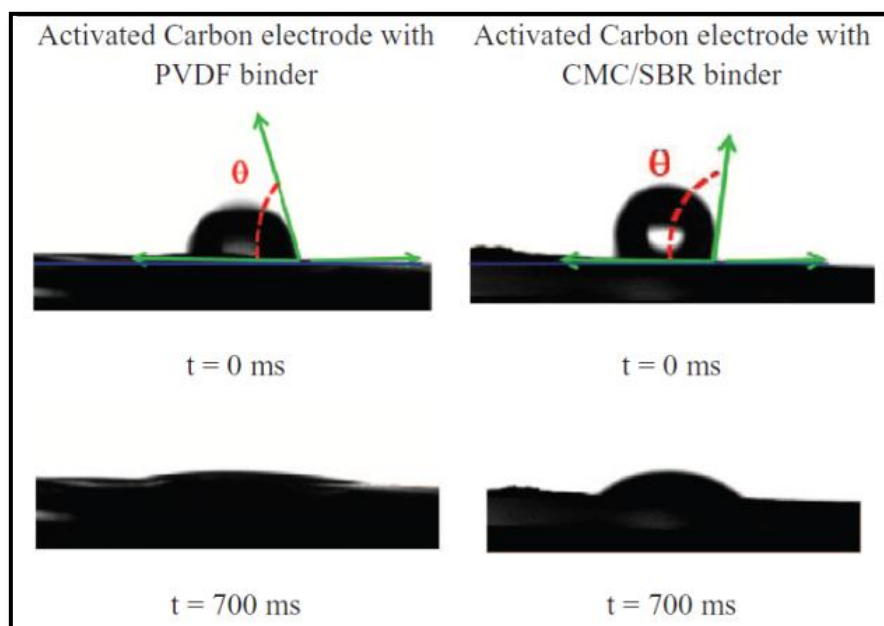


Fig. 32 Contact angle snapshots of [DIPEA][TFSI] on PVDF-AC (left) and CMC-AC electrodes (right), at $t = 0 \text{ ms}$ (top) and after 700 ms (down) [200].

The effect of binder was also investigated in $1 \text{ mol}\cdot\text{L}^{-1} \text{ NaNO}_3$ aqueous electrolyte for AC-based electrodes containing PVDF or polytetrafluoroethylene (PTFE) binder [202]. In both cases, the BET specific surface area decreased from $2066 \text{ m}^2\cdot\text{g}^{-1}$ for the pristine AC to $1544 \text{ m}^2\cdot\text{g}^{-1}$ and $1835 \text{ m}^2\cdot\text{g}^{-1}$ for AC-PVDF and AC-PTFE bound electrodes, respectively [202]. The electrochemical study revealed a higher capacitance with PTFE bound electrodes ($116 \text{ F}\cdot\text{g}^{-1}$ at $0.2 \text{ A}\cdot\text{g}^{-1}$ and 1.6 V) than with PVDF ones ($104 \text{ F}\cdot\text{g}^{-1}$ at $0.2 \text{ A}\cdot\text{g}^{-1}$ and 1.6 V),

confirming that the presence of binder affects the accessible surface area, hence the EDL formation and consequently the obtained capacitance.

Considering the above information, we excluded CMC/SBR electrodes from our study and we focused on a comparative analysis of electrodes comprising PVDF or PTFE, as prospective binders, in terms of wettability and obtained SSA. Overall, the influence of their characteristics on capacitance and coulombic efficiency of PIL-based ECs will be established.

In this section, a commercial strictly microporous activated carbon powder, DLC Supra 30 by Cabot (further referred to as S30), which is designed and firmly established for application in ECs, has been harnessed as active material for electrodes. The self-standing electrodes used in our study contained S30 active material, carbon black as conductive agent (C-ENERGY[®] Super C65 by Imerys) and binder. The S30-PVDF electrodes contained 85% AC, 5% C65, 10% PVDF and the S30-PTFE ones 80% AC, 10% C65, 10% PTFE. The detailed preparation procedure is introduced in Annex (section 4.2.1.). [HN₂₂₂][TFSI], already popularized in the tests on ECs, was applied as PIL electrolyte. In this experiment, the PIL contained around 200 ppm of H₂O, close to the amount in other reports on the utilization of [HN₂₂₂][TFSI] in ECs [178, 197].

2.1. Assessment of electrodes wettability by PIL

As shown in figure 33, when a droplet of [HN₂₂₂][TFSI] is placed on S30-PVDF and S30-PTFE electrodes, it flattens within 200 ms and 1 s, respectively, demonstrating in both cases good electrolyte distribution in the porous network of the electrodes, similarly to [200]. Even if the flattening time is slightly higher in case of the S30-PTFE electrode, the phenomenon still remains very fast, leading to conclude that the two electrodes have comparable wettability.

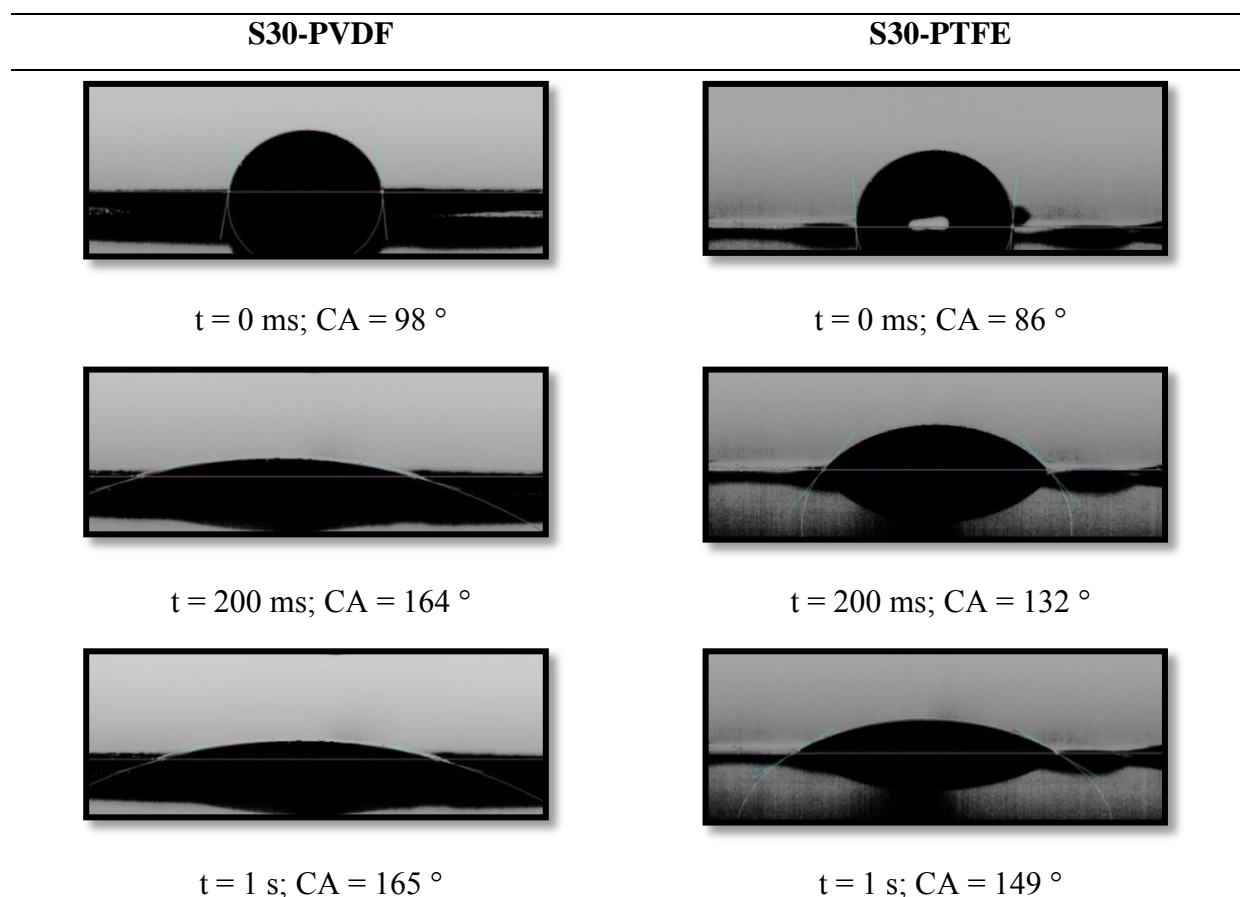


Fig. 33 Contact angle snapshots of [HN₂₂₂][TFSI] on S30-PVDF (left) and S30-PTFE (right) electrodes.

2.2. Porous texture characterization of electrodes

Figure 34 presents the nitrogen adsorption/desorption isotherms obtained at 77 K for the S30 powder and S30-PVDF and S30-PTFE electrodes. In the three cases, the isotherms are of type I typical of microporous materials; the poorly marked knee at low relatively pressure indicates a relatively large pore size distribution in the range of micropores. The textural data reported in table 3 show that the BET specific surface area decreases from 2073 m²·g⁻¹ for the S30 powder to 1725 m²·g⁻¹ and 1372 m²·g⁻¹ for S30-PTFE and S30-PVDF, respectively. Since the electrodes contain both 10 wt. % of binder, and taking into account that the values in figure 34 and table 3 are referred to the mass of carbon, it is clear that the porosity is less perturbed by PTFE than PVDF. As seen in table 3, the type of binder essentially affects the micropore volume. This effect is more quantitatively illustrated by the curves representing the DFT cumulated surface area vs. pore width (Fig. 35); the curves noticeably diverge up to ca. 1.1 nm and are further almost parallel. Hence, one might consider

that micropores smaller than 1.0 – 1.1 nm are essentially blocked by the binder, and that the blockage is more important with PVDF.

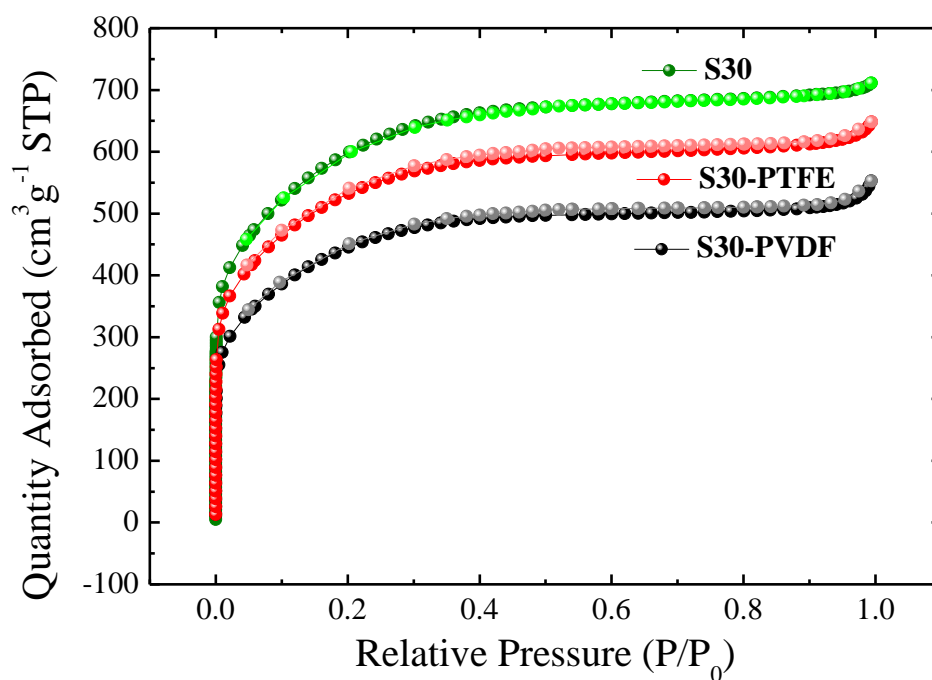


Fig. 34 Nitrogen adsorption/desorption isotherms at 77 K of S30 powder and PTFE- and PVDF-bound electrodes.

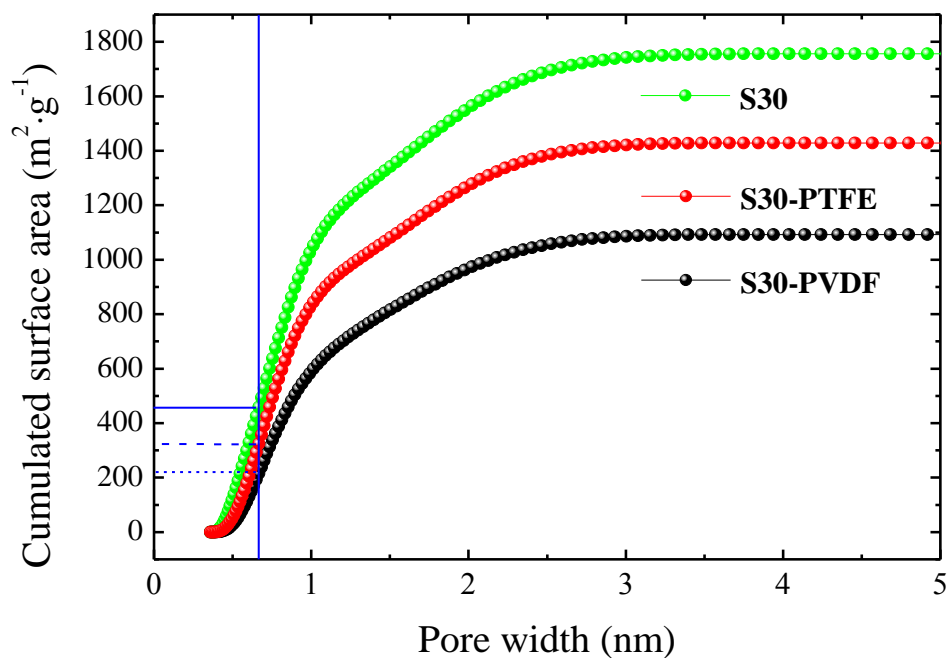


Fig. 35 Cumulated DFT specific surface area of pristine S30, S30-PTFE and S30-PVDF electrodes. The vertical line represents the width of the $[TFSI]^-$ anion.

Table 3 Textural data of the pristine S30 powder, S30-PVDF and S30-PTFE electrodes. For the electrodes, the specific surface area and the pore volumes are referred to the mass of AC; *parameters calculated by the 2D-NLDFT method.

Carbon material name	S_{BET} ($\text{m}^2 \cdot \text{g}^{-1}$)	S_{DFT} ($\text{m}^2 \cdot \text{g}^{-1}$)	V_{total} ($\text{cm}^3 \cdot \text{g}^{-1}$)	V_{micro} < 2 (nm) ($\text{cm}^3 \cdot \text{g}^{-1}$)	V_{meso} 2-50 (nm) ($\text{cm}^3 \cdot \text{g}^{-1}$)	*Average micropores size (L_0) < 2 (nm)
S30	2073	1758	1.001	0.744	0.257	0.94
S30-PTFE	1725	1433	0.850	0.624	0.226	0.97
S30-PVDF	1372	1096	0.678	0.489	0.189	1.01

Considering that the previous data are obtained with nitrogen as probe, it is now interesting to estimate which fraction of electrodes pore volume would be accessible to the ions of the electrolyte. Therefore, the models of the protonated triethylamine $[\text{HN}_{222}]^+$ and $[\text{TFSI}]^-$ anion together with their dimensions determined by COSMO-RS (Conductor-like Screening Model for Real Solvent) computation are presented in figure 36. From these models, we estimated that the larger ion, i.e. the $[\text{TFSI}]^-$ anion, limits the values of electrochemical performance which will be further discussed. Indeed, this hypothesis is logically justified by the equation (3) (chapter I, section 2.1.1.) for capacitance of a two-electrode cell, which shows that the cell capacitance is controlled by the electrode with the smallest capacitance, i.e. the positive one in this case, where the largest ions are adsorbed. Considering that $[\text{TFSI}]^-$ should present its smaller dimension to enter the pores, we have estimated the fraction of DFT specific surface area which corresponds to pores larger than 0.68 nm in figure 35, i.e. which participates to the EDL formation (expressed as $S_{\text{DFT}>0.68}$). The estimated $S_{\text{DFT}>0.68}$ values are as follows: 1299 $\text{m}^2 \cdot \text{g}^{-1}$ for S30, 882 $\text{m}^2 \cdot \text{g}^{-1}$ for S30-PVDF and 1108 $\text{m}^2 \cdot \text{g}^{-1}$ for S30-PTFE. Even if this estimation probably reveals optimistic numbers at the absolute level, the relative values are meaningful, i.e. slightly higher for the S30-PTFE electrode than for the S30-PVDF one. Hence we can predict higher capacitance values in case of the S30-PTFE ones.

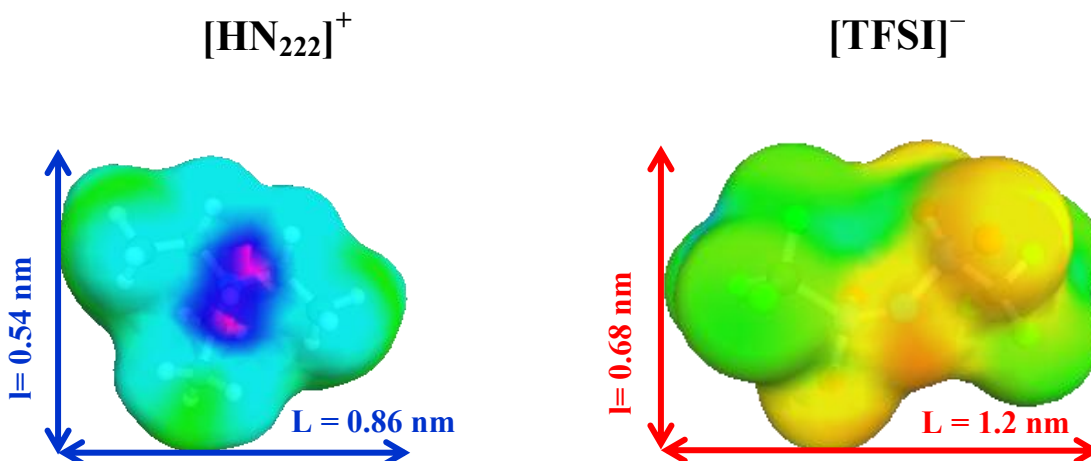


Fig. 36 Van der Waals volume of the $[\text{HN}_{222}]^+$ cation and $[\text{TFSI}]^-$ anion.

2.3. Electrochemical performance of symmetric carbon/carbon capacitors using PVDF and PTFE bound electrodes in $[\text{HN}_{222}][\text{TFSI}]$ electrolyte

Accordingly, electrochemical measurements corroborated the effect of binder on the performance of ECs. It is demonstrated by a greater area of the CVs corresponding to the cells made from the S30-PTFE electrodes (Fig. 37). Sweeps carried out at slow scan rate of $1 \text{ mV}\cdot\text{s}^{-1}$ (Fig. 37a) showed a slightly better charge propagation, seen as more distinctive rectangular shape, for the cell with S30-PTFE electrodes. The beneficial effect of the S30-PTFE electrodes is even more pronounced at faster scan rate of $5 \text{ mV}\cdot\text{s}^{-1}$ (Fig. 37b). Considering table 3, it is explained by a significantly higher impact of mesopores in S30-PTFE electrodes serving as ion diffusion channels facilitating the transport of big ionic species to micropores participating in the EDL formation.

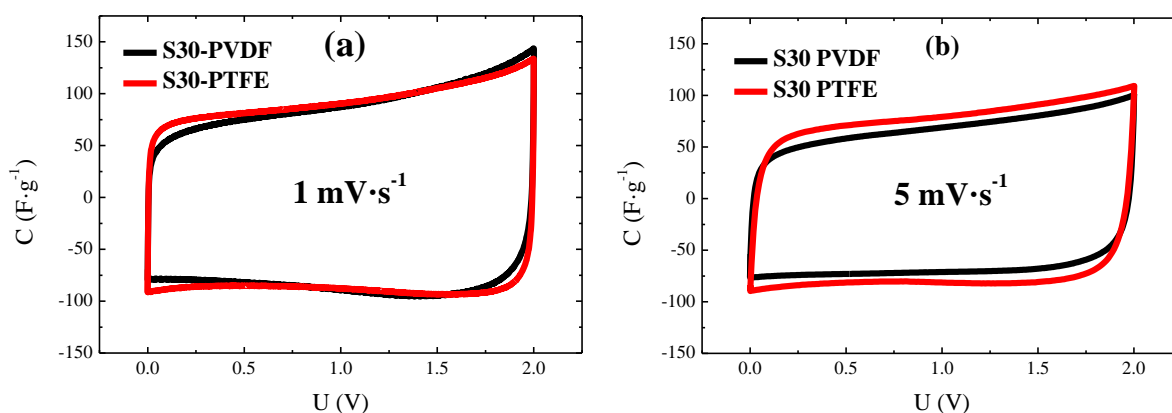


Fig. 37 Cyclic voltammograms of symmetric cells with S30-PVDF and S30-PTFE electrodes in $[\text{HN}_{222}][\text{TFSI}]$ at (a) $v=1 \text{ mV}\cdot\text{s}^{-1}$; (b) $v=5 \text{ mV}\cdot\text{s}^{-1}$.

Figure 38 displays the galvanostatic charge/discharge curves at $0.2 \text{ A}\cdot\text{g}^{-1}$ and $1 \text{ A}\cdot\text{g}^{-1}$. The discharge time is always higher for cells with S30-PTFE electrodes as compared to the S30-PVDF ones, and as for the CV data the difference is more pronounced at higher current. The discharge capacitance at 2.5 V and $0.2 \text{ A}\cdot\text{g}^{-1}$ is 98 and $83 \text{ F}\cdot\text{g}^{-1}$ for cells with S30-PTFE and S30-PVDF electrodes, respectively. At current of $1 \text{ A}\cdot\text{g}^{-1}$ (Fig. 38b), the respective values are 84 and $62 \text{ F}\cdot\text{g}^{-1}$. It again reflects the beneficial effect of mesopores: the larger mesopore volume, the easier ions transport. It also demonstrates that, in the next sections, attention should be paid to investigating the effect of carbon pores size on the capacitance properties.

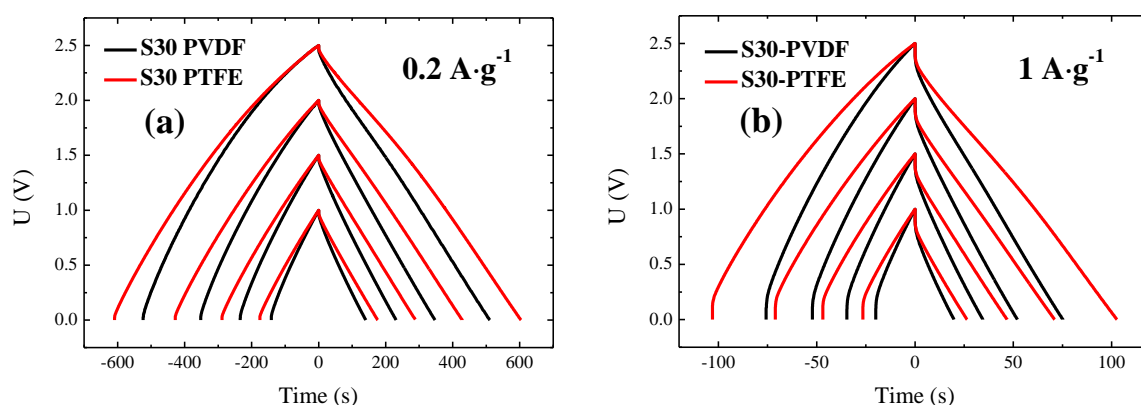


Fig. 38 Galvanostatic charge/discharge of symmetric cells with S30-PVDF and S30-PTFE electrodes in $[\text{HN}_{222}][\text{TFSI}]$ at (a) $0.2 \text{ A}\cdot\text{g}^{-1}$; (b) $1 \text{ A}\cdot\text{g}^{-1}$.

The discharge capacitance and efficiency vs. voltage of symmetric cells with S30-PTFE and S30-PVDF electrodes in $[\text{HN}_{222}][\text{TFSI}]$ are shown in figure 39 for applied currents of $0.2 \text{ A}\cdot\text{g}^{-1}$ and $1 \text{ A}\cdot\text{g}^{-1}$. For all voltages, the capacitance values at a given current are always higher with S30-PTFE electrodes than with S30-PVDF ones. The difference between the capacitance values obtained at $0.2 \text{ A}\cdot\text{g}^{-1}$ and $1 \text{ A}\cdot\text{g}^{-1}$ is slightly higher in case of the S30-PVDF electrodes; this is due to the lower mesopores volume of these electrodes which impacts more significantly charge propagation, especially at $1 \text{ A}\cdot\text{g}^{-1}$. The efficiency of ECs (discharge-to-charge time ratio) at $0.2 \text{ A}\cdot\text{g}^{-1}$ indicates a good reversibility of the processes (not lower than 99%) up to 2.5 V for S30-PTFE, and up to 2.0 V for S30-PVDF.

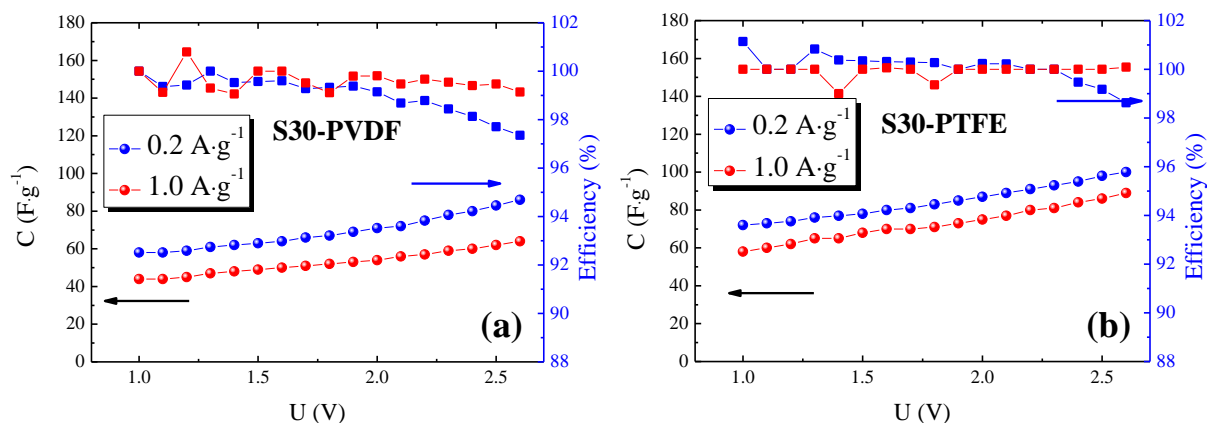


Fig. 39 Discharge capacitance and efficiency at 0.2 and 1.0 A·g⁻¹ vs. voltage for symmetric cells in [HN₂₂₂][TFSI] (a) S30-PVDF electrodes and (b) S30-PTFE electrodes.

In conclusion, the predictions which have been made by considering the porous texture data of electrodes have been validated by the electrochemical measurements. The binder has a noticeable impact on the performance of electrodes. Therefore, when studying the performance of capacitors in any electrolytic medium, it is recommended to discuss the obtained data only in light of electrodes (not of pristine carbon powder) porosity. Here, it is clear that PTFE is a preferable binder to optimize the performance of electrodes in PILs based on the [TFSI]⁻ anion.

3. In search of ACs with porous texture tuned for PIL electrolytes

Considering the relatively large size of ions in [HN₂₂₂][TFSI], we selected three carbons with different amount and size of mesopores: an essentially microporous activated carbon (DLC Supra 30 from Cabot, labeled as S30), a bimodal templated xerogel carbon (AX2000 prepared as described in [197] and kindly provided by Dr A. Arenillas from Instituto Nacional del Carbón CSIC, Oviedo, Spain) and the BP2000 carbon black (from Cabot).

Based on the results from the previous section, self-standing electrodes were prepared with PTFE as binder by mixing carbon - 80%, C-ENERGY[®] Super C65 - 10%, PTFE - 10%. For the three carbons, the contact angle measurements realized with [HN₂₂₂][TFSI] prove fast wetting of the electrodes (Fig. 40): after 1s, the PIL droplet is well-spread on the electrodes.

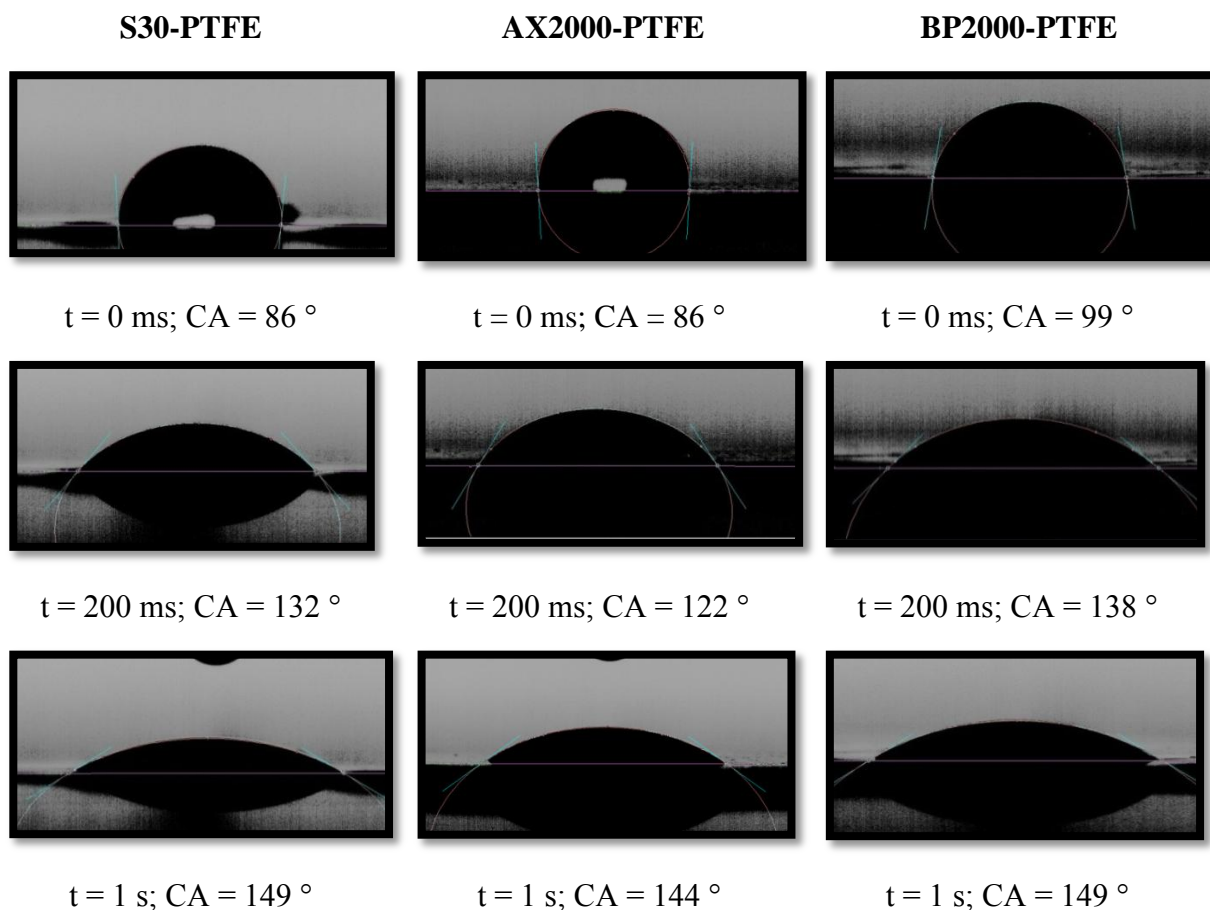


Fig. 40 Contact angle snapshots of [HN₂₂₂][TFSI] on PTFE-bound electrodes containing the S30 (left), AX2000 (middle) and BP2000 (right) active materials.

The nitrogen adsorption/desorption isotherms of the electrodes are presented in figure 41. The isotherm of S30-PTFE displays the classical type I indicating the formation of a monolayer and is attributed to a microporous material. The isotherm of the BP2000-PTFE electrode displays both the characteristics of a microporous material at low relative pressure (formation of a monolayer), and a mesoporous one with an hysteresis loop at high relative pressure, which is typical of pores associated to the external surface, as for example in carbon nanotubes [203]. The isotherm of the AX2000-PTFE electrode combines the characteristics of type I at low relative pressure (micropores), and type IV where the sharp desorption step indicates the interconnectivity of mesopores.

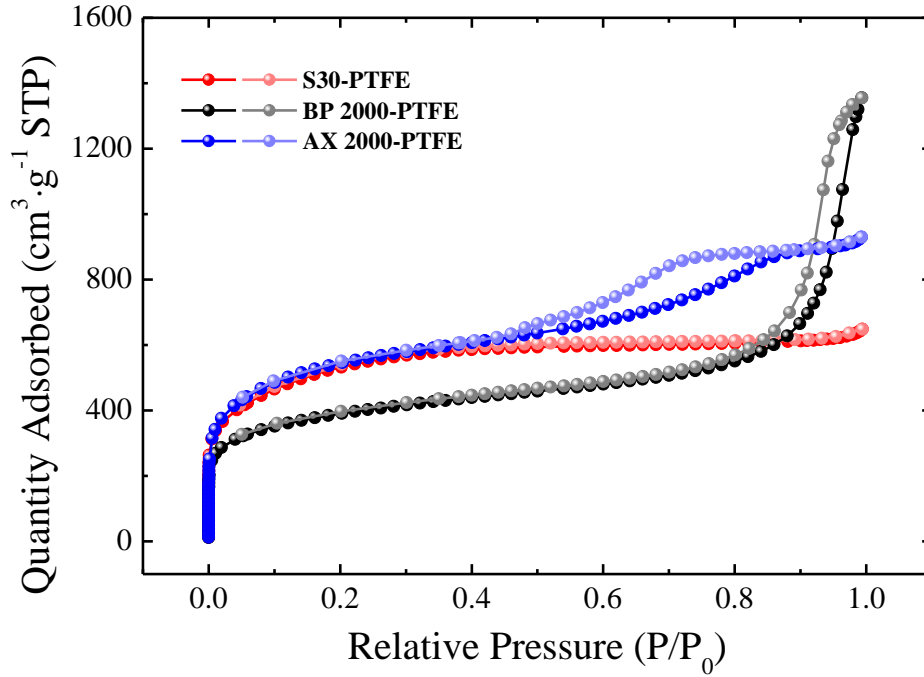


Fig. 41 Nitrogen adsorption/desorption isotherms of S30-PTFE, BP2000-PTFE and AX2000-PTFE electrodes at 77 K.

The pore size distribution (PSD) of the carbon electrodes is compared in figure 42, and the values of micropore and mesopore volumes are given in table 4. The S30-PTFE electrode shows a dominant contribution of micropores with a first peak ca. 0.7 nm followed by a second one ca. 1.8 nm (giving $L_{0\text{micro}} = 0.97$ nm) with a tail extending to small mesopores; the micropore volume represents 73% of the total pore volume. In turn, AX2000-PTFE displays a significant amount of mesopores with a broad PSD in the range of 3-11 nm, in addition to a noticeable amount of micropores (48% of the total pore volume) with $L_{0\text{micro}} = 1.03$ nm. In contrast, the porosity of the BP2000-PTFE electrode varies significantly from the other two materials showing a great impact of mesopores (80% of the total pore volume) in all the range from 2 to 50 nm. Such a wide range represents the outer space between the carbon black spherical particles; in this range, it is nevertheless worth to notice a marked peak at ca. 36 nm. The materials has also micropores able to participate in the EDL formation with $L_{0\text{micro}} = 0.95$ nm.

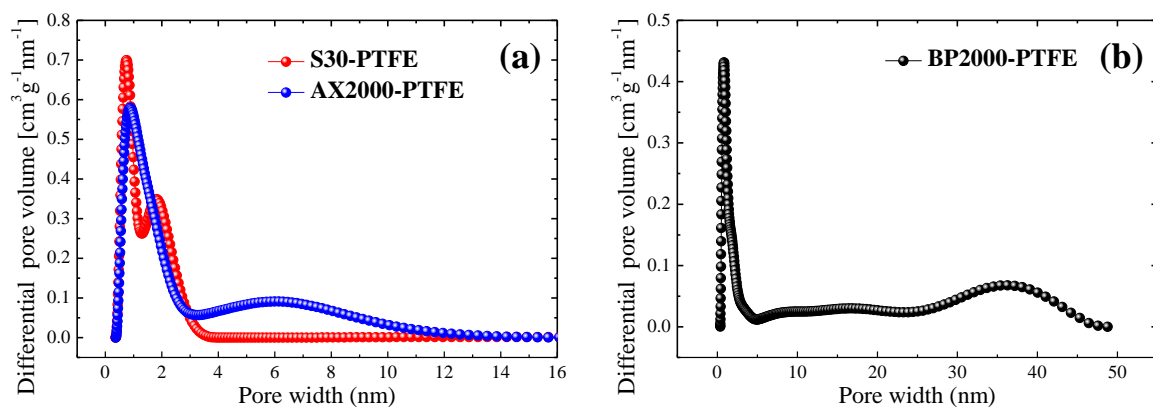


Fig. 42 2D – NLDFT pore size distribution of (a) S30-PTFE and AX2000-PTFE and (b) BP2000-PTFE electrodes.

Table 4 Textural data of S30-PTFE, BP2000-PTFE and AX2000-PTFE electrodes. The values of specific surface area and pore volume are referred to the mass of AC; *parameters calculated by the 2D-NLDFT method.

Carbon material	S_{BET}	$*S_{\text{DFT}}$	$*V_{\text{total}}$	$*V_{\text{micro}}$	$*V_{\text{meso}}$	$*\text{Average}$
	($\text{m}^2 \cdot \text{g}^{-1}$)	($\text{m}^2 \cdot \text{g}^{-1}$)	($\text{cm}^3 \cdot \text{g}^{-1}$)	< 2 (nm) ($\text{cm}^3 \cdot \text{g}^{-1}$)	2-50 (nm) ($\text{cm}^3 \cdot \text{g}^{-1}$)	micropores size (L_0) < 2 (nm)
S30-PTFE	1725	1433	0.850	0.624	0.226	0.97
AX2000-PTFE	1887	1511	1.330	0.639	0.691	1.03
BP2000-PTFE	1210	1061	1.997	0.405	1.592	0.95

As we showed previously when selecting the optimal binder, it is interesting to plot the cumulated DFT surface area and to evaluate the fraction accessible to pores larger than the width of the $[\text{TFSI}]^-$ anion, e.g., 0.68 nm (Fig. 36). It is obviously a more rough estimation than in the case of S30 electrodes with PTFE and PVDF binders due to significantly different texture of the discussed materials, yet still useful for an initial assessment. Correspondingly, the accessible specific surface area, $S_{\text{DFT} > 0.68 \text{ nm}}$, is $1108 \text{ m}^2 \cdot \text{g}^{-1}$ for S30-PTFE, $1288 \text{ m}^2 \cdot \text{g}^{-1}$ for AX2000-PTFE and $845 \text{ m}^2 \cdot \text{g}^{-1}$ for BP2000-PTFE (Figure 43). Hence, from these data, one can expect the highest capacitance values for AX2000-PTFE.

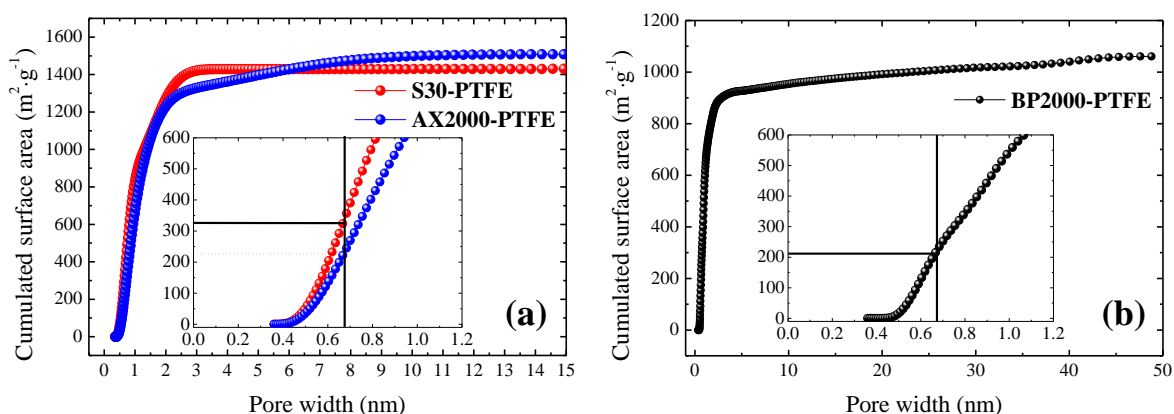


Fig. 43 Cumulated specific surface area of (a) S30-PTFE and AX2000-PTFE electrodes; (b) BP2000-PTFE electrode; the vertical line represents the width of the $[\text{TFSI}]^-$ anion (0.68 nm).

The previous statement is confirmed by figure 44 showing the highest capacitive current for the symmetric cell with AX2000-PTFE electrodes (blue curve). The CVs of cells with S30-PTFE and BP2000-PTFE are almost identical and their overlap suggests comparable capacitance values; although the accessible surface area is smaller in case of BP2000, one might anticipate that the open structure facilitates the access to available micropores. Interestingly, at this slow scan rate of $1 \text{ mV}\cdot\text{s}^{-1}$, where the effect of PIL transport properties can be neglected, the CV of the cell with AX2000-PTFE electrodes is more trapezoidal in contrast to the almost rectangular CVs with S30-PTFE and BP2000-PTFE electrodes.

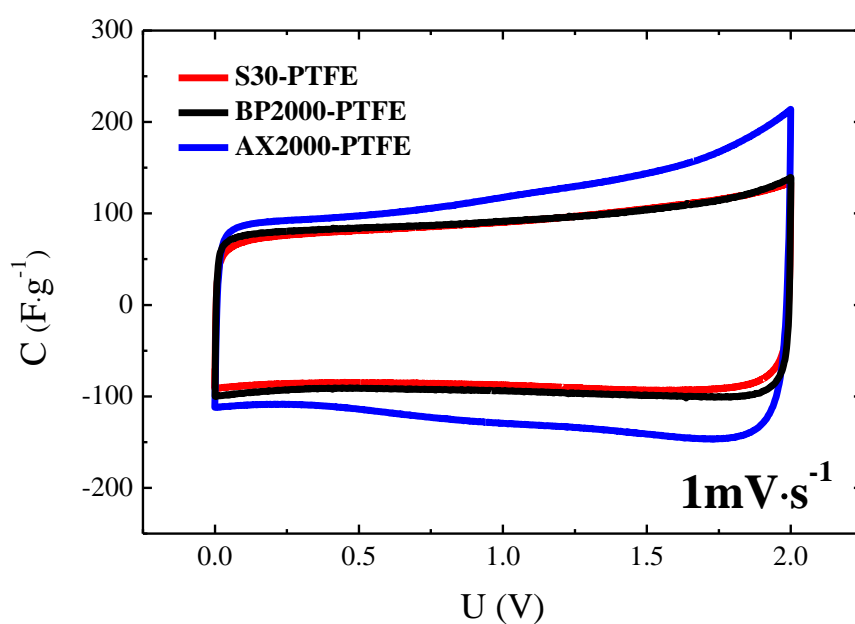


Fig. 44 Cyclic voltammograms ($1 \text{ mV}\cdot\text{s}^{-1}$) of symmetric cells based on S30-PTFE, BP2000-PTFE and AX2000-PTFE electrodes in $[\text{HN}_{222}][\text{TFSI}]$.

In search of an interpretation for these differences depending on the electrode material, cyclic voltammograms have been recorded in two-electrode cells equipped with a silver quasi reference electrode (AgQRE). In figure 45, it can be seen that the positive AX2000-PTFE electrode displays a “butterfly” shape CV with significantly higher capacitance than the S30-PTFE one. These differences of capacitive current are in good fitting with the relative values of accessible specific surface area for $[\text{TFSI}]^-$. This specific performance of AX2000-PTFE is attributed to the beneficial impact of mesopores which both participate in ions transportation to micropores and also take some part in the EDL formation. In turn, the comparison of negative electrodes reveals that hydrogen electrosorption is more pronounced on AX2000-PTFE (Fig. 45) and that, for a cell voltage of 2.0 V, it is initiated at higher potential value, ca. -0.75 V vs. AgQRE, than for S30-PTFE, ca. -1.05 V vs. AgQRE. In this latter case, the cell voltage had to be increased up to 2.5 V to make it visible. Up to a voltage of 2.0 V, the cell with S30-PTFE electrodes in $[\text{HN}_{222}][\text{TFSI}]$ operates mostly by EDL charging (red curves), whereas a slight contribution of hydrogen electrosorption occurs on the negative electrode (brown dotted curve) at higher voltage of 2.5 V. Hence, when the voltage is limited to 2 V (Fig. 45), the cell with AX2000-PTFE electrodes displays better EDL capacitance related with $[\text{TFSI}]^-$ anions at the positive electrode and an additional contribution of hydrogen sorption at the negative one. The more trapezoidal shape of CV for this cell (Fig.44) is essentially due to the contribution of hydrogen sorption/desorption. All these properties are related to the specific porous texture of the AX2000 carbon.

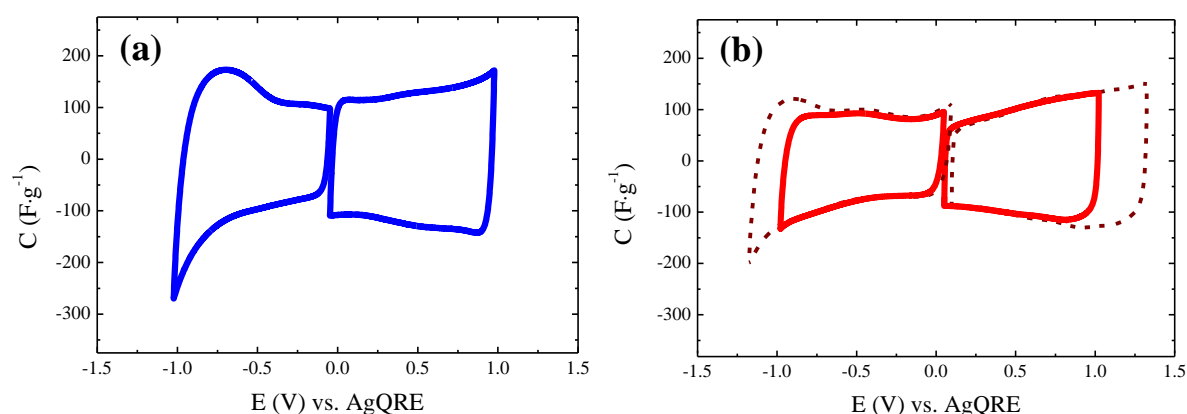


Fig. 45 Cyclic voltammograms ($1 \text{ mV}\cdot\text{s}^{-1}$ per electrode) of symmetric cells with AgQRE in $[\text{HN}_{222}][\text{TFSI}]$: (a) AX2000-PTFE electrodes, (b) S30-PTFE electrodes.

The galvanostatic ($0.2 \text{ A}\cdot\text{g}^{-1}$) charge/discharge curves of symmetric cells based on S30-PTFE, AX2000-PTFE and BP2000-PTFE electrodes in $[\text{HN}_{222}][\text{TFSI}]$ electrolyte are presented in figure 46. These measurements confirm a higher capacitance of $124 \text{ F}\cdot\text{g}^{-1}$

(at a voltage of 2.0 V) with AX2000-PTFE electrodes (in accordance with the highest $S_{DFT>0.68nm}$) in contrast to 92 and 87 $F \cdot g^{-1}$ for BP2000-PTFE and S30-PTFE, respectively. At applied voltage values of 1.0, 1.5 and 2.0 V, the galvanostatic charge/discharge curves are almost symmetrical for each type of carbon. Likewise, in all the cases, the capacitance values increase with voltage, due to the decrease of ion/pore wall distance, in accordance with equation (1), (chapter I, section 2.1.1.) giving the expression of double-layer capacitance. At 2.0 V, the shape of galvanostatic curves fits well with the cyclic voltammograms shown in figures 44, whereas the slightly convex discharge curve of AX2000-PTFE results from more pronounced hydrogen desorption at the negative electrode as shown in figure 45.

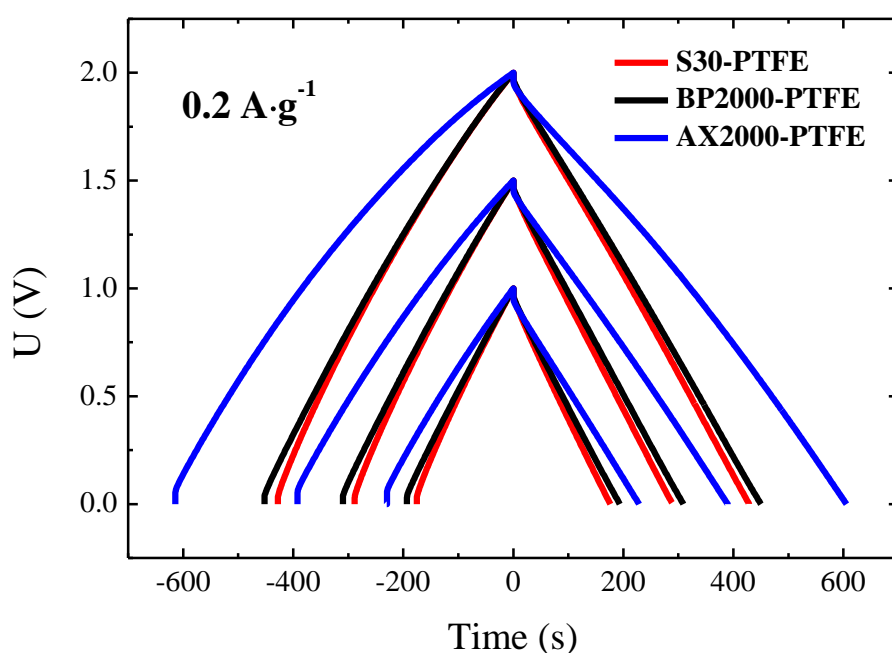


Fig. 46 Galvanostatic ($0.2 A \cdot g^{-1}$) charge/discharge of two-electrode cells based on S30-PTFE, BP2000-PTFE and AX2000-PTFE electrodes in $[HN_{222}][TFSI]$.

The further analysis shows the discharge capacitance and efficiency of AC/AC capacitors at $0.2 A \cdot g^{-1}$ versus voltage. As shown in figure 47a, the already high capacitance of AX2000-PTFE, measured at initial voltage of 1.0 V, rapidly rises with increasing voltage. However, the limit of 99% coulombic efficiency is reached at a voltage of 1.8 V for this material; it is probably due to the production of di-hydrogen at the negative electrode. In turn, the application of BP2000-PTFE (Fig. 47b) contributed to keep coulombic efficiency higher than 99% up to 2.2 V, which is slightly lower than for S30-PTFE with 2.5 V (Fig. 39).

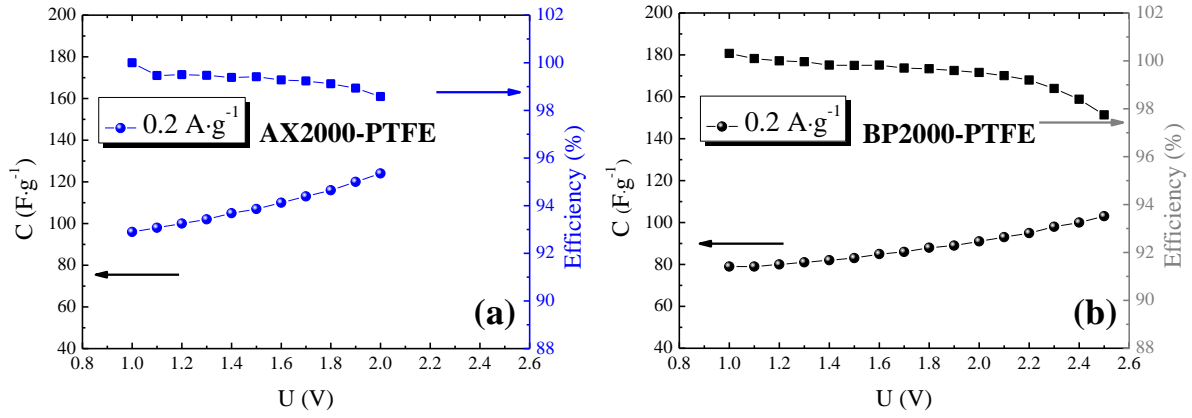


Fig. 47 Discharge capacitance and efficiency of AC/AC capacitors versus voltage at 0.2 A·g⁻¹ operating in [HN₂₂₂][TFSI] obtained at (a) AX2000-PTFE and (b) BP2000-PTFE electrodes.

Finally, energy and power were calculated according to ref [204] from galvanostatic charge/discharge data, using the area under the discharge curve (discharge energy ($E_{int/D}$)) as in equation (24):

eq. 24

$$E_{int/D} = I \int_{t(U_{max})}^{t(U_{min})} U(t) dt$$

and correspondingly the specific energy ($E_{S,int/D}$) is given by equation (25):

eq. 25

$$E_{S,int/D} = \frac{E_{int/D}}{m_{act} \cdot 3.6}$$

and specific power ($P_{S,int/D}$) by equation (26):

eq. 26

$$P_{S,int/D} = \frac{E_{S,int/D}}{t_{dis}}$$

where, I – stays for current, U_{min} and U_{max} – for minimum and maximum voltage, m_{act} is the average mass of active material in one electrode and t_{dis} – is the discharge time. The Ragone plot correlating energy and power is presented in figure 48 taking into account the maximum voltage determined from the limit of 99% coulombic efficiency for each type of electrode.

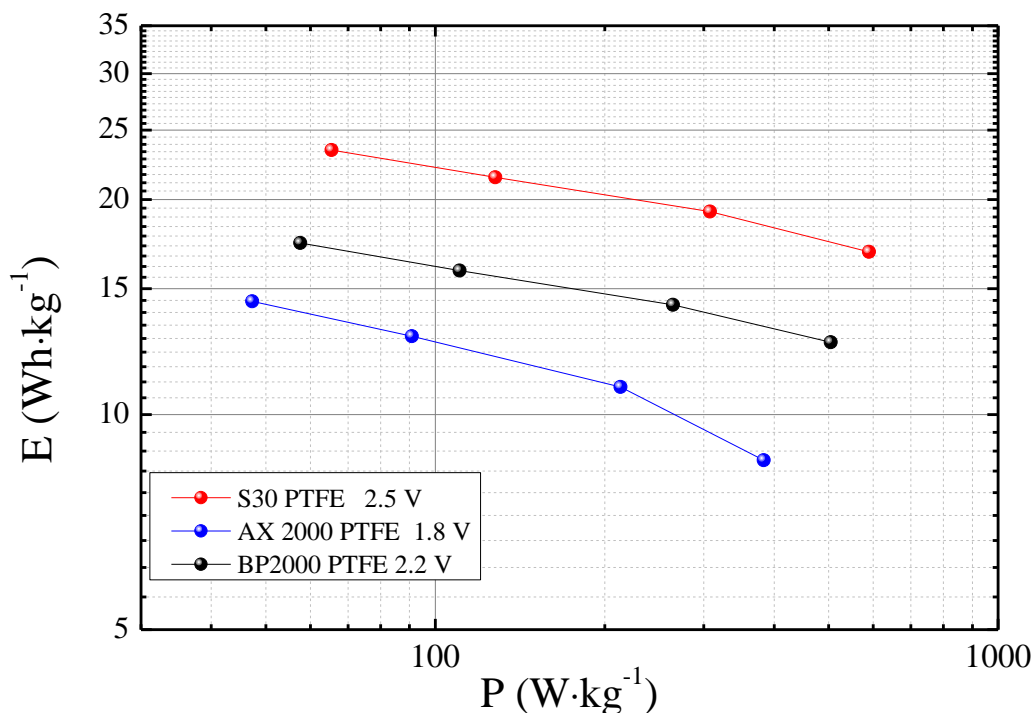


Fig. 48 Ragone plots of ECs with S30-PTFE, BP2000-PTFE and AX2000-PTFE electrodes in $[\text{HN}_{222}][\text{TFSI}]$; each plot is obtained at the maximum voltage enabling to reach 99% efficiency.

It is clearly seen that, among the tested materials, the S30-PTFE electrodes provide the highest specific energy, close to $21.5 \text{ Wh}\cdot\text{kg}^{-1}$ (at $0.2 \text{ A}\cdot\text{g}^{-1}$), owing to the highest cell voltage (2.5 V). This value is greater than values reported for aqueous electrolytes, e.g., $E_{S,int/D}$ in Li_2SO_4 is $8.6 \text{ Wh}\cdot\text{kg}^{-1}$ at 1.2 V or $16.5 \text{ Wh}\cdot\text{kg}^{-1}$ at 1.6 V, yet nearly half lower than the energy in aprotic ionic liquid, e.g., $[\text{C}_2\text{C}_1\text{Im}][\text{TFSI}]$ with $40 \text{ Wh}\cdot\text{kg}^{-1}$ (essentially due to the voltage as high as 3.2 V) [204]. The cell with BP2000-electrodes displays $15.9 \text{ Wh}\cdot\text{kg}^{-1}$ (at $0.2 \text{ A}\cdot\text{g}^{-1}$), which is slightly higher than $12.9 \text{ Wh}\cdot\text{kg}^{-1}$ (at $0.2 \text{ A}\cdot\text{g}^{-1}$) with AX2000-PTFE. In the literature [200], CMC-bound Super 30 electrodes in the same PIL, $[\text{HN}_{222}][\text{TFSI}]$, have been reported to provide $7 \text{ Wh}\cdot\text{kg}^{-1}$ (calculated per total mass of active material, at $2 \text{ A}\cdot\text{g}^{-1}$, 2.4 V), which roughly correlates with the energy value which we found for S30-PTFE electrodes (particularly taking into account that we used smaller current). Hence, although AX2000 is an interesting material on the point of view of reachable capacitance with $[\text{HN}_{222}][\text{TFSI}]$ electrolyte, it is not applicable because of its low stability window. One might anticipate that the material contains a noticeable amount of dangling bonds which favor electrolyte decomposition, thus reducing the stability window as compared to stabilized materials as e.g., the S30 carbon.

4. Conclusion

In this chapter the characteristics of electrodes and ECs based on three carbon materials and two binders were investigated in [HN₂₂₂][TFSI] electrolyte, with the objective to get information on electrode formulation enabling to optimize EC performance.

Contact angles measured on S30-PVDF and S30-PTFE electrodes have revealed comparable wetting by [HN₂₂₂][TFSI]. By contrast, the kind of binder has a strong influence on the reduction of electrodes pore volume, the latter being more reduced when using PVDF. Consequently, the PTFE-based electrodes displayed higher capacitance than the PVDF-based ones. Additionally, S30-PTFE electrodes allowed higher voltage (2.5 V) to be reached than with the S30-PVDF ones (2.0 V). Such difference could be attributed to different potential window of positive and negative electrodes in the two systems, due to different pore blockage.

The application of AX2000-PTFE electrodes resulted in the highest capacitance among all the tested carbon electrode materials, however, their operational voltage was limited in contrast to S30-PTFE and BP2000-PTFE electrodes. The significantly higher capacitance is related to greater accessible surface area as well as facilitated hydrogen electrosorption. Furthermore, similar values of capacitance were obtained for both BP2000-PTFE and S30-PTFE, although the accessible SSA of the former is smaller. It confirms the importance of mesopores as diffusion channels facilitating ions movement during charging and discharging.

As S30-PTFE electrodes allow for the highest operational voltage (2.5 V) providing the highest energy density among the tested materials, they are recommended for ECs based on pure PIL. In turn, AX2000-PTFE electrodes, on which PIL is reduced at higher potential, should be preferably used for hydrogen coupling faradaic contributions such as hydrogen storage.

Chapter III
**Effect of low water content in protic ionic liquid on
ions electrosorption in carbon porosity**

1. Introduction

The presence of even low water content in both organic and ionic liquid electrolytes is known to influence the performance of electrochemical capacitors (ECs), and particularly to reduce their stability window and cycle life. Considering the uniqueness of PILs, which proton tethered on the positively charge cation is prone to react with water to form hydronium, specific transport and electrochemical properties depending on the amount of incorporated H₂O can be anticipated. Although a few papers have dealt with the application of PIL-electrolyte in ECs, mostly using [HN₂₂₂][TFSI], some crucial aspects of their employment, especially hydrogen electrosorption from PIL onto activated carbon (AC) electrode, have not been thoroughly specified with an emphasis to the presence of electroactive water species.

Therefore, chapter III focuses on the performance of AC electrodes as well as AC/AC ECs in PIL electrolyte, namely [HN₂₂₂][TFSI], containing variable amount of water: less than 20, 150, 1000 and 10,000 ppm. Taking into consideration the findings from chapter II, AX2000-PTFE electrodes were selected owing to their high accessible surface area, facilitated EDL charging as well as promotion of hydrogen sorption.

The first section of chapter III reports on a water dependent alteration of [HN₂₂₂][TFSI] phase transitions, as well as an evolution of transport properties, conductivity and viscosity, which serve as subsidiary information for the further interpretation of electrochemical measurements on the AC electrodes and AC/AC ECs in the PIL. The hydrogen electrosorption parameters suspected to be controlled by the amount of incorporated water are studied under negative polarization of AC electrode. Afterwards, the operation of symmetric ECs is investigated using cyclic voltammetry, galvanostatic charge discharge and electrochemical impedance spectroscopy. Two-electrode cells with reference are also used to determine the performance of positive and negative electrodes. The last paragraph discloses the impact of current collectors, aluminum and stainless steel, on ECs operation when using [HN₂₂₂][TFSI] with 1000 and 10,000 ppm of water.

2. Effect of water traces on the thermal and transport properties of [HN₂₂₂][TFSI]

The thermal behavior of [HN₂₂₂][TFSI] with different amounts of water traces (150 and 1000 ppm) was investigated by DSC from -50 to 100 °C. During each DSC measurement, the sample was first heated from RT to 100 °C (step not presented here), then cooled down from 100 to -50 °C and finally heated to 100 °C at 10 °C·min⁻¹. Figure 49 shows the thermograms obtained with 150 ppm of water (Fig. 49a) and 1000 ppm of water (Fig. 49b).

In the presence of 1000 ppm of water, two peaks are observed during heating of the sample (Fig. 49b): melting ($T_m = 2$ °C) and eutectic peak ($T_e = -13.8$ °C) characteristic of the strong interaction between the PIL components and water molecules, similarly to a previous report [178]. At lower amount of water as 150 ppm, no eutectic is observed (Fig. 49a), while T_m is shifted to a higher value ($T_m = 5.9$ °C). At this water content, the interactions between water and ions are not sufficiently strong to participate in eutectic. A similar phenomenon was reported by Martinelli et al. who investigated binary systems of H₂O/ethylimidazolium bis[(trifluoromethyl)sulfonyl]imide, [C₂Im][TFSI], and correlated it with the tendency of PIL species to form separated nanodomains [188]. The occurrence of such nanophases is even more likely if the contradictory nature of hydrophobic anion and hydrophilic cation (significantly enhanced by hydrogen bonded to its central atom) influences their segregation in presence of water.

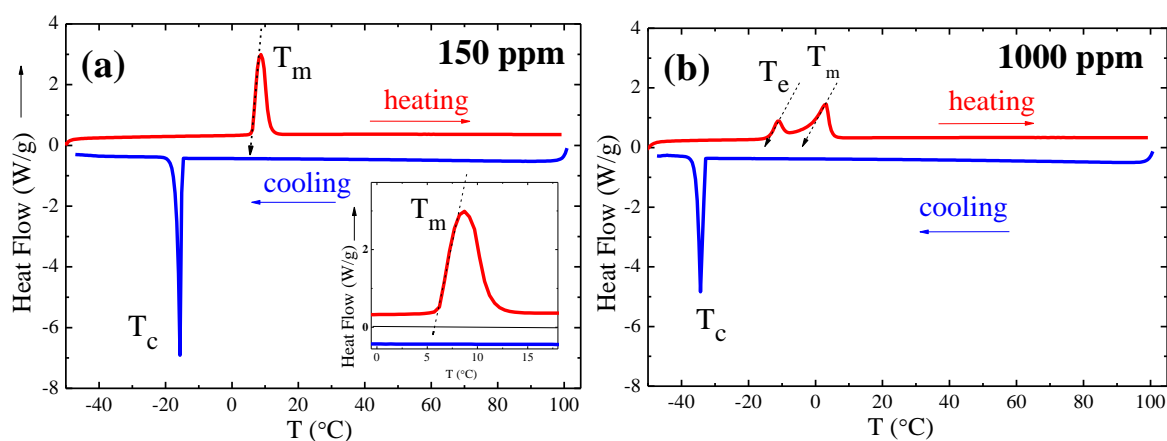


Fig. 49 DSC thermograms of [HN₂₂₂][TFSI] with (a) 150 ppm and (b) 1000 ppm of water.

The transport properties of an electrolyte (ions mobility and fluidity) can be influenced by the ions alkalinity, their size and their relative capacity to form hydrogen bonds, especially

in presence of residual water. The commonly known effect of water on ILs' viscosity decreasing as water content increases was already stated by Seddon et al. [205]. Therefore, the amount of water should be always controlled and indicated to evaluate the associated physicochemical data. In the case of PILs, due to their acid/base character, the transport properties are highly dependent on hydrogen lability. Additionally, van der Waals interactions [171, 206], mass and size of the cation [173] influence significantly the ILs viscosity and conductivity. Figure 50 (a, b) shows the variation of conductivity and viscosity from 273 K to 353 K depending on water content in the PIL (150, 1000, 10,000 ppm). Whatever water content, the shape of the curves is similar over the temperature range, and no significant difference was observed between 150 and 1000 ppm of water, whereas for 10,000 ppm of water, the conductivity differs by 13% at 353 K from the two other cases and the viscosity by 30% at 283 K. Hence, the water content has a stronger effect on viscosity, demonstrating the prevalence of interactions between ions and water molecules when the quantity of water is close to one mole for 6 moles of ions (table 5), especially at low temperature.

Table 5 Water content in the tested PIL solutions and corresponding molar fraction in comparison to the equilibrium amount of H₂O (adsorbed by PIL when handled in outer conditions).

Water content	Very dry PIL <20 ppm	150 ppm	1000 ppm	10,000 ppm	equilibrium > 4%
Mol fraction	$< \frac{1}{2420}$	$\frac{1}{320}$	$\frac{1}{50}$	$\frac{1}{6}$	$\frac{1}{2}$

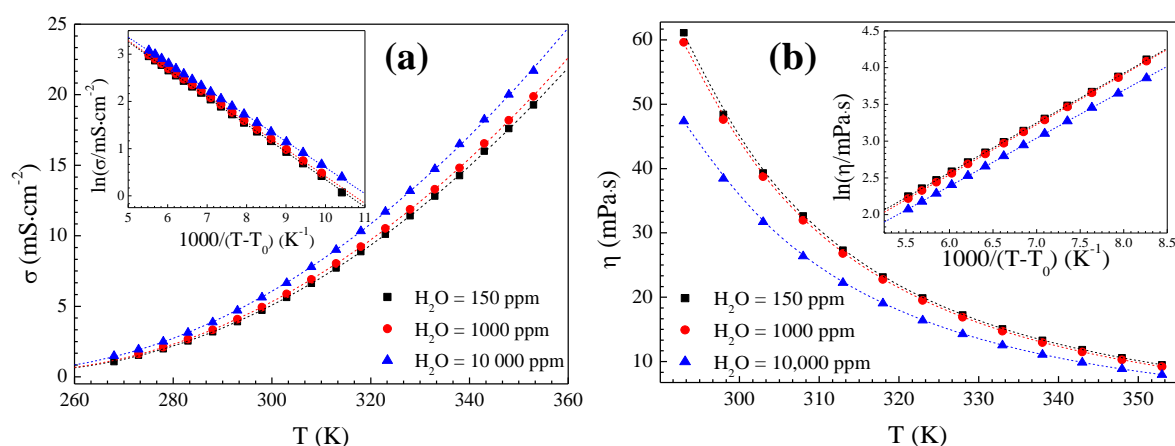


Fig. 50 Effect of temperature on (a) conductivity and (b) viscosity depending on water content (150, 1000 and 10,000 ppm) in [HN₂₂₂][TFSI].

Furthermore, by fitting the conductivity or viscosity values by the Vogel-Tamman-Fulcher (VTF) equations (18 and 20 from chapter I, section 2.4.2.) it also appears that the slopes (B_σ , B_η) are unchanged by water addition, as it is shown in the insets of Fig. 50a and Fig. 50b. Hence, the addition of a small amount of water does not seem to affect the viscous flow mechanism or ions mobility (their activation energy remains unchanged), but only changes the order of magnitude of the variables (σ_0 and η_0). In conclusion, traces of water in pure [HN₂₂₂][TFSI] do not change significantly macroscopic transport properties. However, the occurrence of eutectic around 1000 ppm demonstrates the presence of high microscopic bonding (water-ions interactions).

3. How does various amount of incorporated water in PIL affect the operation of AC electrodes and AC-based ECs?

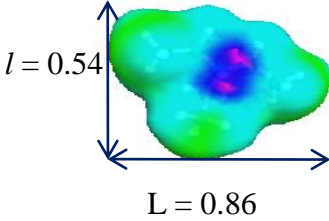
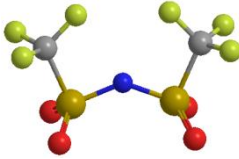
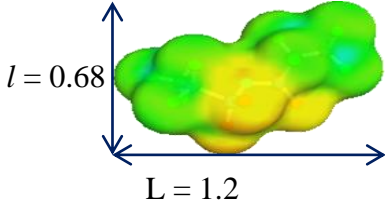
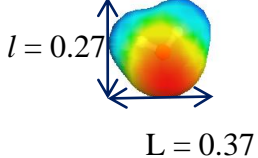
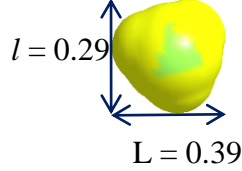
3.1. Characterization of the electrolyte species by computational methods

To understand the dependence of EC performance on electrolyte species nature, [HN₂₂₂]⁺, [TFSI]⁻, hydronium ions and neutral water molecules were generated computationally and are presented in table 6, including the van der Waals volume (V_w), the projected minimal (l) and maximal (L) dimensions, the charge distribution and the polarizability (P). The total charge is calculated from sigma and pi charge components, and displayed on a charge surface profile. The partial charge distribution marked by the colored surface determines the affinity of the molecule with the charged surface of activated carbon. The polarizability (P) expresses the local electric field generated by induced partial charge (induced dipole) of ions spread through interionic cavities in the PIL and can be calculated by the Miller and Savchik method. [207]. This parameter allows the electrical properties of electrolyte species and their response to electronic polarization to be estimated.

All these parameters can explain the expected coulombic interactions between the adsorbed species and the charged carbon surface which can affect ions diffusion into the pores, as well as the electrolyte electrochemical performance depending on water content, pore size and applied potential. It is worth noticing that the [TFSI]⁻ anion volume (V_w) and polarizability (P) are slightly larger than those calculated in the case of the [HN₂₂₂]⁺ cation. However, both ions are widely larger and more polarizable (5 to 10 times higher) than the water molecule or hydronium ion, which may be formed from the labile proton and residual water molecules. These observations should be taken into consideration to discuss the

accessibility of such species to the electrode/electrolyte interface and their diffusion in the pores. This issue will be discussed more extensively below in light of the electrochemical results.

Table 6 Structure, abbreviation, charge profile, van der Waals volume (V_w in nm), dimensions (l , L in nm) and polarizability (P) of the electrolyte ions or molecules.

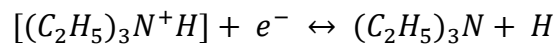
Structure and abbreviation	Charge profile  Dimensions of species l , L (nm)	van der Waals volume ($10^{-3} \cdot \text{nm}$)	Polarizability P
 [HN ₂₂₂] ⁺	 $l = 0.54$ $L = 0.86$	129	13.2
 [TFSI] ⁻	 $l = 0.68$ $L = 1.2$	169	15.7
 H ₂ O	 $l = 0.27$ $L = 0.37$	19.51	1.47
 H ₃ O ⁺	 $l = 0.29$ $L = 0.39$	21.91	2.95

3.2. Cathodic behavior of AC in [HN₂₂₂][TFSI] with various water contents

Figure 3 represents the three-electrode cyclic voltammograms (CVs) of AC (with aluminum current collectors) in [HN₂₂₂][TFSI] containing <20 ppm, 150 and 1000 ppm of H₂O, while the lower vertex potential is shifted by -100 mV steps. These curves resemble the CVs characteristics observed when an activated carbon electrode is negatively polarized in an aqueous electrolyte; at low potential, water or hydronium is reduced and nascent hydrogen is weakly chemisorbed in the porosity of carbon [101, 102]. For the high values of vertex potential, the CVs in [HN₂₂₂][TFSI] display the typical rectangular shape due to electrical double-layer charging. When the vertex potential decreases, a negative current leap attributed to electrolyte reduction appears and is accompanied by an anodic peak during the positive scan. Interestingly, for a given amount of water in the PIL, the position of the positive peak is independent of the vertex potential value. However, when comparing the CVs obtained with varying the water content in [HN₂₂₂][TFSI], one can observe that the peak position is shifted to lower values when the water content increases, e.g., -0.42, -0.54 and -0.76 V vs. AgQRE, with <20 ppm, 150 ppm and 1000 ppm of water, respectively. Hence, the strength of the carbon-hydrogen bond decreases with increasing water content. To explain these differences, and similarly to the mechanisms suggested in acidic or basic aqueous electrolyte, [102] one may consider that different kinds of species may be available for reduction in the PIL medium depending on water content.

For low amount of water (<20 ppm), [HN₂₂₂]⁺ is the only cationic species present in the medium. When the AC electrode potential is decreased, this cation is reduced as in equation (eq. 27), and the produced nascent hydrogen is chemisorbed in the porosity of AC, represented by <C> (equation (eq. 28)):

eq. 27

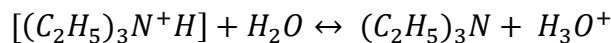


eq. 28



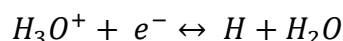
In presence of higher amount of water (1000 ppm), the Brønsted [HN₂₂₂]⁺ acid reacts with water as in equation (eq. 29):

eq. 29



and the hydronium cation which is formed serves as nascent hydrogen source (eq. 30):

eq. 30



which is then electrosorbed in carbon as in equation (eq. 28).

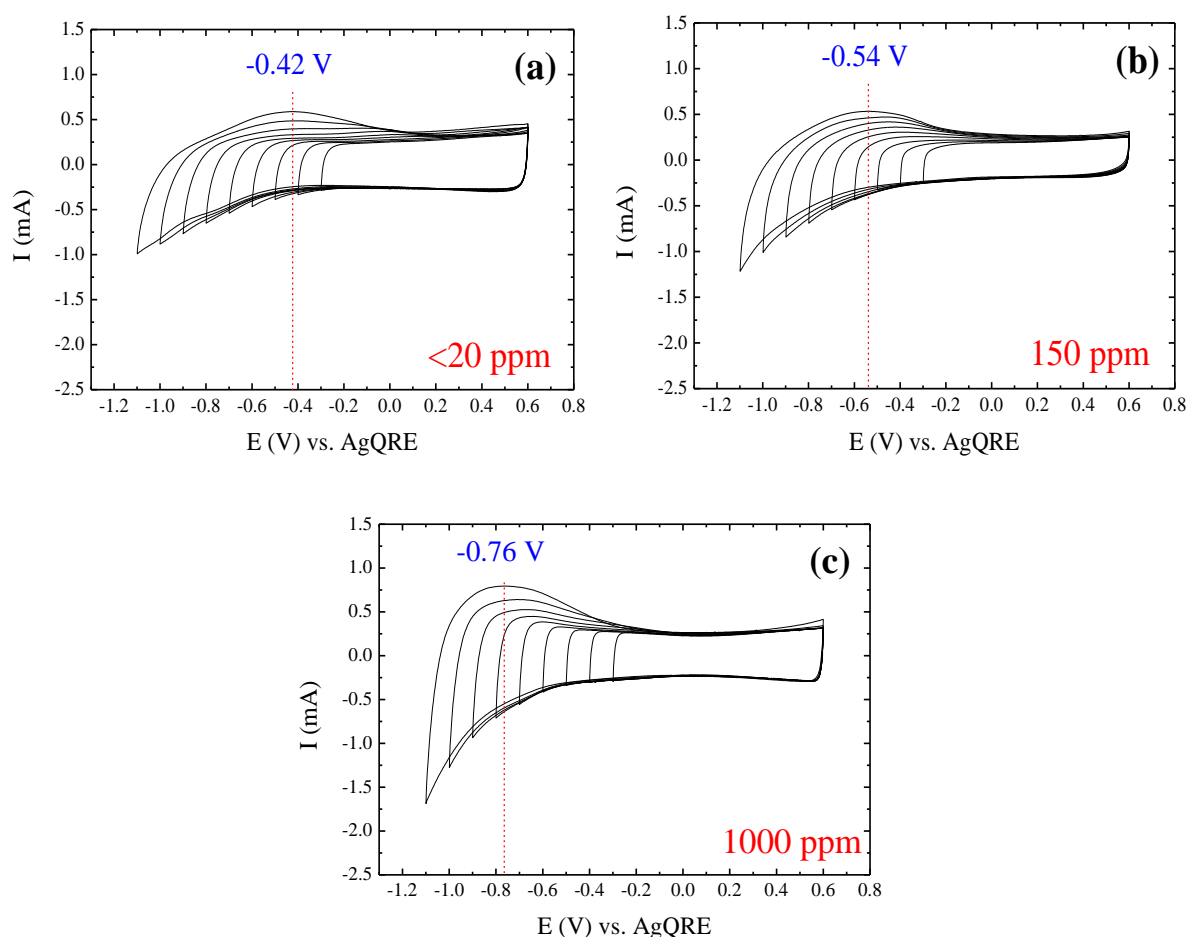


Fig. 51 Three-electrode cyclic voltammograms ($1\text{mV}\cdot\text{s}^{-1}$) of AC in $[\text{HN}_{222}][\text{TFSI}]$ with various water contents: (a) <20 ppm; (b) 150 ppm and (c) 1000 ppm.

From figure 51, it is likely that hydrogen recombination leading to molecular hydrogen evolution (so-called Tafel reaction, e.g., $\text{H} + \text{H} \leftrightarrow \text{H}_2$) is less favored at low water content than with the PIL containing 1000 ppm of water. Similar observations were made in ref [102] for aqueous electrolytes, where the shift of the anodic peak vs. the equilibrium potential was much lower in $3\text{ mol L}^{-1} \text{H}_2\text{SO}_4$ than in $6\text{ mol L}^{-1} \text{KOH}$. In aqueous KOH and in PIL with low water content, hydrogen in the zero oxidation state is formed by reduction of H_2O and $[\text{HN}_{222}]^+$, respectively, whereas in H_2SO_4 and in the PIL with 1000 ppm of water, the

protons are directly available in the electrode/electrolyte interface for the redox process. Therefore, in the PIL with 1000 ppm of water, hydrogen evolution as well as its oxidation proceeds more easily with a smaller polarization than in the dry PIL (<20 ppm water). In case of the PIL containing 150 ppm of water, one may suggest that there is a contribution of both equations (eq. 27) and (eq. 30), leading to the intermediate position of the anodic peak at -0.54 V vs. AgQRE.

3.3. Cyclic voltammograms of AC-based ECs in [HN₂₂₂][TFSI] with various water contents

A two-electrode cell with aluminum current collectors and AgQRE was employed to record the cyclic voltammograms (CVs) of the positive and negative AC electrodes separately, using [HN₂₂₂][TFSI] with <20 ppm, 150 and 1000 ppm of water. Figure 52 shows the CVs of electrodes for maximum values of voltage varying from 1 V to 2 V by steps of 100 mV. Whatever the water content, the CVs of positive and negative electrodes display a marked asymmetry of shape. This distinction is related to differentiated diffusion and adsorption of the [TFSI]⁻ anion (positive side) and [HN₂₂₂]⁺/[H₃O]⁺ cation (negative side), and also to faradaic processes. For the negative electrode, the CVs are in line with those which were obtained in three-electrode cell (see paragraph 3.2.); the faradaic contribution is affected by the water content and the nature of the reduced species, either [HN₂₂₂]⁺ at <20 ppm of water or H₃O⁺ at 1000 ppm of water.

In case of the positive electrode, scanning to gradually increasing maximum voltage significantly alters the Stern layer composition, while reversible peaks appear for the cell using the PIL with <20 ppm of water (Fig. 52a), revealing that potential-induced ions adsorption/rearrangements are easy processes for anions. For 150 ppm and 1000 ppm of water, adsorption peaks are no longer observed for the positive electrode, and the CVs display a “butterfly” shape typical for EDL charging (Fig. 52b and Fig. 52c).

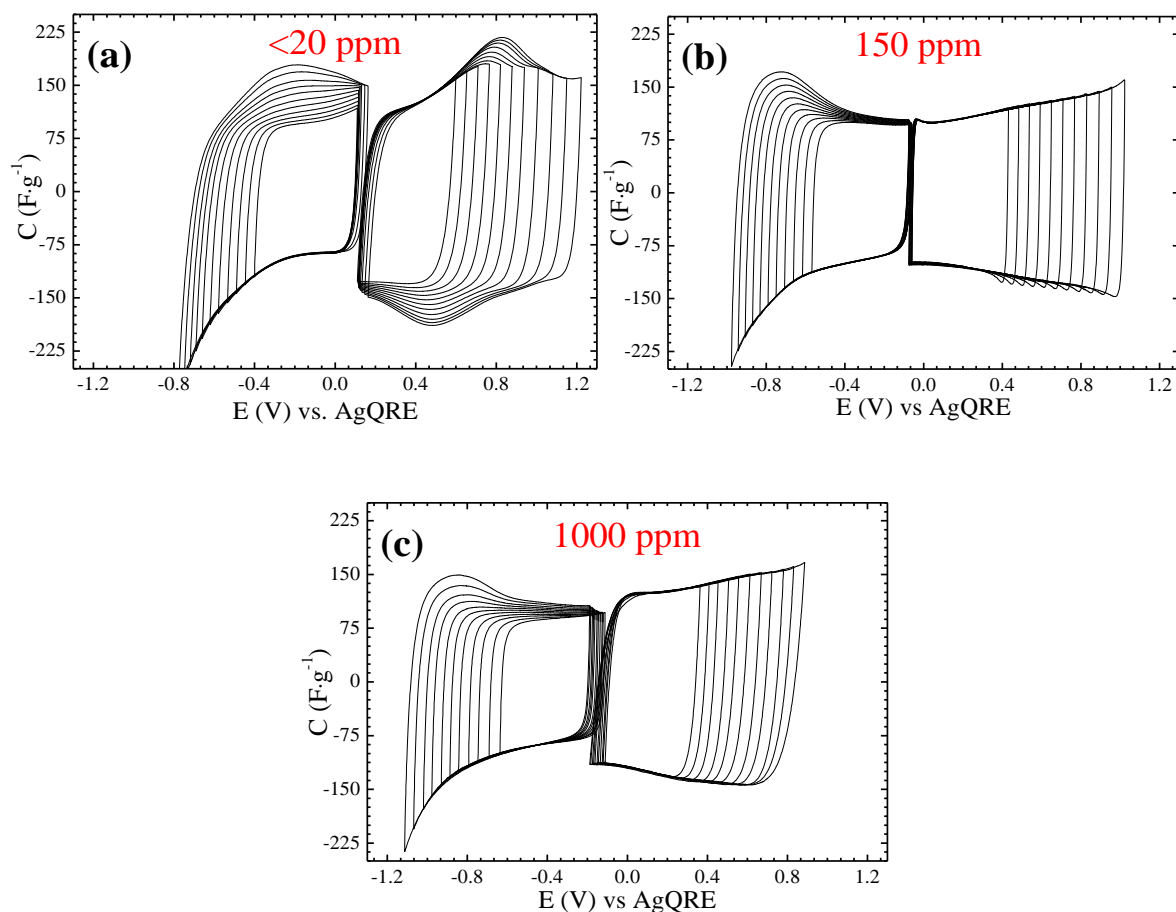


Fig. 52 CVs ($1 \text{ mV}\cdot\text{s}^{-1}$ per one electrode) of individual electrodes for AC/AC cells with AgQRE using $[\text{HN}_{222}][\text{TFSI}]$ electrolyte with (a) $<20 \text{ ppm}$, (b) 150 ppm and (c) 1000 ppm H_2O .

To understand the electrochemical behavior of the positive electrode, the electrolyte organization under polarization should be considered. Through molecular dynamic simulations of the ionic liquid, 1-ethyl-3-methylimidazolium bis[(trifluoromethyl)sulfonyl]imide ($[\text{C}_1\text{C}_2\text{Im}][\text{TFSI}]$), confined in slit-shaped nanopores, both neutral and charged, Hung et al. [208] showed that the ion dynamics is highly heterogeneous and depends strongly on the distance of imidazolium and $[\text{TFSI}]^-$ ions from the pore walls; charged pore walls induce important reductions in the dynamics of the counter ion especially in its neighboring ion layers [208]. Based on this conclusion and on the extended Stern model of EDL by Bockris et al., we propose the figure 53 to represent the effect of water content on the pore wall anion adsorption and its consequence on the CVs shape. In the PIL with 150 ppm or 1000 ppm of water (Fig. 53b), the polar water molecules interact with the electrode and cover its surface forming an oriented layer, while the plane going through their centers of gravity determines the inner Helmholtz plane (IHP). The anions create an adherent layer and the plane passing through their centers of gravity defines the outer

Helmholtz plane (OHP). As a result, anions which are non-specifically adsorbed in the OHP display mostly electrostatic charging when the potential is increased. For low water amount in the PIL (<20 ppm, Fig. 53a), the attractive image force IF (eq. 31):

eq. 31

$$IF = -\frac{Ze^2}{4\pi\epsilon\epsilon_0(2x)^2}$$

of some of the large and polarizable $[TFSI]^-$ anions ($P = 15.3$) is so strong that they are specifically adsorbed on the electrode surface when its potential is sufficiently high; the use of a mesoporous carbon electrode with accessible surface obviously favors this process. For the case of specifically adsorbed anions, the extended Stern model by Bockris, Devanathan and Muller, [15] predicts a hump in the CVs at high positive potentials, which is experimentally clearly observed in figure 52a at the positive electrode. This is due to the increasing repulsion that contact-adsorbed ions exert on each other as the contact adsorption increases. Of course, the contact-adsorbed $[TFSI]^-$ anions are expelled from the electrode surface when the potential scan is reversed.

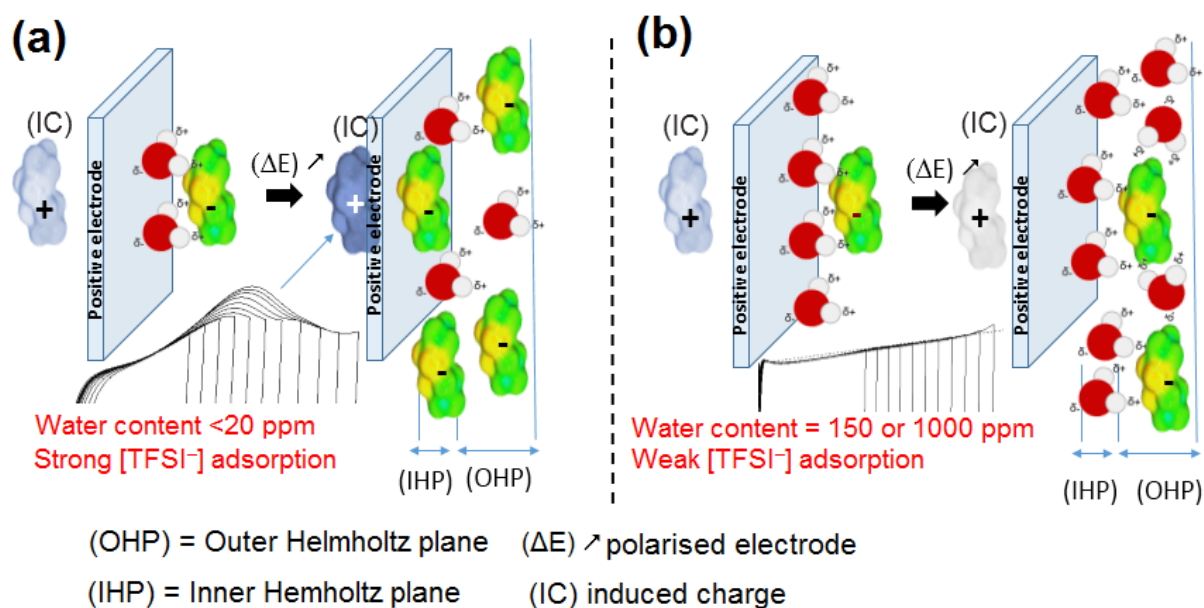


Fig. 53 Schematic representation of $[TFSI]^-$ anions adsorption by image force of induced charge in the extended Stern model by Bockris *et al.* and its consequence on the CVs shape.

The absence of reversible peaks for the positive electrode in presence of PIL with 150 or 1000 ppm of water confirms that H_2O has partially displaced $[TFSI]^-$ from the Stern layer. The smaller and polar H_2O molecules are packed more tightly on the AC surface than

[TFSI]⁻, inducing a decrease of available surface area, thus smaller counter-charge is required to neutralize the charge of the anion. As a result, the Faradaic contribution disappears and the EDL capacitance dominates on the positive electrode. Water is preferably adsorbed with its negative pole against the electrode surface, whereas all other orientations are unstable (flip-flop water). Such trend has been recently described by Warr et al., [209] from amplitude modulation atomic force microscopy (AM-AFM) images at the [C₂C₁Im⁺][TFSI⁻]/HOPG interface. Their results demonstrate asymmetrical evolution of the Stern layer nanostructure at positive and negative potentials, reflecting different surface affinity, packing constrains, and charges localization of the IL cations and anions. The Stern layer structure represents the best compromise between these effects and the surface potential.

3.4. Capacitance of AC-based ECs in [HN₂₂₂][TFSI] with various water contents

The galvanostatic charge/discharge profiles of ECs (with aluminum current collectors) incorporating [HN₂₂₂][TFSI] with various water contents (Fig. 54) reflect the above stated performance of positive and negative electrodes. Up to 1.0 V, all cells exhibit symmetric and linear curves indicating pure EDL charging. For higher values of maximum voltage (1.5 and 2.0 V), the characteristics of the cells based on the PIL with 150 and 1000 ppm of water (red and blue curves, respectively) are still relatively close to the standard triangular shape, whereas in case of the driest PIL (<20 ppm water) the curves are strongly distorted (black curves). In all cases, the coulombic efficiency is close to 100 % whatever the value of maximum voltage.

Taking into account these non-linear profiles at voltages higher than 1.0 V, the specific discharge capacitance $C_{int/D}$ was estimated according to equation (eq. 32) following the procedure described in ref [204]:

eq. 32

$$C_{int/D} = \frac{2E_{int/D}}{U_{max}^2}$$

where $E_{int/D}$ is the discharge energy determined by integration, U_{max} is the maximal voltage. The capacitance for a single electrode was then expressed by:

eq. 33

$$C_{el/D} = \frac{C_{int/D}}{0.5 \cdot m_{el}}$$

where m_{el} (g) is the total mass of electrodes. The capacitance values are given in table 7. Whatever the water content in the PIL, they increase with the maximum voltage, owing to the decrease of ion/pore wall distance, and also the contribution of hydrogen storage in the negative electrode when the voltage reaches 2.0 V. Overall, taking into account the approximation of the calculation method, the discharge capacitance values appear almost independent of the water content for a given value of voltage.

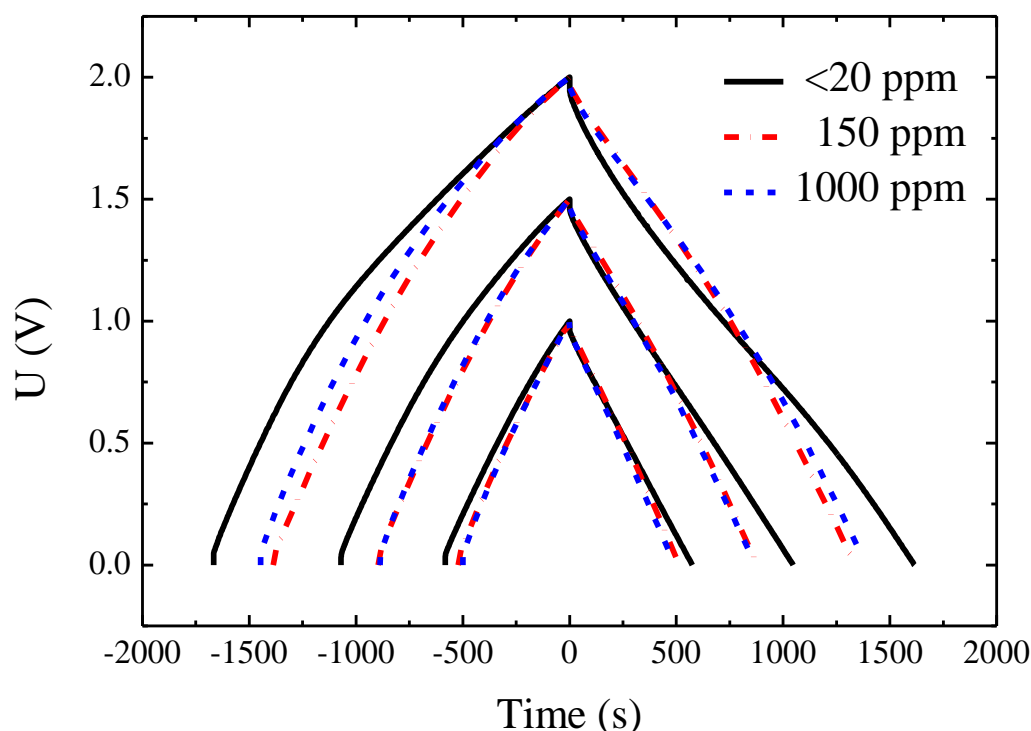


Fig. 54 Galvanostatic ($i = 0.1 \text{ A}\cdot\text{g}^{-1}$) charge/discharge of AC/AC cells (aluminum current collectors) using $[\text{HN}_{222}][\text{TFSI}]$ with various water contents.

Table 7 Specific capacitance of a single electrode for AC/AC cells in $[\text{HN}_{222}][\text{TFSI}]$ with various water contents.

Cell potential (V)	<20 ppm H ₂ O	150 ppm H ₂ O	1000 ppm H ₂ O
1.0	108	103	96
1.5	131	122	119
2.0	150	143	146

Therefore, electrochemical impedance spectroscopy (EIS) has been used to better trace the impact of faradaic contributions on the performance of AC/AC cells using $[\text{HN}_{222}][\text{TFSI}]$ with various water contents; the Nyquist plots are shown at 0 V (Fig. 55) and at voltage of

2.0 V (Fig. 55b). The almost vertical line at low frequency for the discharged cells characterizes a capacitive behavior (Fig. 55a). By contrast, at 2.0 V, the low frequency characteristics noticeably deviate from vertical (Fig. 55b); the highest deviation is noticed for [HN₂₂₂][TFSI] with <20 ppm of H₂O pointing out faradaic contributions originating from both electrodes, as already shown in figure 52a. The series resistance R_s , depending essentially on the electrolyte resistance, is the same for all solutions (Fig. 55), showing a good agreement with conductivity measurements, whereas the charge transfer resistance R_{ct} of cells charged at 2.0 V increases when the water content decreases (Fig. 55). R_{ct} is related to the charge-transfer barriers, including the “electron transfer” between the current collectors and the active material and the “ion transfer” between the active material and the electrolyte. Therefore, the relatively low R_{ct} values with the electrolyte containing 1000 ppm of water (Table 8) can be attributed to the easy transfer of water molecules which partially displace the [TFSI]⁻ ions in the Stern layer as discussed above; this interpretation is supported by the increase of R_{ct} from 36 to 45 Ω when the voltage is decreased from 2 V to 0 V. Obviously, for the cell with the PIL containing <20 ppm of water, R_{ct} increases from 56 to 90 Ω when the voltage is increased from 0 V to 2 V (Table 8). In contrast, R_{ct} remains constant for the PIL with 150 ppm of H₂O regardless polarization, which is explained by a limited rearrangement of ions at the electrode/electrolyte interface. In the case of the EC with the PIL containing 1000 ppm of water, a second semi-circle is observed before the Warburg region (Fig. 55, blue curve); the two semicircles are attributed to the presence of two different interfaces with ions/water segregation as discussed above. Besides, the electrical distributed resistance (EDR) of the PIL with less than 20 ppm of H₂O increases along with applied polarization from 78 Ω for the discharged cell to 111 Ω at 2.0 V, in contrast to the samples containing 150 and 1000 ppm of H₂O for which this parameter retains almost constant (Table 8). As EDR reflects the charge redistribution process in the porous network matrix, the observed discrepancy between “dry” and “wet” samples illustrates the influence of the hydrogen sorption mechanisms, which contribution arises above 1 V and is considerably different according to equations 27-30.

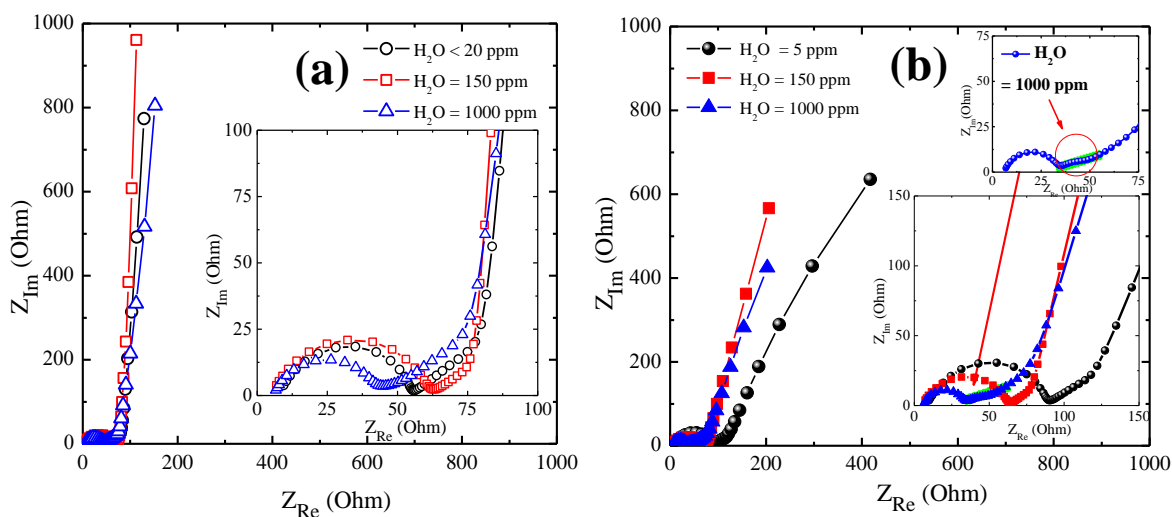


Fig. 55 Nyquist plots of AC/AC cells using $[\text{HN}_{222}][\text{TFSI}]$ with various water contents (a) discharged cell and (b) cell charged up to 2.0 V.

Table 8 Values of charge transfer resistance R_{ct} , equivalent distributed resistance EDR and capacitance C_{EIS} at 1 mHz for the charged and discharged AC/AC cells in dependence of water content in $[\text{HN}_{222}][\text{TFSI}]$.

Cell potential	<20 ppm H_2O			150 ppm H_2O			1000 ppm H_2O		
	R_{ct} (Ω)	EDR (Ω)	C_{EIS} ($\text{F}\cdot\text{g}^{-1}$)	R_{ct} (Ω)	EDR (Ω)	C_{EIS} ($\text{F}\cdot\text{g}^{-1}$)	R_{ct} (Ω)	EDR (Ω)	C_{EIS} ($\text{F}\cdot\text{g}^{-1}$)
0 V	56	78	109	63	76	98	45	74	89
2.0 V	90	111	133	63	77	167	36	70	170

The plots of capacitance vs. frequency, depending on water content in the PIL and voltage, are shown in figure 56. The horizontal plateau at low frequency for the curves obtained at 0 V confirms a pure EDL behavior whatever the water content in the PIL. The capacitance values at 0 V (Table 8) are comparable to the values determined by galvanostatic discharge for a maximum voltage of 1 V (Table 7). When the AC/AC cells are polarized at 2 V, one can observe a sloppy region below 0.01 Hz (Fig. 56) which traduces faradaic contributions. The highest capacitance values at 1 mHz (around $170 \text{ F}\cdot\text{g}^{-1}$) are demonstrated by the cells with the PIL containing 150 and 1000 ppm of H_2O , suggesting the beneficial impact of the hydronium cations (see 3.2.3) in hydrogen electrosorption under voltage hold of 2 V. For low water content (<20 ppm) in the PIL, the capacitance at 1 mHz is noticeably lower ($133 \text{ F}\cdot\text{g}^{-1}$), meaning that $[\text{HN}_{222}]^+$ as source of hydrogen is less effective than

hydronium. The comparison of capacitance values obtained at 2 V from galvanostatic discharge (Table 7) and EIS (Table 8) shows some discrepancies. As already pointed out, due to non-linearity of the discharge curves, the former values were estimated from integration, which might be the explanation for the fair agreement at 2 V; therefore, in this case, results from EIS appear more reliable.

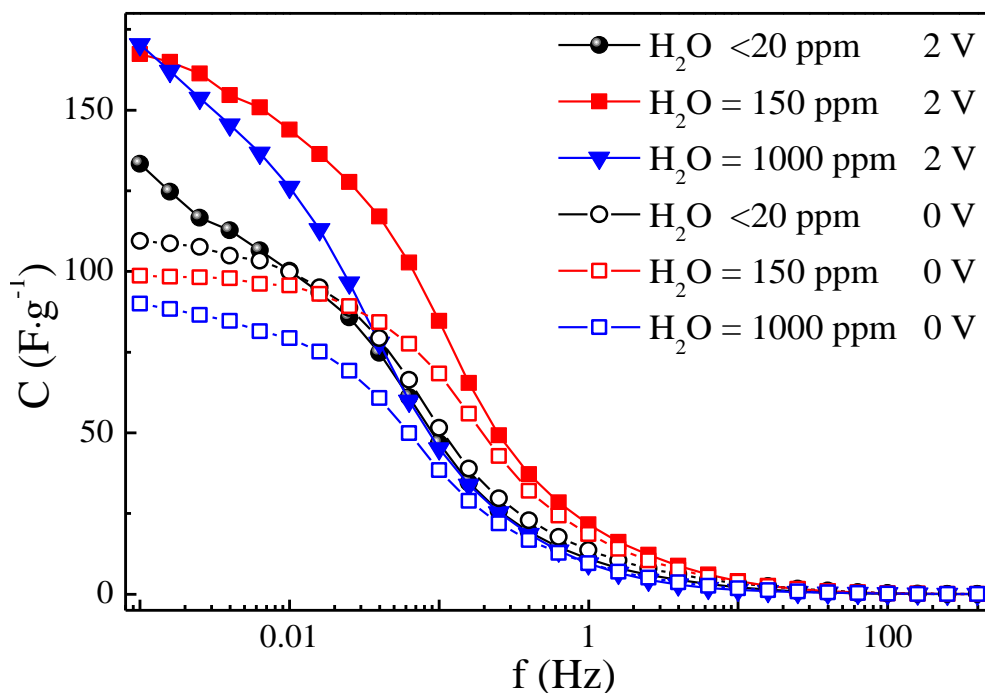


Fig. 56 Capacitance vs. frequency of AC/AC cells using $[(C_2H_5)_3N^+H][TFSI^-]$ with various water contents.

As expected, the capacitance decreases when frequency increases (Fig. 56), although there is a shift to higher frequency for the cell with the PIL containing 150 ppm of water. Considering that the loss of capacitance with frequency is related to the kinetics of the processes, these results seem to indicate that both charging mechanisms (EDL and hydrogen sorption) are facilitated in PIL containing 150 ppm of water as compared to the two other cases. These facts can be attributed to the weaker mobility of free ions in the porosity with the two other solutions: i) in the PIL with 1000 ppm of water, the mobility of ions is reduced by their hydration shell; ii) in the “dry” PIL (<20 ppm of water), the bulky $[HN_{222}]^+$ cation has a smaller mobility than the hydronium one existing in PIL with higher water content. In other words, 150 ppm is an optimal value for diffusion and adsorption of ions, whereas higher amount of water is unfavorable due to the limited diffusion. Hence, it can be considered that highly drying PILs is not worth to enhance the performance of AC/AC capacitors despite the impact of faradaic contribution originating from selective adsorption.

3.5. Impact of current collectors on the performance of AC-based ECs in [HN₂₂₂][TFSI] with high water content

Besides considering the interactions between the electrolyte and the active electrode material, it is also necessary to take into account the interactions between the electrolyte and the inactive components such as current collectors. The basic principle for achieving high-power capability of an electrode is to minimize the overall resistance of the electrode coating and collector. Accordingly, the effect of current collectors on the electrochemical stability of AC-based electrodes using [HN₂₂₂][TFSI] with 1000 ppm of water has been investigated by comparing two types of current collectors, i.e., the already used aluminum (Al) and now introduced stainless steel (SSt). The replacement of aluminum by stainless steel made it also possible to examine PIL with 10,000 ppm of water, which was impossible on Al due to its corrosion.

Two-electrode cells with AgQRE were employed to record the cyclic voltammograms (CVs) of the positive and negative AC electrodes separately; the voltage was varied from 1 V to 2 V by steps of 100 mV. The CVs of the AC-based electrodes on aluminum and stainless steel collectors in [HN₂₂₂][TFSI] with 1000 ppm of water are shown in figure 57 (a, b) and in figure 57c for 10,000 ppm of H₂O and stainless steel collectors. The CVs of the positive electrode in presence of [HN₂₂₂][TFSI] with 1000 ppm of water and Al collector display the “butterfly” shape characteristic of charging an electrical double-layer (Fig. 57a), whereas a vertex oxidation peak and its negative counterpart ca. 0.35 V vs. AgQRE are observed in addition to the EDL characteristics in case of the SSt collectors (Fig. 57b); these two peaks grow when the amount of water is increased tenfold (Fig. 57c). In the case of aluminum, the purely EDL charging can be explained by a passive layer formation (Al₂O₃) when its surface is electrochemically treated with an IL comprising the [TFSI]⁻ anion, as previously reported in [178]; hence, the surface of current collectors is electrochemically inactive for side reactions. Such layer is weakly soluble in water protecting Al with moderate amount of water (1000 ppm). However, in highly water-rich PIL (10,000 ppm), excess water would hinder the protective layer formation, and corrosion would occur. For stainless steel, the presence of water facilitates the electrodecomposition of [TFSI]⁻ while its products participate to the reversible peak ca. 0.35 V vs. AgQRE and cause corrosion of SSt by fluorinated species.

Considering now the negative electrode, the CVs slightly differ with the nature of current collectors and amount of water in [HN₂₂₂][TFSI] (Fig. 57). For high values of vertex

potential, the CVs are rectangular proving electrical double-layer charging. As the vertex potential decreases, a negative current leap attributed to reduction of the cation (here essentially H_3O^+) appears and is accompanied by an anodic signature during the positive scan, but some differences are observed depending on water amount and type of collectors. With 1000 ppm of water, the maximum of the desorption hump is located ca. -0.85 V vs. AgQRE on aluminum (Fig. 57a), whereas on SSt the impact of the hydrogen related reactions at this potential is limited, and a new contribution growing from around -0.2 V vs. AgQRE is observed (Fig. 57b). In the PIL with 10,000 ppm of H_2O and SSt current collectors, this later contribution is more important (Fig. 57c). Such high desorption potential with SSt collectors suggests stronger hydrogen bonding on AC when hydronium cations are reduced.

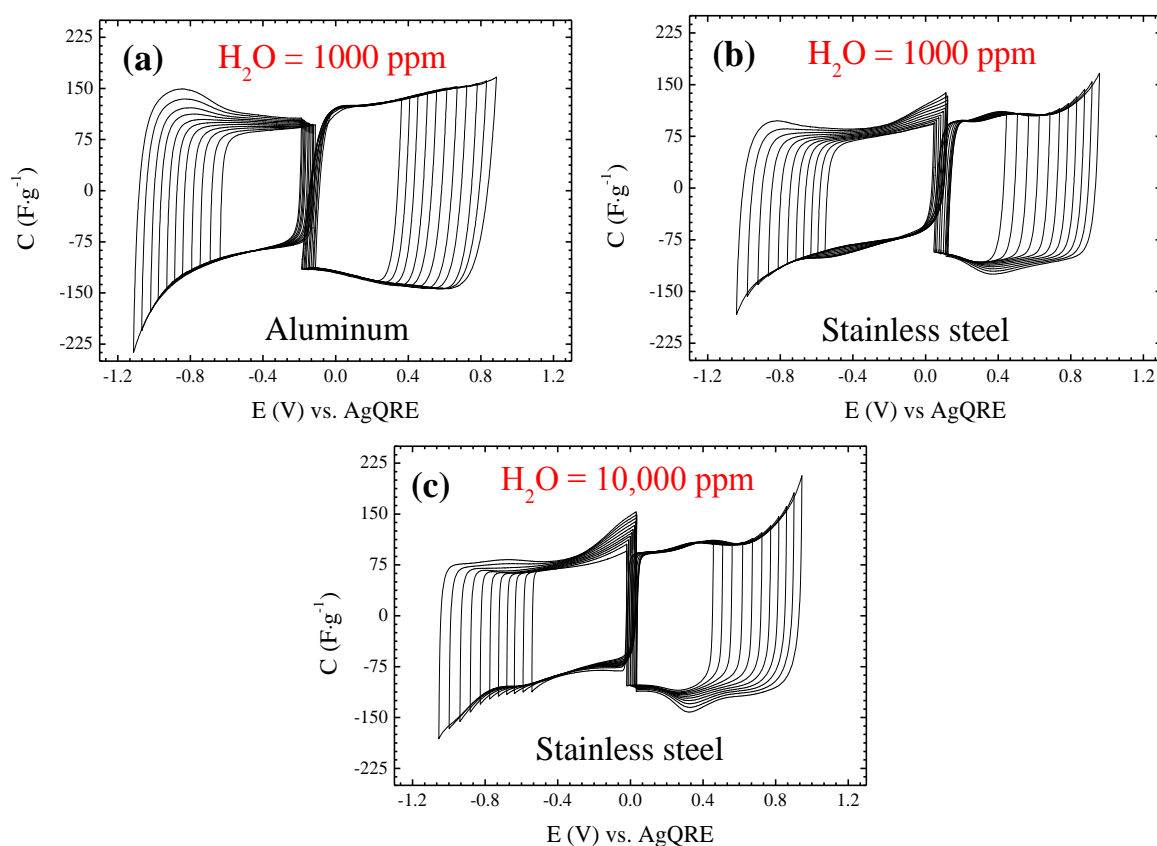


Fig. 57 CVs ($1\text{ mV}\cdot\text{s}^{-1}$ per one electrode) of individual electrodes in AC/AC cells with AgQRE using Al (a) and SSt (b, c) current collectors and $[\text{HN}_{222}][\text{TFSI}]$ with 1000 ppm (a, b) and 10,000 ppm of water (c). The cell potential is varied by steps of 100 mV.

These results are consistent with the quite different polarization behavior of the two metals in protic medium, and can be explained when considering the difference of their corrosion potentials (E_{corr}) reported in ref [210] to be ($E_{\text{corr}}(\text{Al}) = -0.47\text{ V}$ vs. SCE (saturated calomel electrode) and $E_{\text{corr}}(\text{SSt}) = -0.07\text{ V}$ vs. SCE) and coinciding with the open circuit

potential (OCP) values. The same tendency is also found in our experiments (Fig. 57) when considering the different OCP values observed on aluminum ($E_{\text{OCP(Al)}} = -0.18$ vs. AgQRE) in contrast to $E_{\text{OCP(SSt)}} = 0.11$ V vs. AgQRE). In the comparative study of kinetic and thermodynamic parameters of Al and SSt corrosion by potentiodynamic polarization and EIS measurements, [210] Alvarez *et al* indicated the presence of non-faradaic currents due to the charge/discharge of capacitive layers. Therefore, for the analysis of capacitive behavior presented in figure 57, it is necessary to consider the impact of the collectors which play an important role in the polarization of activated carbon throughout the applied potential range. Thus, SSt promotes a positive polarization whereas Al is more strongly polarized at negative values in accordance with the E_{corr} shift at OCP of the two collectors in protic medium.

Figure 58 compares voltammograms of AC/AC cells at different scan rates, depending on the collector nature and using [HN₂₂₂][TFSI] with 1000 and 10,000 ppm of water as electrolyte. Considering the PIL electrolyte incorporating 1000 ppm of water, it is clear that the CVs of cells based on aluminum current collectors (Fig. 58a) deviate more rapidly than the SSt-based ones (Fig. 58b) from rectangular shape when increasing the scan rate. This difference indicates a more resistive character of cells with Al collectors due to the presence of a passive oxide layer on their surface. Another obvious difference between the two cells (Fig. 58a and b) is a different asymmetry of the CVs shape especially at low scan rate ($\nu = 1$ mV·s⁻¹), closer to rectangular with SSt than with Al. Since the latter has a larger polarizing current, it is likely that the more polarizable species e.g., [TFSI]⁻, are preferentially adsorbed, whereas stainless steel promotes the mixed H₂O, [TFSI]⁻ adsorption to compensate the adsorption of cations on the negative electrode as discussed previously. In turn, figure 58c shows improved charge propagation in PIL with 10,000 ppm of H₂O in contrast to the cell with 1000 ppm (Fig. 58b), which is consistent with enhanced transport properties of more hydrated PIL (section 2., Fig. 50a and b).

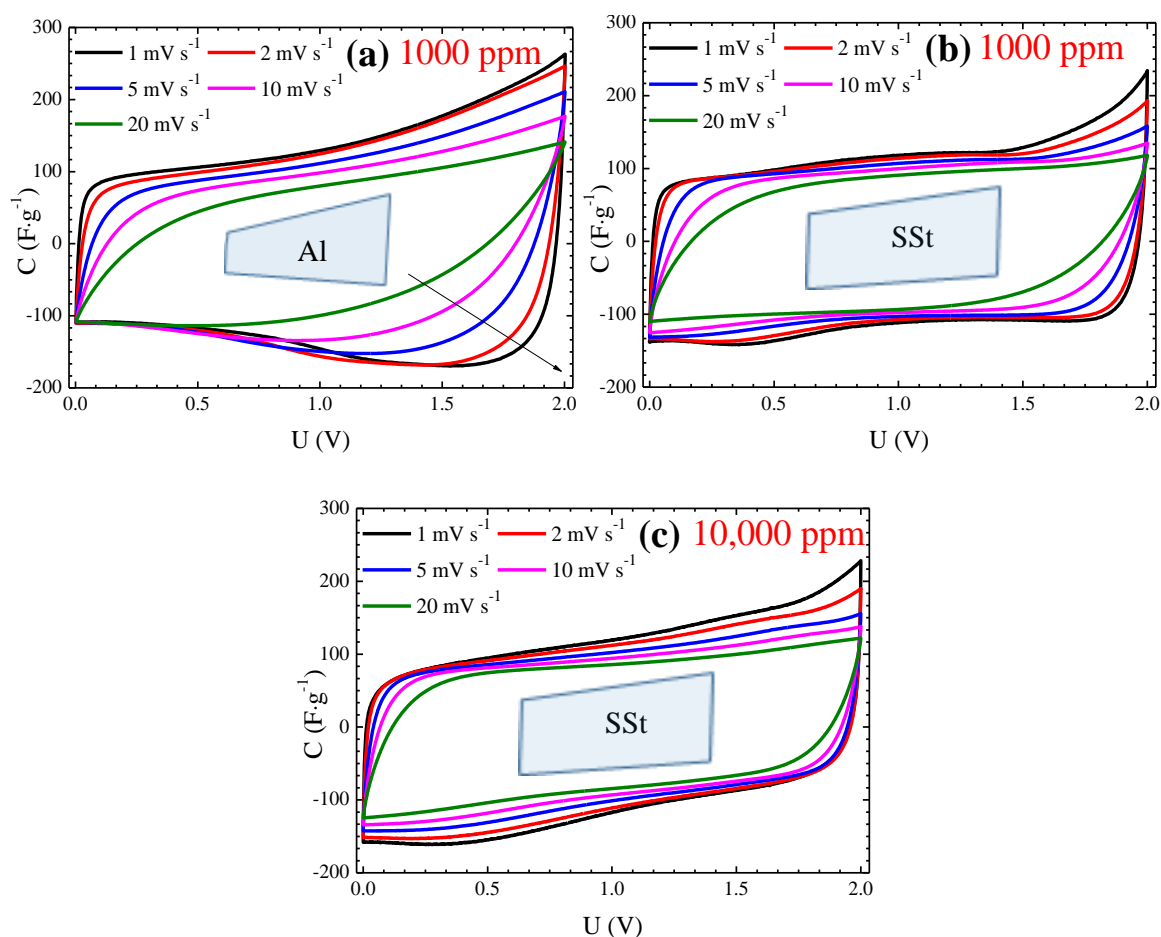


Fig. 58 CVs (1 to 20 mV s^{-1}) of AC/AC cells in $[\text{HN}_{222}][\text{TFSI}]$ electrolyte with various water contents and in presence of Al and SSt current collectors. Specific capacitance C_{sp} ($\text{F}\cdot\text{g}^{-1}$) was calculated from current density using formula $C_{sp} = 2 I dt/m dV$, where I (A) is the discharge current, dV/dt the scan rate ($\text{V}\cdot\text{s}^{-1}$), and m (g) the average carbon mass (g) in one electrode.

The Nyquist plots of AC/AC cells in $[\text{HN}_{222}][\text{TFSI}]$ electrolyte with 1000 ppm of water and the two kinds of current collectors are shown for various values of voltage in figure 59. They essentially differ by the high frequency region (insets in Fig. 59a, b), where the large semi-circle in case of Al collectors is attributed to the occurrence of an aluminum oxide layer at the surface of aluminum. The decrease of R_{ct} values with increasing voltage is more pronounced for Al than SSt (Table 9), which can suggest changes on superficial layer composition of aluminum current collectors. In turn, the EDR values are almost constant regardless of voltage, however around half lower for SSt and likewise Warburg part shorter. It means that the electrodes are better polarized using SSt, hence the transport/diffusion of ions in the porous electrode network is facilitated. The further comparison of results obtained on Al and SSt collectors indicates higher capacitance values obtained at low frequency (for 1 mHz) on Al than on SSt (170 vs. $128 \text{ F}\cdot\text{g}^{-1}$ at 2 V, Table 5). In the former case, it originates

from the promotion of the faradaic contribution related with hydrogen electroadsorption, owing to cell operation at more negative potentials (Fig. 57a and b).

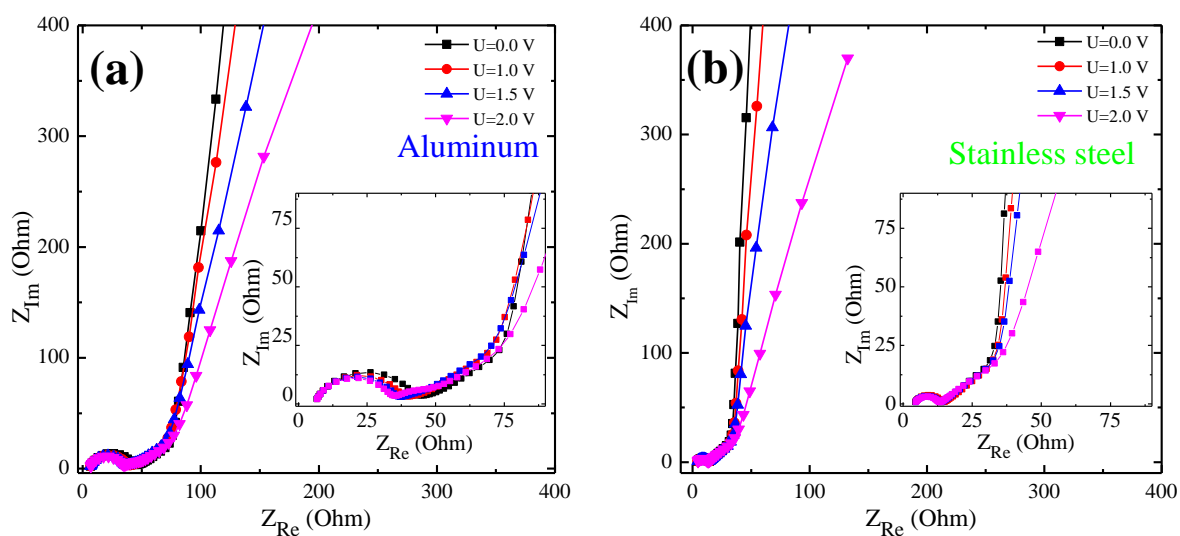


Fig. 59 Nyquist plots of AC/AC cells as function of applied cell potential. The electrolyte was [HN₂₂₂][TFSI] with 1000 ppm of water and the current collectors were from aluminum (a) or stainless steel (b).

Table 9 Values of charge transfer resistance R_{ct} , equivalent distributed resistance EDR and capacitance C_{EIS} at 1 mHz of AC/AC cells with Al and SSt current collectors in [HN₂₂₂][TFSI] with 1000 ppm of water.

Cell potential	Al collectors			SSt collectors		
	R_{ct} (Ω)	EDR (Ω)	C_{EIS} ($F \cdot g^{-1}$)	R_{ct} (Ω)	EDR (Ω)	C_{EIS} ($F \cdot g^{-1}$)
0 V	45.2	74	78	14.2	33	95
1.0 V	39.6	70	111	14.7	34	92
1.5 V	37.1	69	146	13.7	33	98
2.0 V	35.4	70	170	13.4	32	128

4. Conclusion

This study establishes the impact of low water content in [HN₂₂₂][TFSI] PIL on its physico-chemical properties as well as, if applied as electrolyte, on hydrogen electroadsorption onto AC and electrochemical performance of AC-based ECs. The obtained results show that water in low content does not affect the macroscopic properties of PIL, as conductivity and viscosity, in contrast to visibly disrupted microscopic properties reflected in modifications of

phase transitions (eutectic appearance) as well as the interface characteristics of double – Helmholtz and Stern – layers at AC-based electrodes. Distinctive electrochemical hydrogen sorption/desorption occurring at AC electrodes under negative polarization is observed in dependence of the water amount in PIL. The impact of faradaic current evidencing hydrogen storage increases along with increasing water content, whereas the resulting desorption peak is shifted toward lower potential values which reveal lower sorption energy. Two kinds of reduction/hydrogen storage mechanisms are reasoned, involving either directly the $[\text{HN}_{222}]^+$ cations for the dry PIL or the hydronium cations which are formed if water is present in PIL.

The examination of AC-based ECs by cyclic voltammetry (CV), electrical impedance spectroscopy (EIS), and galvanostatic charge–discharge (GC/GD) demonstrates that the Stern layer nanostructure evolution at positive and negative potentials is asymmetrical. The operation of the negative electrode follows the above defined hydrogen electrosorption characteristics. In turn, the performance of the positive one reflects the different surface affinities, packing constraints, and charge localizations of the PIL cations and anions as well as water molecules according to their size, polarizability and availability in the inner Helmholtz plane, sufficiently close that the image force (IF) is strong enough to pull some of them on to the surface. As a result, specific adsorption of the $[\text{TFSI}]^-$ anions into IHP was observed in PIL with less than 20 ppm of water, whereas in more hydrated samples charging involves only electrostatic attraction of anions within OHP. The EIS measurements evidenced advantageous operation of the electrochemical capacitors in PIL with 150 ppm of water proven by better capacitance retention in higher frequencies. The test involving two types of current collectors, aluminum (Al) and stainless steel (SSt), demonstrates that the potential range of electrode operation is shifted toward lower potential for the former one. As a consequence, the impact of faradaic contribution is greater, enhancing the overall system capacitance. Although, SSt provides better polarization of electrodes due to its higher conductivity, Al covered by the passive layer is more protected against corrosion, as long as water amount in the PIL does not exceed 1000 ppm. In summary, the adsorption/ desorption effectiveness of species in the porosity of carbon depends on several factors: the voltage, the nature of ions (polarizability and dimensions) but also the ability of current collectors to communicate the polarization to activated carbon. Taking heed of all the results, around 150 ppm of H_2O in PILs is optimal for their application in ECs.

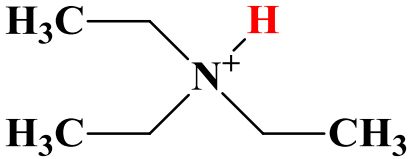
Chapter IV

Development of a novel family of protic ionic liquids

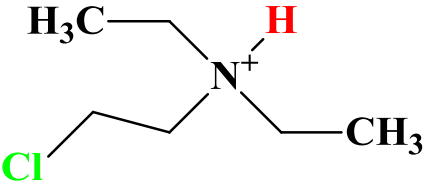
Abbreviations of cation names used in the following

Numerous protic ionic liquids will be introduced in the following parts of the manuscript. As usual, long full names will be represented by their acronyms to facilitate reading. Taking into consideration the variety of cation structures and their specific substituents, the way of generating such abbreviations will be briefly explained below. Independently, the studied compounds will be presented one by one together with their structures and they are also listed in the section “Abbreviation and symbols”.

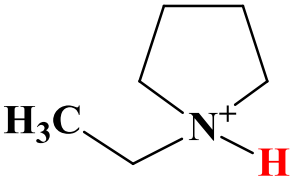
1. Protonated alkylammonium cations:

<ul style="list-style-type: none">e.g., triethylammonium: “H” stands for hydrogen, the ethyl substituent is referred to as “2” and there are three ethyl substituents, hence the acronym is $[\text{HN}_{222}]^+$.	
---	--

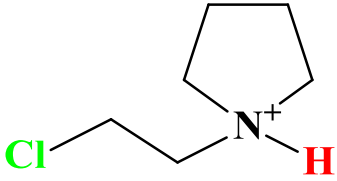
2. Protonated functionalized-alkyl ammonium cations:

<ul style="list-style-type: none">e.g., chloroethyldiethylammonium: “H” stands for hydrogen, the ethyl substituent is referred to as “2” (there are two ethyl substituents), chloroethyl is denoted as “2-cl”, hence the acronym is $[\text{HN}_{2\text{-cl}22}]^+$.	
---	--

3. Protonated alicyclic ammonium cations:

<ul style="list-style-type: none">e.g., ethylpyrrolidinium: “ethyl” is referred to as “C₂”, whereas pyrrolidinium is abbreviated as Pyrr, hence the acronym is $[\text{C}_2\text{Pyrr}]^+$.	
---	---

4. Protonated functionalized alicyclic ammonium cations:

<ul style="list-style-type: none">e.g., chloroethylpyrrolidinium: chloroethyl is denoted as “C_{2-cl}”, whereas pyrrolidinium is abbreviated as Pyrr, hence the acronym is $[\text{C}_{2\text{-cl}}\text{Pyrr}]^+$.	
--	--

The core of the amine structure may be different of pyrrolidinium, e.g., morpholinium referred to as “Morph”, piperidinium “Pip”, “Tr” triazolium and many others if required.

1. Introduction

The matrix of cations and anions making up ILs is estimated to be 10^{18} . Although it seems to be almost unlimited, yet, in practice some of them have dominated the field of ionic liquids. PILs with anions such as $[\text{NO}_3]^-$, $[\text{COO}]^-$, $[\text{CH}_3\text{COO}]^-$, $[\text{CF}_3\text{COO}]^-$ together with other anions derived from oxoacids or carboxylic acids are the most popular owing to their low cost, easy synthesis procedure and relatively good transport properties [211]. However, their electrochemical stability window (EW) is rather narrow, e.g., $[\text{Pyrr}][\text{HCOO}]$ with EW of 2.55 V on glassy carbon (GC), 1.82 V on Au and 1.45 V on Pt [211] or 50% wt. $[\text{Pyrr}][\text{NO}_3]$ in PC with EW of 2.6 V on GC [198]. These values are even smaller on high surface area activated carbons (ACs), where $[\text{Pyrr}][\text{COO}]$ and $[\text{Pyrr}][\text{NO}_3]$ as well as the mixture of $[\text{Pyrr}][\text{NO}_3]$ and PC display an operational voltage of 1.2 V [198]. In contrast, it is known that $[\text{PF}_6]^-$, $[\text{BF}_4]^-$ and $[\text{TFSI}]^-$ anions provide enhanced electrochemical stability. However, the coupling of $[\text{PF}_6]^-$ and $[\text{BF}_4]^-$ anions with common ammonium cations results mostly in PILs which are solid at RT or even protic molten salts (with melting temperature higher than 100 °C, according to ILs definition [171]). In addition, it was found that $[\text{PF}_6]^-$ (and to lesser extent $[\text{BF}_4]^-$) are sensitive to residual water, undergoing a slow hydrolysis with the concomitant release of HF [212, 213]. Therefore, the commonly reported values of water in PILs from 100 to 1000 ppm are sufficient to impact the anion instability and PILs decomposition, thus precluding their use in ECs. Besides, it is claimed that the $[\text{TFSI}]^-$ anion is not susceptible to hydrolysis, owing to very stable C-F bond in comparison to the relatively labile P-F bond of $[\text{PF}_6]^-$, [214]. It leads to the assumption that $[\text{TFSI}]^-$ should be preferred to the other above introduced anions, while similar electrochemical stability is maintained.

Countless publications report on AILs with the $[\text{TFSI}]^-$ anion, whereas the most significant part of research on PILs with the $[\text{TFSI}]^-$ anion was presented by Watanabe et al. for applications in fuel cells, owing to the presence of a dry labile proton [174, 185, 215]. Among a long list of common amines combined with the $[\text{TFSI}]^-$ anion: pyrrolidine, pyridine, piperidine, acridine, butylamine, dibutylamine, triethylamine, diphenylamine, imidazole, pyrazole, pyrazine, piperazine, benzimidazole, morpholine, quinoxaline, 4,4'-trimethylenedipyridine, 4,4'-trimethylene-dipiperidine, 1,2,4-triazole, 1,2,3-benzotriazole, only $[\text{NH}_{222}][\text{TFSI}]$ showed a melting point below RT (here 3.5 °C) followed by PILs with *close-to-ambient* melting temperature, e.g., 1,2,4-triazolium bis[(trifluoromethyl)sulfonyl]imide and $[\text{Pyrr}][\text{TFSI}]$ (22.8 and 35.0 °C, respectively) [177].

Recently, a number of PILs with [TFSI]⁻ anion and cyclic ammonium cations were reported by Balducci et al. focusing on the cation influence [216]; still, the melting temperature of the PILs was higher than RT, except for the one incorporating the ethylimidazolium cation (9 °C).

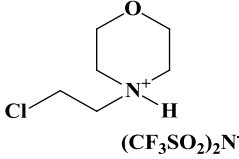
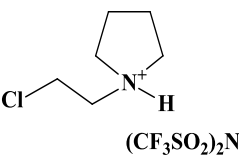
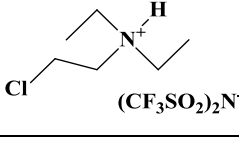
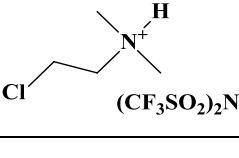
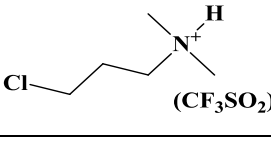
For the purposes of this dissertation, where we are looking for ECs electrolytes, it is mandatory that PILs be liquid at least at room temperature. Since it is predicted that most PILs including short alkyl or small cyclic ammonium cations and [TFSI]⁻ anion do not meet such specification, functionalized cations were employed in PILs formulation accordingly to the strategy presented in chapter I, section 2.4.4. (where it is explained that the melting temperature of ILs can be lowered by the introduction of functionalized cations). We propose to employ chloroalkyl functionalized amines in PILs for the same reasons, keeping in mind that such PILs have not yet been reported in the literature. The reports on aprotic counterpart have focused on the (2-chloroethyl)trimethylammonium cation to prepare biologically active AILs [217-219].

2. Synthesis and characterization of PILs with N-chloroalkyl functionalized cations

2.1. Synthesis

A series of PILs comprising the [TFSI]⁻ anion and the following cations: 4-(2-chloroethyl)morpholinium [**C_{2-Cl-Morph}**]⁺, 1-(2-chloroethyl)piperidinium [**C_{2-Cl-Pip}**]⁺, 1-(2-chloroethyl)pyrrolidinium [**C_{2-Cl-Pyrr}**]⁺, (2-chloroethyl)diethylammonium [**HN_{2-Cl-22}**]⁺, (2-chloroethyl)-dimethylammonium [**HN_{2-Cl-11}**]⁺, (3-chloropropyl)dimethylammonium [**HN_{3-Cl-11}**]⁺ was synthesized according to the procedure introduced in sections Annex (section 3). All PILs have less than 200 ppm water. The names, abbreviations and structural formulas, are indicated in table 10.

Table 10 Name, abbreviation and structural formula of the synthesized PILs ([220] - Reproduced by permission of The Royal Society of Chemistry).

Name	Abbreviation	Structural formula
4-(2-chloroethyl)morpholinium bis[(trifluoromethyl)sulfonyl]imide	[C _{2-Cl-Morph}][TFSI]	
1-(2-chloroethyl)piperidinium bis[(trifluoromethyl)sulfonyl]imide	[C _{2-Cl-Pip}][TFSI]	
1-(2-chloroethyl)pyrrolidinium bis[(trifluoromethyl)sulfonyl]imide	[C _{2-Cl-Pyrr}][TFSI]	
(2-chloroethyl)diethylammonium bis[(trifluoromethyl)sulfonyl]imide	[HN _{2-Cl-22}][TFSI]	
(2-chloroethyl)dimethylammonium bis[(trifluoromethyl)sulfonyl]imide	[HN _{2-Cl-11}][TFSI]	
(3-chloropropyl)dimethylammonium bis[(trifluoromethyl)sulfonyl]imide	[HN _{3-Cl-11}][TFSI]	

2.2. Structural characterization of the PILs by NMR

The structures of the PILs were confirmed by ¹H, ¹³C and ¹⁹F NMR (402.64 MHz for ¹H, 378.82 MHz for ¹⁹F and 101.25 MHz for ¹³C NMR) using DMSO-*d*₆ as solvent. The ¹H and ¹³C chemical shifts (in ppm) were referred to TMS internal standard, and for ¹⁹F to CFCl₃. The values obtained for the various PILs were as follows (bs-broad singlet, t-triplet, s-singlet, m-multiplet):

[C_{2-Cl-Morph}][TFSI]: ¹H NMR (DMSO-*d*₆) δ ppm = 3.16 (bs, 2H); 3.47 (bs, 2H); 3.56 (t, J = 6.23 Hz, 2H); 3.72 (bs, 2H); 3.99 (t, J = 6.20 Hz, 4H); 9.78 (s, 1H broad peak); ¹³C NMR

(DMSO- d_6) δ ppm = 124.32; 121.15; 117.97; 114.79; 63.14; 56.79; 51.43; 37.22; ^{19}F NMR (DMSO- d_6) δ ppm = -78.35.

[C₂-Cl-Pip][TFSI]: ^1H NMR (DMSO- d_6) δ ppm = 1.40 (s, 2H); 1.70 (bs, 2H); 1.81 (bs, 2H); 2.95 (bs, 2H); 3.47 (t, J = 6.51 Hz, 4H); 3.97 (t, J = 6.68 Hz, 2H); 9.46 (s, 1H broad peak); ^{13}C NMR (DMSO- d_6) δ ppm = 124.33; 121.14; 117.97; 114.79; 56.49; 52.50; 37.45; 22.33; 21.11; ^{19}F NMR (DMSO- d_6) δ ppm = -78.37.

[C₂-Cl-Pyrr][TFSI]: ^1H NMR (DMSO- d_6) δ ppm = 1.96 (m, 4H); 3.12 (s, 2H); 3.57 (t, J = 6.17 Hz, 2H); 3.95 (t, J = 6.00 Hz, 2H); 9.57 (s, 1H broad peak); ^{13}C NMR (DMSO- d_6) δ ppm = 125.99; 121.72; 117.46; 113.19; 54.99; 53.81; 39.37; 22.49; ^{19}F NMR (DMSO- d_6) δ ppm = -78.34.

[HN₂-Cl-22][TFSI]: ^1H NMR (DMSO- d_6) δ ppm = 1.21 (t, J = 7.25 Hz, 6H); 3.20 (m, 4H); 3.49 (q, J = 6.37 Hz, 2H); 3.97 (t, J = 6.35 Hz, 2H); 9.22 (s, 1H broad peak); ^{13}C NMR (DMSO- d_6) δ ppm = 124.33; 121.15; 117.97; 114.79; 52.13; 46.93; 37.96; 8.36; ^{19}F NMR (DMSO- d_6) δ ppm = -78.33.

[HN₂-Cl-11][TFSI]: ^1H NMR (DMSO- d_6) δ ppm = 2.84 (s, 6H); 3.49 (t, J = 6.23 Hz, 2H); 3.98 (t, J = 6.11 Hz, 2H); 9.46 (s, 1H broad peak); ^{13}C NMR (DMSO- d_6) δ ppm = 125.95; 121.68; 117.42; 113.15; 57.24; 42.57; 38.08; ^{19}F NMR (d DMSO- d_6) δ ppm = -78.35.

[HN₃-Cl-11][TFSI]: ^1H NMR (DMSO- d_6) δ ppm = 2.11 (m, 2H); 2.81 (s, 6H); 3.17 (t, J = 8.00 Hz, 2H); 3.71 (t, J = 6.35 Hz, 2H); 9.36 (s, 1H broad peak); ^{13}C NMR (DMSO- d_6) δ ppm = 124.31; 121.13; 117.95; 114.77; 54.58; 42.44; 42.00; 26.91; ^{19}F NMR (DMSO- d_6) δ ppm = -78.35.

2.3. Computational evaluation of the ions properties

Literature reports [221-223] that two conformers of the [TFSI]⁻ anion coexist in ionic liquids in their liquid state: the first one, when the CF₃⁻ groups are positioned on opposite sides of the S—N—S plane (*transoid* - conformer 1), and the second when the CF₃⁻ groups are situated on the same side of this plane (*cisoid* - conformer 2); both conformers are presented in figure 60. The energy difference between the two conformers is only a few kJ, which explains the high flexibility of the anion due to the easy conversion of these conformers [221]. Owing to the —SO₂⁻ groups in the [TFSI]⁻ anion, the negative charge is extensively delocalized by mesomery across the backbone, nitrogen and four oxygen atoms, yellow marked on the surface representing the charge density (Fig. 60) [224]. Consequently, the coordinating power of [TFSI]⁻ is lowered. Since the [TFSI]⁻ anion is also bulky and asymmetric, its ionic interactions

with the cations making up ILs are lowered, leading to the decrease of ILs melting point. The molecular structure of the [TFSI]⁻ anion was already interpreted using the COSMOTermX program [225]. The polar electronic charge distribution is represented as polarization charge density of the surface (Fig. 60), which results from the distribution of polarization charges given in sigma profiles (Fig. 60). As indicated in ref [225], the sigma profile of [TFSI]⁻ given in figure 60 shows two peaks, one at 0.011 e·Å⁻² corresponding to the -SO₂- groups acting as weak hydrogen acceptors, and the other between -0.0082 and 0.0082 e·Å⁻² in the non-polar region due to the impact of the CF₃- groups.

Apart from the impact of anion, which is common for all the investigated PILs, the role of cation type needs to be considered, particularly taking into account the effect of the chlorine substituent. Therefore, table A1 (Annex, section 4.1.4) compares the Cosmo volumes of N-chloroalkyl functionalized cations and their corresponding non-chlorinated analogues. The Cosmo volume of ions containing chlorine is 21-24 Å³ higher than for their non-functionalized analogues, e.g., [C_{2-Cl}-Pyrr]⁺ with 174.11 Å³ vs. [C₂Pyrr]⁺ with 150.86 Å³ (Fig. 60). This difference is due to the higher asymmetry of the molecule when replacing one hydrogen atom by chlorine with higher van der Waals radius and longer bond length to carbon. The strong electron withdrawing effect of chlorine provokes a charge delocalization toward the halogen atom marked yellow, contrasting with light green on hydrogen atoms and pale-blue on carbon atoms of the alkyl chains or alicyclic part of the ammonium cation ring. Accordingly, in the sigma profiles, the single peak characteristic of the non-functionalized cations (Fig. A1 e, g, i, k and m, Annex, section 4.1.4.) is split by the presence of chlorine in the N-chloroalkyl functionalized cations (Fig A1, f, h, j, l and n, Annex, section 4.1.4.). The peaks of the non-functionalized cations are mostly located in the non-polar region (in the range of -0.0082 to 0.0082 e·Å⁻²) [225] and partially out of it, below -0.0082 e·Å⁻² and in the latter case are attributed to the hydrogen bond donor region which results from the presence of acidic hydrogen (Fig. A1 c to n, Annex, section 4.1.4.). In the case of the N-chloroalkyl functionalized cations, the second smaller peak is related to the presence of the terminal chlorine, and indicates weak hydrogen acceptor sites. In contrast to the other discussed cations, the different sigma profiles of the two morpholinium cations, [C₂Morph]⁺ and [C_{2-Cl}-Morph]⁺ (Fig. A1. c and d, respectively, Annex, section 4.1.4.), with negative polar segment above 0.01 e·Å⁻², are attributed to the impact of oxygen as hydrogen acceptor in the morpholinium ring.

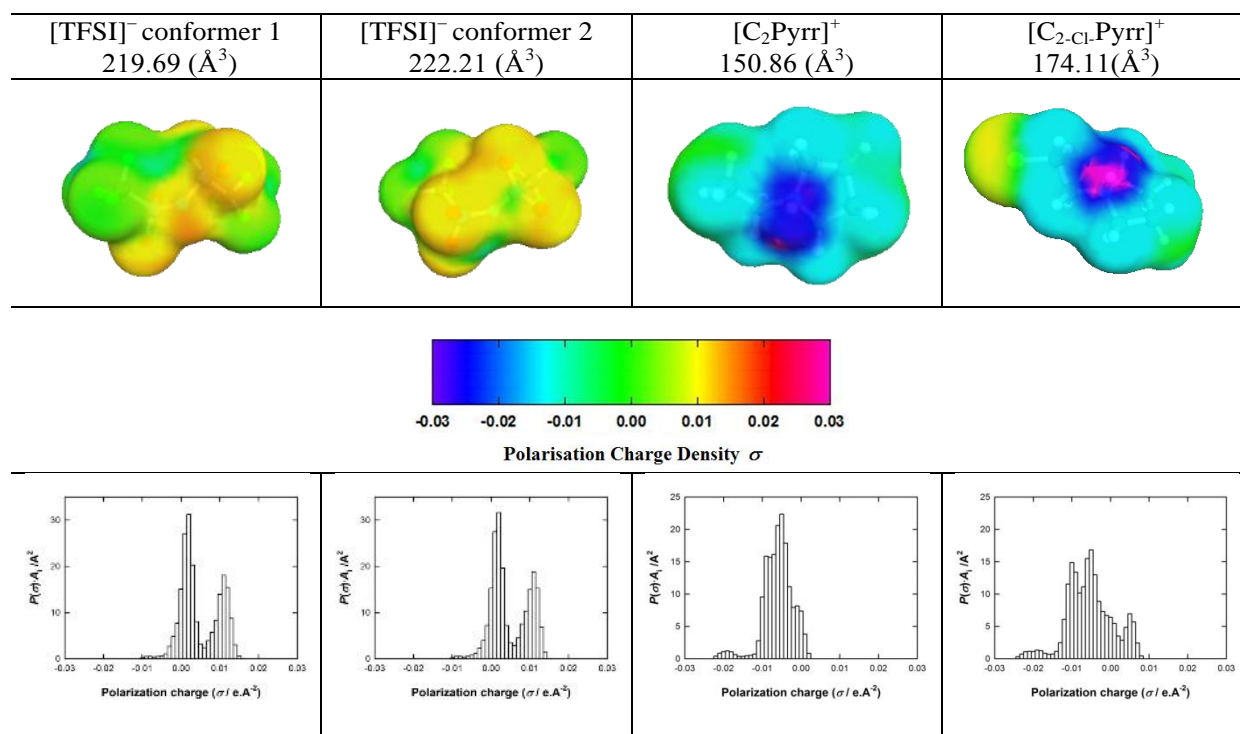


Fig. 60 Structure, Cosmo volume and Sigma profiles of the TFSI anion and the [C_{2-Cl}.Pyrr]⁺ chloro-functionalized cation and its [C₂Pyrr]⁺ non-chlorinated analogue ([220] - Reproduced by permission of The Royal Society of Chemistry).

2.4. Thermal properties of the PILs

2.4.1. Phase transitions

The DSC thermograms of the PILs with N-chloroalkyl functionalized cations are shown in figure 61, and the corresponding thermodynamic data are reported in table 11. For all studied PILs, the melting temperature T_m is lower than for their homologues with non chloro-substituted cations, and close to ambient temperature, from ca. 22 °C to 34 °C, except for [HN_{2-Cl-22}][TFSI] with $T_m = -8.5$ °C. In order to evaluate the effect of chlorine in the alkyl substituent on lowering the PILs melting temperature, these data on PILs with chloroalkyl-substituted cations were compared with reported literature data on their homologues with non chloro-substituted cations. The greatest melting temperature shift is observed for [C_{2-Cl}.Morph][TFSI] with 22.5 °C in contrast to [Morph][TFSI] with 58.5 °C [177]. In the case of the piperidinium PILs, no significant T_m shift is detected ([Pip][TFSI] with 37.9 °C [177] and [C_{2-Cl}.Pip][TFSI] with 34.1 °C). A similar effect is observed for pyrrolidinium, where the two representatives [Pyrr][TFSI] and [C_{2-Cl}.Pyrr][TFSI] have very close T_m of 35.0 °C and 29.4 °C, respectively. In turn, the T_m shift toward lower values was more pronounced for all the aliphatic (linear) ammonium PILs. The [HN_{2-Cl-22}][TFSI] displays T_m

of $-8.5\text{ }^{\circ}\text{C}$ in contrast to the non-chloro $[\text{HN}_{222}][\text{TFSI}]$, with melting temperature of $-0.8\text{ }^{\circ}\text{C}$ [178] or $3.5\text{ }^{\circ}\text{C}$ [177]. Also, when one hydrogen of the ethyl group of the dimethylethylammonium cation is substituted by chlorine, we showed that the melting temperature decreases from $56.97\text{ }^{\circ}\text{C}$ or $66.0\text{ }^{\circ}\text{C}$ [174] in $[\text{HN}_{211}][\text{TFSI}]$ to $24.2\text{ }^{\circ}\text{C}$ in $[\text{HN}_{2\text{-Cl-11}}][\text{TFSI}]$. The more significant shift with alkylammonium PILs in comparison to alicyclic ones can be explained by more delocalized, or precisely more alkyl-shielded charge, as well as by a higher number of rotational and vibrational degrees of freedom of linear alkyl substituents in the former ions [109]. Additionally, lower T_m and correspondingly ΔH_m values (Table 5) for $[\text{C}_{2\text{-Cl-Morph}}][\text{TFSI}]$ and $[\text{HN}_{2\text{-Cl-22}}][\text{TFSI}]$ indicate weaker intermolecular interactions in these PILs [187].

The studied PILs displayed two types of thermal behavior reflected in the DSC curves (Fig. 61). In the first group, including $[\text{C}_{2\text{-Cl-Pip}}][\text{TFSI}]$, $[\text{C}_{2\text{-Cl-Pyrr}}][\text{TFSI}]$, $[\text{HN}_{2\text{-Cl-11}}][\text{TFSI}]$ and $[\text{HN}_{3\text{-Cl-11}}][\text{TFSI}]$, first-order transition peaks corresponding to crystallization (T_c) and melting (T_m), with supercooling in the range of $37 - 50\text{ }^{\circ}\text{C}$, are well-visible. For the second group, including $[\text{C}_{2\text{-Cl-Morph}}][\text{TFSI}]$ and $[\text{HN}_{2\text{-Cl-22}}][\text{TFSI}]$, the supercooling domain is much larger, and a crystallization peak could not be observed down to $-100\text{ }^{\circ}\text{C}$ upon cooling. During heating, the two supercooled liquids demonstrated a glass transition (T_g) followed by cold crystallization (T_{cc}) before melting (Fig. 61a and d). Such cold crystallization is typically observed in glass-forming liquids and polymers and associated with viscous ILs incorporating bulky ions [187]. As previously reported, [138] due to the increasing ILs viscosity upon decreasing temperature, the formation of crystal nuclei required for crystallization is hindered, facilitating the occurrence of supercooled liquid below its melting point. In the case of $[\text{C}_{2\text{-Cl-Morph}}][\text{TFSI}]$ and $[\text{HN}_{2\text{-Cl-22}}][\text{TFSI}]$, the lack of such nuclei is maintained under the applied scan rate down to $-100\text{ }^{\circ}\text{C}$. Yet, during the reverse scan, and going up to higher temperatures, these liquid-like systems with significant viscosity exhibit a glass transition (T_g). Such glass transitions have a kinetic nature, and glasses or supercooled liquids are considered as metastable in contrast to the energetically favorable formation of crystals within the liquid-crystallization transition having a thermodynamic nature. To make crystallization possible, the molecules in the melt must adapt their conformation (change of thermal energy), which is reflected by the (cold) crystallization upon heating [138, 187].

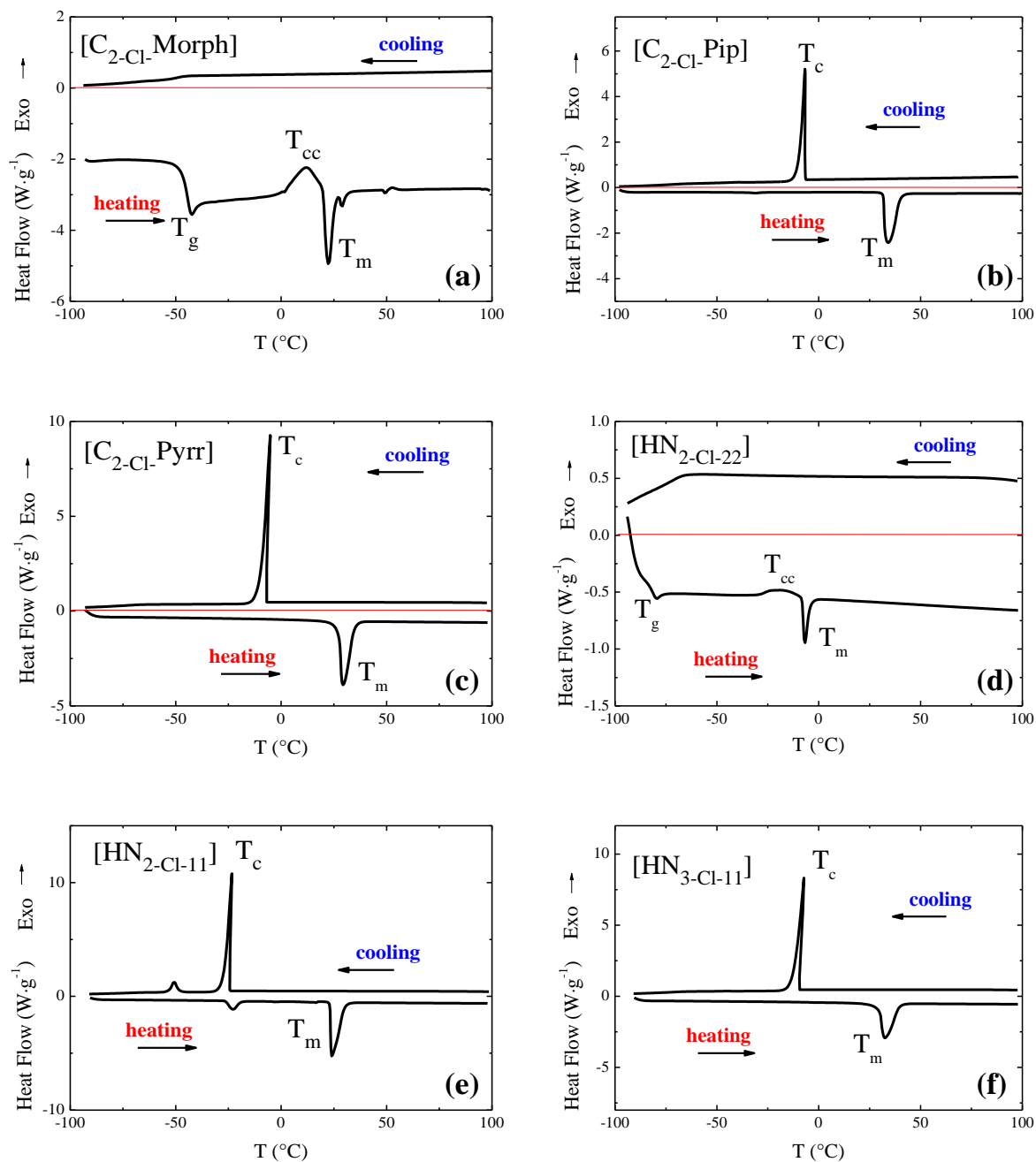


Fig. 61 DSC thermograms of the PILs with various N-chloroalkyl functionalized cations and [TFSI] anion: (a) $[\text{C}_{2\text{-Cl-Morph}}]$; (b) $[\text{C}_{2\text{-Cl-Pip}}]$; (c) $[\text{C}_{2\text{-Cl-Pyrr}}]$; (d) $[\text{HN}_{2\text{-Cl-22}}]$; (e) $[\text{HN}_{2\text{-Cl-11}}]$; (f) $[\text{HN}_{3\text{-Cl-11}}]$; scan rate $10^{\circ}\text{C}/\text{min}$ ([220] - Reproduced by permission of The Royal Society of Chemistry).

Table 11 Thermal properties determined from DSC on the PILs with various N-chloroalkyl functionalized cations: Glass transition (T_g), Crystallization (T_c), Melting (T_m), Cold Crystallization (T_{cc}) temperatures in °C; Crystallization (ΔH_c), Melting (ΔH_m) and Cold Crystallization (ΔH_{cc}) enthalpies in $\text{kJ}\cdot\text{mol}^{-1}$ ([220] - Reproduced by permission of The Royal Society of Chemistry).

PILs	T_g	T_c	T_m	T_{cc}	ΔH_c	ΔH_m	ΔH_{cc}
[C _{2-Cl} -Morph][TFSI]	-45.6	/	22.5	11.9	/	2.2	2.4
[C _{2-Cl} -Pip][TFSI]	/	-8.2	34.1	/	26.4	32.8	/
[C _{2-Cl} -Pyrr][TFSI]	/	-8.1	29.4	/	41.6	45.4	/
[HN _{2-Cl-22}][TFSI]	-81.3	/	-8.5	-18.6	/	2.9	2.5
[HN _{2-Cl-11}][TFSI]	/	-25.5	24.2	/	39.3	47.8	/
[HN _{3-Cl-11}][TFSI]	/	-10.8	32.4	/	37.2	40.9	/

2.4.2. Thermal stability

In general, it is worth noticing that the thermal decomposition of ionic liquids consisting of organic cations and [TFSI]⁻ anion appears at higher temperatures than with more coordinating anions like [BF₄]⁻ or [PF₆]⁻, [138] e.g., [C₄C₁Im][TFSI] with 439 °C vs. [C₄C₁Im][BF₄] with 403 °C and [C₄C₁Im][PF₄] with 349 °C. [226] The thermal stability of the tested PILs was investigated by thermogravimetric analysis and determined by the onset temperature corresponding to 5 wt. % mass loss ($T_{5\% \text{onset}}$). All the N-chloroalkyl functionalized PILs show high thermal stability with $T_{5\% \text{onset}}$ in the range 280–337 °C (Fig. 62). However, [C_{2-Cl}-Morph][TFSI] exhibits a shift of baseline (particularly close to 100 °C) which suggests moisturizing upon contact with atmosphere, due to oxygen in the ring serving as strong hydrogen bond acceptor thus enhancing water uptake. For the PILs with ring-membered cations, the lowest thermal stability was detected for [C_{2-Cl}-Morph][TFSI], followed by [C_{2-Cl}-Pip][TFSI] and [C_{2-Cl}-Pyrr][TFSI] (Fig. 62a), which is consistent with the general trend [226]. In the case of the alkyl ammonium PILs (Fig. 62b), the order of stability was [HN_{2-Cl-22}][TFSI] < [HN_{2-Cl-11}][TFSI] < [HN_{3-Cl-11}][TFSI], and the last one was the most thermally stable among all the PILs investigated in this paper.

Whereas the thermal decomposition of the majority of ILs is reported to occur in one step with complete mass loss and volatilization of the component fragments [109], in case of the N-chloroalkyl functionalized PILs, it occurs in two steps (Fig. 62). The mass loss during the first step ranges from 10% to 17%, which seems to correspond to E2 elimination with

chloroethene (vinyl chloride) release. Yet, the E2 elimination of the N-substituent from imidazolium quaternary halides has been already proved as the thermal degradation pathway and presumed as the inverse of the S_N2 substitution during their formation [109].

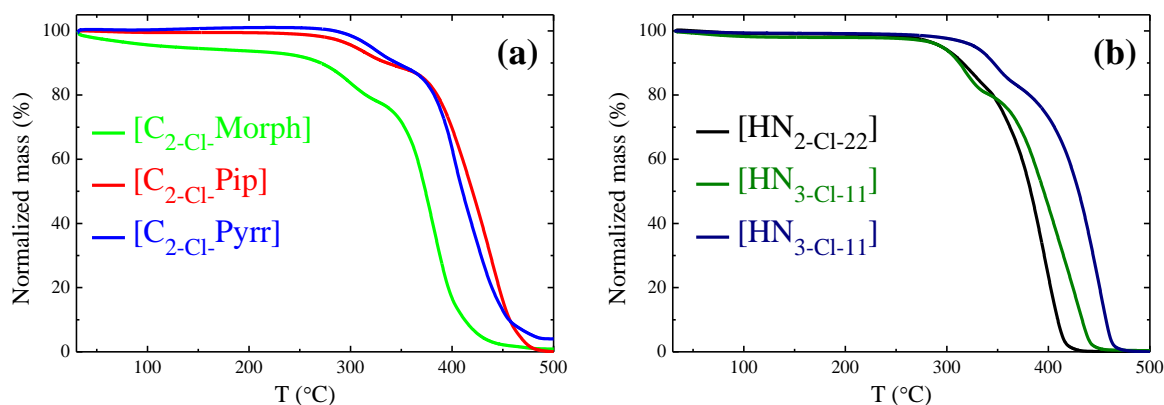


Fig. 62 Thermogravimetric analysis of the PILs with N-chloroalkyl functionalized cations (a) alicyclic (b) aliphatic ([220] - Reproduced by permission of The Royal Society of Chemistry).

2.5. Physicochemical properties

Mindful of providing reliable data on new ILs, basic physicochemical properties of all the investigated PILs were measured and discussed.

2.5.1. Density

Generally, the density of ILs is in the range $1.2 - 1.6 \text{ g}\cdot\text{cm}^{-3}$ at room temperature [138]; in the case of the obtained PILs with N-chloroalkyl functionalized cations, the density values are between 1.5045 and $1.6141 \text{ g}\cdot\text{cm}^{-3}$ at 293K (Table 12). It mainly results from the contribution of the $[\text{TFSI}]^-$ anion claimed as providing higher density in comparison to ILs comprising e.g., $[\text{BF}_4]^-$ or $[\text{PF}_6]^-$, [109]. As already extensively reported for both AILs and PILs, [109, 171] the density decreases when the length of the alkyl chains in the cation and steric hindrance increases, which is confirmed by the lowest value of $1.5045 \text{ g}\cdot\text{cm}^{-3}$ for the PIL with $[\text{HN}_{2\text{-Cl-}22}]^+$ cation. Accordingly, the reduction of carbon atoms number in the alkyl substituent leads to the increase of density for $[\text{HN}_{3\text{-Cl-}11}][\text{TFSI}]$ and $[\text{HN}_{2\text{-Cl-}11}][\text{TFSI}]$. The highest value was measured for $[\text{C}_{2\text{-Cl-Morph}}][\text{TFSI}]$, which is consistent with the general observation of higher density of PILs with heterocyclic ammonium cations than with alkylammonium ones [171]. The effect of chlorine molecular weight is well-demonstrated by the higher density of $[\text{HN}_{2\text{-Cl-}22}][\text{TFSI}]$ ($1.5045 \text{ g}\cdot\text{cm}^{-3}$) as compared to its non-substituted analogue $[\text{HN}_{222}][\text{TFSI}]$ ($1.42 \text{ g}\cdot\text{cm}^{-3}$ taken from ref. [227]). The density of PILs plotted vs.

temperature shows a linear decrease with increasing temperature (Fig. 63), which in the tested (narrow) range can be represented by equation (eq. 34):

eq. 34

$$\rho = b + aT$$

where a and b are fitting parameters and T is the temperature in K. As evidenced by the high values of the obtained correlation coefficients, r^2 , (>0.999), the relationship is highly linear in the analyzed temperature range. The similar values of slope indicate comparable sensitivity to the temperature variation.

Table 12 Density (ρ) at 293 K (20 °C), fitting parameters (a and b) and correlation coefficient of fitting for density (r^2) of the investigated PILs ([220] - Reproduced by permission of The Royal Society of Chemistry).

PILs	ρ at 293 K (g·cm ⁻³)	b (g·cm ⁻³)	$10^4 a$ (g·cm ⁻³ ·K ⁻¹)	r^2
[C ₂ -Cl-Morph][TFSI]	1.6141	1.9259	-10.630	0.99994
[C ₂ -Cl-Pip][TFSI]	1.5363	1.8381	-10.290	0.99997
[C ₂ -Cl-Pyrr][TFSI]	1.5420	1.8526	-10.583	0.99986
[HN ₂ -Cl-22][TFSI]	1.5045	1.8071	-10.312	0.9999
[HN ₂ -Cl-11][TFSI]	1.5875	1.9032	-10.756	0.99994
[HN ₃ -Cl-11][TFSI]	1.5384	1.8422	-10.357	0.99993

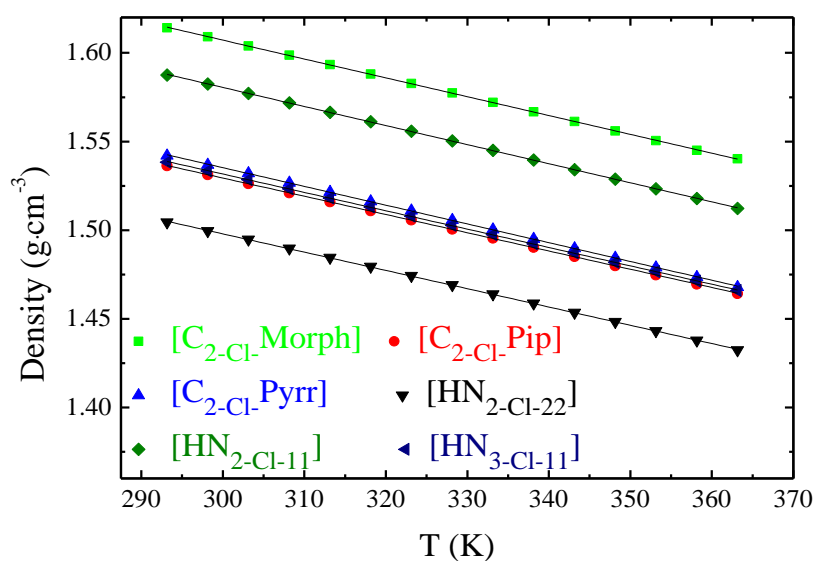


Fig. 63 Density of the PILs vs. temperature ([220] - Reproduced by permission of The Royal Society of Chemistry).

2.5.2. Refractive index and molar refractivity

The refractive index (n_D) is a value characterizing the deviation of a light beam when it propagates from one medium to another. For all investigated PILs, n_D at 293 K was in the range of 1.4163 to 1.4391 (Table 13), which corresponds mostly to the impact of the [TFSI]⁻ anion [228]. As already pointed out, in general, the refractive index decreases with the chain length in the cation [173]. The smallest value was measured for [HN_{2-Cl-11}][TFSI] ($n_D = 1.4163$), and it increases with the number of carbon atoms in the chloroalkyl chain, like in the case of [HN_{3-Cl-11}][TFSI] ($n_D = 1.4190$), as well as for the other chains like in the case of [HN_{2-Cl-22}][TFSI] ($n_D = 1.4230$). The highest values of refractive index were measured for PILs composed of cyclic cations. Whilst the refractive index is very close for the two PILs with the six-membered ring cations - ([C_{2-Cl-Morph}][TFSI] and [C_{2-Cl-Pip}][TFSI]), the smaller value for the PIL with five-membered ring cation ([C_{2-Cl-Pyrr}][TFSI]) can be noted. Figure 64 shows the plot of the refractive index vs temperature for the studied PILs and it can be seen, for all of them, that n_D decreases linearly while temperature increases. The temperature dependence of refractive index can be described by the following equation (eq. 35):

eq. 35

$$n_D = b + aT$$

where a and b are fitting parameters and T is temperature. The values of slope are in a narrow range pointing to a similar effect of temperature change on the refractive index of these PILs.

Table 13 Refractive index (n_D) at 293 K, fitting parameters (a and b) and fitting correlation coefficient for the refractive index (r^2) of the investigated PILs ([220] - Reproduced by permission of The Royal Society of Chemistry).

PILs	n_D at 293 K	b	$10^4 a$ (K ⁻¹)	r^2
[C _{2-Cl-Morph}][TFSI]	1.4391	1.5121	-2.506	0.99848
[C _{2-Cl-Pip}][TFSI]	1.4368	1.5141	-2.640	0.99987
[C _{2-Cl-Pyrr}][TFSI]	1.4295	1.4959	-2.285	0.99731
[HN _{2-Cl-22}][TFSI]	1.4230	1.4961	-2.498	0.99976
[HN _{2-Cl-11}][TFSI]	1.4163	1.4921	-2.5012	0.99974
[HN _{3-Cl-11}][TFSI]	1.4190	1.4856	-2.375	0.99898

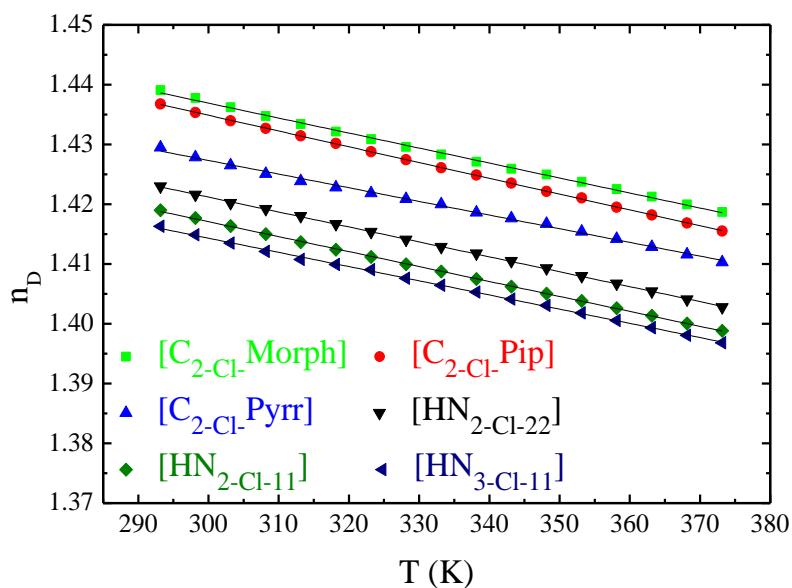


Fig. 64 Refractive index of the PILs vs. temperature ([220] - Reproduced by permission of The Royal Society of Chemistry).

It is worth mentioning that the refractive index is related to the electronic polarizability of ions and local field inside the material. It indicates the dielectric response to an electrical field induced by electromagnetic radiations, namely light. In turn, it allows the electrical properties of materials and their response to an electronic polarization to be estimated. Hence, the evaluation of refractive index can serve as an approximate method of assessing ILs electronic properties. For this purpose, both density (Table 12) and refractive index (Table 13) were employed in the Lorenz-Lorenz equation (eq. 36) to calculate the molar refractivity (M_R) which is a measure of the total polarizability of one mole of substance:

eq. 36

$$M_R = \frac{M_w}{\rho} \frac{n_D^2 - 1}{n_D^2 + 2}$$

where M_w is the molecular weight ($\text{g}\cdot\text{mol}^{-1}$), ρ the density ($\text{g}\cdot\text{cm}^{-3}$), and n_D the refractive index. The values of M_R and M_w are collected in table 14 for the series of studied PILs with $[\text{TFSI}]^-$ anion. The M_R values calculated according to eq. 36 are in the range of 61.491 to 73.091 $\text{cm}^3\cdot\text{mol}^{-1}$ at 293 K; for comparison, M_R of acetonitrile at the same temperature is 11.11 $\text{cm}^3\cdot\text{mol}^{-1}$. The M_R difference between chlorinated and non-chlorinated analogues, e.g., $[\text{HN}_{2-\text{Cl}-22}][\text{TFSI}]$ and $[\text{HN}_{222}][\text{TFSI}]$ is 3.846 $\text{cm}^3\cdot\text{mol}^{-1}$ and is in the same range as the contribution of a single chlorine atom, i.e. 5.967 $\text{cm}^3\cdot\text{mol}^{-1}$ [229]. Hence, as suggested in ref [171], the molar refractivity of PILs can be tailored using appropriate cation and anion couple.

Table 14 Molecular weight (M_w), Molar refractivity (M_R) at 293 K and Surface Tension (γ) at 293K of the prepared PILs ([220] - Reproduced by permission of The Royal Society of Chemistry).

PILs	M_w ($\text{g}\cdot\text{mol}^{-1}$)	M_R at 293 K ($\text{cm}^3\cdot\text{mol}^{-1}$)	γ at 293 K ($\text{mN}\cdot\text{m}^{-1}$)
[C _{2-Cl} -Morph][TFSI]	430.77	70.210	41.1
[C _{2-Cl} -Pip][TFSI]	428.80	73.091	37.7
[C _{2-Cl} -Pyr][TFSI]	414.77	69.410	36.9
[HN _{2-Cl-22}][TFSI]	416.79	70.542	36.7
[HN _{2-Cl-11}][TFSI]	388.74	61.491	37.7
[HN _{3-Cl-11}][TFSI]	402.76	66.1161	38.4
([HN ₂₂₂][TFSI])	382.34	65.8165	35.9

2.5.3. Air-liquid surface tension

The measured values of the air-liquid surface tension of the N-chloroalkyl functionalized PILs are in the very narrow range of 36.7-38.4 $\text{mN}\cdot\text{m}^{-1}$, except for [C_{2-Cl}-Morph][TFSI] with 41.1 $\text{mN}\cdot\text{m}^{-1}$ (Table 14). These results are consistent with literature data on AILs, [230] showing that the surface tension is significantly altered when [BF₄]⁻, [PF₆]⁻ and [TFSI]⁻ anions are coupled with the [C₂C₁Im] cation, e.g., 44.0, 40.9 and 33.0 $\text{mN}\cdot\text{m}^{-1}$, at 298 K, respectively, in contrast to AILs with [TFSI]⁻ and diverse cations with values ranging from 31.3 to 34.4 $\text{mN}\cdot\text{m}^{-1}$ (at 298 K). According to [143], the higher values of surface tension are related with the increase of PIL cohesiveness, owing to the formation of hydrogen bonds. Such trend was also observed in [230], where ILs consisting of [TFSI]⁻ and cations with hydroxyl group in their structure displayed increased surface tension of 34.0-38.0 $\text{mN}\cdot\text{m}^{-1}$ at 298 K in contrast to non-hydroxyl functionalized analogues. The significant impact of hydrogen bonding is clearly demonstrated by comparing the two PILs with six-membered ring cations, e.g., [C_{2-Cl}-Morph][TFSI] and [C_{2-Cl}-Pip][TFSI]. The higher value for the former one is attributed to the oxygen atom in the morpholinium ring serving as hydrogen bond acceptor.

2.6. Transport properties of PILs

2.6.1. Viscosity

Most ILs are classified as Newtonian fluids [133, 134] demonstrating constant shear stress/shear rate ratio, unlike non-Newtonian fluids which do not exhibit this constant ratio. In

figure 65a which represents the shear stress vs. shear rate for the PILs with N-chloroalkyl functionalized cations, one can observe linearity (Newtonian behavior) until a shear rate of 500 s^{-1} and a negative deviation corresponding to non-Newtonian shear thinning behavior for higher values of shear rate. Examples of non-Newtonian ILs, both aprotic and protic, have been already published [135-137]. Separovic et al. [136] have correlated the non-Newtonian viscous shear thinning occurring in ILs with the presence of a considerable amount of hydrogen bonds, especially when donor functional groups are present on the cation. These authors also indicated liquid-phase ordering or aggregation and pointed out the possible need for an active proton capable of creating such hydrogen bonding to participate in the aggregates formation. Accordingly, owing to the presence of chlorine, N-chloroalkyl functionalized PILs are susceptible to form an enhanced amount of hydrogen bonds, and consequently undergo the tendency in non-Newtonian shear thinning behavior.

In the PILs with N-chloroalkyl functionalized cations, the highest viscosity, determined at shear rate of 500 s^{-1} and $20 \text{ }^\circ\text{C}$, was measured for $[\text{C}_{2-\text{Cl}}\text{-Morph}][\text{TFSI}]$ with $0.5953 \text{ Pa}\cdot\text{s}$, which was 3 times larger than for $[\text{C}_{2-\text{Cl}}\text{-Pip}][\text{TFSI}]$ with $0.2097 \text{ Pa}\cdot\text{s}$ and 7-9 times larger than for aliphatic and pyrrolidinium based PILs (Table. 15). The viscosity values of ILs are commonly in the range from 0.01 to $0.500 \text{ Pa}\cdot\text{s}$,¹ which places the N-chloroalkyl functionalized PILs in the upper values. Generally, viscosity is dependent on the ion-ion interactions, including van der Waals forces and hydrogen bonds enhancing these interactions, and as a result leading to higher values of viscosity [171]. It is reported that viscosity increases when the length of alkyl chains increases and in presence of a hydroxyl group, which has the ability to form hydrogen bonds [110]. It explains the difference in viscosity of $[\text{C}_{2-\text{Cl}}\text{-Morph}][\text{TFSI}]$ and $[\text{C}_{2-\text{Cl}}\text{-Pip}][\text{TFSI}]$, where the structures vary only by oxygen present in the ring of the former one, participating in hydrogen bond formation which enhances viscosity. The higher viscosity of the PIL with six-membered ring $[\text{C}_{2-\text{Cl}}\text{-Pip}][\text{TFSI}]$ than five-membered ring $[\text{C}_{2-\text{Cl}}\text{-Pyrr}][\text{TFSI}]$ is consistent with literature reports and attributed to the more stable chair-like conformation of piperidine in contrast to the pyrrolidine with lower energy difference between conformers [231]. In the case of alkylammonium-based PILs, $[\text{HN}_{2-\text{Cl}-22}][\text{TFSI}]$ displays the lowest viscosity ($0.0665 \text{ Pa}\cdot\text{s}$) among all the N-chloroalkyl functionalized PILs, yet significantly higher in comparison to literature values for $[\text{HN}_{222}][\text{TFSI}]$, $0.039 \text{ Pa}\cdot\text{s}$ [178] or $0.048 \text{ Pa}\cdot\text{s}$ [227]. This suggests that the strength of interactions between molecules, and thus viscosity, is intensified by the presence of the terminal chlorine, with a partial negative charge facilitating the occurrence of van der Waals

forces, which overcompensate the negative charge delocalization of the [TFSI]⁻ anion, even more when chlorine is present, and promotes the formation of induced dipoles [110, 185].

Figure 65b shows the evolution of the logarithm of viscosity *vs.* 1/T, in the temperature range from 293 to 353 K, at a shear rate of 500 s⁻¹ where the PILs still exhibit a Newtonian behavior. Apart from [HN_{3-Cl-11}][TFSI] which slightly deviates from linearity, suggesting the influence of the distance between chlorine and the positively charged nitrogen, all the other PILs exhibit a typical Arrhenius dependence of viscosity *vs.* temperature and follow the equation (eq. 37):

eq. 37

$$\eta = \eta_0 \exp \left[\frac{B_\eta}{T} \right]$$

For [HN_{3-Cl-11}][TFSI], the VTF equation (eq. 18 from chapter I, section 242) was utilized to establish the temperature dependence of viscosity. The fitted parameters for the Arrhenius and VTF models are presented in table 15.

The product B_ηR or B'_ηR (where R stands for the molar gas constant) is referred to as pseudo-activation energy corresponding to the activation energy (E_{an}) for a viscous flow. Literally, it means that a smaller activation energy value indicates a lower sensitivity to a temperature variation, whereas a larger activation energy value shows that the compound viscosity is more responsive to a temperature change. The highest B_η values were determined for [C_{2-Cl}-Pip][TFSI] with 2935.2, [HN_{2-Cl-11}][TFSI] with 2908.8 and [C_{2-Cl}-Morph][TFSI] with 2873.5. The elevated B_η value of [C_{2-Cl}-Morph][TFSI] results from a stronger domination of hydrogen bonds, which in turn are susceptible to become considerably weaker with the increase of temperature, whereas in the case of [C_{2-Cl}-Pip][TFSI] the temperature impact overcomes the energetic barrier of the ring conformers transition. The latter is higher than for the five-membered ring conformers of [C_{2-Cl}-Pyr][TFSI] with B_η value of 2485.2, suggesting that the viscosity is less sensitive to temperature. Notwithstanding, the B_η values are comparable for all the PILs with 2-chloroethyl substituent due to the dominant interactions caused by the chlorine presence, namely the induced dipoles formation in contrast to the PIL with 3-chloropropyl substituent in the cation displaying lower B'_η value. It suggests that the viscosity of PILs is more sensitive to temperature when chlorine is on the carbon in β position of nitrogen as compared to the γ one. In the latter case, the range of chlorine withdrawing effect does not affect the molecule as much as in the β position, hence the charge is less

diffused, leading to weaker formation of induced dipoles and ion pairing, thus causing a weaker temperature effect on PIL viscosity.

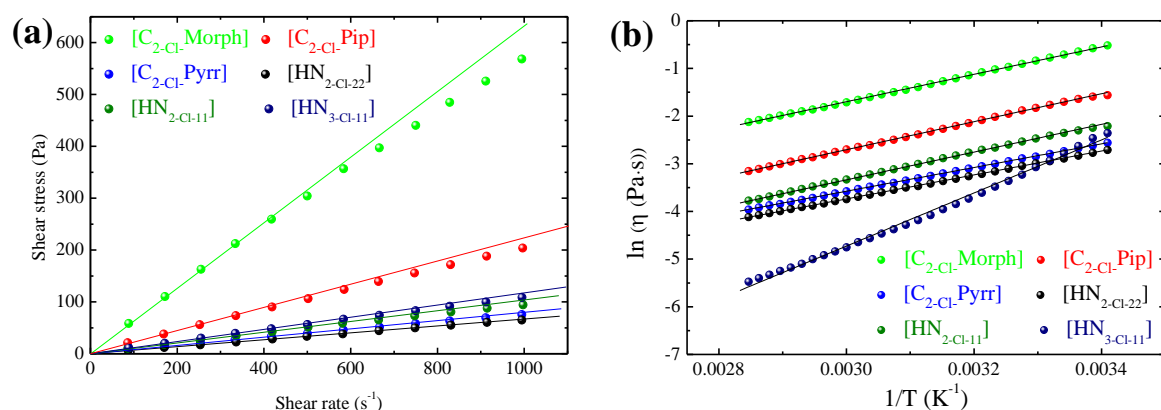


Fig. 65 (a) Shear stress vs. shear rate at 293 K and (b) Ln viscosity vs. $1/T$ of the PILs with N-chloroalkyl functionalized cations. The experimental data are fitted by straight solid lines ([220] - Reproduced by permission of The Royal Society of Chemistry).

Table 15 Viscosity (η at 293K) of the PILs with N-chloroalkyl functionalized cations and their Arrhenius equation parameters: η_0 (Pa·s) pre-exponential factor, B_η fitting parameter (K), T temperature (K). For $[\text{HN}_{3-\text{Cl}-11}][\text{TFSI}]$, the VTF equation was applied, replacing B_η by B'_η ; T_0 stands either for temperature at which the viscosity goes to zero ideal or for glass transition temperature, r^2 is the correlation coefficient ([220] - Reproduced by permission of The Royal Society of Chemistry).

PILs	η (Pa·s)	η_0 (Pa·s)	B_η (K)	r^2	
$[\text{C}_{2-\text{Cl}}\text{-Morph}][\text{TFSI}]$	0.5953	$3.300 \cdot 10^{-5}$	2873.5	0.9996	
$[\text{C}_{2-\text{Cl}}\text{-Pip}][\text{TFSI}]$	0.2097	$1.004 \cdot 10^{-5}$	2935.2	0.9993	
$[\text{C}_{2-\text{Cl}}\text{-Pyrr}][\text{TFSI}]$	0.0801	$1.619 \cdot 10^{-5}$	2485.2	0.9996	
$[\text{HN}_{2-\text{Cl}-22}][\text{TFSI}]$	0.0665	$1.271 \cdot 10^{-5}$	2512.2	0.9997	
$[\text{HN}_{2-\text{Cl}-11}][\text{TFSI}]$	0.1093	$5.769 \cdot 10^{-5}$	2908.8	0.9989	
	η (Pa·s)	η_0 (Pa·s)	B'_η (K)	r^2	T_0 (K)
$[\text{HN}_{3-\text{Cl}-11}][\text{TFSI}]$	0.0945	$1.018 \cdot 10^{-5}$	1006.1	0.9998	126

2.6.2. Conductivity

ILs with $[\text{TFSI}]^-$ anion are usually characterized by lower values of conductivity in comparison to both inorganic ($[\text{PF}_6]^-$, $[\text{NO}_3]^-$) and organic ($[\text{HCOO}]^-$, $[\text{CH}_3\text{COO}]^-$) anions [232]. Susan et al [177] reported conductivity values for a wide range of PILs with non-functionalized ammonium cations and the $[\text{TFSI}]^-$ anion which can help to estimate the trend

of cation-conductivity dependence. The conductivity of PILs with N-chloroalkyl functionalized cations follows the same evolution as for their non-chlorinated analogues. The conductivity values at 293 K increased from 0.18 mS·cm⁻¹ for [C_{2-Cl}-Morph][TFSI], to 0.73 mS·cm⁻¹ for [C_{2-Cl}-Pip][TFSI], 1.23 mS·cm⁻¹ for [HN_{2-Cl-22}][TFSI], 1.35 mS·cm⁻¹ for [HN_{3-Cl-11}][TFSI], 1.38 mS·cm⁻¹ for [C_{2-Cl}-Pyrr][TFSI] and 1.71 mS·cm⁻¹ for [HN_{2-Cl-11}][TFSI]. These values are very low when compared to AILs with the [TFSI]⁻ anion, e.g., [C₂C₁Im][TFSI] with 8.7 mS·cm⁻¹, whereas the difference is not so significant as compared to [C₁Pyrr][TFSI] with 2.2 mS·cm⁻¹ [233]. The direct impact of the chlorine atom is clearly visible when comparing the conductivity of [HN_{2-Cl-22}][TFSI] (1.2 mS·cm⁻¹) with [HN₂₂₂][TFSI] (4.4 - 5.0 mS·cm⁻¹) [177, 178]. The presence of chlorine in the alkyl substituent of the discussed family of PILs alters their charge distribution in comparison to the non-functionalized analogues, in turn causing strengthened interactions between cation and anion, their association and ion pair formation, resulting in decreased ions mobility and consequently lowering of conductivity.

The evolution of conductivity with temperature was first represented in an Arrhenius plot:

eq. 38

$$\sigma = \sigma_0 \exp \left[\frac{-B_\sigma}{T} \right]$$

where [HN_{2-Cl-22}][TFSI], [HN_{2-Cl-11}][TFSI], [HN_{3-Cl-11}][TFSI] and [C_{2-Cl}-Pyrr][TFSI] displayed negligible negative deviation, whereas the deviation became significant in the case of [C_{2-Cl}-Pip][TFSI] and [C_{2-Cl}-Morph][TFSI]. Therefore, the VTF equation was harnessed to describe the temperature dependence of conductivity, and in this case the data could be fitted by a linear dependence for the six PILs (Fig. 66). The fitting parameters for the VTF model are presented in table16.

The product B'_σR corresponds to the activation energy (E_{Aσ}) for the ionic conduction. Similarly to B'_ηR, higher values of B'_σR indicate a higher sensitivity to temperature changes. All N-chloroalkyl functionalized PILs display comparable B'_σ values of slope, except [HN_{2-Cl-11}][TFSI] with much smaller B'_σ of 940.2 demonstrating less steep temperature variation.

The different behavior of the studied PILs in the investigated temperature range, Arrhenius for viscosity (except [HN_{3-Cl-11}][TFSI]), and non-Arrhenius for conductivity,

suggests that these two parameters are dominated by different interactions. Whilst viscosity is strongly related to van der Waals interactions which predominate in these PILs, conductivity is dominated by Coulombic forces.

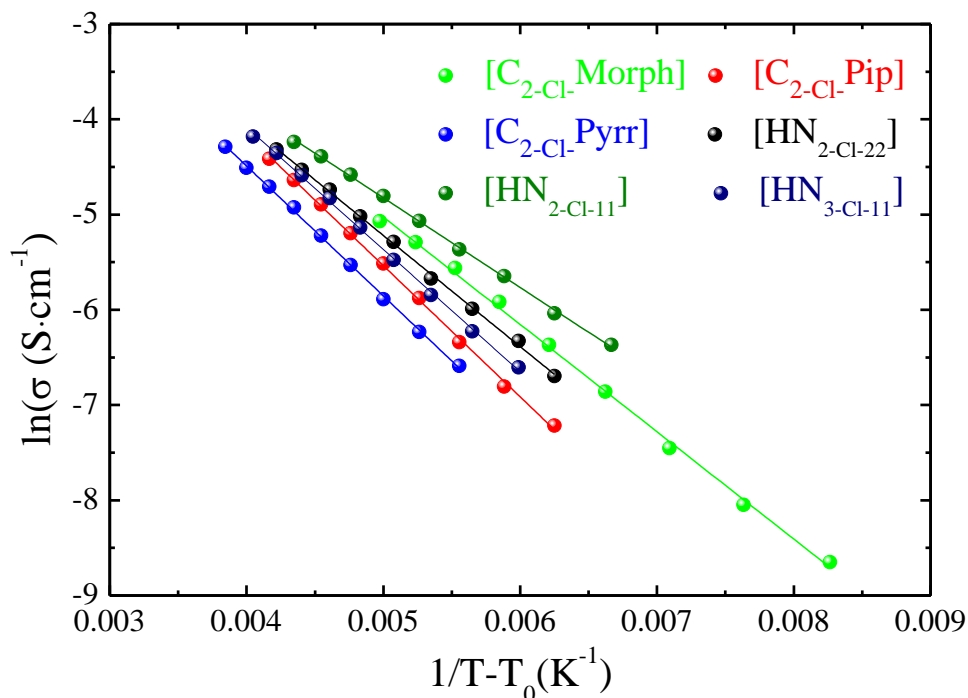


Fig. 66 Ln (ionic conductivity) vs. $(1/T-T_0)$ of the PILs with chloroalkyl functionalized cations. The experimental data are fitted by solid lines ([220] - Reproduced by permission of The Royal Society of Chemistry).

Table 16 Conductivity (σ at 293 K), molar conductivity (Λ , at 293 K) and VTF equation parameters of the PILs with N-chloroalkyl functionalized cations: σ_0 (Pa·s) pre-exponential factor, B'_σ fitting parameter (K), T_0 stands either for the temperature at which the conductivity goes to zero ideal or for glass transition temperature. r^2 is the correlation coefficient ([220] - Reproduced by permission of The Royal Society of Chemistry).

PILs	σ ($\text{mS}\cdot\text{cm}^{-1}$)	Λ ($\text{S}\cdot\text{cm}^2\cdot\text{mol}^{-1}$)	σ_0 ($\text{S}\cdot\text{cm}^{-1}$)	T_0 (K)	B'_σ (K)	r^2
[C ₂ -Cl-Morph]	0.18	0.0467	1.834	172	1126.8	0.9982
[C ₂ -Cl-Pip]	0.73	0.2051	3.857	133	1377.4	0.9989
[C ₂ -Cl-Pyrr]	1.38	0.3699	2.630	113	1364.4	0.9991
[HN ₂ -Cl-22]	1.23	0.3419	1.849	136	1166.8	0.9989
[HN ₂ -Cl-11]	1.71	0.4197	1.132	143	940.2	0.9991
[HN ₃ -Cl-11]	1.35	0.3543	2.860	126	1283.5	0.9989

2.6.3. Ionicity

The ionicity of the PILs with N-chloroalkyl functionalized cations was assessed by the Walden plot (Fig. 67) showing log (molar conductivity) vs. log fluidity (η^{-1}) of the medium; values were plotted every 10 °C in the temperature range from 20 to 90 °C [141, 142, 167].

The molar conductivity Λ is calculated using the relation (eq. 22):

eq. 22

$$\Lambda = \frac{\sigma \cdot M_W}{\rho}$$

(values at 293K in table 16). The so-called ideal line (solid line from one corner to the other in figure 67, established by using a 0.01 mol·L⁻¹ solution) indicates that the mobility of ions is determined only by the medium viscosity, and that the number of ions present in the equivalent volume is the one indicated by the salt composition, i.e. all available ions contribute equally [143]. As clearly visible, the points representing the tested PILs are located below the “ideal line” and according to IL classification proposed by Angell [141] should be categorized as “poor ILs”. In terms of Walden rule, the PILs represented by points located below the “ideal line” have strongly interacting ions which partially associated together. [HN₂-Cl-22][TFSI], [HN₂-Cl-11][TFSI], [C₂-Cl-Pyrr][TFSI] and [C₂-Cl-Pip][TFSI] display almost parallel traces (similar slope), approaching the region of “good ILs” (here, above the dashed line), characterized in ref [141] as ILs where each ion is surrounded by a relatively uniform shell of ions of opposite charge. A dramatic influence of temperature is observed for [C₂-Cl-Morph][TFSI], where hydrogen bonding caused by oxygen presence in the cation predominates. At elevated temperature (above 70-80 °C), hydrogen bonding to the fluorinated anion is reduced, thus viscosity is reduced and fluidity enhanced, and at the same time conductivity is improved, allowing this PIL to be rated as “good” one. As established before, the transport properties also significantly depend on the chain length between nitrogen and terminal chlorine. This is well-illustrated in figure 67 by the different temperature dependence of [HN₃-Cl-11][TFSI], which diverges from the trend observed for other N-chloroalkyl functionalized PILs; this particular behavior is ascribed to T-dependent ion-pairing [142].

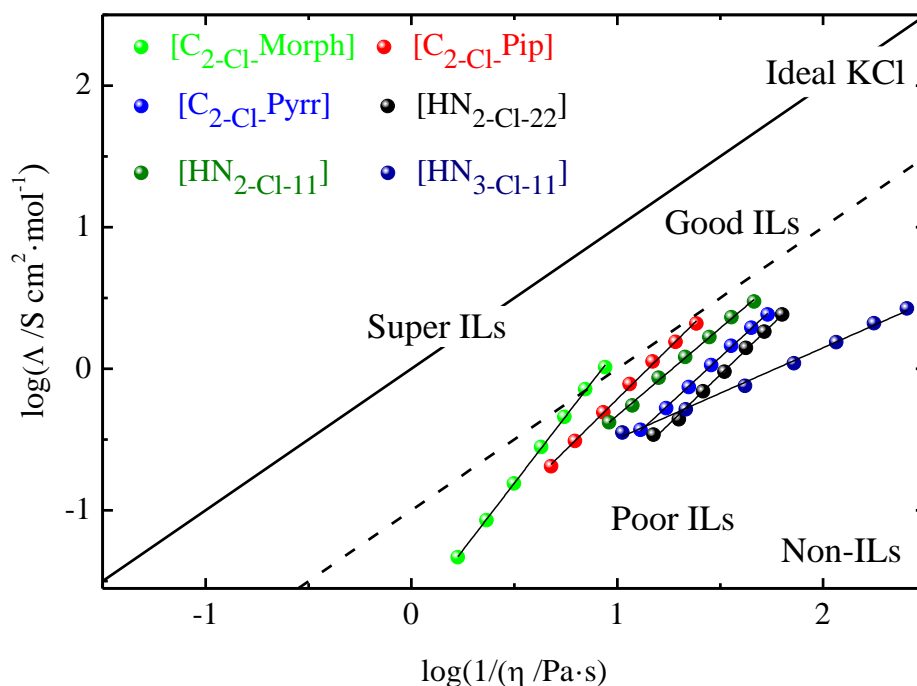


Fig. 67 Walden plot representing \log (molar conductivity) vs. \log fluidity of the PILs with N-chloroalkyl functionalized cations. The points are plotted every 10 °C in the temperature range 20–90 °C. The solid line is the “ideal” Walden product line obtained with 0.01 mol·L⁻¹ aqueous KCl ([220] - Reproduced by permission of The Royal Society of Chemistry).

3. Conclusion

In summary, motivated by the demand for designing new PILs for electrochemical capacitors, a new series of PILs composed of N-chloroalkyl functionalized ammonium cations and $[\text{TFSI}]^-$ anion was synthesized and characterized. For a number of properties, the new PILs were compared to their non-chlorinated analogues in order to determine the impact of chlorine on the various parameters. The application of chloro-functionality was proven to be an effective strategy for decreasing the PILs melting point. Owing to the characteristics of the $[\text{TFSI}]^-$ anion, the obtained series of PILs displays an excellent thermal stability, even up to ca. 300 °C, hence a wide range of liquid state. The chlorine atom increases the values of density and refractive index, and consequently of calculated molar refractivity, suggesting that these PILs are more polarizable than non-functionalized ones, in good agreement with computed charge distribution. The investigated PILs are classified as shear-thinning non-Newtonian fluids typical of ILs with functional atoms and groups on the cation. The temperature dependence of viscosity and conductivity revealed a strong domination of hydrogen bonds hampering the transport properties at RT; however, at high temperature, the

impact of hydrogen bonds becomes negligible and the PILs approach the region of so called “good ionic liquids”.

The described characteristics suggest that the N-chloroalkyl functionalized PILs are suitable for electrochemical devices operating at elevated temperatures. Hence, this chapter demonstrates that the functionalization of cations is a good strategy to design PILs with optimized properties.

Chapter V
**Evaluation of protic ionic liquids with N-chloroalkyl
functionalized cations as electrolytes for ECs**

1. Introduction

Generally, ILs are claimed to be promising electrolytes owing to their wide electrochemical stability window evaluated on inert electrodes such as glassy carbon (GC). However, the electrochemical stability of ILs diminishes in contact with other materials such as elements of ECs: metallic current collectors and electrodes made of activated carbon. This matter is widely discussed in reports which disclose the designing of ILs-based ECs and establish reliable operating conditions for ECs [163, 235].

Therefore, Chapter V intends to present information about the electrochemical performance of electrodes and ECs in presence of the new PILs with N-chloroalkyl functionalized cations designed in chapter IV. The first section shows the electrochemical stability window of these PILs on GC and discusses the obtained values in light of the computational prediction of HOMO/LUMO orbitals. The second section focuses on the electrochemical behavior of the PILs on stainless steel and aluminum which are usually applied as current collectors for ECs. In the third section, the maximum electrochemical potential window of N-chloroalkyl functionalized PILs is determined on AC-based electrodes intended for application in ECs. In the fourth section, these stability data are used to interpret the voltage limits of symmetric two-electrode cells implementing electrodes made from the same carbon. Finally, the performance of ECs based on the PILs with N-chloroalkyl functionalized cations is determined. Taking into account the findings of chapter III on the beneficial water content in PIL, stated to be around 150 ppm, this content did not exceed 200 ppm for all the PILs investigated in this chapter (consistently with the indications in chapter IV).

2. Electrochemical potential window of the PILs

2.1. Evaluation of the PILs electrochemical stability by computational methods

As already suggested by Wilkes et al., the electrochemical oxidation potential of anions and reduction potential of cations comprised in ILs are correlated to the energy (in eV) of the highest occupied molecular orbital (HOMO) and the lowest unoccupied molecular orbital (LUMO), respectively [115]. Higher LUMO energy of the cations characterizes higher stability toward reduction (lower reduction potential). Recently, computational methods including HOMO/LUMO values calculation showed fairly good agreement with existing

experimental data [145]. Hence, by comparing the level of frontier orbital energy of the N-chloroalkyl or non-chloroalkyl functionalized PILs, their oxidation/reduction stability toward the same electrode material, here glassy carbon (GC), could be predicted. As seen in table 17, all the N-chloroalkyl functionalized cations display lower LUMO energy than their alkylammonium counterparts, e.g., [C_{2-Cl}-Pip]⁺ with -4.07 eV vs. [C₂Pip]⁺ with -3.24 eV and [HN_{2-Cl-22}]⁺ with -3.96 eV vs. [HN₂₂₂]⁺ with -3.27 eV. Accordingly, the presence of chlorine provokes an increase in reduction potentials of N-chloroalkyl functionalized cations and thereby restricts the electrochemical window. It is consistent with the findings of Ceder et al. classifying electron-donating functional groups (e.g., alkyl or hydroxyalkyl) as cation stabilizing groups, in opposition to electron-withdrawing groups such as halogen, cyanide and trifluoromethane [145, 236]. The LUMO energy values of N-chloroalkyl functionalized cations are comparable to those of aprotic imidazolium cations, with their reported values in the range from -4.92 to -4.51 eV [237], whereas non-functionalized PILs have values similar to typical alkylammonium cations (-3.22 for trimethylpropylammonium cation, [N₁₁₁₃]⁺, and -3.13 eV for trimethylhexylammonium cation, [N₁₁₁₆]⁺) [237].

Table 17 Energies of HOMO and LUMO orbitals of N-chloroalkyl functionalized cations and their non-functionalized analogues ([220] - Reproduced by permission of The Royal Society of Chemistry).

N-chloroalkyl functionalized PILs	HOMO (eV)	LUMO (eV)	Non-functionalized analogues	HOMO (eV)	LUMO (eV)
[C _{2-Cl} -Morph][TFSI]	-11.92	-4.32	[C ₂ Morph][TFSI]	-11.79	-3.63
[C _{2-Cl} -Pip][TFSI]	-11.88	-4.07	[C ₂ Pip][TFSI]	-13.35	-3.24
[C _{2-Cl} -Pyrr][TFSI]	-11.93	-4.21	[C ₂ Pyrr][TFSI]	-13.76	-3.70
[HN _{2-Cl-22}][TFSI]	-11.93	-3.96	[HN ₂₂₂][TFSI]	-14.27	-3.27
[HN _{2-Cl-11}][TFSI]	-12.10	-4.55	[HN ₂₁₁][TFSI]	-14.68	-3.98
[HN _{3-Cl-11}][TFSI]	-11.30	-4.13	[HN ₃₁₁][TFSI]	-13.52	-3.90

2.2. Practical electrochemical stability of the PILs evaluated on glassy carbon

The experimental stability limits of the PILs with N-chloroalkyl functionalized cations were detected by linear sweep voltammetry using GC as working electrode. As shown in figure 68 comparing the cathodic/anodic stability limits of $[\text{HN}_{2-\text{Cl}-22}][\text{TFSI}]$ and $[\text{HN}_{222}][\text{TFSI}]$, with potential values of -1.69/2.43 V vs. AgQRE and -1.88/2.45 V vs. AgQRE, respectively, the significance of the HOMO/LUMO calculations is warranted.

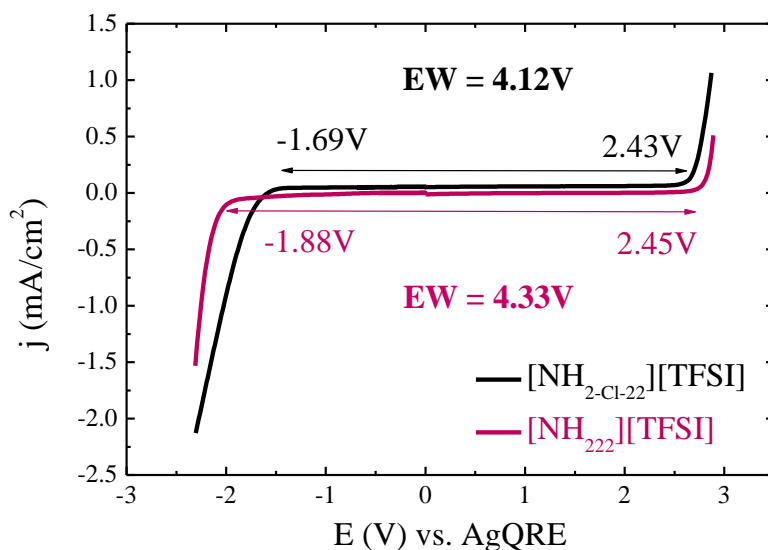


Fig. 68. Comparison of the electrochemical stability limits of $[\text{HN}_{2-\text{Cl}-22}][\text{TFSI}]$ and $[\text{HN}_{222}][\text{TFSI}]$ determined by linear sweep voltammetry ($v=10 \text{ mV}\cdot\text{s}^{-1}$) on glassy carbon electrode ([220] - Reproduced by permission of The Royal Society of Chemistry).

However, when considering the various PILs with N-chloroalkyl functionalized cations (Fig. 69), it can be seen that there is no straightforward correlation between the trend of increasing LUMO energy values reported in table 17, e.g., $[\text{HN}_{2-\text{Cl}-11}]^+ < [\text{C}_{2-\text{Cl}}\text{-Morph}]^+ < [\text{C}_{2-\text{Cl}}\text{-Pyr}]^+ < [\text{HN}_{3-\text{Cl}-11}]^+ < [\text{C}_{2-\text{Cl}}\text{-Pip}]^+ < [\text{HN}_{2-\text{Cl}-22}]^+$ and the practical reduction potential values. The viscosity of PILs has a significant influence on the detected cathodic stability values which depend on the electrolyte mass transport: the higher viscosity, the lower specific current densities, thus greater stability. Besides, it is hypothesized that this discrepancy in the trend could result from contributions of interactions between cations and anions. The widest electrochemical window (EW) of 5.07 V was measured for $[\text{C}_{2-\text{Cl}}\text{-Morph}][\text{TFSI}]$ - the most viscous PIL, whereas the other five PILs displayed EWs in the range of 4.12 - 4.42 V. The cathodic limits slightly vary in the band of -1.69 to -2.05 V vs. AgQRE, except for $[\text{C}_{2-\text{Cl}}\text{-Morph}][\text{TFSI}]$ with -2.39 V vs. AgQRE. As anticipated, owing to the impact of $[\text{TFSI}]^-$,

the oxidation limit of all the PILs is situated in the narrow range of 2.37 - 2.68 V vs. AgQRE, making it possible to significantly enlarge the stability window in contrast to values reported for [HPyrr][HCOO] with EW of 2.55 V or [HPyrr][NO₃] with EW of 2.6 V on GC [198].

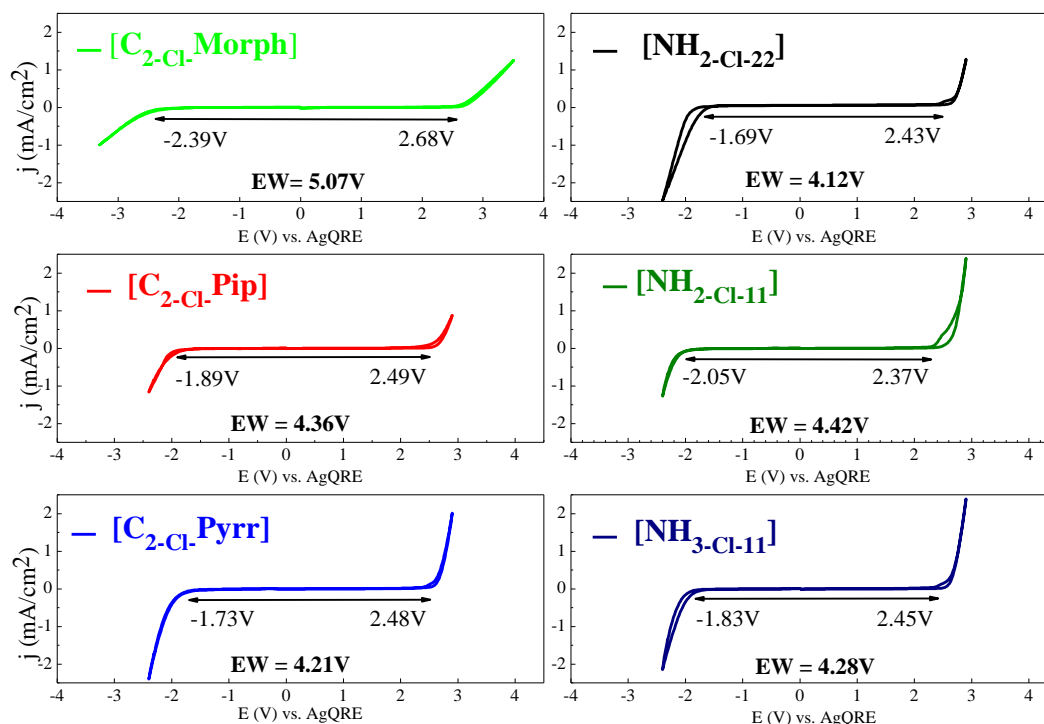


Fig. 69 Electrochemical stability window of the PILs with N-chloroalkyl functionalized cations determined by linear sweep voltammetry ($v=10 \text{ mV}\cdot\text{s}^{-1}$) on glassy carbon electrode ([220] - Reproduced by permission of The Royal Society of Chemistry); the cut-off current density at the onset of reduction and oxidation is $0.1 \text{ mA}\cdot\text{cm}^{-2}$ [144].

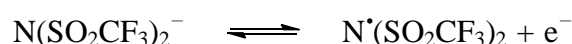
3. Electrochemical behavior of aluminum and stainless steel current collectors in the tested PILs

3.1. Electrochemical stability of N-chloroalkyl functionalized PILs on stainless steel 316L

Considering the complexity of stainless steel 316L (here referred to as SSt), consisting not only from carbon and iron, but also of the admixture of various elements such as chromium (16%), nickel (10%) and molybdenum (2%) etc., this paragraph aims at the determination of safe potential limits of the PILs on SSt and/or the indication of corrosion if it occurs.

The electrochemical stability of the N-chloroalkyl functionalized PILs on SSt was investigated under positive and negative polarization in separated cells to avoid parasitic effects. The vertex potential was increased (or decreased) by 0.1 V steps starting from 1.0 V vs. AgQRE (or -0.5 V vs. AgQRE) till the appearance of significant oxidation (or reduction) current. Among the CVs obtained for positive (or negative) polarization, the ones recorded for the most positive (or negative) vertex potential, yet not exceeding 0.1 mA·cm⁻² cut-off and not displaying additional peaks during discharge (also evidencing PIL instability) were considered to correspond to safe stability limits. The evaluation for the positive and negative polarization (Fig. 70 and Fig. 71, respectively) is shown for the example of [HN_{2-Cl-22}][TFSI]. Accordingly, no distinctive oxidation peak up to 2.1 V vs. AgQRE (Fig. 70) or reduction one down to -1.5 V vs. AgQRE (Fig. 71), respectively, was observed. The safe stability limits of the other N-chloroalkyl functionalized PILs are listed in table 18. The cathodic potentials of these PILs, depending on the cation reduction and hydrogen generation, range from -1.4 to -1.6 V vs. AgQRE and they are higher (thus stability is lower) than in the case of GC working electrode. The anodic limits, attributed to the anion oxidation, vary from 2.0 to 2.3 V vs. AgQRE and they are a slightly lower as compared to GC (consequently stability is also lower). Importantly, for all the N-chloroalkyl functionalized PILs, the oxidation peak at vertex potential exceeding the maximum safe potential is followed by a cathodic peak at ca. 0.55-1.15 V vs. AgQRE (Fig. 70). As the oxidation of the [TFSI]⁻ anion is assumed to occur according to eq. 39:

eq. 39



where, N*(SO₂CF₃)₂ is a nitrogen centered radical [238] the observed cathodic peak is attributed to SSt corrosion due to the presence of active radicals.

Table 18 Potential limits vs. AgQRE of the N-chloroalkyl functionalized PILs on SSt electrode for positive ($PL_{SSt/pos}$) and negative ($PL_{SSt/neg}$) polarization.

PIL→ ↓Stability (V) vs. AgQRE	[C _{2-Cl-Morph}] [TFSI]	[C _{2-Cl-Pip}] [TFSI]	[C _{2-Cl-Pyrr}] [TFSI]	[HN _{2-Cl-22}] [TFSI]	[HN _{2-Cl-11}] [TFSI]	[HN _{3-Cl-11}] [TFSI]
$PL_{SSt/pos}$	2.0	2.3	2.1	2.1	2.0	2.0
$PL_{SSt/neg}$	-1.6	-1.5	-1.5	-1.5	-1.4	-1.4

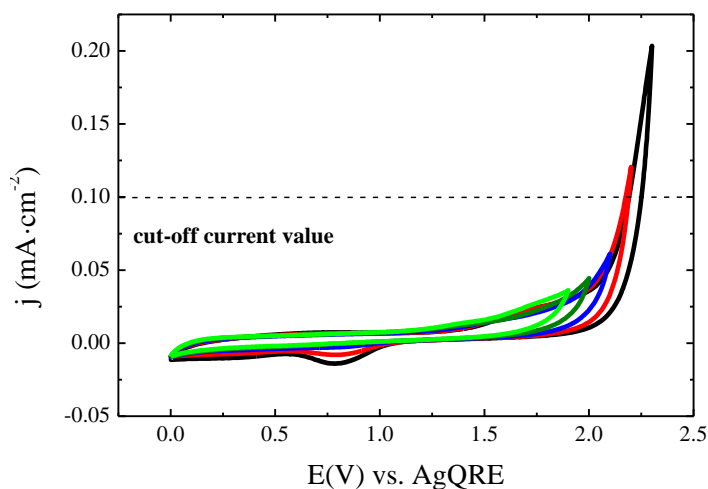


Fig. 70 Linear sweep voltammetry ($v=5\text{mV}\cdot\text{s}^{-1}$) of a SSt electrode in $[\text{HN}_{2-\text{Cl}_{22}}][\text{TFSI}]$ under positive polarization; the blue curve represents the safe stability limit where the current density at the onset of oxidation is below $0.1\text{ mA}\cdot\text{cm}^{-2}$.

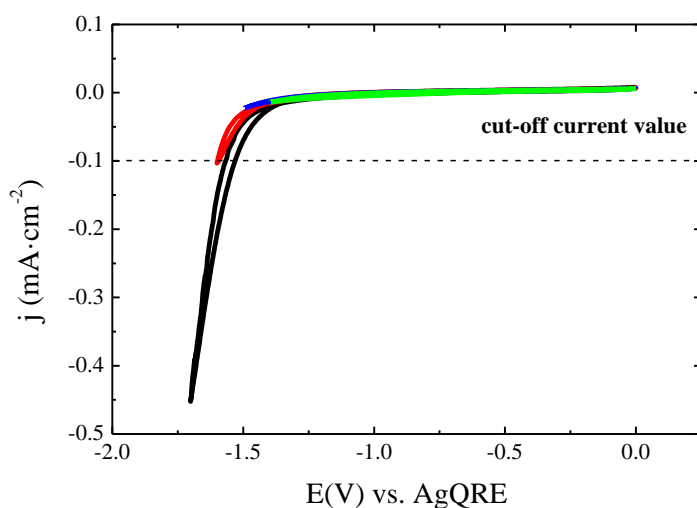


Fig. 71 Linear sweep voltammetry ($v=5\text{mV}\cdot\text{s}^{-1}$) of a SSt electrode in $[\text{HN}_{2-\text{Cl}_{22}}][\text{TFSI}]$ under negative polarization; the blue curve represents the safe stability limit where the current density at the onset of reduction is below $0.1\text{ mA}\cdot\text{cm}^{-2}$.

3.2. Electrochemical behavior of aluminum in N-chloroalkyl functionalized PILs

Aluminum fulfills a number of requirements for current collector materials, such as relatively low-cost, good thermal and electrical conductivity and low-density leading to lightness of the device. However, the main concern is its possible undesired corrosion. A significant body of work on electrolytes containing the $[\text{TFSI}]^-$ anion and aluminum current collectors is dedicated to lithium ion batteries (LIBs) using Al as cathode current collector. In the case of organic electrolytes, the instability of aluminum during anodic polarization was

proven for imide-salts such as [Li][TFSI] and [Li][BETI]. However, the Al surface can be passivated by the addition of [Li][PF₆] leading to the formation of a protective fluoride-rich film of AlF₃ [239].

By contrast, aluminum corrosion does not take place in [TFSI]⁻ based RTILs [240]. As shown in Fig. 72, which compares the cyclic voltammograms of Al foil using [Li][TFSI] in EC/DMC (Fig. 72a) and its mixtures with [TFSI]⁻ based ILs (Fig. 72b-d), the current density of the first scan is reduced by three orders of magnitude in the mixtures containing ILs. For [Li][TFSI] in EC/DMC (Fig. 72a), the significant increase of current at about 5.0 V vs Li⁺/Li during the first anodic scan is attributed to the dissolution of the Al surface, followed by its corrosion in the next cycles, reflected in even higher anodic current. However, when ILs are added to the electrolyte (Fig. 72b-d), the anodic current decreases, owing to the formation of a passive layer [240]. Analogously, Al corrosion is suppressed owing to Al(TFSI)₃ formation if an IL with [TFSI]⁻ anion, e.g., [C₁C₄Pyr][TFSI], is added to the [Li][TFSI] based organic electrolyte [241]. It has been shown that Al is better passivated in [C₁C₄Pyr][TFSI] than in [C₁C₄Pyr][FSI], again confirming the benefits of employing the [TFSI]⁻ anion [157].

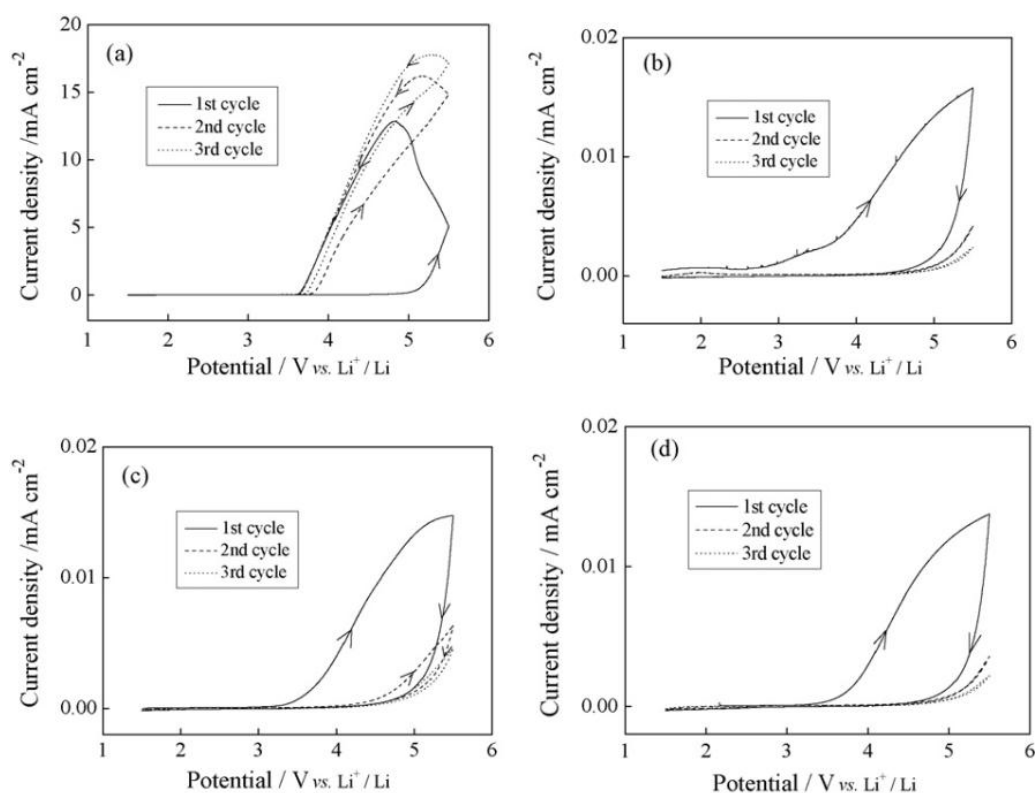


Fig. 72 Cyclic voltammograms (10 mV·s⁻¹) of Al foil electrode in (a) 1 mol·L⁻¹ [Li][TFSI]/EC+DMC; (b) 1 mol·L⁻¹ [Li][TFSI]/[C₂C₁Im][TFSI]; (c) 1 mol·L⁻¹ [Li][TFSI]/[C₃C₁Im][TFSI]; (d) 1 mol·L⁻¹ [Li][TFSI]/[C₄C₁Im][TFSI] (from [240]).

In the case of PILs themselves, the formation of an Al_2O_3 protective layer has been already reported for $[\text{HN}_{222}][\text{TFSI}]$ with water content in the range of 100-200 ppm [178]. As shown in figure 73, during the first cycle, a loop (initiated at about 0.25 V vs. Ag, with maximum at 1.1 V vs. Ag) is recorded, whereas the current becomes significantly lower in the following scans; such finding proves the formation of a protective passivation layer and that aluminum can be safely utilized in the potential range from -1.5 to 1.5 V vs. Ag.

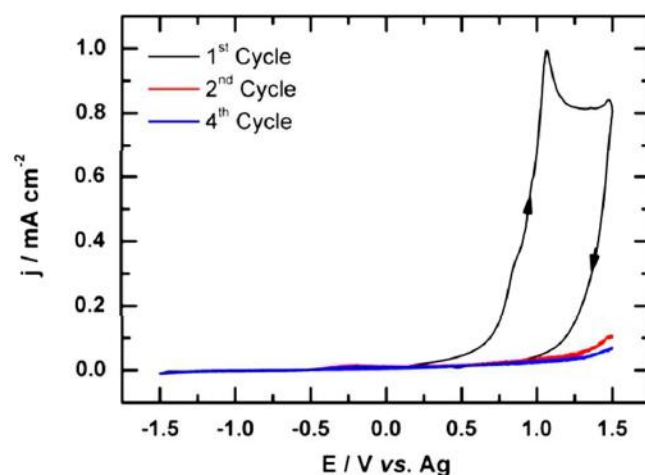


Fig. 73 Cyclic voltammograms ($5 \text{ mV}\cdot\text{s}^{-1}$) of an Al electrode in $[\text{HN}_{222}][\text{TFSI}]$ at $20 \text{ }^\circ\text{C}$ (from [178]).

The electrochemical behavior of all the PILs with N-chloroalkyl functionalized cations was evaluated on pretreated aluminum foil (kindly provided by Blue Solutions, France) using the conditions described in reference [151].

Similarly to the data presented above for ILs with $[\text{TFSI}]^-$ anion, the cyclic voltammograms of aluminum foil immersed in the PILs with N-chloroalkyl functionalized cations display a high current density in the first scan, around $0.9 \text{ mA}\cdot\text{cm}^{-2}$ for $[\text{C}_{2\text{-Cl}}\text{-Pip}][\text{TFSI}]$, $[\text{C}_{2\text{-Cl}}\text{-Pyr}][\text{TFSI}]$, $[\text{HN}_{2\text{-Cl-22}}][\text{TFSI}]$ and $[\text{HN}_{3\text{-Cl-11}}][\text{TFSI}]$, $0.7 \text{ mA}\cdot\text{cm}^{-2}$ for $[\text{HN}_{2\text{-Cl-11}}][\text{TFSI}]$ and only $0.4 \text{ mA}\cdot\text{cm}^{-2}$ for $[\text{C}_{2\text{-Cl}}\text{-Morph}][\text{TFSI}]$, while in the subsequent scans the current density decreases evidencing metal passivation (Fig. 74). The lower current density in the first cycle when using $[\text{C}_{2\text{-Cl}}\text{-Morph}][\text{TFSI}]$ is attributed to its high viscosity influencing the diffusion of ions to the surface of aluminum foil. Strikingly, with $[\text{HN}_{2\text{-Cl-22}}][\text{TFSI}]$ and $[\text{HN}_{2\text{-Cl-11}}][\text{TFSI}]$, the current density remains at the level of $0.3 \text{ mA}\cdot\text{cm}^{-2}$ after 10 cycles. This remaining current leap is located in a potential range corresponding to the standard potential of the Cl^-/Cl_2 redox couple ($E^\circ = +1.36 \text{ V}$), suggesting Cl^- release from the two alkylammonium cations with 2-chloroethyl substituent. Taking into account the reports indicating that the composition of the passive layer may vary depending

on the ions making up the IL and the electrochemical conditions of the passivation process [242], it suggests in these two cases that the superficial layer may include AlCl_3 in addition to Al_2O_3 .

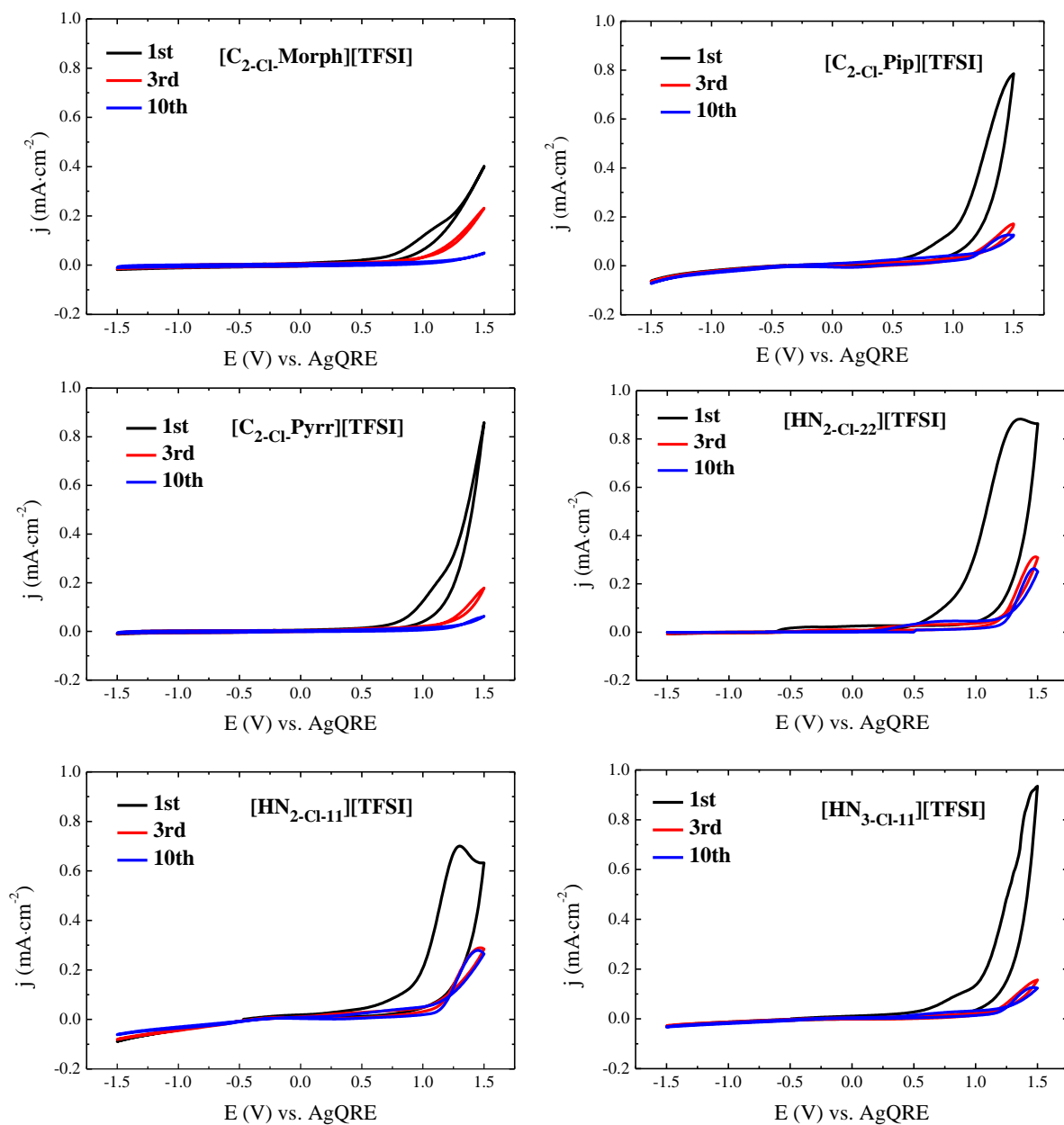


Fig. 74 Linear sweep voltammetry ($v=5\text{mV}\cdot\text{s}^{-1}$) of aluminum electrode in N-chloroalkyl functionalized PILs.

Apart from anodic behavior of aluminium, the stability under negative polarization was evaluated. Again, $[\text{HN}_2\text{-Cl-22}][\text{TFSI}]$ served as representative PIL, and $0.1\text{ mA}\cdot\text{cm}^{-2}$ cut-off was adopted as stability limit. Although at -1.6 V vs. AgQRE the faradaic current is only slightly higher than the borderline, -1.5 V vs. AgQRE was acknowledged as minimum value to ensure a lack of parasitic effects with released hydrogen. Analogously, the cathodic stability of -1.5 V vs. AgQRE was established for all the PILs with N-chloroalkyl

functionalized cations, except for [C_{2-Cl}-Morph][TFSI] with -1.7 V vs. AgQRE. These values are comparable with cathodic stability limits detected on SSt current collectors, and alike higher, thus stability lower, if compared to the stability limits detected on GC (chapter V, section 2.2.).

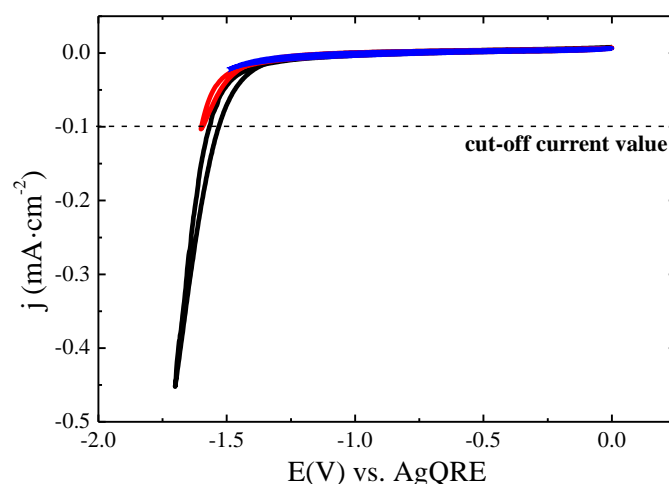


Fig. 75 Linear sweep voltammetry ($v = 5 \text{ mV} \cdot \text{s}^{-1}$) of Al electrode in [HN_{2-Cl-22}][TFSI] under negative polarization; the blue curve represents the safe stability limit where the current density at the onset of reduction is below $0.1 \text{ mA} \cdot \text{cm}^{-2}$.

3.3. Conclusions on current collector applicability

The conducted experiments showed a relatively good stability of the tested N-chloroalkyl functionalized PILs on both types of current collectors. On stainless steel, the potential window is in the range of 3.4 to 3.8 V. However, corrosion may entail a risk of cell failure beyond the safe potential limit under positive polarization. The cathodic stability limits on Al and stainless steel are comparable. Hence, owing to the formation of a passive layer during anodic sweeps, aluminum can be also applied as current collector. Taking into account that Al is significantly lighter and cheaper, it has been selected as current collector material for the further studies on AC electrodes and electrochemical capacitors.

4. Stability limits of N-chloroalkyl functionalized PILs on AC electrode

4.1. Literature background

Since the electrochemical stability of PILs is expected to be altered on high surface area ACs, their safe potential limits on such electrodes need to be determined. Based on

previous work disclosed by Xu et al. [235], Kötzer et al. proposed an accurate window opening method to evidence the reliable stability limits of electrolytes (organic and ionic liquid) on activated carbon electrodes [164]. The experiments are conducted in 3-electrode configuration, where positive and negative polarization is always investigated in separate cells. The vertex potential of anodic sweeps is gradually increased, firstly to 0.5 V, 0.75 V, 1.0 V vs. RE and then by 0.1 V steps up to 2.5 V vs. RE, whereas the negative potential is analogically decreased stepwise down to -2.5 V vs. RE. For each potential step, three cyclic voltammograms are recorded to avoid the parasitic effects which may occur during the first cycle; an example of the obtained cyclic voltammograms is shown in figure 76.

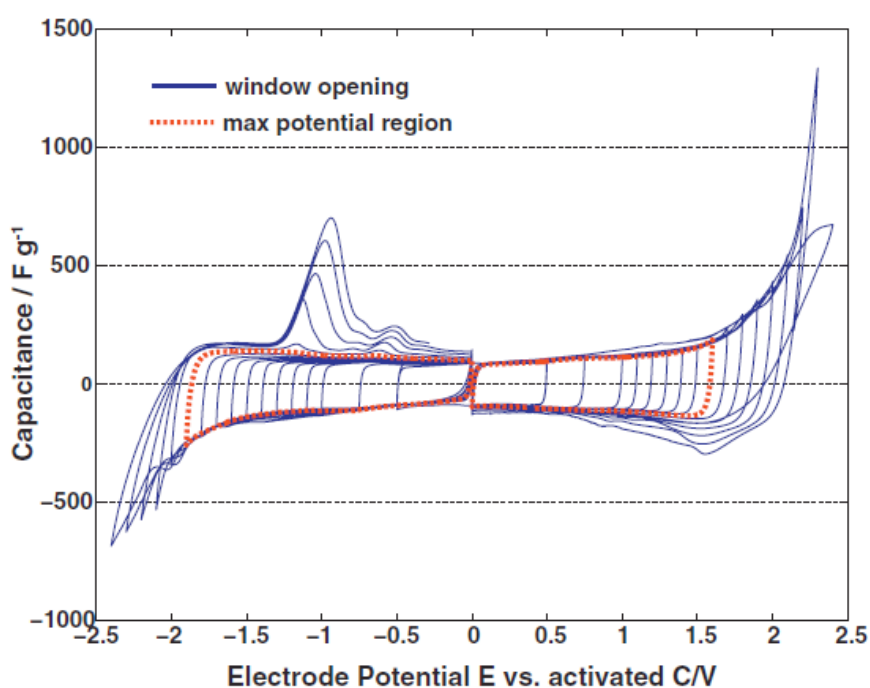


Fig. 76 Cyclic voltammograms ($1 \text{ mV}\cdot\text{s}^{-1}$) of a BP2000 electrode in $[\text{C}_2\text{C}_1\text{Im}][\text{BF}_4]$ with potential window opening; RE and CE: YP17. The CVs marked in red indicate the maximum potential excursion found when using the fixed stability limits (from [164]).

Subsequently, according to the method of Xu et al. [235], the charges accumulated during each charge/anodic scan ($Q_+ = Q_A$ which corresponds to the surface area limited by the anodic curve indicated by points a-b-c-d) and discharge/cathodic scan ($Q_- = Q_C$ which is the surface area limited by the cathodic curve, indicated by points d-e-f-a), as shown in figure 77, are employed to calculate the S-values according to equations 40 and 41:

eq. 40

$$S_{pos} = \frac{Q_+}{Q_-} - 1$$

eq. 41

$$S_{neg} = \frac{Q_-}{Q_+} - 1$$

where S_{pos} and S_{neg} refer to positive and negative polarization, respectively.

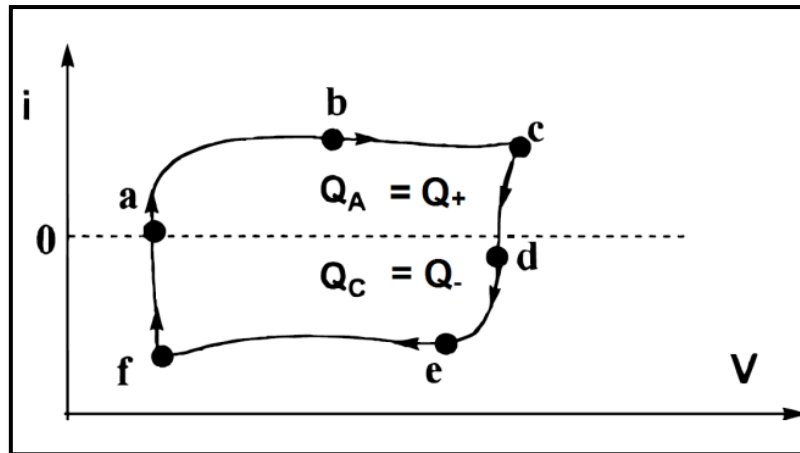


Fig. 77 Schematic description of Q_+ ($= Q_A$) and Q_- ($= Q_C$) determination according to Xu et al. (adapted from [235]).

Then, the S -values are plotted vs. the corresponding vertex potentials as presented in figure 78, which includes the ‘constant S -value criterion’ recommended by Xu et al. [235], and ‘new criterion’ defined by Kötzt et al [164]. The ‘constant S -value criterion’ was established arbitrarily as not exceeding $S = 0.1$, which corresponds to 10% of faradaic contribution, due to reasoned electrolyte decomposition beyond this limit. However, Kötzt et al [164] pointed out that the constant criterion might be not sufficiently appropriate indicator of stability. Therefore, Kötzt et al postulated that a system is considered to be unstable if at least one of its electrodes operates beyond the potential at which the faradaic current impact exceeds 5% of the overall current per 1 V potential step. It results in the limit of 0.005 for 0.1 V step which means that the difference between S -value of two successive points should not exceed 0.005 ($\Delta_1 - \Delta_2 < 0.005$, ‘new stability criterion’) as illustrated in figure 78. The CVs corresponding to the established maximum vertex potentials according to the ‘new stability criterion’ are marked red in figure 76.

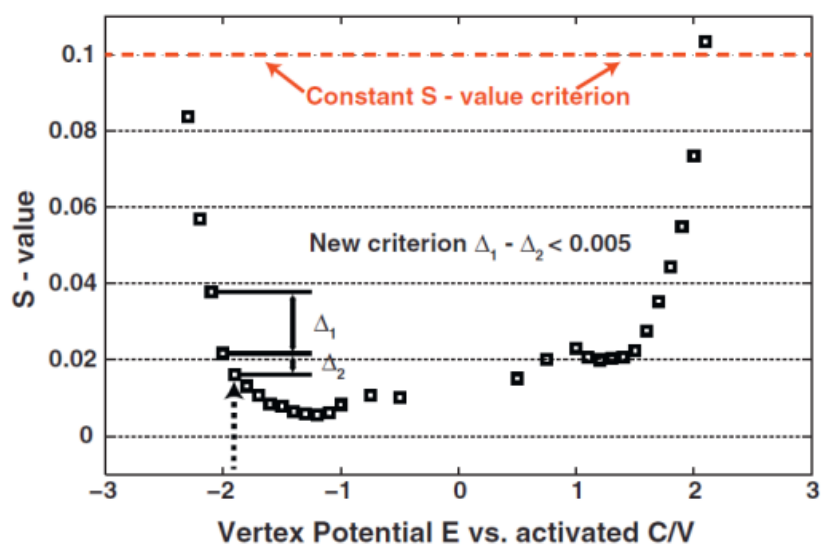


Fig. 78 Plot of S-values vs. vertex potential determined from the cyclic voltammograms ($1 \text{ mV}\cdot\text{s}^{-1}$) of a BP2000 electrode in $[\text{C}_2\text{C}_1\text{Im}][\text{BF}_4]$ shown in figure 76 (from [164]).

4.2. Potential limits of N-chloroalkyl functionalized PILs on AC electrode

The above 3-electrode methodology was adopted in our CV experiments, using aluminum current collectors and electrodes made from the commercial activated carbon DLC Super 30 (from Norit) designed for ECs applications, and further named as AC. The working self-standing electrodes (10 mm diameter, mass ~ 5 mg) contained: AC (85 wt.%), conductivity additive (C-ENERGY[®] Super C65, Imerys, 5 wt.%) and polyvinylidene difluoride (PVDF, 10 wt.%) binder. The counter electrodes (also from AC) were oversized in mass (~ 15 mg), in order to be able to accommodate a superior charge capacity. Silver wire quasi reference electrode (AgQRE) was harnessed as commonly indicated in reports on AIL- and PIL- based electrolytes for ECs [197]. In separate 3-electrode cells, with the scan rate of $1 \text{ mV}\cdot\text{s}^{-1}$, the positive vertex potential was gradually increased by 0.1 V steps from 0.5 V vs. AgQRE up to 2.5 V vs. AgQRE, whereas the negative vertex potential was decreased by 0.1 V steps from -0.5 V vs. AgQRE down to -2.0 V vs. AgQRE.

The experiments were carried out with $[\text{HN}_{222}][\text{TFSI}]$, as model PIL electrolyte for application in ECs for comparative purpose, and PILs with N-chloroalkyl functionalized cations characterized by reasonable values of transport properties (see chapter IV, section 2.5.), i.e. $[\text{C}_{2-\text{Cl}}\text{Pyr}][\text{TFSI}]$, $[\text{HN}_{2-\text{Cl}-22}][\text{TFSI}]$, $[\text{HN}_{2-\text{Cl}-11}][\text{TFSI}]$ and $[\text{HN}_{3-\text{Cl}-11}][\text{TFSI}]$. $[\text{C}_{2-\text{Cl}}\text{Pip}][\text{TFSI}]$ and $[\text{C}_{2-\text{Cl}}\text{Morph}][\text{TFSI}]$ which display high viscosity and rather low conductivity were excluded from these experiments. By analogy to the source publication

[164], the S -values obtained from the various CVs differing by 0.1 V potential steps (figures 81 to 85) were calculated according to eq. 40 or eq. 41 and then plotted in figure. 79 and figure. 80. The stability limits (indicated by red vertical lines) were determined based on the statement that the change in difference of S -values between two successive points should not exceed 0.005 ($\Delta_1 - \Delta_2 < 0.005$) and are listed in table 19.

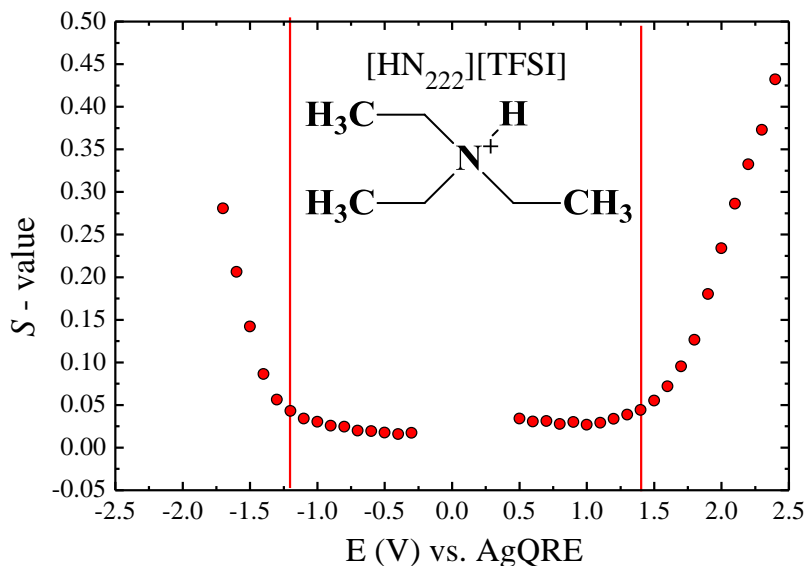


Fig. 79 Plot of S -value vs. vertex potential for $[\text{HN}_{222}][\text{TFSI}]$.

Interestingly, as shown in the S -values vs. vertex potential plot for $[\text{HN}_{222}][\text{TFSI}]$ (Fig. 79), a slight decrease of S -values is observed in the potential range from 0.5 to 1.0 V vs. AgQRE. A similar effect was observed for AILs with the $[\text{TFSI}]^-$ anion, such as $[\text{C}_1\text{C}_3\text{Pyr}][\text{TFSI}]$, $[\text{C}_1\text{C}_2\text{Im}][\text{TFSI}]$ and $[\text{C}_1\text{C}_2\text{Im}][\text{BF}_4]$, [164]. These descending points were attributed to wetting or more precisely “pushing” big $[\text{TFSI}]^-$ anions to micropores. The same effect was observed during positive polarization for $[\text{HN}_{3-\text{Cl}-11}][\text{TFSI}]$, $[\text{C}_{2-\text{Cl}}\text{-Pyrr}][\text{TFSI}]$ and $[\text{HN}_{2-\text{Cl}-22}][\text{TFSI}]$ (Fig. 80). Besides, during negative polarization, with the smaller $[\text{HN}_{222}]^+$ cation, the S -value slightly rises with decrease of vertex potential till it reaches irreversibility of hydrogen sorption/desorption below -1.2 V vs. AgQRE. The same behavior was observed for the four PILs with N-chloroalkyl functionalized cations.

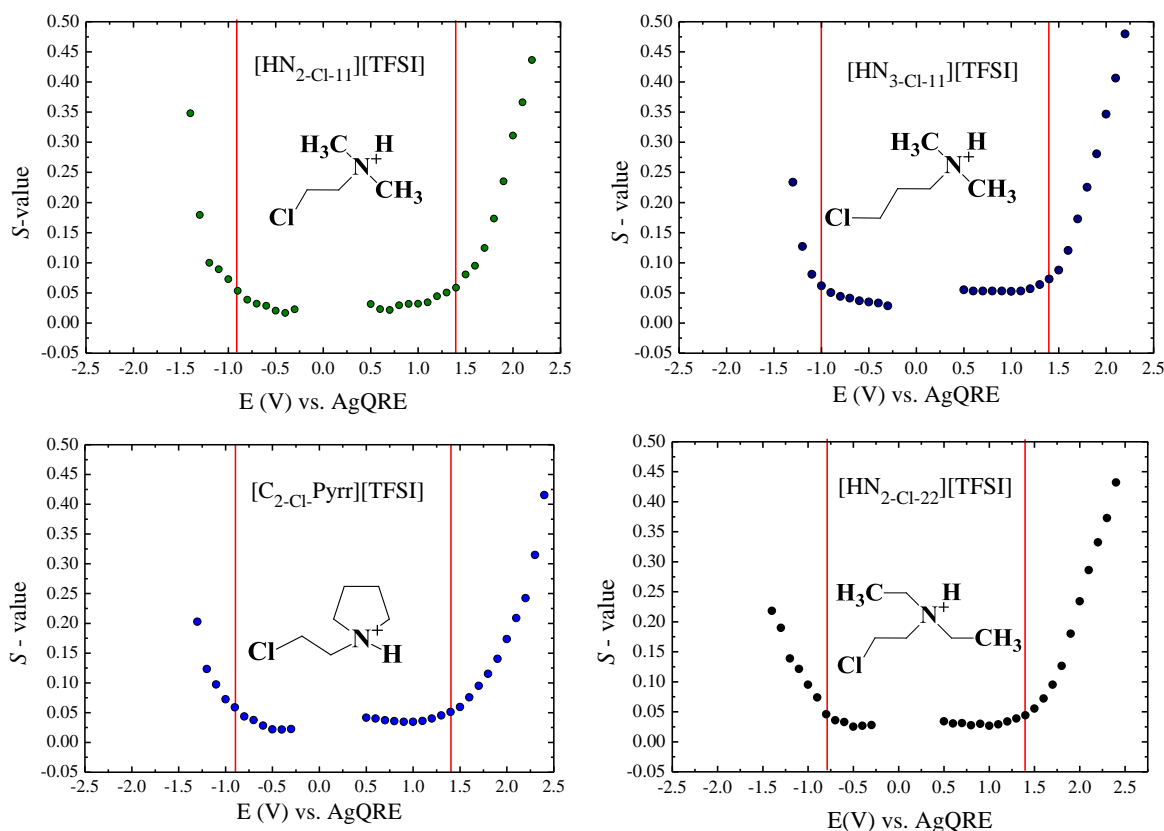


Fig. 80 Plot of S -value vs. vertex potential for the N-chloroalkyl functionalized PILs.

The stability limits of the PILs determined from the plots of S -values and $\Delta_1 - \Delta_2 < 0.005$ criterion, for positive and negative polarization, are indicated in table 19. The anodic limit of all the tested PILs is comparable, ca. 1.4V vs. AgQRE, which roughly correlates with the positive stability limit of 1.4-1.5 V vs. carbon reference electrode detected for AILs and PILs incorporating the $[\text{TFSI}]^-$ anion in the source publication [164]. In turn, $[\text{HN}_{222}][\text{TFSI}]$ has the lowest cathodic stability limit, -1.2 V vs. AgQRE, hence it is the most stable against reduction. In the case of PILs with N-chloroalkyl functionalized cations, the cathodic stability turns out to be restricted. From these investigations, for AC/AC cells with equal mass of electrodes, the highest voltage window is expected for cells using $[\text{HN}_{222}][\text{TFSI}]$ electrolyte, and the lowest for all PILs with 2-chloroethyl substituent in cation: $[\text{C}_{2\text{-Cl-Pyrr}}][\text{TFSI}]$, $[\text{HN}_{2\text{-Cl-11}}][\text{TFSI}]$ and $[\text{HN}_{2\text{-Cl-22}}][\text{TFSI}]$. The negative potential stability values found here are in the range of data given for another protic ionic liquid in ref [164], $[\text{HC}_4\text{Pyrr}][\text{TFSI}]$, using also aluminum current collectors, and are higher than for aprotic ionic liquids where the reduction potentials range from -1.7 to -2.0 V vs. carbon reference electrode (chapter I, section 2.4.3.).

Table 19 Potential limits vs. AgQRE of the PILs on S30-PVDF electrodes for positive (PL_{pos}) and negative (PL_{neg}) polarization.

PIL→ ↓Stability (V) vs. AgQRE	[HN ₂₂₂] [TFSI]	[HN _{3-Cl-11}] [TFSI]	[HN _{2-Cl-11}] [TFSI]	[HN _{2-Cl-22}] [TFSI]	[C _{2-Cl} .Pyrr] [TFSI]
PL_{pos}	1.4	1.4	1.4	1.4	1.4
PL_{neg}	-1.2	-1.0	-0.9	-0.8	-0.9
Potential window	2.6	2.4	2.3	2.2	2.3

The calculated stability limits (Table 19) have formed the basis for further results interpretation. The obtained cyclic voltammograms (CVs) of potential window opening experiments can provide also complementary information on the faradaic phenomena, especially on hydrogen sorption/desorption reversibility. Generally, for the positive sweeps, the CVs are similar for all the discussed PILs, being logically dominated by electroadsorption of the [TFSI]⁻ anion (domain A) followed by increasing, undesired faradaic contribution (domain B), whereas the separation between these two domains is based on the calculated PL_{pos} of PIL (Fig. 81 to Fig. 85):

domain A – includes CVs with quasi rectangular shape (black solid lines) attributed to electrostatic charge accumulation in the EDL;

domain B – with increase of vertex potential, new redox peaks appear around 0.8 V vs. AgQRE in addition to the vertex oxidation peaks. These redox peaks were not observed for AILs with [BF₄]⁻ anion [164], suggesting their correlation with a higher activity of [TFSI]⁻ on aluminum current collectors.

For the negative sweeps, redox processes involving hydrogen electroadsorption occur in addition to EDL charging. As the PILs contained ca. 200 ppm of H₂O, two hydrogen donation mechanisms may contribute to hydrogen chemisorption on carbon: direct through reduction of the protonated cation and, in lesser extent, using hydronium cation as intermediate proton carrier (see chapter III). Nonetheless, the tested PILs fall into two types of cathodic behaviors. The first type, where hydrogen chemisorption and desorption is clearly evidenced in [HN₂₂₂][TFSI] and [HN_{3-Cl-11}][TFSI], results in CVs similar to those already reported for [HN₂₂₂][TFSI] in chapter III. In this case, the CVs keep a rectangular shape typical of EDL charging till a given vertex potential from which the ammonium cation is reduced causing the

evolution of nascent hydrogen further sorbed in the activated carbon. During the anodic scan, the positive peak on the CVs indicates hydrogen desorption from the active material. On the CVs curves recorded during negative sweeps, in these two PILs, three domains can then be distinguished (Figures 81 and 82):

domain C –corresponds to the typical EDL behavior with quasi-rectangular CVs (black solid line) and is limited to the negative vertex potential where hydrogen generation starts as a result of cation (protonated amine) reduction (deprotonation);

domain D – is the region of overpotential (blue solid line) where hydrogen is reversibly chemisorbed in the AC porosity, giving a cathodic current leap followed by a positive hump during the anodic scan;

domain E – where the vertex potential is so low that, beside hydrogen chemisorption, an important part of hydrogen combines into molecular hydrogen (blue dashed line CVs). The border between domains D and E is the PL_{neg} value given in table 19.

Taking into consideration that both $[HN_{222}][TFSI]$ and $[HN_{3-Cl-11}][TFSI]$ contained similar amount of water (≤ 200 ppm of H_2O), the detected disparity between the potentials of hydrogen generation, -0.9 and -0.7 V vs. AgQRE, respectively, seems to be related with the pK_a difference (ΔpK_a) between the two cations. The $[HN_{222}]^+$ cation with $pK_a = 10.21$ (computational value) is a weaker acid than $[HN_{3-Cl-11}]^+$ with $pK_a = 8.68$, meaning that the proton of the later is more available, and consequently its reduction potential is higher.

In contrast, a noticeably different behavior of AC electrodes in the three PILs with 2-chloroethyl substituents tethered on their cations is observed under negative polarization (Fig. 83-Fig. 85). Although the electrodes were negatively polarized even down to -2.0 V vs. AgQRE, hydrogen sorption/desorption was not observed (lack of domain D), and instead a substantial decrease of capacitive current is noticed (rapid flattening of CVs, grey lines). A similar phenomenon was observed by Xu et al. [235] testing organic electrolytes, e.g., $1.0 \text{ mol}\cdot\text{L}^{-1}$ tetraethylphosphonium hexafluorophosphate in 50:50 EC/DMC, and is explained to result from the formation of a passive layer due to electrolyte decomposition on the active sites of carbon, blocking AC micropores, hence decreasing the active surface area.

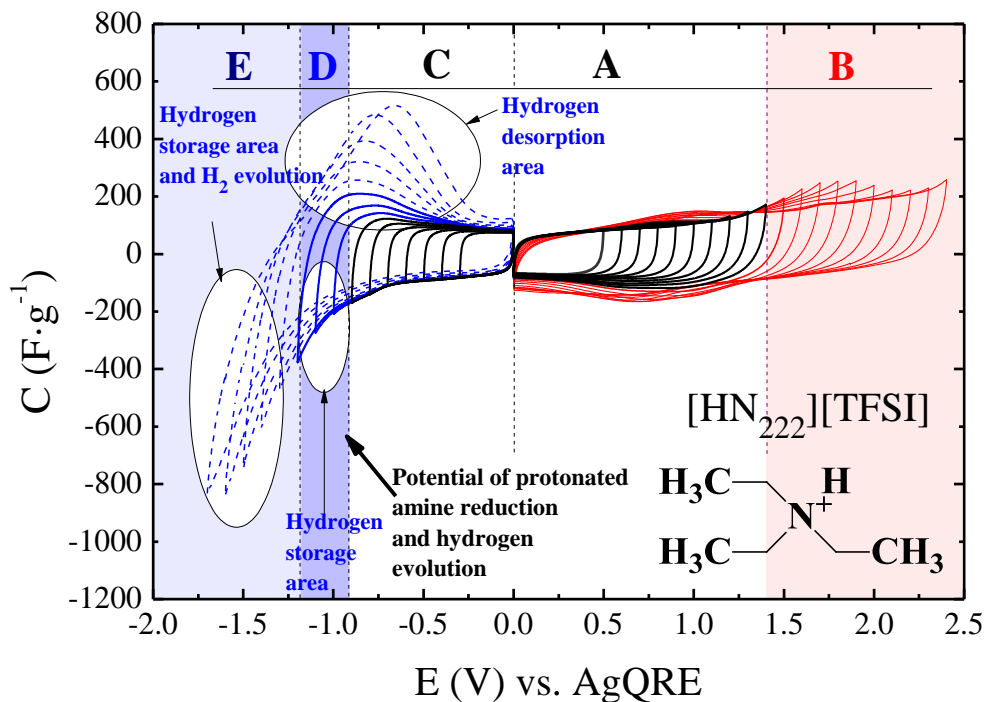


Fig. 81. Cyclic voltammograms ($1 \text{ mV}\cdot\text{s}^{-1}$) of S30-PVDF working electrode in $[\text{HN}_{222}][\text{TFSI}]$ with potential window opening.

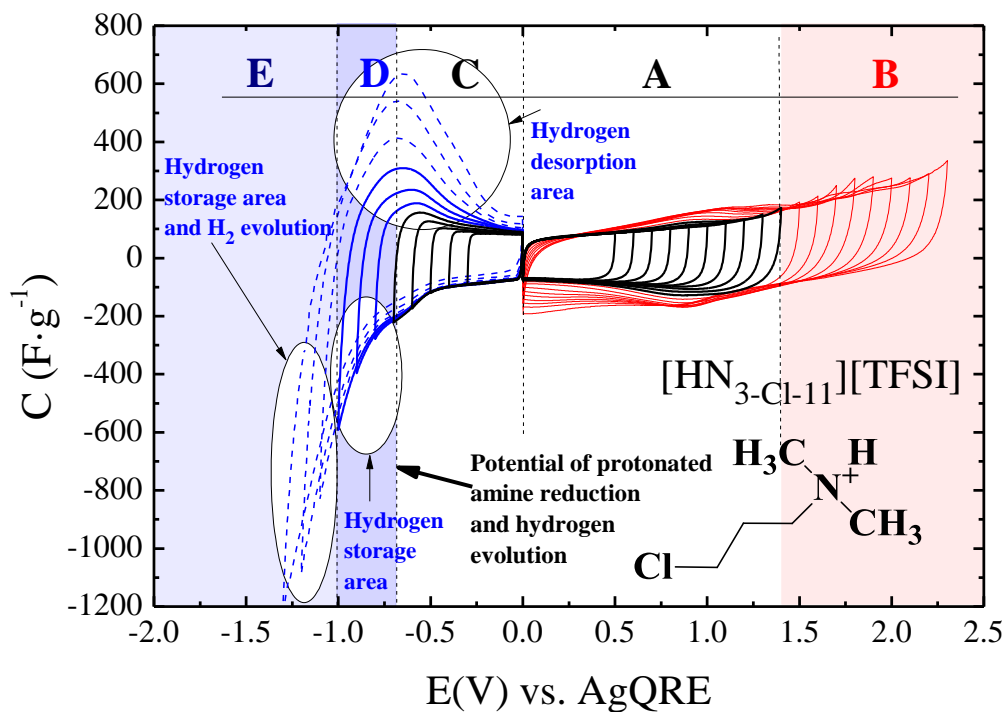


Fig. 82 Cyclic voltammograms ($1 \text{ mV}\cdot\text{s}^{-1}$) of S30-PVDF working electrode in $[\text{HN}_{3-\text{Cl}-11}][\text{TFSI}]$ with potential window opening.

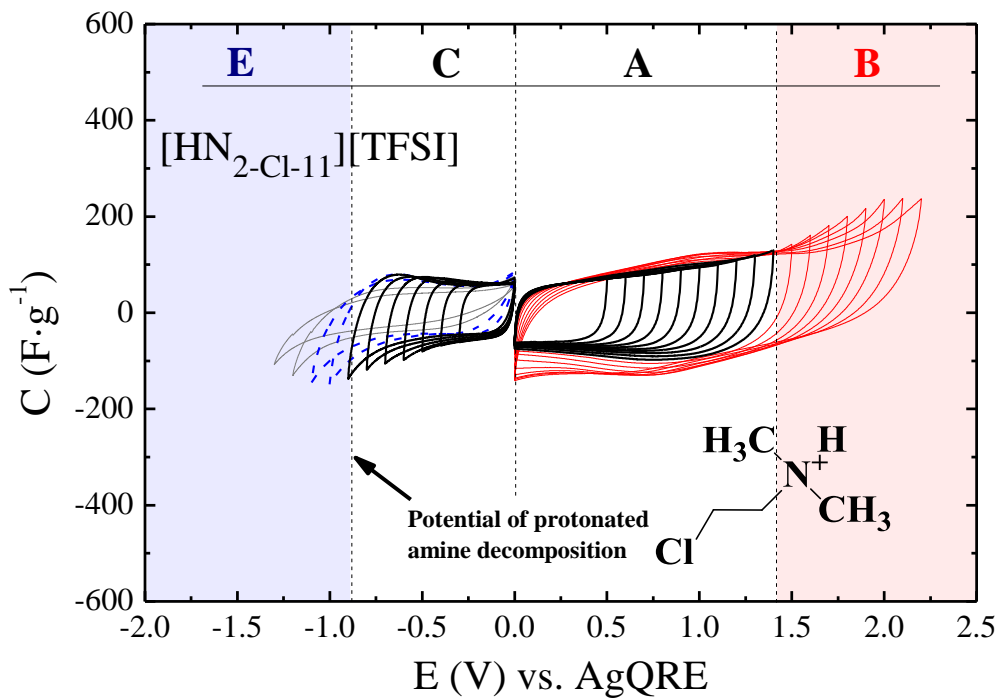


Fig. 83 Cyclic voltammograms ($1 \text{ mV}\cdot\text{s}^{-1}$) of S30-PVDF working electrode in $[\text{HN}_{2-\text{Cl}-11}][\text{TFSI}]$ with potential window opening.

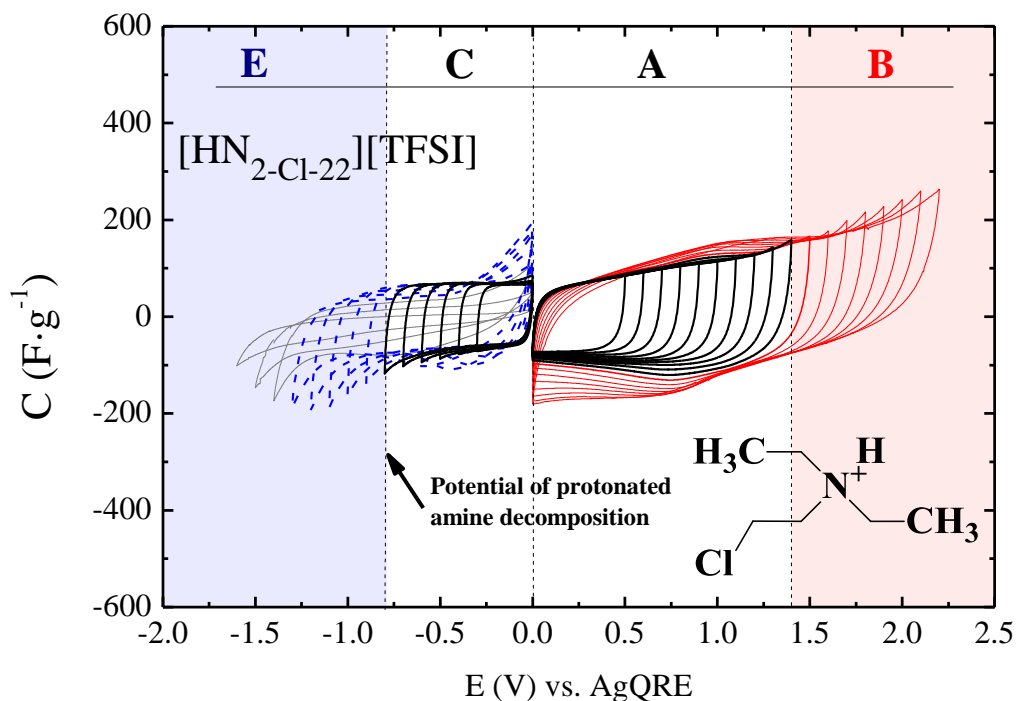


Fig. 84 Cyclic voltammograms ($1 \text{ mV}\cdot\text{s}^{-1}$) of S30-PVDF working electrode in $[\text{HN}_{2-\text{Cl}-22}][\text{TFSI}]$ with potential window opening.

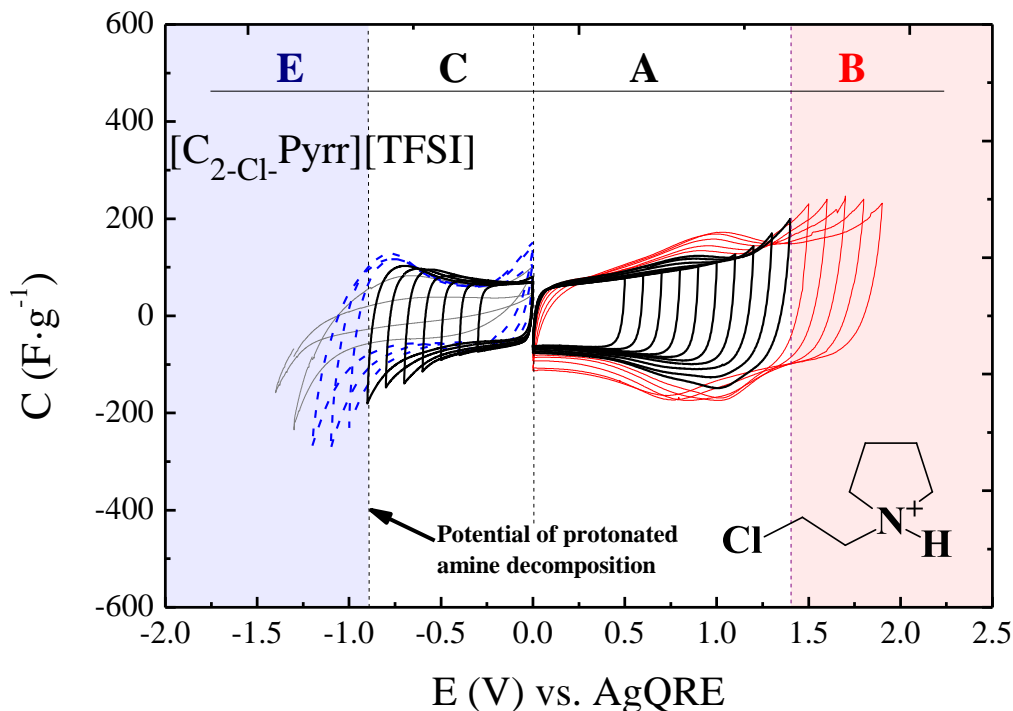


Fig. 85 Cyclic voltammograms ($1 \text{ mV}\cdot\text{s}^{-1}$) of S30-PVDF working electrode in $[\text{C}_{2\text{-Cl}}\text{Pyrr}][\text{TFSI}]$ with potential window opening.

5. Symmetric AC/AC electrochemical capacitors based on N-chloroalkyl functionalized PILs

During charging/discharging of AC/AC cells, the charge stored in the positive and negative electrodes is the same, and can be expressed by the equation 42:

eq. 42

$$m_+ \cdot C_+ \cdot \Delta E_+ = m_- \cdot C_- \cdot \Delta E_-$$

where C_+ , C_- is capacitance, m_+ , m_- mass and ΔE_+ , ΔE_- potential range of positive and negative electrode, respectively. Consequently, the potential range of electrodes during charging/discharging (and their potential extrema) is adapted spontaneously by the system itself, and it cannot be expected that the maximum stability window of the cell, $\Delta E_+ + \Delta E_-$, should be as high as the potential window values reported in table 19. This property is well illustrated by figure 86 showing the results of cyclic voltammetry experiments on AC/AC cells having electrodes of equal mass, and including a reference electrode to monitor the potential excursion of positive and negative electrodes. The voltage of the cells with

N-chloroalkyl functionalized PILs was increased by 100 mV step starting from 1.0 V till the potential of one of the two electrodes approached the stability limit found in table 19.

In case of the cells incorporating PILs with 2-chloroethyl functionalized cations, the minimum potential of the negative electrode reaches the PL_{neg} value (table 19) for a cell voltage of 2.0 V (Fig. 86c-e); beyond this limit, the electrolyte is dramatically decomposed (see section 4). Hence, the voltage of the cells with these three electrolytes is by 200 to 300 mV lower than the potential window measured for an AC electrode (table 19). By contrast, when limiting the voltage to 2 V for the cell containing the PIL with 3-chloropropyl substituent on the cation, the minimum potential of the negative electrode is 200 mV higher than PL_{neg} for this electrolyte (Fig. 86b), suggesting that the symmetric AC/AC cell with $[HN_{3-Cl-11}][TFSI]$ could be operated up to 2.2 V. Similarly, for $[HN_{222}][TFSI]$, which presents some analogies with $[HN_{3-Cl-11}]$ under negative polarization (see Fig. 81 and Fig. 82), the maximum voltage can reach a higher value of 2.5 V (Fig. 86a). Taking into account that, in all cells with N-chloroalkyl functionalized PILs, the maximum potential of the positive electrode is ca. 200 mV lower than the PL_{pos} limit, the voltage could be slightly enhanced by adapting the electrodes mass ratio.

Alike in the tests carried out in 3-electrode cells, the CV profiles of the negative AC electrodes in PILs with 2-chloroethyl substituent tethered on the cation are different from the two other PILs, $[HN_{3-Cl-11}][TFSI]$ and $[HN_{222}][TFSI]$. For the two latter PILs, the OCP (open circuit potential) values are similar (ca. 0 V vs. AgQRE) and the positive electrode displays the characteristic butterfly shape of EDL charging. Higher values of OCP, in the range of 0.25 to 0.30 V vs. AgQRE, are observed when implementing PILs with 2-chloroalkyl functionalized cations.

In summary of this part, the operating potential range of positive electrodes is substantially the same in all the tested PILs, owing to the common $[TFSI]^-$ anion. In case of negative electrodes, differences were observed between PILs with N-chloroethyl and N-chloropropyl functionalized cations. All the former are decomposed at relatively high cathodic potential, whereas $[HN_{3-Cl-11}][TFSI]$ is electroreduced with nascent hydrogen formation and storage in AC. Its analogy of properties with $[HN_{222}][TFSI]$ suggests that, contrary to the case of the N-chloroethyl functionalized PILs, the withdrawing effect of chlorine on the N-H bond is negligible; this assumption is confirmed by the analogy of pK_a values for $[HN_{3-Cl-11}][TFSI]$ and $[HN_{222}][TFSI]$.

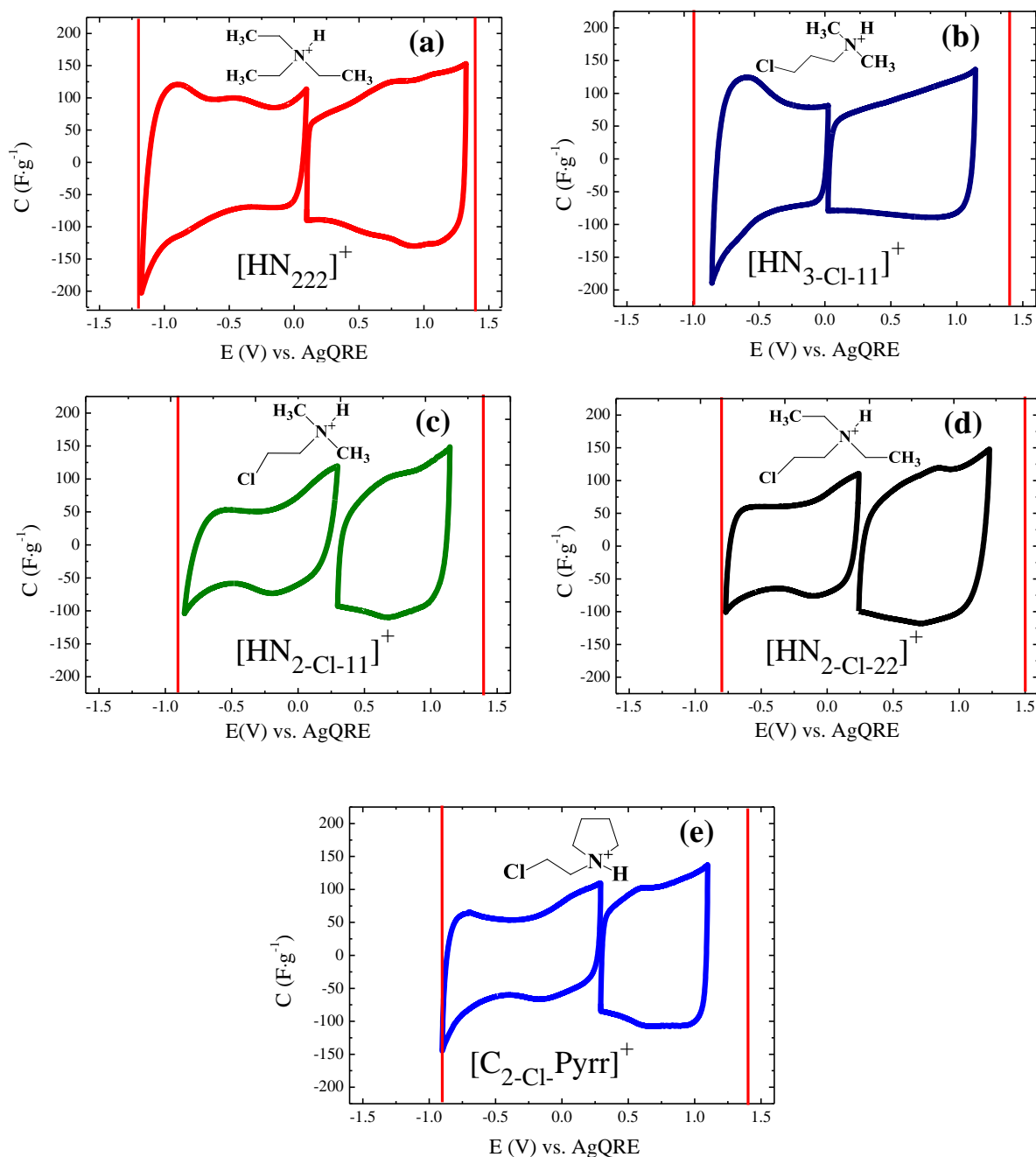


Fig. 86 CVs of electrodes in symmetric AC/AC (S30–PVDF) cells with AgQRE in (a) $[\text{HN}_{222}][\text{TFSI}]$, (b) $[\text{HN}_{3\text{-Cl-11}}][\text{TFSI}]$, (c) $[\text{HN}_{2\text{-Cl-11}}][\text{TFSI}]$, (d) $[\text{HN}_{2\text{-Cl-22}}][\text{TFSI}]$, (e) $[\text{C}_{2\text{-Cl-Pyrr}}][\text{TFSI}]$. The vertical red lines represent the safe stability potentials determined from the S -values and $\Delta_1\text{-}\Delta_2 < 0.005$ criterion [164].

Since the foregoing has evidenced distinctive differences in electrochemical performance of PILs with 2-chlorethyl substituent on the cation, contrasting to $[\text{HN}_{222}][\text{TFSI}]$ and $[\text{HN}_{3\text{-Cl-11}}][\text{TFSI}]$, it is worth visualizing changes on cyclic voltammograms of ECs incorporating the investigated PILs (Fig. 87 and Fig. 88). As seen in figure 87 the CVs of the AC/AC cells in the PILs with 2-chlorethyl substituent on the cation are quite identical. The

relatively fair charge propagation reflects the moderate conductivity of the PILs ([HN_{2-Cl-22}][TFSI] with 1.23 mS·cm⁻¹; [HN_{2-Cl-11}][TFSI] with 1.71 mS·cm⁻¹; [C_{2-Cl}-Pyrr][TFSI] with 1.38 mS·cm⁻¹; chapter IV, section 2.5.2.). The CVs of cells with [HN_{3-Cl-11}][TFSI] and [HN₂₂₂][TFSI] display some visible faradaic contributions at voltages higher than 1 V (Fig. 88). These contributions are obviously related with hydrogen chemisorption/desorption as shown in the voltammograms of AC electrodes in these PILs under negative polarization (Fig. 81, 82 and 86).

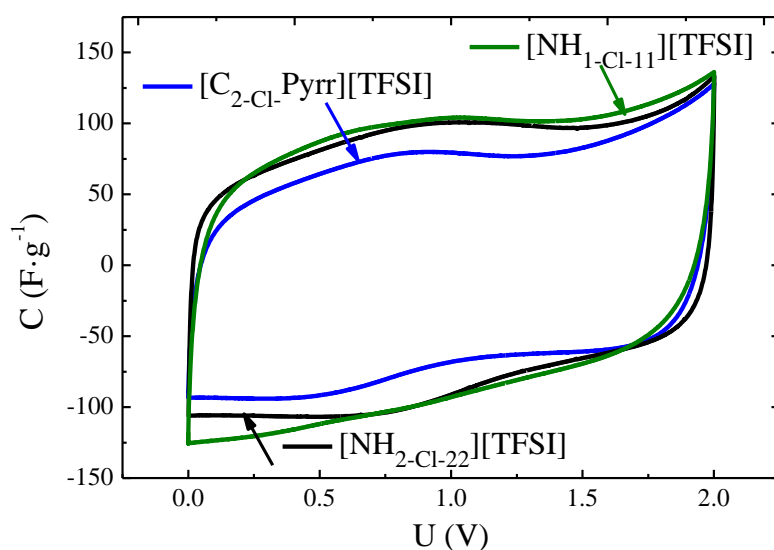


Fig. 87 Cyclic voltammograms (1 mV·s⁻¹) of symmetric AC/AC cells (S30-PVDF electrodes) in 2-chloroalkyl functionalized PILs: [C_{2-Cl}-Pyrr][TFSI] - blue curve; [NH_{2-Cl-22}][TFSI] - black curve; [NH_{2-Cl-11}][TFSI] - green curve.

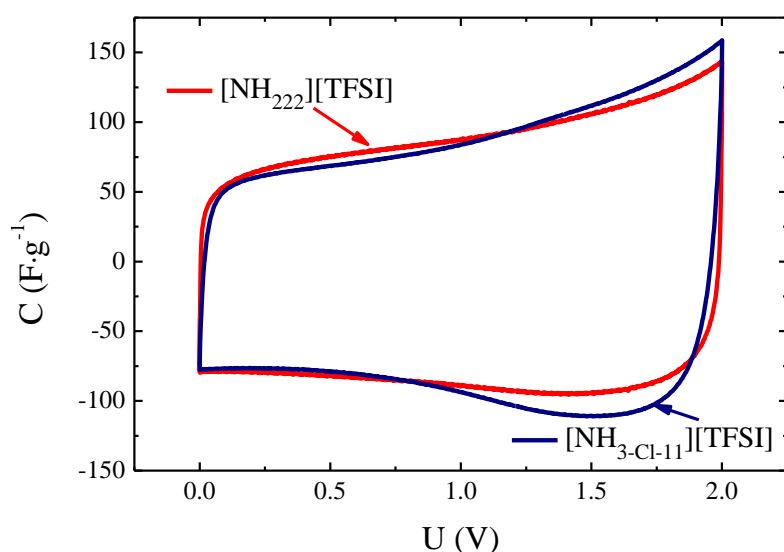


Fig. 88 Cyclic voltammograms (1 mV·s⁻¹) of symmetric AC/AC cells (S30-PVDF electrodes) in [NH₂₂₂][TFSI] - red curve and [NH_{3-Cl-11}][TFSI] - dark blue curve.

The galvanostatic charge/discharge (GC/GD) profiles of AC/AC cells based on the various PILs shown in figures 89 and 90 are consistent with the CVs (Fig. 87 and 88). In the case of ECs incorporating $[\text{HN}_{2\text{-Cl-22}}][\text{TFSI}]$ and $[\text{HN}_{2\text{-Cl-11}}][\text{TFSI}]$ (Fig. 22), the curves are almost superimposed. Likewise, the GC/GD profiles of ECs with $[\text{HN}_{3\text{-Cl-11}}][\text{TFSI}]$ and $[\text{HN}_{222}][\text{TFSI}]$ are similar, both slightly rounded owing to already discussed hydrogen chemisorption/desorption. The ohmic drop is lower for the cell with $[\text{HN}_{222}][\text{TFSI}]$ than with $[\text{HN}_{3\text{-Cl-11}}][\text{TFSI}]$, which is consistent with conductivity values of these PILs, $5 \text{ mS}\cdot\text{cm}^{-1}$ [178] vs. $1.35 \text{ mS}\cdot\text{cm}^{-1}$, respectively.

Since the GC/GD profiles were not linear, the capacitance of ECs based on the tested PILs was evaluated by integration according to ref [204] and by applying equations eq. 32 and 33 as given in chapter III section 3.4 (Table 20). As it could be expected, the highest capacitance values are obtained for ECs with $[\text{HN}_{222}][\text{TFSI}]$ and $[\text{HN}_{3\text{-Cl-11}}][\text{TFSI}]$, $84 \text{ F}\cdot\text{g}^{-1}$ and of $81 \text{ F}\cdot\text{g}^{-1}$, respectively. In case of $[\text{HN}_{2\text{-Cl-22}}][\text{TFSI}]$ and $[\text{HN}_{2\text{-Cl-11}}][\text{TFSI}]$, the values are around $10 \text{ F}\cdot\text{g}^{-1}$ lower, and even significantly lower for $[\text{C}_{2\text{-Cl}}\text{Pyrr}][\text{TFSI}]$ demonstrating its inferior performance.

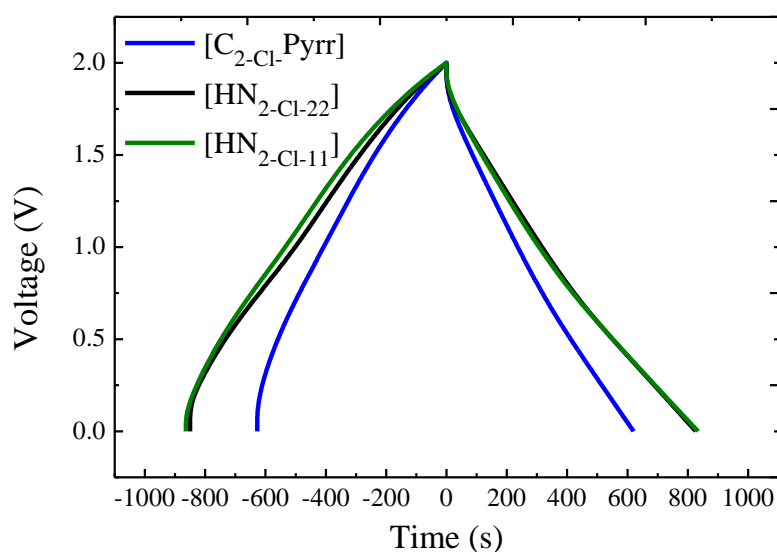


Fig. 89 Galvanostatic ($0.1 \text{ A}\cdot\text{g}^{-1}$) charge/discharge of symmetric cells with S30-PVDF electrodes in 2-chloroalkyl functionalized PILs: $[\text{C}_{2\text{-Cl}}\text{Pyrr}][\text{TFSI}]$ - blue curve; $[\text{HN}_{2\text{-Cl-22}}][\text{TFSI}]$ - black curve; $[\text{HN}_{2\text{-Cl-11}}][\text{TFSI}]$ - green curve.

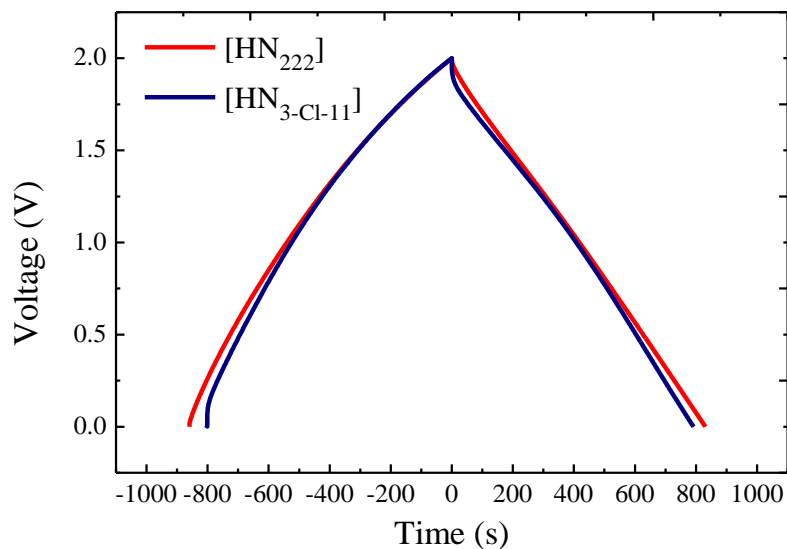


Fig. 90 Galvanostatic ($0.1 \text{ A}\cdot\text{g}^{-1}$) charge/discharge of symmetric cells with S30-PVDF electrodes in $[\text{HN}_{222}][\text{TFSI}]$ – red curve and $[\text{HN}_{3\text{-Cl-11}}][\text{TFSI}]$ - dark blue curve.

Table 20 Capacitance from galvanostatic ($0.1 \text{ A}\cdot\text{g}^{-1}$) discharge calculated from integrated area under the curve.

PIL	$[\text{C}_{2\text{-Cl-Pyrr}}]^+$	$[\text{HN}_{2\text{-Cl-11}}]^+$	$[\text{HN}_{3\text{-Cl-11}}]^+$	$[\text{HN}_{2\text{-Cl-22}}]^+$	$[\text{HN}_{222}]^+$
Capacitance ($\text{F}\cdot\text{g}^{-1}$)	54	72	81	73	84

6. Conclusion

The main objective of this chapter was to determine the safe operation conditions of ECs based on PILs with N-chloroalkyl functionalized cations as electrolytes. The electrochemical stability window of the PILs in presence of the various electrode components was first evaluated. The obtained results corroborated high electrochemical stability of the tested PILs, 4.12 - 5.07 V, on GC working electrode, owing to the $[\text{TFSI}]^-$ anion displaying superior electrochemical stability as compared to oxoacid derived anions. However, the PILs with N-chloroalkyl functionalized cations displayed slightly lower stability than their non-functionalized analogues, which is consistent with the predictions based on computations.

The investigation of electrochemical stability and behavior of these new PILs in contact with stainless steel and aluminum electrodes provided information on the safe potential limits for their employment as current collectors. For both metals, our measurements revealed a decrease of stability in comparison to GC working electrode. In the case of SSt, the

cathodic stability ranged from -1.4 to -1.6 V vs. AgQRE, whereas the anodic one was from 2.0 to 2.3 V vs. AgQRE. Regarding Al, the safe negative potential limit was found to be in a narrow range from -1.5 to -1.6 vs. AgQRE, which is comparable to the indications for SSt. Importantly, during anodic sweeps, aluminum is passivated ca. 1.5 V vs. AgQRE, and is consequently preserved from corrosion and degradation. Owing to its low density and low cost, aluminum is generally considered to be more realistic for application to ECs, thus it was used for our further studies in this chapter.

The determination of stability criteria on porous AC electrodes made it possible to establish safe operational limits for the utilization of PILs with N-chloroalkyl functionalized cations in ECs. The study revealed almost identical operation characteristics for all PILs under positive polarization owing to the common [TFSI]⁻ anion, whereas under negative one the performance of PILs fall into two types of behaviors. The PILs with 2-chloroethyl substituted cation are rapidly decomposed beyond the negative stability limit, whereas the one with [HN_{3-Cl-11}]⁺ cation performed with the contribution of hydrogen electrosorption alike [HN₂₂₂][TFSI]. However, [HN_{3-Cl-11}]⁺ is reduced at higher potential than [HN₂₂₂]⁺, which is logical when considering the respective pK_a values of the two cations.

The comparative analysis of the tested ECs based on N-chloroalkyl functionalized PILs and [HN₂₂₂][TFSI] revealed similar capacitance values for [HN₂₂₂][TFSI] and [HN_{3-Cl-11}][TFSI], which were higher than for [HN_{2-Cl-22}][TFSI] and [HN_{2-Cl-11}][TFSI], whereas [C_{2-Cl}-Pyrr][TFSI] demonstrated noticeably inferior performance. It should be emphasized that hydrogen chemisorption is at the origin of the enhanced capacitance of [HN_{3-Cl-11}][TFSI] alike [HN₂₂₂][TFSI], hence [HN_{3-Cl-11}][TFSI] is considered to be superior among all the PILs with N-chloroalkyl functionalized cations.

General conclusion

Motivated by the demand for high-performance, cost effective and ecofriendly electrochemical capacitors (ECs), protic ionic liquids (PILs) have been considered in this thesis as alternative electrolytes for ECs. They were expected to share the characteristics of aprotic ionic liquids (AILs) such as high electrochemical stability, relatively good conductivity, negligible vapor pressure and low toxicity, while simultaneously, owing to the proton tethered on the positively charged central atom of the cation, to display properties typical of protic (aqueous) medium. Literally, it was expected that PILs would favor reversible redox reactions rising faradaic contributions that will enhance the capacitance of ECs.

Therefore, this dissertation reports the results of research carried out on the formulation and application of PILs as electrolytes for activated carbon (AC) based electrodes and electrochemical capacitors.

Likewise in the development of all kinds of AC-based ECs, to gain the best possible performance of the system, the electrode material needs to be well tuned to the electrolyte. Accordingly, it was proven that a greater capacitance is achieved using ACs with a high ratio of meso-to-micropore volume, which is better adapted for bulky ions of PIL, hence providing higher accessible pore volume and effective surface area for electrical double-layer formation. Besides, it was found that, with electrodes made of xerogel carbon, the cation electroreduction is initiated at higher potential than with activated carbon, while the process itself is more pronounced. In this regard, PILs resemble aqueous electrolytes, where electrosorption was proven to be dependent on AC characteristics.

We demonstrated that water present in small amount in PILs has a considerable influence on their physico- and electrochemical properties. Analogously to AILs, along with an increment of water content in PIL, the viscosity decreases, whereas conductivity increases. In turn, unlike in the case of AILs, the phase transitions of PIL are significantly altered with the increase of water amount, due to interactions between water molecules and ions, especially enhanced hydrogen bonding to the protonated cation, which leads to nanodomains separation and eutectic fraction appearance.

The interactions between protonated cations and electroactive water molecules, enhanced by their mutual affinity, affect significantly the PIL electrochemical behavior. As a result, in dependence on the amount of incorporated water, the performance of AC electrodes in PIL under negative polarization varies. Along with increasing water content in

PIL, the impact of faradaic current related with hydrogen storage increases, whereas the resulting desorption peaks are shifted toward lower potential values, evidencing lower chemisorption energy when hydrogen is stored from moisture containing PIL. Therefore, two kinds of reduction/hydrogen storage mechanisms were reasoned, either involving directly the protonated cations of the dry PIL (< 20 ppm water), which are the only source of protons or, if water is present in larger amount (150 or 1000 ppm), hydronium ions which are formed by reaction of water with the protonated cations. The various electrochemical measurements proved that 150 ppm of H₂O in PIL, typical amount remaining after regular drying of PIL, is an optimal value for diffusion and adsorption of ions. As a result, such PIL provides the highest capacitance together with a good retention at higher frequencies. Higher (>1000 ppm) or lower (<20 ppm) amount of water in PIL is unfavorable, due to the constrained diffusion or limited electrosorption, respectively, both deteriorating ECs operation. Hence, it is postulated that drying PILs more thoroughly than standard (100-200 ppm of H₂O content) is not justified.

Considering the demand for high electrochemical performance, N-chloroalkyl functionalized cations were employed together with bis[(trifluoromethyl)sulfonyl]imide anion, [TFSI]⁻, for the formulation of PILs which are liquid at least at room temperature. Despite effective melting point depression of the PILs with functionalized cations, which T_m is lower than T_m of their non-functionalized analogues, the manipulation in the cation structure resulted in a slight deterioration of the transport properties as well as a decrease of their cathodic stability limit. Hence, adjusting one property of PILs turned out to be realized through compromise with effectiveness of their other physicochemical parameters.

Electrochemical measurements on AC electrodes with the PILs based on N-chloroalkyl functionalized cations revealed a moderate electrochemical stability of all PILs even though they consist of [TFSI]⁻ anion. Whereas [TFSI]⁻ itself contributed to their high anodic stability, comparable with AILs likewise consisting of [TFSI]⁻, their minimal potentials of cathodic excursion were higher, thus stability lower than for AILs. Besides, the comparative analysis of two PILs demonstrating hydrogen electrosorption onto AC revealed that the protonated cation reduction under negative polarization does not only depend on the type of carbon material and amount of water incorporated in PIL but also on the cation pK_a: the weaker acidity of the protonated cation, the lower reduction potential.

In summary, two PILs, triethylammonium [TFSI]⁻ and 3-chloropropyl-dimethylammonium [TFSI], enable the expected proton-dependent activity similar to the aqueous medium, e.g., they are electrochemically reduced with release of nascent hydrogen which is chemisorbed onto AC electrodes, leading to the contribution of faradaic current enhancing capacitance. However, ECs based on PIL with propitious amount of ca. 150 ppm of water require assembling in moisture-free atmosphere, generating similar manufacturing cost to ECs incorporating AIL electrolytes, while the performance of PIL-based ECs is inferior to their AIL counterpart in terms of specific energy and power. Therefore, at this stage of the research, it might be concluded that the application of PILs as electrolytes for ECs is not substantiated by their operation characteristics, no more than by economic reasons. However, taking into account that PILs incorporating the [TFSI]⁻ anion display low vapor pressure and high thermal stability as well as their electrochemical stability window is wider than aqueous electrolytes, they could still remain an interesting medium for ECs at elevated temperatures, which are unworkable for aqueous medium.

Hence, knowing that the weak point of PILs as electrolytes for ECs is their limited cathodic stability, the negative electrode performance needs to be controlled. A prospective strategy could be the realization of a hybrid system understood as employing a negative AC electrode grafted with electroactive molecules which display redox activity at potentials slightly higher than the reduction potential of the PILs. Thus, the potential excursion of the negative electrode would be blocked, and it would be preserved from irreversible hydrogen evolution. As a result of the high capacity of the battery-like negative electrode, the potential excursion of the positive electrode would be extended to higher potentials which are still affordable by the [TFSI]⁻ anions.

Annex

1. Abbreviations and symbols

1.1. Abbreviations

2D-NLDFT – two dimensional nonlinear density functional theory

AC – activated carbon

ACC – activated carbon cloth

ACFs – activated carbons fabrics

ACN – acetonitrile

AgQRE – silver-wire *quasi* reference electrode

AILs – aprotic ionic liquids

Al – aluminum

BET – Brunauer-Emmett-Teller

CBs – carbon blacks

CDCs – carbide derived carbons

CE – counter electrode

CMC – carboxymethyl cellulose

CNTs – carbon nanotubes

COSMO-RS – Conductor-like screening model for real solvent

CV – cyclic voltammetry or cyclic voltammogram

DFT – density functional theory

DMC – dimethyl carbonate

E_{AL} – potential of stability limit of compound toward oxidation

E_{CL} – potential of stability limit of compound toward reduction

EC – ethylene carbonate

ECPs – electrically conducting polymers

ECs – electrochemical capacitors

EDL – electrical double-layer

EDLCs – electrical double-layer capacitors

EIS – electrochemical impedance spectroscopy

EQCM – electrochemical quartz crystal microbalance

ESR – equivalent series resistance

EVs – electric vehicles

EW – electrochemical window

Fc/Fc⁺ – ferrocene/ferrocenium redox couple

GC – glassy carbon

GC/GD – galvanostatic charge/discharge

HEVs – hybrid electric vehicles

HOMO – highest occupied molecular orbital

IHP – inner Helmholtz plane

ILs – ionic liquids

IUPAC – International Union of Pure and Applied Chemistry

L₀ – average pore size

L_{0micro} – average micropore size

LIBs – lithium-ion batteries

LUMO – lowest unoccupied molecular orbital

MWNTs – multi-walled nanotubes

NEC – Nippon Electric Company

NMR – nuclear magnetic resonance

OCP – open circuit potential

OHP – outer Helmholtz plane

OLCs – onion like carbons

PAN – poly(acrylonitrile)

PANI – polyaniline

PC – propylene carbonate

PEDOT – poly[3,4-ethylenedioxythiophene]
PILs – protic ionic liquids
PL_{neg} – negative safe potential limit determined by the method developed in reference (3).
PL_{pos} – positive safe potential limit determined by the method developed in reference (3).
PMT – poly[3-methylthiophene]
PPy – polypyrrole
PSD – pore size distribution
PtQRE – platinum-wire *quasi* reference electrode
PT – polythiophene
PTFE – polytetrafluoroethylene
PVDC – polyvinylidene chloride
PVDF – polyvinylidene fluoride
RE – reference electrode
RTILs – room temperature ionic liquids
S_{BET} – specific surface area calculated based on BET model
S_{DFT} – total specific surface area calculated based on DFT model
SBR – styrene-butadiene rubber
SOHIO – Standard Oil Company of Ohio
SSA – specific surface area
SSt – stainless steel
SWNTs – single-walled nanotubes
WE – working electrode
VTF – Vogel–Tammann–Fulcher
ZILs – zwitterionic liquids
*V_{meso} – cumulative pore volume of mesopores by 2D-NLDFT method
*V_{micro} – cumulative pore volume of micropores by 2D-NLDFT method
*V_{total} – total pore volume by 2D-NLDFT method

1.2. Abbreviations and Symbols in Equations

A – surface area

B – constant; incorporated in $B_{\eta}R$, $B'_{\eta}R$ or $B'_{\sigma}R$ (where R stands for the molar gas constant) is referred to as pseudo-activation energy corresponding to the activation energy ($E_{a\eta}$ or $E_{a\sigma}$, respectively)

C – capacitance

C_{+} – capacitance of positive electrode

C_{-} – capacitance of negative electrode

C_{dl} – EDL capacitance

C_{diff} – capacitance of the diffusion region

C_H – Helmholtz (compact) double-layer capacitance

E – specific energy

E_a – activation energy for viscous flow or electrical conduction

$E_{int/D}$ – discharge energy

$E_{S,int/D}$ – specific energy ($W \cdot kg^{-1}$) calculated from $E_{int/D}$

M_R – molar refractivity

M_w – molecular weight

P – specific power

$P_{S,int/D}$ – specific power ($Wh \cdot kg^{-1}$) calculated from $E_{S,int/D}$

R – gas constant ($8.314 J \cdot K \cdot mol^{-1}$)

R_f – resistance to faradaic current at the electrode surface also called charge transfer resistance

R_S – equivalent series resistance

T – temperature

T_0 – temperature at which the conductivity or viscosity goes to zero ideal or glass transition temperature

T_c – crystallization temperature

T_{cc} – cold crystallization temperature

T_e – eutectic temperature

T_g – glass transition temperature

T_m – melting temperature

U – cell voltage

U_{min} , U_{max} – minimum and maximum cell voltage

V_m – molar volume

d – distance

f – frequency

m_+ – mass of positive electrode

m_- – mass of negative electrode

m_{act} – average mass of active material in one electrode

n – refractive index

t_{dis} – discharge time

Λ – molar conductivity

ΔH_c – Crystallization Enthalpy

ΔH_{cc} – Cold Crystallization Enthalpy

ΔH_m – Melting Enthalpy

Ψ_0 – potential at the electrode surface

Ψ – potential at the electrode/electrolyte interface

ε_r – relative permittivity

ε_0 – vacuum permittivity

η – viscosity

η_0 – maximum viscosity (at infinite temperature)

ρ – density

σ – specific conductivity

σ_0 – maximum electrical conductivity (at infinite temperature)

γ – surface tension

Anions

$[\text{AlCl}_4]^-$, $[\text{Al}_2\text{Cl}_7]^-$ – chloroaluminates

$[\text{AsF}_6]^-$ – hexafluoroarsenate

$[\text{B}(\text{CN})_4]^-$ – tetracyanoborate

$[\text{BETI}]^- = [(\text{C}_2\text{F}_5\text{SO}_2)_2\text{N}]^-$ – bis(perfluoroethylsulfonyl)imide

$[\text{BF}_3\text{C}_2\text{F}_5]^-$ – perfluoroalkyltrifluoroborate

$[\text{BF}_4]^-$ – tetrafluoroborate

$[\text{B}(\text{CN})_4]^-$ – tetracyanoborate

$[\text{Br}]^-$ – bromide

$[\text{CF}_3\text{CO}_2]^-$ – trifluoroacetate

$[\text{CF}_3\text{SO}_3]^-$ – trifluoromethanesulfonate

$[\text{CH}_3\text{COO}]^-$ – acetate

$[\text{CH}_3\text{SO}_3]^-$ – methane sulfonate

$[\text{COO}]^-$ – formate

$[\text{C}_2\text{H}_5\text{OSO}_3]^-$ – ethylsulphate

$[\text{C}_3\text{F}_7\text{CO}_2]^-$ – heptafluorobutyrate

$[\text{Cl}]^-$ – chloride

$[\text{F}]^-$ – fluoride

$[\text{FAP}]^-$ - tris(pentafluoroethyl)trifluorophosphate

$[\text{FSI}]^-$ – bis(fluorosulfonyl)imide

$[\text{FTFSI}]^-$ – fluorosulfonyl-(trifluoromethanesulfonyl)imide

$[\text{HSO}_4]^-$ – hydrogensulfate

$[\text{I}]^-$ – iodide

$[\text{IO}_3]^-$ – iodate

$[\text{N}(\text{CN})_2]^-$ – dicyanamide

$[\text{N}(\text{CN})_4]^-$ – tetracyanamide

$[\text{NO}_2]^-$ – nitrite

$[\text{NO}_3]^-$ – nitrate

$[\text{PF}_6]^-$ – hexafluorophosphate

$[\text{SO}_4^{2-}]^-$ – sulfate

$[\text{TFSI}]^- = [\text{TfSA}]^- = [\text{NTf}_2]^- = [\text{N}(\text{CF}_3\text{SO}_2)_2]^-$ – bis[(trifluoromethyl)sulfonyl]imide

Cations

Aprotic

$[\text{C}_{1(201)}\text{Pyr}]^+ = [\text{Pyr}_{1(201)}]^+$ – N-methyl-N-(2-methoxyethyl)pyrrolidinium

$[\text{C}_{13}\text{Pyr}]^+ = [\text{Pyr}_{13}]^+$ – 1-methyl-1-propylpyrrolidinium

$[\text{C}_{14}\text{Azp}]^+ = [\text{Azep}_{14}]^+$ – N-butyl-N-methylazepanium

$[\text{C}_{14}\text{Pyr}]^+ = [\text{Pyr}_{14}]^+$ – 1-methyl-1-butylpyrrolidinium

$[\text{C}_{16}\text{Azep}]^+ = [\text{Azep}_{16}]^+$ – N-hexyl-N-methylazepanium

$[\text{C}_1\text{C}_2\text{C}_4\text{Tr}]^+$ – 1,2,4-triazolium

$[\text{C}_2\text{C}_1\text{Im}]^+ = [\text{Im}_{12}]^+ = [\text{EMIm}]^+ = [\text{MeEtIm}]^+$ – 1-ethyl-3-methylimidazolium

$[\text{C}_4\text{C}_1\text{Im}]^+ = [\text{Im}_{14}]^+ = [\text{BMIm}]^+$ – 1-butyl-3-methylimidazolium

$[\text{N}_{1111}]^+ = [(\text{C}_1\text{H}_3)_4\text{N}]^+$ – tetramethylammonium

$[\text{N}_{1113}]^+ = [(\text{C}_1\text{H}_3)_3\text{N}(\text{C}_3\text{H}_9)]^+$ – trimethylpropylammonium

$[\text{N}_{2221}]^+ = [(\text{C}_2\text{H}_5)_3\text{N}(\text{CH}_3)]^+$ – triethylmethylammonium

$[\text{N}_{221(201)}]^+ = [(\text{C}_2\text{H}_5)_2(\text{CH}_3)\text{N}(\text{C}_2\text{H}_5\text{OCH}_3)]^+$ – N,N-diethyl-N-methyl-N-(2-methoxyethyl)ammonium

$[\text{N}_{3333}]^+ = [(\text{C}_3\text{H}_7)_4\text{N}]^+$ – tetrapropylammonium

$[\text{N}_{4444}]^+ = [(\text{C}_4\text{H}_9)_4\text{N}]^+$ – tetrabutylammonium

$[\text{N}_{5555}]^+ = [(\text{C}_5\text{H}_{11})_4\text{N}]^+$ – tetrapentylammonium

$[\text{N}_{6662}]^+ = [(\text{C}_6\text{H}_{13})_3\text{N}(\text{C}_2\text{H}_5)]^+$ – trihexylethylammonium

$[\text{N}_{6666}]^+ = [(\text{C}_6\text{H}_{13})_4\text{N}]^+$ – tetrahexylammonium

$[\text{N}_{8444}]^+ = [(\text{C}_4\text{H}_9)_3\text{N}(\text{C}_8\text{H}_{17})]^+ - \text{octyltributylammonium}$

$[\text{N}_{8888}]^+ = [(\text{C}_8\text{H}_{17})_4\text{N}]^+ - \text{tetraoctylammonium}$

$[\text{N}_{\text{RRRR}}]^+ = \text{alkylammonium cation}$

$[\text{P}_{666,14}]^+ = [(\text{C}_6\text{H}_{13})_3\text{P}(\text{C}_{14}\text{H}_{29})]^- - \text{trihexyltetradecylphosphonium}$

$[\text{P}_{666,\text{R-O-1}}]^+ = [(\text{C}_6\text{H}_{13})_3\text{P}(\text{ROCH}_2)]^{+-} - \text{alkoxymethyltrihexylphosphonium}$

$[\text{TEA}]^+ = [(\text{C}_2\text{H}_5)_4\text{N}]^+ = [\text{Et}_4\text{N}]^+ = [\text{N}_{2222}]^+ - \text{tetraethylammonium}$

Protic

$[\text{C}_2\text{Im}]^+ = [\text{HEIm}]^+ - \text{1-ethylimidazolium}$

$[\text{C}_2\text{Morph}]^+ - \text{4-ethylmorpholinium}$

$[\text{C}_{2-\text{Cl}}\text{Morph}]^+ - \text{4-(2-chloroethyl)morpholinium}$

$[\text{C}_2\text{Pip}]^+ - \text{1-ethylpiperidinium,}$

$[\text{C}_{2-\text{Cl}}\text{Pip}]^+ - \text{1-(2-chloroethyl)piperidinium}$

$[\text{C}_{2-\text{Cl}}\text{Pyrr}]^+ - \text{1-(2-chloroethyl)pyrrolidinium}$

$[\text{C}_4\text{Im}]^+ = [\text{HBIm}]^+ - \text{1-butylimidazolium}$

$[\text{DIPEA}]^+ - \text{diisopropylethylammonium}$

$[\text{HN}_{111}]^+ = [(\text{C}_1\text{H}_3)_3\text{NH}]^+ - \text{trimethylammonium}$

$[\text{HN}_{122}]^+ = [(\text{C}_2\text{H}_5)_2\text{NH}(\text{C}_1\text{H}_3)]^+ - \text{diethylmethylammonium}$

$[\text{HN}_{211}]^+ - \text{ethyl dimethylammonium}$

$[\text{HN}_{222}]^+ = [(\text{C}_2\text{H}_5)_3\text{NH}]^+ - \text{triethylammonium}$

$[\text{HN}_{2-\text{Cl-11}}]^+ - \text{(2-chloroethyl)dimethylammonium}$

$[\text{HN}_{2-\text{Cl-22}}]^+ - \text{(2-chloroethyl)diethylammonium}$

$[\text{HN}_{3-\text{Cl-11}}]^+ - \text{(3-chloropropyl)dimethylammonium}$

$[\text{HP}_{444}]^+ = [(\text{C}_4\text{H}_9)_3\text{PH}]^+ = \text{tributylphosphonium}$

$[\text{Im}]^+ - \text{imidazolium}$

$[\text{Pyrr}]^+ - \text{pyrrolidinium}$

2. Reagents, chemicals and carbons

The following reagents were utilized for the synthesis of ionic liquids:

- 4-(2-chloroethyl)morpholine hydrochloride (99%), Sigma Aldrich;
- 1-(2-chloroethyl)piperidine hydrochloride (98%), Sigma Aldrich;
- 1-(2-chloroethyl)pyrrolidine hydrochloride (98%); Sigma Aldrich;
- 2-chloro-N,N-diethylethylamine hydrochloride (99%), Sigma Aldrich;
- 2-chloro-N,N-dimethylethylamine hydrochloride (99%), Sigma Aldrich;
- 3-dimethylamino-1-propyl chloride hydrochloride (96%) Sigma Aldrich;
- triethylamine hydrochloride ($\geq 99\%$), Sigma Aldrich;
- hydrochloric acid (35-38% water solution, pure p. a.), POCH;
- toluene (99,5%, pure p. a.), POCH;
- lithium bis[(trifluoromethyl)sulfonyl]imide, Fluorad HQ-115 from 3M™.

All reagents were used without further purification.

The following chemicals were utilized for electrode preparation:

- ethanol (96%, pure p. a.), POCH;
- polytetrafluoroethylene - PTFE- (60 wt % dispersion in H₂O), Sigma Aldrich;
- poly(vinylidene fluoride - PVDF - Kynar HSV900, Arkema, France.

Carbons:

- AX 2000 – xerogel templated carbon synthesized according to the procedure described in reference (4).

Thanks to Dr A. Arenillas and Dr J.A. Menéndez from Instituto Nacional del Carbón, CSIC, Oviedo, Spain for providing the xerogel carbon AX2000.

- BP 2000 – carbon black, Cabot;
- C-ENERGY® Super C65 – conductive carbon black Imerys
- S30 –activated carbon SUPRA 30 for electrochemical capacitors, Cabot;

Other components:

- pretreated aluminium foil, Blue Solutions, France.

*I would like to acknowledge the companies **Blue Solutions**, **Arkema**, **Imerys**, **Cabot**, for kindly supplying the materials used during this thesis.*

3. Preparation of PILs

Triethylammonium hydrochloride, $[\text{HN}_{222}][\text{Cl}]$, was synthesized through a proton transfer between HCl (Brønsted acid, 0.1 mol) and triethylamine (Brønsted base, 0.11 mol). Since the neutralization reaction is highly exothermic, to avoid local overheating and to better distribute the released heat, the amine was dissolved in 150 mL of toluene and cooled down to 0 °C. Then, 0.1 mol of hydrochloric acid (water solution in dropping funnel) was gradually added to the amine solution under stirring. Later, stirring was continued for 4 hours, while temperature of the mixture gradually equalized to ambient temperature. Triethylammonium hydrochloride remaining in the water phase was separated from toluene, and purified by rinsing with small aliquots of fresh toluene to remove unreacted amine if present. The remaining water and residual toluene were evaporated under reduced pressure using rotary evaporator, and $[\text{HN}_{222}][\text{Cl}]$ dried under reduced pressure overnight at 80 °C in a vacuum dryer – Büchi Glass Oven B-585.

All the PILs with N-chloroalkyl functionalized cations and $[\text{TFSI}]$ anion, and the representative non-functionalized analogue, $[\text{HN}_{222}][\text{TFSI}]$, were synthesized in a simple metathesis reaction involving the replacement of chlorine anion by the $[\text{TFSI}]^-$ one. The relevant hydrochloride (0.2 mol) was dissolved in 20 mL of water. In a separate vessel, an equimolar amount of $[\text{Li}][\text{TFSI}]$ (0.2 mol) was dissolved in 30 mL of water. The two solutions were mixed together in a beaker and stirred for 1 hour at room temperature. The obtained PILs were isolated from the aqueous solution as a second (bottom) phase using a separation funnel. Afterwards, the lithium chloride byproduct and residual unreacted starting materials were eliminated by rinsing a few times with small aliquots of water until the test with silver nitrate did not reveal the presence of chlorides. Finally, the synthesized PILs were dried at 80 °C under reduced pressure of 100 mPa for 24 h in a vacuum dryer – Büchi Glass Oven B-585.

4. Characterization of PILs

4.1. Nuclear magnetic resonance spectroscopy (NMR)

The NMR analyses were performed in Środowiskowe Laboratorium Unikalnej Aparatury Chemicznej at Adam Mickiewicz University, Poznań. All the PILs were identified by ^1H , ^{13}C and ^{19}F NMR using Varian VNMRS spectrometer (402.64 MHz for ^1H , 378.82

MHz for ^{19}F and 101.25 MHz for ^{13}C NMR) and DMSO-*d*6 as solvent. The ^1H NMR and ^{19}F NMR data were reported as follows in ppm, from the internal standard (TMS, 0.0 ppm and CFCl_3 , 0.0 ppm respectively); chemical shift (multiplicity, coupling constant recorded in Hz, integration). The ^{13}C chemical shifts are referenced to the middle signal of the solvent (δ 39.50 ppm).

4.2. Karl-Fischer titration

Dried PILs were examined with Karl Fisher titration using 831 KF Coulometer by Metrohm in order to determine their water content. Averagely, 1 mL of product was injected into the measurement vessel for analysis. Each IL was subjected to triplicate measurement in order to obtain reliable results.

4.3. Physicochemical properties

The thermal stability of the PILs was measured by thermogravimetric analysis (TGA) with nitrogen as shielding gas using TGA / DSC 1 (Mettler Toledo). The samples were heated from 30 to 450 °C at a rate of 10 °C/min. The maximum stability temperature of the PILs was determined as the onset temperature corresponding to 5 wt. % mass loss ($T_{5\% \text{onset}}$).

The DSC measurements presented in chapter III, section 2.1., were performed with NETZSCH DSC 204 F1 Phoenix using IntraCooler. Firstly, the sample was heated from 25 to 100 °C, then cooled from 100 to -50 °C and again heated to 100 °C, all at a rate of 10 °C min⁻¹.

The study on phase transitions presented in chapter IV, section 2.4.1., was performed with DSC1 by Mettler Toledo, coupled with intracooler Huber TC 125-MT. The samples were heated from 25 to 100 °C, and then cooled down to -100 °C and finally heated to 100 °C at a rate of 10 °C min⁻¹.

A densimeter DDM 2911 (Rudolph Research Analytical) was used to measure the density (ρ) with $\pm 0.00002 \text{ g}\cdot\text{cm}^{-3}$ accuracy in a temperature range from 20 to 90 °C ± 0.02 °C.

The refractive index (n_D) was measured with accuracy of ± 0.00005 at atmospheric conditions in the temperature range from 20 to 90 °C ± 0.02 °C using a J357 Automatic Refractometer (Rudolph Research Analytical).

The surface tension (γ) was measured at room temperature by the platinum ring method using a Lauda tensiometer (Germany); all measurements were repeated at least twice.

The viscosity values presented in chapter III were measured from 10 °C to 80 °C (± 0.02 °C) using a Lovis 2000M/ME Anton Parr rolling-ball viscometer. The values of dynamic viscosity were calculated by taking into account the effect of sample density and ball buoyancy as a function of temperature; the uncertainty was less than 1%.

In chapter IV, the dynamic viscosity (η) was determined in a temperature range from 20 to 80 °C ± 0.01 °C at an operating speed of 500 rad s⁻¹ using a rotational rheometer AR 1000 (TA Instruments) with a conical geometry coupled with an integrated thermostat; the uncertainty on viscosity did not exceed ± 0.01 Pa·s.

The conductivity values presented in chapter III were measured from -10 to 80 °C ± 0.5 °C on a Crison (GLP 31) digital multifrequency conductimeter. The temperature was maintained by a JULABO F25 thermostated bath. The instrument was calibrated with KCl standard solutions (0.1 and 0.01 mol·L⁻¹); the uncertainty for the conductivity values did not exceed 2%. Each value was recorded when the stability was superior to 1% within 2 min.

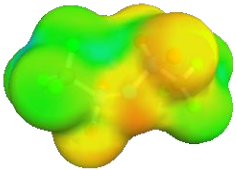
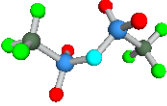
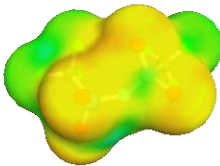
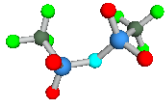
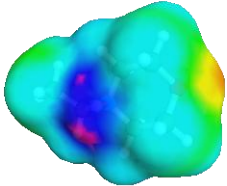
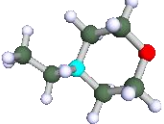
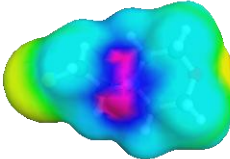
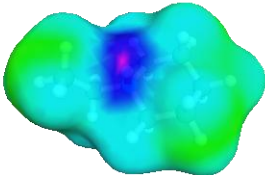
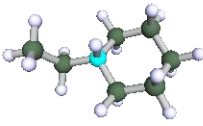
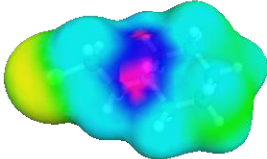
In chapter IV, the conductivity (σ) was determined at temperatures from 20 to 100 °C ± 0.5 °C on an electrode/electrolyte/electrode system assembled in a glove box under argon atmosphere, using electrochemical impedance spectroscopy (EIS, VMP3, Biologic); the frequency range was 500 kHz - 1 Hz and the amplitude of ± 5 mV; a 0.1 mol·L⁻¹ KCl solution was used to calibrate the cell. The resistance values (R) were determined from the intersection of the Nyquist plot with the real axis (Z'), and the conductivity was calculated according to the equation: $\sigma = l/RA$ where l is the distance between the two electrodes in the cell and A is the surface area of the electrodes.

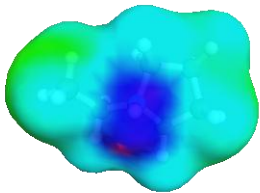
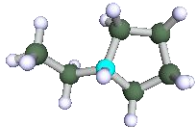
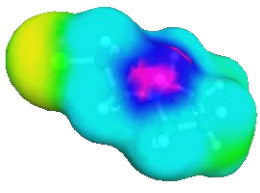
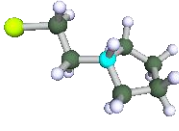
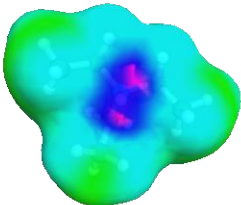
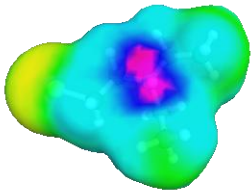
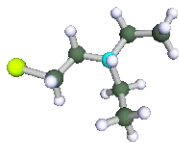
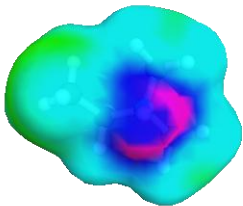
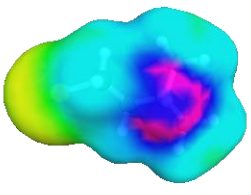
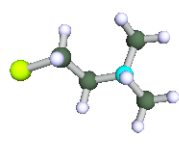
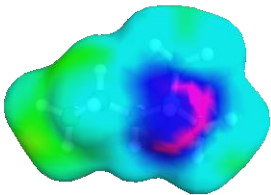
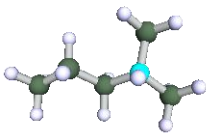
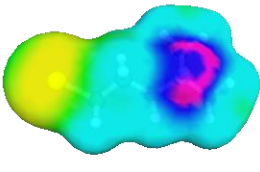
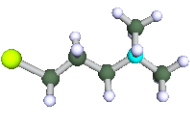
4.4. Computational methods

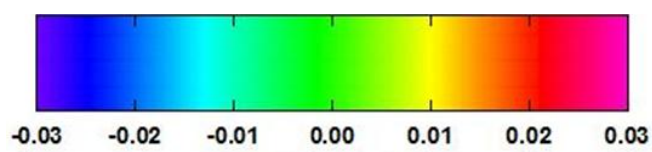
Computational methods were utilized to expound the differences in structure, charge distribution and volume between the various chloroalkyl functionalized cations, as well as between their non-chlorinated analogues (considered here as reference compounds with a simplified structure making possible to determine and describe the impact of chlorine), as previously presented in ref [200, 243]. Firstly, each structure was optimized using the density functional theory (DFT Gaussian version 3.0 utilizing the B3LYP (Becke, 3-parameter, Lee-Yang-Parr) method and the DGTZVP (DGauss triple zeta valence polarization) basic set. The optimized structure of each ion was then input for the generation of the COSMO file within the Turbomole program, using the BP-DFT (Becke-Perdew-density

functional theory) method and the Ahlrichs-TZVP (Triple Zeta Valence Plus Polarization) basic set [244]. The COSMO volume and the sigma profile of each ion were then generated by using COSMO-RS (Conductor-like Screening Model for Real Solvent) methodology within the COSMOTermX program (version 2.1, release 01.08) (Table A1 and Fig A1).

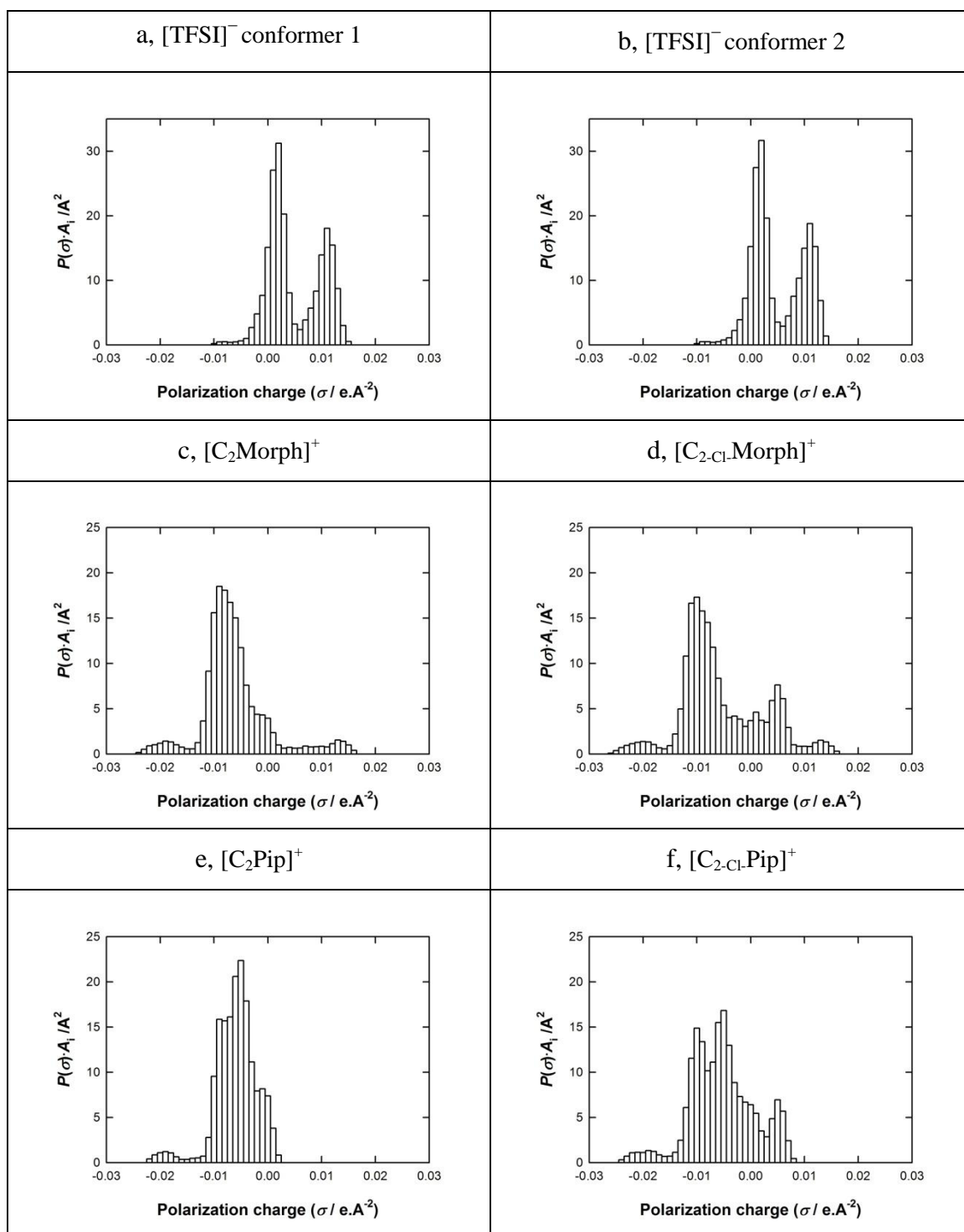
Table A1 Structure, abbreviation and Cosmo volume of the TFSI anion and the studied cations and their non-chlorinated analogues.

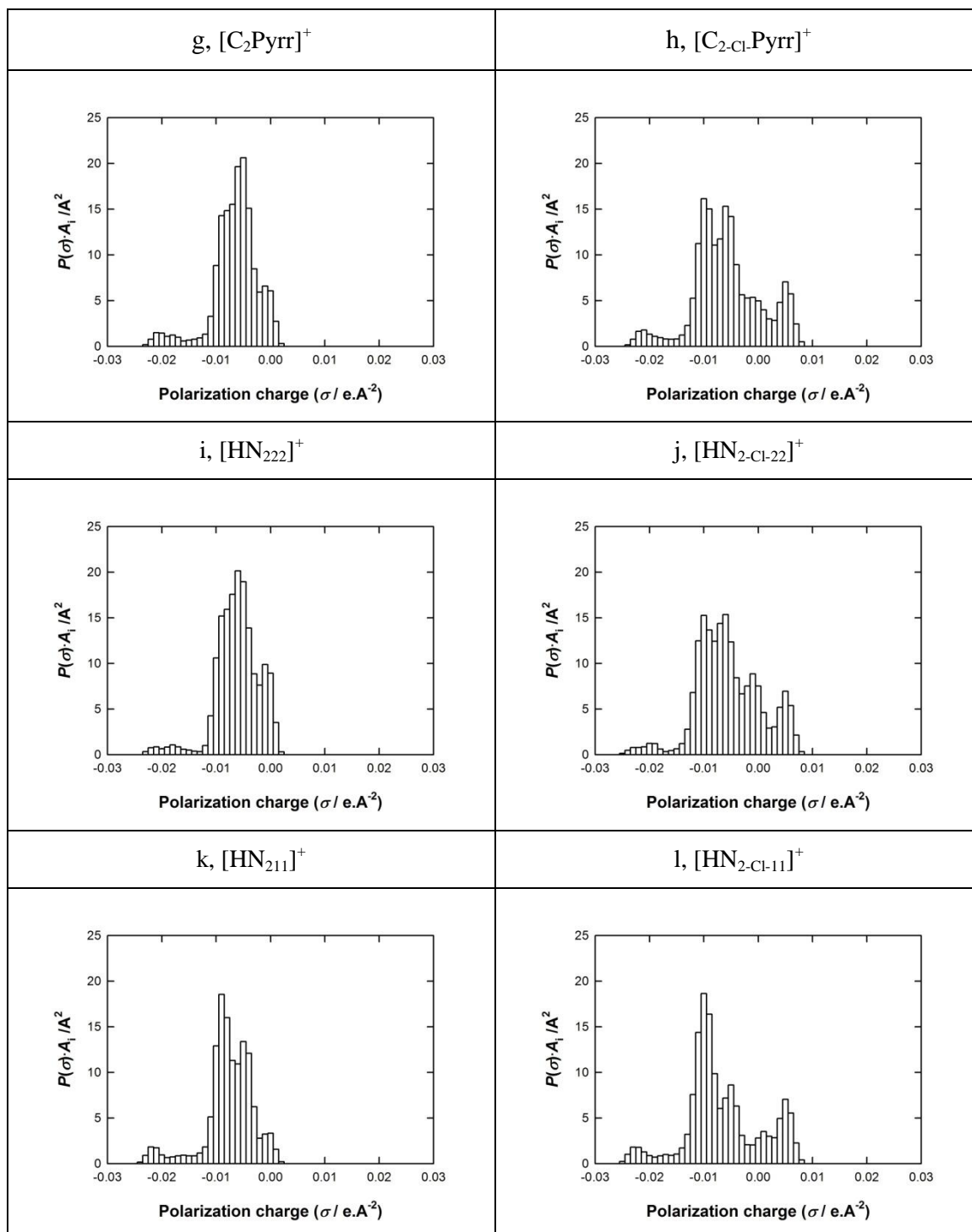
Structure and abbreviation	Cosmo Volume (\AA^3)	Structure and abbreviation	Cosmo Volume (\AA^3)
 [TFSI] ⁻ conformer 1	 219.69	 [TFSI] ⁻ conformer 2	 222.21
 [C ₂ Morph] ⁺	 159.75	 [C _{2-cl} -Morph] ⁺	 182.91
 [C ₂ Pip] ⁺	 170.25	 [C _{2-cl} -Pip] ⁺	 191.74

Structure and abbreviation	Cosmo Volume (Å ³)	Structure and abbreviation	Cosmo Volume (Å ³)
			
[C ₂ Pyrr] ⁺	150.86	[C ₂ -Cl-Pyrr] ⁺	174.11
			
[HN ₂₂₂] ⁺	165.51	[HN ₂ -Cl-22] ⁺	188.22
			
[HN ₂₁₁] ⁺	121.98	[HN ₂ -Cl-11] ⁺	144.67
			
[HN ₃₁₁] ⁺	143.53	[HN ₃ -Cl-11] ⁺	166.96



Polarisation Charge Density σ





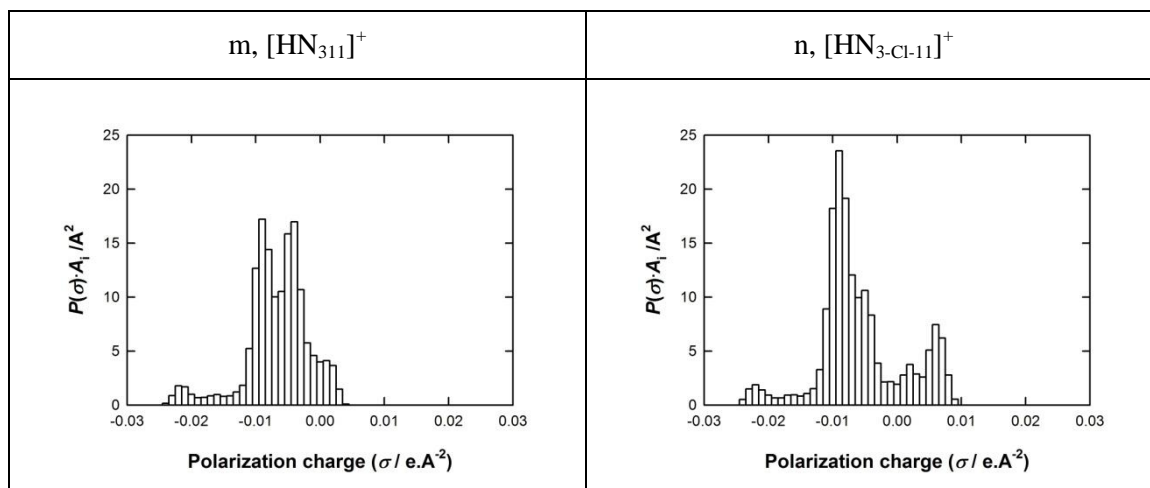
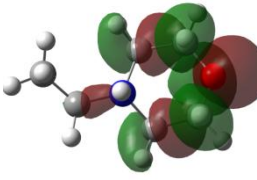
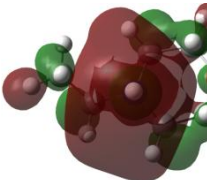
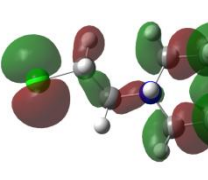
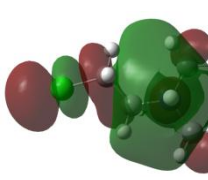
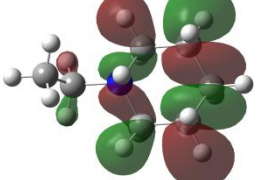
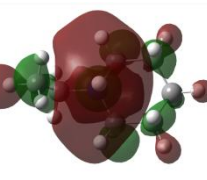
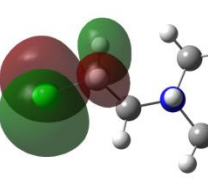
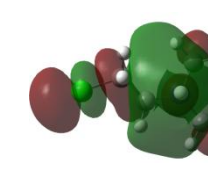
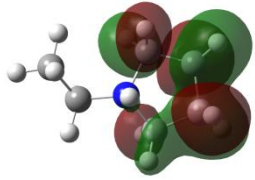
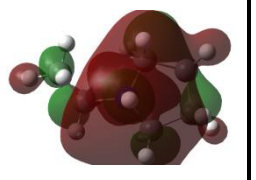
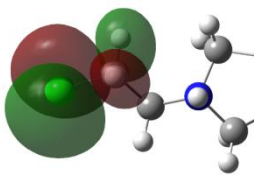
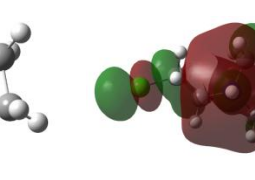
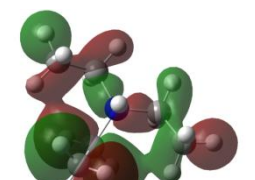
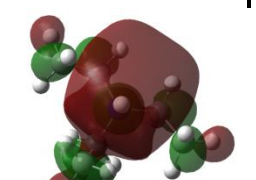
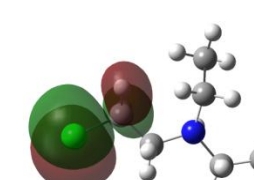
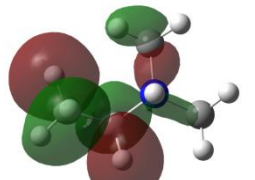
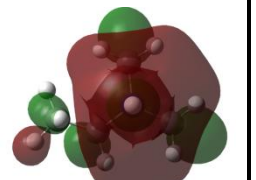
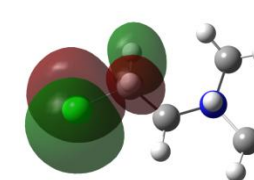
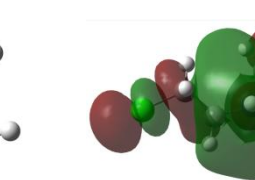
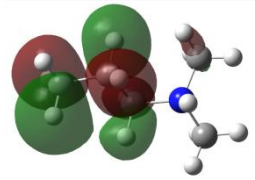
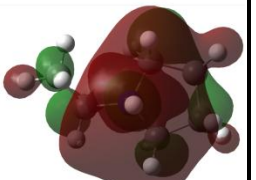
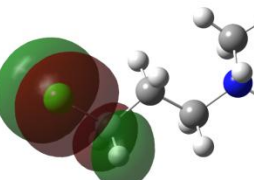
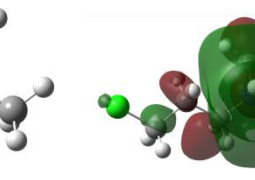


Fig. A1 Sigma profiles of the [TFSI]⁻ anion and of the studied cations and their non-chlorinated analogues.

Table A2 Orbital, abbreviation and Cosmo volume evaluated by COSMOTHERMX interface of studied ions.

HOMO Orbital Energy (eV)	LUMO Orbital Energy (eV)	HOMO Orbital Energy (eV)	LUMO Orbital Energy (eV)
[C ₂ Morph]		[C _{2-Cl} -Morph]	
 -11.79	 -3.63	 -11.92	 -4.32
[C ₂ Pip]		[C _{2-Cl} -Pip]	
			

HOMO Orbital Energy (eV)	LUMO Orbital Energy (eV)	HOMO Orbital Energy (eV)	LUMO Orbital Energy (eV)
-13.35	-3.24	-11.88	-4.07
[C ₂ Pyrra]		[C ₂ -Cl.Pyrra]	
			
-13.76	-3.70	-11.93	-4.21
[HN ₂₂₂]		[HN ₂ -Cl-22]	
			
-14.27	-3.27	-11.93	-3.96
[HN ₂₁₁]		[HN ₂ -Cl-11]	
			
-14.68	-3.98	-12.10	-4.55
[HN ₃₁₁]		[HN ₃ -Cl-11]	
			
-13.52	-3.90	-11.30	-4.13

Thanks to Dr. J. Jacquemin from Queen's University, Belfast, for realizing the computations.

5. Electrochemical characterizations

5.1. Electrodes preparation

The active materials (AC) in the studies were DLC Supra 30 denoted as S30, xerogel carbon AX2000 and Black Pearls 2000 (by Cabot) referred to as BP2000. AC-based electrodes were prepared either with PVDF or PTFE binder. PVDF-based electrodes were composed of active material (AC, 85 wt. %), conducting agent (C-ENERGY[®] Super C65, 5 wt. %) and PVDF (Kynar HSV900, Arkema, 10 wt. %). All the components were mixed with acetone and continuously triturated in a mortar till solvent evaporation. The electrodes were formed as pellets (1 cm diameter, thickness ca. 0.3 mm and mass 5–8 mg) by pressing under $4.87 \text{ kg}\cdot\text{cm}^{-2}$ and dried under vacuum at 120 °C for 12 h. PTFE-based electrodes were composed of active material (AC, 80 wt. %), conducting agent (C-ENERGY[®] Super C65, 10 wt. %) and PTFE (10 wt. %). The PTFE water suspension (PTFE - 60 wt. % in water) was mixed with ethanol and blended with the other components. The mixture was stirred at 120 °C till ethanol evaporation. Then, the obtained dough was rolled for giving a sheet with 0.3 mm thickness, from which 9 mm diameter electrodes were cut and dried under vacuum at 120 °C for 12 h.

5.2. Porous texture characterization of carbons and electrodes

The porous texture of activated carbons, both pristine and bound in electrodes (see electrodes preparation in section 5.1.), was determined by nitrogen adsorption/desorption at 77 K employing Accelerated Surface Area and Porosimetry analyzer (ASAP 2020–Micromeritics, USA). Prior to each measurement, the samples were degassed for 24 h, electrodes at 140 °C, and pristine carbon at 350 °C. Later, based on to the N₂ adsorption isotherm data, the SSA was calculated using the BET equation or the DFT model, respectively. In turn, the pore size distribution assessment was calculated based on the two dimensional non-local density functional theory (2D-NLDFT). All the porous texture data of electrodes were referred to the active mass of the material.

Thanks to MSc Eng. P. Przygocki from Poznan University of Technology for realizing gas adsorption analysis.

5.3. Silver wire quasi reference electrode

For experiments in 3-electrode cell and 2-electrode cell with reference electrode, a silver wire quasi reference electrode (AgQRE) was applied. It was prepared by immersing a freshly polished Ag wire as working electrode and a graphite rod as counter electrode in $0.1 \text{ mol}\cdot\text{L}^{-1}$ HCl. Silver was electrooxidized applying a low current density to form a blackish AgCl layer.

5.4. Cells construction

5.4.1. Electrochemical stability of PILs on GC

The measurements were conducted, separately for positive and negative polarization, in an electrochemical vessel equipped with glassy carbon working electrode, platinum counter electrode and silver wire (AgQRE). Using cyclic voltammetry (scan rate of $10 \text{ mV}\cdot\text{s}^{-1}$), the vertex potential was gradually increased by 0.1 V steps from 0.5 V vs. AgQRE up to 2.8 V vs. AgQRE for positive polarization or decreased from -0.5 V vs. AgQRE down to -2.8 V vs. AgQRE for negative one. Five cycles were scanned at each potential step.

5.4.2. Electrochemical behavior of PILs on Al

The study was performed in an electrochemical vessel filled with the tested PILs, where the working electrode was aluminum foil (10 mm x 10 mm) hang on gold hook, the counter electrode platinum and the reference electrode a silver wire (AgQRE). 10 CVs were swept from OCV to 1.5 V vs. AgQRE, then to -1.5 V vs. AgQRE at scan rate of $5 \text{ mV}\cdot\text{s}^{-1}$.

5.4.3. Electrochemical behavior of PILs on stainless steel

The study was performed in teflon Swagelok® type vessel, where the working electrode was a stainless steel (316L grade) cylinder, separated by glass microfiber paper (GF/A, Whatman™, 0.26 mm) from a S30-PVDF pellet counter electrode contacted with a SSt cylinder as current collector. A silver wire was used as *quasi*-reference electrode. The positive and negative potential domains were investigated in separate cells, while the potential was gradually increased (or decreased) starting from 0.5 V vs. AgQRE (or -0.5 V vs. AgQRE) by 0.1 V step up to 2.8 V vs. AgQRE (-2.0 V vs. AgQRE). The scan rate was $5 \text{ mV}\cdot\text{s}^{-1}$.

5.4.4. Manufacturing of three- and two-electrode cells with AC electrodes

Two AC pellet electrodes sandwiching a glass microfiber paper porous membrane (GF/A, Whatman™, 0.26 mm) were soaked with the electrolyte in a Teflon Swagelok® type vessel using aluminum or stainless steel (316L grade) current collectors. For the purposes of 3-electrode cell experiments, the counter electrode had 3-5 times higher mass than the working electrode. Assembling with PILs containing less than 200 ppm of water was done under moisture-free atmosphere in an argon-filled glove box. As particularly specified in the text, cells with PILs containing 1000 and 10,000 ppm of water were built in air atmosphere.

5.5. Electrochemical measurements

Cyclic voltammetry (CV; 1 to 20 mV s⁻¹), galvanostatic cycling with potential limitation (GCPL; 0.1 – 1 A g⁻¹) and electrochemical impedance spectroscopy (EIS; from 1 mHz to 100 kHz with sinusoidal signal of ± 5 mV s⁻¹) were carried out at RT using VMP3 multichannel potentiostat/galvanostat by BioLogic, France.

The capacitance values were calculated as follows:

- from cyclic voltammetry using equation (A1):

eq. A1

$$C_{cv} = \frac{2I}{\left(\frac{dU}{dt}\right) \cdot m_{am}}$$

where I stands for current (A), dU/dt (V·s⁻¹) scan rate and m_{am} average mass of active material (g) in one electrode.

- from galvanostatic cycling with potential limitation:
 - if the galvanostatic profiles were linear, based on the slope of the galvanostatic discharge characteristics, the capacitance was calculated according to equation A2:

eq. A2

$$C_{GD} = \frac{2 I_{dch}}{(dU/dt) \cdot m_{am}}$$

where I_{dch} is the discharge current (A), dU/dt the slope of the discharge curve (V·s⁻¹), m_{am} is the average mass (g) of AC in one electrode.

- if the galvanostatic profiles were non-linear, the specific discharge capacitance was calculated according to the procedure described in ref [204] using the energy-capacitance relation (A3):

eq. A3

$$C_{int/D} = \frac{2E_{int/D}}{U_{max}^2}$$

where $E_{int/D}$ is the discharge energy determined by integration (area under the curve) and U_{max} is the maximum voltage. The capacitance of a single electrode is expressed by equation (A4):

eq. A4

$$C_{el/D} = \frac{C_{int/D}}{m_{am}}$$

where m_{am} (g) is the average mass of active material in one electrode.

- from EIS measurements, the capacitance values were calculated at each applied frequency from equation (A5):

eq. A5

$$C = 2 \cdot \frac{1}{2 \cdot \pi \cdot f \cdot (-Im(Z)) \cdot m_{am}}$$

where C - capacitance, f - frequency, $-Im(Z)$ - imaginary component and m_{am} (g) is the average mass of active material in one electrode.

References

- [1] T. Pandolfo, V. Ruiz, S. Sivakkumar, J. Nerkarey, Supercapacitors: Materials, Systems and Applications, (F. Béguin, E. Frackowiak ed) Ch. 2, Wiley-VCH, Weinheim, 2013, pp. 69-109.
- [2] A. G. Pandolfo, A. F. Hollenkamp, *J. Power Sources*, **157** (2006) 11-27.
- [3] H. Becker, U.S. Patent no. 2800616.
- [4] R. Righmire, U.S. Patent no. 3,288,641.
- [5] Donald L. Boos, U.S. Patent no. 3,536,963.
- [6] J. Miller, Batteries & Energy Storage Technology, AUTUMN (2007) 61-78.
- [7] J. R. Miller, Supercapacitors: Materials, Systems and Applications, (F. Béguin, E. Frackowiak ed) Ch. 14, Wiley-VCH, Weinheim, 2013, pp. 509-516.
- [8] <http://www.marketresearchmedia.com/?p=912>.
- [9] P. Simon, Y. Gogotsi, *Nature Materials*, **7** (2008) 845-854.
- [10] R. Kötz, M. Carlen, *Electrochim. Acta*, **45** (2000) 2483-2498.
- [11] http://batteryuniversity.com/learn/article/whats_the_role_of_the_supercapacitor.
- [12] J. B. Goodenough, H. D. Abruna, M. V. Buchanan, Basic research needs for electrical energy storage. Report of the basic energy sciences workshop for electrical energy storage, 186 (2007).
- [13] L. L. Zhang, X. S. Zhao, *Chem. Soc. Rev.*, **38** (2009) 2520-2531.
- [14] F. Béguin, V. Presser, A. Balducci, E. Frackowiak, *Adv. Mater.*, **26** (2014) 2219-2251.
- [15] S. Srinivasan, Fuel Cells, From Fundamentals to Applications, Ch.2, Springer eBooks, 2006, pp. 27-92.
- [16] O. A. Esin, B. F. Markov, *Zh. Fiz. Khim.*, **13** (1939) 318.
- [17] D. C. Grahame, *J. Electrochem Soc.*, **98** (1951) 313.
- [18] M. A. V. Devanathan, *Trans. Faraday Soc.*, **50** (1954) 373.
- [19] J. O'M Bockris, M. A. V Devanathan, K. Mueller, *Proc. Roy. Soc., Ser.A*, **274** (1963) 55-79.
- [20] <http://what-when-how.com/nanoscience-and-nanotechnology/electrical-double-layer-formation-part-1-nanotechnology/>.
- [21] E. Frackowiak, G. Lota, J. Pernak, *Appl. Phys. Lett.*, **86** (2005) 164104/1-164104/3.
- [22] P. Simon, Y. Gogotsi, B. Dunn, *Science*, **343** (2014) 1210-1211.
- [23] T. Brousse, D. Bélanger, J. W. Long, *J. Electrochem. Soc.*, **162** (2015) A5185-A5189.
- [24] L. Guana, L. Yub, G. Z. Chen, *Electrochim. Acta*, **206** (2016) 464-478.
- [25] B. Akinwolemiwa, C. Peng, G. Z. Chen, *J. Electrochem. Soc.*, **162** (2015) A5054-A5059.
- [26] S. Roldán, D. Barreda, M. Granda, R. Menéndez, R. Santamaría, C. Blanco, *Phys. Chem. Chem. Phys.*, **17** (2015) 1084-1092.

- [27] E. Frackowiak, Supercapacitors: Materials, Systems and Applications, (F. Béguin, E. Frackowiak ed) Ch. 6, Wiley-VCH, Weinheim, 2013, pp. 207-237.
- [28] G. A. Snook, P. Kao, A. Best., *J. Power Sources*, **196** (2011) 1-12.
- [29] G. Z. Chen, M. S. P. Shaffer, D. Coleby, G. Dixon, W. Zhou, D. J. Fray, A. H. Windle, *Adv. Mater.*, **12** (2000) 522-526.
- [30] B. Kim, H. Chung, W. Kim, *J. Phys. Chem. C*, **114** (2010) 15223-15227.
- [31] K. Lota, V. Khomenko, E. Frackowiak, *J. Phys. Chem. Solids*, **65** (2004) 295-301.
- [32] M. Hughes, M. S. P. Shaffer, A. C. Renouf, C. Singh, G. Z. Chen, D. J. Fray, A. H. Windle, *Adv. Mater.*, **14** (2002) 382-385.
- [33] V. Khomenko, E. Frackowiak, F. Béguin, *Electrochim. Acta*, **50** (2005) 2499-2506.
- [34] B. E. Conway, W. G. Pell, *J. Solid State Electrochem.*, **7** (2003) 637-644.
- [35] Z.-S. Wu, D.-W. Wang, W. Ren, J. Zhao, G. Zhou, F. Li, H.-M. Cheng, *Adv. Funct. Mater.*, **20** (2010) 3595-3602.
- [36] T. Cottineau, M. Toupin, T. Delahaye, T. Brousse, D. Bélanger, *Appl. Phys. A*, **82** (2006) 599-606.
- [37] C.D. Lokhande, D.P. Dubal, Oh-Shim Joo, *Curr. Appl. Phys.*, **11** (2011) 255-270.
- [38] C. Xu, F. Kanga, B. Li, H. Du, *J. Mater. Res.*, **25** (2010) 1421-1432.
- [39] V. Khomenko, E. Raymundo-Piñero, F. Béguin., *J. Power Sources*, **153** (2006) 183-190.
- [40] M. Inagaki F. Béguin, E. Frackowiak, Carbons for Electrochemical Energy Storage and Conversion Systems (F. Béguin, E. Frackowiak ed) Ch. 2, CRC Press, 2009, pp 37-77.
- [41] P. Simon, Y. Gogotsi., *Acc. Chem. Res.*, **46** (2013) 1094-1103.
- [42] Y. Gao, Y. S. Zhou, M. Qian, X. N. He, J. Redepenning, P. Goodman, H. M. Li, L. Jiang, Y. F. Lu, *Carbon*, **84** (2015) 584-598.
- [43] C. Portet, G. Yushin, Y. Gogotsi, *Carbon*, **45** (2007) 2511-2518.
- [44] J. K. McDonough, Y. Gogotsi, *Electrochem. Soc. Interface*, **22** (2013) 61-65.
- [45] Y. Zhai, Y. Dou, D. Zhao, P. F. Fulvio, R. T. Mayes, S. Dai, *Adv. Mater.*, **23** (2011) 4828-4850.
- [46] De Volder, M.F.L., Tawfick, S.H., Baughman, R.H., Hart, A.J., *Science*, **339** (2013), 535-539.
- [47] G. Lota, K. Fic, E. Frackowiak, *Energy Environ. Sci.*, **4** (2011) 1592-1605.
- [48] A. K. Geim, K. S. Novoselov, *Nat. Mater.*, **6** (2007) 183-191.
- [49] K. Parvez, Z.-S. Wu, R. Li, X. Liu, R. Graf, X. Feng, K. Müllen, *J. Am. Chem. Soc.*, **136** (2014) 6083-6091.
- [50] S. R. C. Vivekchand, Chandra Sekhar Rout, K. S. Subrahmanyam, A. Govindaraj, C. N. R. Rao, *J. Chem. Sci.*, **120** (2008) 9-13.
- [51] L. L. Zhang, R. Zhou, X. S., Zhao, *J. Mater. Chem.*, **20** (2010) 5983-5992.

- [52] P. Simon, P.-L. Taberna, F. Béguin, *Supercapacitors: Materials, Systems and Applications*, (F. Béguin, E. Frackowiak ed) Ch. 4, Wiley-VCH, Weinheim, 2013, pp. 131-165.
- [53] H. Marsh, F. Rodríguez-Reinoso, *Activated Carbon*, 1st Edition, Ch. 5, Elsevier Science, 2006, pp. 243-321.
- [54] P. Simon, A. Burke, *Electrochem. Soc. Interface*, (2008) 38-42.
- [55] P. Kleszyk, P. Ratajczak, P. Skowron, J. Jagiello, Q. Abbas, E. Frackowiak, F. Béguin, *Carbon*, **81** (2015) 148-157.
- [56] V. Presser, M. Heon, Y. Gogotsi, *Adv. Funct. Mater.*, **21** (2011) 810-833.
- [57] J. Yan, Q. Wang, T. Wei, Z. Fan, *Adv. Energy Mater.*, **4** (2014) 1300816.
- [58] E. G. Calvo, J. Á. Menéndez, A. Arenillas, Ch. 9, *Designing Nanostructured Carbon Xerogels, Nanomaterials*, InTech, 2011, pp. 187-235.
- [59] P. Kossyrev, *J. Power Sources*, **201** (2012) 347-352.
- [60] R. Franklin, *Proc. Roy. Soc., London, Series A*, **209** (1951) 196-218.
- [61] I. Mochida, S.-H. Yoon, W. Qiao, *Braz. Chem. Soc.*, **17** (2006) 1059-1073.
- [62] K. S. W. Sing, D. H. Everett, R. A. V. Haul, L. Moscou, R. A. Pierotti, J. Rouquerol, T. Siemieniowska, *Pure and Applied Chemistry*, **57** (1985) 603-619.
- [63] F. Rodríguez-Reinoso, *Carbon*, **36** (1998) 159-175.
- [64] M. Thommes, *Chemie Ingenieur Technik*, **82** (2010) 1059-1073.
- [65] E. Frackowiak, P. Ratajczak, F. Béguin, *Electrochemistry of Carbon Electrodes*, (R.C. Alkire, P.N. Bartlett, J. Lipkowski ed) Ch 8, Wiley-VCH, Weinheim, 2015, pp. 285-378.
- [66] T. A. Centeno, F. Stoeckli, *Carbon*, **48** (2010) 2478-2486.
- [67] O. Barbieri, M. Hahn, A. Herzog, R. Kötz, *Carbon*, **43** (2005) 1303-1310.
- [68] C. O. Ania, J. Pernak, F. Stefaniak, E. Raymundo-Piñero, F. Béguin, *Carbon*, **44** (2006) 3126-3130.
- [69] R. Mysyk, V. Ruiz, E. Raymundo-Piñero, R. Santamaria, F. Béguin, *Fuel Cells*, **10** (2010) 834-839.
- [70] C. Largeot, C. Portet, J. Chmiola, P.-L. Taberna, Y. Gogotsi, P. Simon, *J. Am. Chem. Soc.*, **130** (2008) 2730-2731.
- [71] R. Lin, P. Huang, J. Ségalini, C. Largeot, P.L. Taberna, J. Chmiola, Y. Gogotsi, P. Simon, *Electrochim. Acta*, **54** (2009) 7025-7032.
- [72] C. Vix-Guterl, E. Frackowiak, K. Jurewicz, M. Friebe, J. Parmentier, F. Béguin, *Carbon*, **43** (2005) 1293-1302.
- [73] J. Chmiola, G. Yushin, Y. Gogotsi, C. Portet, P. Simon, P.-L. Taberna, *Science*, **313** (2006) 1760-1763.
- [74] E. Raymundo-Piñero, K. Kierzek, J. Machnikowski, F. Béguin, *Carbon*, **44** (2006) 2498-2507.

- [75] J. Chmiola, C. Largeot, P.-L. Taberna, P. Simon, Y. Gogotsi, *Angew. Chem. Int. Ed.*, **47** (2008) 3392–3395.
- [76] M. Deschamps, E. Gilbert, P. Azais, E. Raymundo-Piñero, M. R. Ammar, P. Simon, D. Massiot, F. Béguin, *Nature Materials*, **12** (2013) 351-358.
- [77] J. M. Griffin, A. C. Forse, W.-Y. Tsai, P.-L. Taberna, P. Simon, C. P. Grey, *Nature Materials*, **14** (2015) 812-819.
- [78] R. Mysyk, E. Raymundo-Piñero, F. Béguin, *Electrochem. Comm.*, **11** (2009) 554-556.
- [79] R. Mysyk, E. Raymundo-Piñero, J. Pernak F. Béguin, *J. Phys. Chem. C*, **113** (2009) 13443-13449.
- [80] J. L. Figueiredo, M. F. R. Pereira, *Catal. Today*, **150** (2010) 2-7.
- [81] P. J. Hall, M. Mirzaeian, S. I. Fletcher, F.B. Sillars, A. J. R. Rennie, G. O. Shitta-Bey, G. Wilson, A. Cruden, R. Carter, *Energy Environ. Sci.*, **3** (2010) 1238-1251.
- [82] P. S. Guin, S. Das, P. C. Mandal, *Int. J. Electrochem.*, (2011) 816202.
- [83] E. Raymundo-Piñero, F. Leroux, F. Béguin, *Adv. Mater.*, **18** (2006) 1877-1882.
- [84] M. A. Montes-Morán, D. Suárez, J. A. Menéndez, E. Fuente, *Carbon*, **42** (2004) 1219-1225.
- [85] H. A. Andreas, B. E. Conway, *Electrochim. Acta*, **51** (2006) 6510-6520.
- [86] A. Śliwak, B. Grzyb, J. Ćwikła, G. Gryglewicz, *Carbon*, **64** (2013) 324-333.
- [87] D. Hulicova-Jurcakova, M. Seredych, G. Q. Lu, T. J. Bandoz, *Adv. Funct. Mater.*, **19** (2009) 438-447.
- [88] E. Frackowiak, G. Lota, J. Machnikowski, C. Vix-Guterl, F. Béguin, *Electrochim. Acta*, **51** (2006) 2209-2194.
- [89] K. Jurewicz, K. Babel, A. Ziolkowski, H. Wachowska, M. Kozłowski, *Fuel Process. Technol.*, **77–78** (2002) 191-198.
- [90] K. Jurewicz, K. Babel, A. Ziolkowski, H. Wachowska, *Electrochim. Acta*, **48** (2003) 1491-1498.
- [91] T. J. Bandoz, C. O. Ania, *Activated Carbon Surfaces in Environmental Remediation*, (T. J. Bandoz ed) Ch. 4, Elsevier, Oxford, 2006, pp.159-230.
- [92] B. Fang, L. Binder, *J. Power Sources*, **163** (2006) 616-622.
- [93] W. Gu, G. Yushin, *Wiley Interdisciplinary Reviews: Energy and Environment*, **3** (2014) 424-473.
- [94] V. Ruiz, R. Santamaria, M. Granda, C. Blanco, *Electrochim. Acta*, **54** (2009) 4481- 4486.
- [95] L. Demarconnay, E. Raymundo-Piñero, F. Béguin, *Electrochem Commun.*, **12** (2010) 1275-1278.
- [96] M. P. Bichat, E. Raymundo-Piñero, F. Béguin, *Carbon*, **48** (2010) 4351-4361.
- [97] K. Fic, G. Lota, M. Meller, E. Frackowiak, *Energy Environ. Sci.*, **5** (2012) 5842-5850.

- [98] Q. Gao, L. Demarconnay, E. Raymundo-Piñero, F. Béguin, *Energy Environ. Sci.*, **5** (2012) 9611-9617.
- [99] P. Ratajczak, K. Jurewicz, P. Skowron, Q. Abbas, F. Béguin, *Electrochim. Acta*, **130** (2014) 344-350.
- [100] K. Lota, A. Sierczynska, I. Acznik, *Chemik*, **67** (2013) 1138-1145.
- [101] F. Béguin, M. Friebe, K. Jurewicz, C. Vix-Guterl, J. Dentzer, E. Frackowiak, *Carbon*, **44** (2006) 2392-2398.
- [102] K. Jurewicz, E. Frackowiak, F. Béguin., *Appl. Phys.*, **A78** (2004) 981-987.
- [103] S.-E. Chun, J.F. Whitacre, *J. Power Sources*, **242** (2013) 137-140.
- [104] G. Lota, K. Fic, K. Jurewicz, E. Frackowiak, *Cent. Eur. J. Chem.*, **9** (2011) 20-24.
- [105] F. Béguin, K. Kierzek, M. Friebe, A. Jankowska, J. Machnikowski, K. Jurewicz, E. Frackowiak, *Electrochim. Acta*, **51** (2006) 2161-2167.
- [106] K. Jurewicz, E. Frackowiak, F. Béguin, *Electrochem. Solid-State Lett.*, **4** (2001) A27-A29.
- [107] C. Zhong, Y. Deng, W. Hu, J. Qiao, L. Zhangd, J. Zhang, *Chem. Soc. Rev.*, **44** (2015) 7484-7539.
- [108] A. Laheäär, H. Kurig, A. Jänes, E. Lust, *Electrochim. Acta*, **54** (2009) 4587-4594.
- [109] P. Wasserscheid, T. Welton, *Ionic liquid in synthesis*, Wiley-VCH Verlag, Weinheim 2007.
- [110] P. Bonhôte, A.-P. Dias, N. Papageorgiou, K. Kalyanasundaram, M. Gratzel, *Inorg. Chem.*, **35** (1996) 1168-1178.
- [111] N. V. Plechkova, K. R. Seddon, *Chem. Soc. Rev.*, **37** (2008) 123-150.
- [112] R. D. Rogers, K. R. Seddon, *Science*, **302** (2003) 792-793.
- [113] M. J. Earle, K. R. Seddon, *Pure Appl. Chem.*, **72** (2000) 1391-1398.
- [114] P. Walden, *Bull. Acad. Imper. Sci. St. Petersburg*, **8** (1914) 405-422.
- [115] J. S. Wilkes, *Green Chem.*, **4** (2002) 73-80.
- [116] J. S. Wilkes, M. J. Zaworotko, *J. Chem. Soc., Chem. Commun.* (1992) 965-967.
- [117] M. Armand, F. Endres, D. R. MacFarlane, H. Ohno, B. Scrosati, *Nature Materials*, **8** (2009) 621-629.
- [118] D. R. MacFarlane, S. A. Forsyth, J. Golding, G. B. Deacon, *Green Chem.*, **4** (2002) 444-448.
- [119] J. Sun, M. Forsyth, D. R. MacFarlane, *J. Phys. Chem. B*, **102** (1998) 8858-8864.
- [120] K. J. Fraser, D. R. MacFarlane, *Aust. J. Chem.*, **62** (2009) 309-3021.
- [121] M. Anouti, L. Timperman, M. El hilali, A. Boisset, H. Galiano, *J. Phys. Chem. C*, **116** (2012) 9412-9418.

- [122] Q. Zhang, S. Liu, Z. Li, J. Li, Z. Chen, R. Wang, L. Lu, Y. Deng, *Chem. Eur. J.*, **15** (2009) 765-778.
- [123] J. Jacquemin, P. Goodrich, W. Jiang, D. W. Rooney, C. Hardacre, *J. Phys. Chem. B*, **117** (2013) 1938-1949.
- [124] H. Matsumoto, H. Kageyama, Y. Miyazaki, *Chem. Commun.*, (2002) 1726-1727.
- [125] M. Montanino, M. Carewska, F. Alessandrini, S. Passerini, G. B. Appetecchi, *Electrochim. Acta*, **57** (2011) 153-159.
- [126] D. R. MacFarlane, P. Meakin, J. Sun, N. Amini, M. Forsyth, *J. Phys. Chem. B*, **103** (1999) 4164-4170.
- [127] G. B. Appetecchi, M. Montanino, D. Zane, M. Carewska, F. Alessandrini, S. Passerini, *Electrochim. Acta*, **54** (2009) 1325-1332.
- [128] M. Galinski, I. Stepniak, *J. Appl. Electrochem.*, **39** (2009) 1949-1953.
- [129] K. Stappert, D. Unal, B. Mallicka, A.-V. Mudring, *J. Mater. Chem. C*, **2** (2014) 7976-7986.
- [130] W. Xu, C. A. Angell, *Science*, **302** (2003) 422-425.
- [131] M. Yoshizawa, A. Narita, H. Ohno, *Electrochemical Aspects of Ionic Liquids*, (Ohno, H. ed) Ch. 20 (2005) pp. 245-258.
- [132] J. Reiter, S. Jeremias, E. Paillard, M. Wintera, S. Passerini, *Phys. Chem. Chem. Phys.*, **15** (2013) 2565-2571.
- [133] J. Jacquemin, P. Husson, A. A. H. Padua, V. Majer, *Green Chem.*, **8** (2006) 172-180.
- [134] K. R. Seddon, A. Stark, M. J. Torres, Eds. M. Abraham, L. Moens, *ACS Symposium Series*, **819** (2002) 34-49.
- [135] P. S. Kulkarni, L. C. Branco, J. G. Crespo, M. C. Nunes, A. Raymundo, C. A. M. Afonso, *Chem.-Eur. J.*, **13** (2007) 8478-8488.
- [136] G. L. Burrell, N. F. Dunlop, F. Separovic, *Soft Matter*, **6** (2010) 2080-2086.
- [137] J. Jacquemin, M. Anouti, D. Lemordant, *J. Chem. Eng. Data*, **56** (2011) 556-564.
- [138] M. Galiński, A. Lewandowski, I. Stepniak, *Electrochim. Acta*, **51** (2006) 5567-5580.
- [139] H. Liu, Y. Liu, J. Li, *Phys. Chem. Chem. Phys.*, **12** (2010) 1685-1697.
- [140] C. A. Angell, N. Byrne, J.-P. Belieres, *Acc. Chem. Res.*, **40** (2007) 1228-1236.
- [141] W. Xu, E. I. Cooper, C. A. Angell, *J. Phys. Chem. B*, **107** (2003) 6170-6178.
- [142] M. Yoshizawa, W. Xu, C. A. Angell, *J. Am. Chem. Soc.*, **125** (2003) 15411-15419.
- [143] D. R. MacFarlane, M. Forsyth, E. I. Izgorodina, A. P. Abbott, G. Annat, K. Fraser, *Phys. Chem. Chem. Phys.*, **11** (2009) 4962-4967.
- [144] H. Matsumoto, *Electrochemical Aspects of Ionic Liquids*, (H. Ohno, ed) Ch. 4 (2005) pp. 35-54.
- [145] S. P. Ong, O. Andreussi, Y. Wu, N. Marzari, G. Ceder, *Chem. Mater.*, **23** (2011) 2979-2986.

- [146] V. R. Koch, C. Nanjundiah, J. L. Goldman, in Proc. 5th Int. Sem. Double Layer Capacitors.
- [147] V. R. Koch, C. Nanjundiah, R. T. Carlin, U.S. Patent no 5827602 (1998).
- [148] A. Balducci, R. Dugas, P. L. Taberna, P. Simon, D. Plée, M. Mastragostino, S. Passerini, *J. Power Sources*, **165** (2007) 922-927.
- [149] M. Lazzari, M. Mastragostino, F. Soavi, *Electrochem. Commun.*, **9** (2007) 1567-1572.
- [150] M. Lazzari, M. Mastragostino, A. G. Pandolfo, V. Ruiz, F. Soavi, *J. Electrochem. Soc.*, **158** (2011) A22-A25.
- [151] M. Lazzari, F. Soavi, M. Mastragostino, *J. Power Sources*, **178** (2008) 490-496.
- [152] G. H. Lane, *Electrochim. Acta*, **83** (2012) 513-528.
- [153] R. Palm, H. Kurig, K. Tönurist, A. Jänes, E. Lust, *Electrochim. Acta*, **85** (2012) 139-144.
- [154] A. Krause, A. Balducci, *Electrochem. Comm.*, **13** (2011) 814-817.
- [155] S. Pohlmann, T. Olyschläger, P. Goodrich, J. A. Vicente, J. Jacquemin, A. Balducci, *Electrochim. Acta*, **153** (2015) 426-432.
- [156] N. Handa, T. Sugimoto, M. Yamagata, M. Kikuta, M. Kono, M. Ishikawa, *J. Power Sources*, **185** (2008) 1585-1588.
- [157] R.-S. Kühnel, A. Balducci, *J. Power Sources*, **249** (2014) 163-171.
- [158] Z.-B. Zhou, M. Takeda, M. Ue, *J. Fluorine Chem.*, **125** (2004) 471-476.
- [159] H. Kurig, M. Vestli, A. Jänes, E. Lust, *Electrochem. Solid-State Lett.*, **14** (2011) A120-A122.
- [160] H. Kurig, M. Vestli, K. Tönurist, A. Jänes, E. Lust, *J. Electrochem. Soc.*, **159** (2012) A944-A951.
- [161] T. Sato, G. Masuda, K. Takagi, *Electrochim. Acta*, **49** (2004) 3603-3611.
- [162] C. Arbizzani, M. Bisio, D. Cericola, M. Lazzari, F. Soavi, M. Mastragostino, *J. Power Sources*, **185** (2008) 1575-1579.
- [163] S. Pohlmann, T. Olyschläger, P. Goodrich, J. Alvarez Vicente, J. Jacquemin, A. Balducci, *J. Power Sources*, **273** (2015) 931-936.
- [164] D. Weingarh, H. Noh, A. Foelske-Schmitz, A. Wokaun, R. Kötz, *Electrochim. Acta*, **103** (2013) 119-124.
- [165] J. S. Wilkes, J. A. Levisky, R. A. Wilson, C. L. Hussey, *Inorg. Chem.*, **21** (1982) 1263-1264.
- [166] J. Reiter, E. Paillard, L. Grande, M. Winter, S. Passerini, *Electrochim. Acta*, **91** (2013) 101-107.
- [167] T.-Y. Wu, S.-G. Su, K.-F. Lin, Y.-C. Lin, H. P. Wang, M.-W. Lin, S.-T. Gung, I.-Sun, *Electrochim. Acta*, **56** (2011) 7278- 7287.

- [168] H. Every, A. G. Bishop, M. Forsyth, D. R. MacFarlane, *Electrochim. Acta*, **45** (2000) 1279-1284.
- [169] M. Kunze, S. Jeong, E. Paillard, M. Winter, S. Passerini, *J. Phys. Chem. C*, **114** (2010) 12364-12369.
- [170] W.-Y. Tsai, R. Lin, S. Murali, L. L. Zhang, J. K. McDonough, R. S. Ruoff, P.-L. Taberna, Y. Gogotsi, P. Simona, *Nano Energy*, **2** (2013), 403-411.
- [171] T. L. Greaves, C. J. Drummond, *Chem. Rev.*, **108** (2008) 206-237.
- [172] T. L. Greaves, C. J. Drummond, *Chem. Rev.*, **115** (2015) 11379-11448.
- [173] T. L. Greaves, A. Weerawardena, C. Fong, I. Krodkiewska, C. J. Drummond, *J. Phys. Chem. B*, **110** (2006) 22479-22487.
- [174] H. Nakamoto, M. Watanabe, *Chem. Commun.*, (2007) 2539-2541.
- [175] T. L. Greaves, D. F. Kennedy, S. T. Mudie, C. J. Drummond, *J. Phys. Chem. B*, **114** (2010) 10022-10031.
- [176] T.-Y. Wu, S.-G. Su, Y.-C. Lin, H. P. Wang, M.-W. Lin, S.-T. Gung, I.-W. Sun, *Electrochim. Acta*, **56** (2010) 853-862.
- [177] Md. A. B. H. Susan, A. Noda, S. Mitsushima, M. Watanabe, *Chem. Commun*, **9** (2003) 938-939.
- [178] L. Timperman, P. Skowron, A. Boisset, H. Galiano, D. Lemordant, E. Frackowiak, F. Béguin, M. Anouti, *Phys. Chem. Chem. Phys.*, **14** (2012) 8199-81207.
- [179] S. Menne, T. Vogl, A. Balducci, *Chem. Commun.*, **51** (2015) 3656-3659.
- [180] L. Timperman, H. Galiano, D. Lemordant, M. Anouti, *Electrochem. Commun.*, **13** (2011) 1112-1115.
- [181] J. A. Bautista-Martinez, L. Tang, J.-P. Belieres, R. Zeller, C. A. Angell, C. Friesen, *J. Phys. Chem. C*, **113** (2009) 12586-12593.
- [182] D. R. MacFarlane, J. M. Pringle, K. M. Johansson, S. A. Forsyth, M. Forsyth, *Chem. Commun.*, **14** (2006) 1905-1917.
- [183] E. I. Izgorodina, D. R. MacFarlane, *Phys. Chem. Chem. Phys.*, **12** (2010) 10341-10247.
- [184] T. Ueki, M. Watanabe, *Macromolecules*, **41** (2008) 3739-3749.
- [185] A. Noda, Md. A. B. H. Susan, K. Kudo, S. Mitsushima, K. Hayamizu, M. Watanabe, *J. Phys. Chem. B*, **107** (2003) 4024-4033.
- [186] J. W. Blanchard, J.-P. Belieres, T. M. Alam, J. L. Yarger, G. P. Holland, *J. Phys. Chem. Lett.*, **2** (2011) 1077-1081.
- [187] J. L. Lebga-Nebane, S. E. Rock, J. Franclemont, D. Roy, S. Krishnan, *Ind. Eng. Chem. Res.*, **51** (2012) 14084-14098.
- [188] N. Yaghini, L. Nordstierna, A. Martinelli, *Phys. Chem. Chem. Phys.*, **16** (2014) 9266-9275.
- [189] M. Anouti, J. Jacquemin, P. Porion, *J. Phys. Chem. B*, **116** (2012) 4228-4238.

- [190] D. Rochefort A.-L. Pont, *Electrochem. Comm.*, **8** (2006) 1539-1543.
- [191] L. Mayrand-Provencher D. Rochefort, *J. Phys. Chem. C*, **113** (2009) 1632-1639.
- [192] L. Mayrand-Provencher S. Lin, D.Lazzerini, D. Rochefort, *J. Power Sources*, **195** (2010) 5114-5121.
- [193] N. L. Nguyen, D. Rochefort, *Electrochim. Acta*, **147** (2014) 96-103.
- [194] A. C. Ruiz, D. Bélanger, D. Rochefort, *J. Phys. Chem. C*, **117** (2013) 20397-20405.
- [195] R. Mysyk, E. Raymundo-Piñero, M. Anouti, D. Lemordant, F. Béguin, *Electrochem. Commun.*, **12** (2010) 414-417.
- [196] M. Anouti, L. Timperman, *Phys. Chem. Chem. Phys.*, **15** (2013) 6539-6584.
- [197] L. Demarconnay E.G. Calvo, L. Timperman, M. Anouti, D. Lemordant, E. Raymundo-Piñero, A. Arenillas, J. A. Menéndez, F. Béguin, *Electrochim. Acta.*, **108** (2013) 361-368.
- [198] A. Brandt, J. Pires, M. Anouti, A. Balducci, *Electrochim. Acta*, **108** (2013) 226-231.
- [199] L. Timperman, A. Vigeant, M. Anouti, *Electrochim. Acta* , **155** (2015) 164-173.
- [200] L. Timperman, F. Béguin, E. Frackowiak, M. Anouti, *J. Electrochem. Soc.*, **161** (2014) A228-A238.
- [201] E. Coadou, L. Timperman, J. Jacquemin, H. Galiano, C. Hardacre, M. Anouti, *J. Phys. Chem. C*, **117** (2013) 10315-10325.
- [202] Q. Abbas D. Pajak, E. Frackowiak, F. Béguin, *Electrochim. Acta*, **140** (2014) 132-138.
- [203] E. Raymundo-Pinero, D. Cazorla-Amoros, A. Linares-Solano, S. Delpeux, E. Frackowiak, K. Szostak, F. Beguin, *Carbon*, **40** (2002) 1597–1617.
- [204] A. Laheäär, P. Przygocki, Q. Abbas, F. Béguin, *Electrochem. Comm.*, **60** (2015) 21–25.
- [205] K. R. Seddon, A. Stark, M.-J. Torres, *Pure Appl. Chem.*, **72** (2000) 2275-2287.
- [206] D. R. McFarlane, J. Sun, J. Golding, P. Meakin, M. Forsyth, *Electrochim. Acta*, **45** (2000) 1271-1278.
- [207] K. J. Miller, J. A. Savchik, *J. Am. Chem. Soc.*, **101** (1979) 7206-7213.
- [208] N. N. Rajput, J. Monk, F. R. Hung, *J. Phys. Chem. C*, **116** (2012) 14504-14513.
- [209] A. A. Elbourne, S. McDonald, K.Vořchovsky, F. Endres, G.G. Warr, R. Atkin, *ACS Nano*, **9** (2015) 7608–7620.
- [210] A. Carreon-Alvarez, R. C. Valderrama, J. A. Martínez, A. E.-Vargas, S. Gómez-Salazar, M. Barcena-Soto, N. Casillas, *Int. J. Electrochem. Sci.*, **7** (2012) 7877-7877.
- [211] X. Lu, G. Burrell, F. Separovic, C. Zhao, *J. Phys. Chem. B*, **116** (2012) 9160-9170.
- [212] J. G. Huddleston, A. E. Visser, W. M. Reichert, H. D. Willauer, G. A. Broker, R. D. Rogers, *Green Chem.*, **3** (2001) 156-164.
- [213] M. G. Freire, C. M. S. S. Neves, I. M. Marrucho, J. A. P. Coutinho, A. M. Fernandes, *J. Phys. Chem. A*, **114** (2010) 3744-3749.

- [214] W. A. Henderson, *Electrolytes for Lithium and Lithium-Ion Batteries*, (T. R. Jow, K. Xu, O. Borodin, M. Ue, ed) Ch. 1, Springer, 2014, pp. 1-92.
- [215] S. Y. Lee, A. Ogawa, M. Kanno, H. Nakamoto, T. Yasuda, M. Watanabe, *J. Am. Chem. Soc.*, **132** (2010) 132, 9764-9773.
- [216] T. Vogl, P. Goodrich, J. Jacquemin, S. Passerini, A. Balducci, *J. Phys. Chem. C*, **120** (2016) 8525-8533.
- [217] J. Pernak, A. Syguda, D. Janiszewska, K. Materna, T. Praczyk, *Tetrahedron*, **67** (2011) 4838-4844.
- [218] J. Pernak, M. Niemczak, K. Materna, K. Marcinkowska, T. Praczyk, *Tetrahedron*, **69** (2013) 4665-4669.
- [219] J. Pernak, M. Niemczak, K. Zakrocka, T. Praczyk, *Tetrahedron*, **69** (2013) 8132-8136.
- [220] B. Gorska, L. Timperman, M. Anouti, J. Pernak, F. Béguin, *RSC Adv.*, **60** (2016) 55144-55158.
- [221] A. Martinelli, A. Matic, P. Johansson, P. Jacobsson, L. Borjesson, A. Fernicola, S. Panero, B. Scrosati, H. Ohno, *J. Raman Spectrosc.*, **42** (2011) 522-528.
- [222] K. Fujii, T. Fujimori, T. Takamuku, R. Kanzaki, Y. Umehayashi, S.-i. Ishiguro, *J. Phys. Chem. B*, **110** (2006) 8179-8183.
- [223] F. M. Vitucci, F. Trequattrini, O. Palumbo, J.-B. Brubach, P. Roy, M. A. Navarra, S. Panero and A. Paolone, *J. Phys. Chem. A*, **118** (2014) 8758-8764.
- [224] K. Xu, *Chem. Rev.*, **104** (2004) 4303-4417.
- [225] J. Palomar, J. S. Torrecilla, J. Lemus, V. R. Ferro, F. Rodríguez, *Phys. Chem. Chem. Phys.*, **12** (2010) 1991-2000.
- [226] C. Maton, N. De Vos, C. V. Stevens, *Chem. Soc. Rev.*, **42** (2013) 5963-5977.
- [227] H. Matsumoto, H. Sakae Be, K. Tatsumi, *J. Power Sources*, **146** (2005) 45-50.
- [228] N. Papaiconomou, J. Estager, Y. Traore, P. Bauduin, C. Bas, S. Legeai, S. Viboud, M. Draye, *J. Chem. Eng. Data*, **55** (2010) 1971-1979.
- [229] J. A. Dean, *Lange's Handbook of Chemistry*, Fifteenth Edition, McGRAW-HILL, INC., (1998).
- [230] H. Jin, B. O'Hare, J. Dong, S. Arzhantsev, G. A. Baker, J. F. Wishart, A. J. Benesi, M. Maroncelli, *J. Phys. Chem. B*, **112** (2008) 81-92.
- [231] T. Yim, H. Y. Lee, H.-J. Kim, J. Mun, S. Kim, S. M. Oh, Y. G. Kim, *Bull. Korean Chem. Soc.*, **28** (2007) 1567-1572.
- [232] H. Ohtani, S. Ishimura, M. Kumai, *Anal. Sci.*, **24** (2008) 1335-1340.
- [233] S. Fang, Z. Zhang, Y. Jin, L. Yang, S.-i. Hirano, K. Tachibana and S. Katayama, *J. Power Sources*, **196** (2011) 5637-5644.
- [234] M. Yoshizawa, W. Xu, C. A. Angell, *J. Am. Chem. Soc.*, **125** (2003) 15411-15419.
- [235] K. Xu, S. P. Ding, T. R. Jow, *J. Electrochem. Soc.*, **146** (1999) 4172-4178.

- [236] S. P. Ong, G. Ceder, *Electrochim. Acta*, **55** (2010) 3804-3811.
- [237] W. Buijs, G.-J. Witkamp, M. C. Kroon, *Int. J. Electrochem. Sci.*, (2012).
- [238] P. C. Howlett, E. I. Izgorodina, M. Forsyth, D. R. MacFarlane, *Z. Phys. Chem.*, **220** (2006) 1483–1498.
- [239] M. Morita, T. Shibata, N. Yoshimoto, M. Ishikawa, *Electrochim. Acta*, **47** (2002) 2787-2793.
- [240] C. Peng, L. Yang, Z. Zhang, K. Tachibana, Y. Yang, *J. Power Sources*, **173** (2007) 510-517.
- [241] R.-S. Kühnel, M. Lübke, M. Winter, S. Passerini, A. Balducci, *J. Power Sources*, **214** (2012) 178-184.
- [242] K. Tateishi, A. Waki, H. Ogino, T. Ohishi, M. Murakami, *Electrochemistry*, **80** (2012) 556-560.
- [243] N. Ab. Manan, C. Hardacre, J. Jacquemin, D. W. Rooney, T. G. A. Youngs, *J. Chem. Eng. Data*, **54** (2009) 2005-2022.
- [244] A. Schäfer, C. Huber, R. Ahlrichs, *J. Chem. Phys.*, **100** (1994) 5829-5835.

Scientific Achievements

1. Publications

- 1.1. **B. Gorska**, L. Timperman, M. Anouti and F. Béguin,
Effect of low water content in protic ionic liquid on ions electrosorption in carbon porosity. Application to electrochemical capacitors, submitted to Phys. Chem. Chem. Phys.
- 1.2. **B. Gorska**, L. Timperman, M. Anouti, J. Pernak and F. Béguin,
Physicochemical and electrochemical properties of a new series of protic ionic liquids with N-chloroalkyl functionalized cations, RSC Adv., 60 (2016) 55144-55158.
IF: 3.289
- 1.3. K. Wasiński, **B. Górska**, M. Popławski, R. Kordala,
Ciecz jonowa w procesie bezprądowego wydzielania miedzi, (Use of ionic liquid in electroless copper plating), Zakład Wydawniczy „Przemysł Chemiczny”, 91 (2012) 2235-2239.
IF: 0.367

2. Patents

- 2.1. Pernak, **B. Górska**, F. Béguin,
Protonowe cieczy jonowe z kationem 1-(2-chloroetylo)pirolidyniowym oraz sposób ich otrzymywania, Data zgłoszenia: 25-05-2012; PL. 399306; (Udzielenie patentu 24-11-2016 r.)
- 2.2. J. Pernak, F. Béguin, **B. Górska**, A. Kurzawska, K. Marcinkowska, T. Praczyk,
(Chloroalkilo)dimetylowe protonowe cieczy jonowe z anionem tiocyjanianowym oraz sposób ich otrzymywania; Data zgłoszenia: 2013-11-18, PL. 223416; (Udzielenie patentu 2015 r.)
- 2.3. J. Pernak, F. Béguin, **B. Górska**, A. Kurzawska, K. Marcinkowska,
(Hydroksyalkilo)dimetyloamoniowe protonowe cieczy jonowe z anionem tiocyjanianowym oraz sposób ich otrzymywania; PL. 222467, Data zgłoszenia: 2013-11-18; (Udzielenie patentu 01-12-2015 r.)

- 2.4.** J. Pernak, **B. Górski**, F. Béguin,
Protonowe ciecze jonowe z kationem(chloroetylo)dimetyloamoniowym oraz sposób ich otrzymywania, PL. 221139, Data zgłoszenia: 25-05-2012. (Udzielenie patentu 22-01-2015 r.)
- 2.5.** J. Pernak, **B. Górski**, F. Béguin, M. Niemczak,
Protonowe ciecze jonowe z kationem 1-(2-chloroetylo)piperidyniowym oraz 1-(2-chloroetylo)morfoliniowym oraz sposób ich otrzymywania; PL. 220868, Data zgłoszenia: 10-09-2012. (Udzielenie patentu 23-04-2015 r.)
- 2.6.** J. Pernak, **B. Górski**, F. Béguin, M. Niemczak,
Protonowe ciecze jonowe z kationem (2-chloroetylo)dietyloamoniowym oraz sposób ich otrzymywania; PL. 220135, Data zgłoszenia: 10-09-2012. (Udzielenie patentu 16-01-2014 r.)
- 2.7.** J. Pernak, M. Kot, **B. Górski**,
Sposób odsiarczania ropy naftowej z wykorzystaniem protonowych morfoliniowych cieczy jonowych z anionem krotonianowym, PL. 219771, Data zgłoszenia: 2011-10-28. (Udzielenie patentu 25-11-2014 r.)
- 2.8.** J. Pernak, M. Kot, **B. Górski**,
Sposób odsiarczania ropy naftowej z wykorzystaniem mleczanu 4-alkilomorfoliniowego i 4-(hydroksyalkilo)morfoliniowego, PL. 219770, Data zgłoszenia: 2011-10-28. (Udzielenie patentu 25-11-2014 r.)
- 2.9.** J. Pernak, M. Niemczak, **B. Górski**, R. Giszter,
Sposób otrzymywania czwartorzędowych oraz trzecio-rzędowych azotanów(V) amoniowych, PL. 218724, Data zgłoszenia: 2012-07-16. (Udzielenie patentu 18-06-2014 r.)
- 2.10.** J. Pernak, M. Szymkowiak, **B. Górski**,
4-(2-hydroksyetylo)morfoliniowe ciecze jonowe z anionem organicznym aromatycznym oraz sposób ich otrzymywania, PL.215252, Data zgłoszenia: 2011-04-11. (Udzielenie patentu 29-11-2013 r.)
- 2.11.** J. Pernak, M. Szymkowiak, **B. Górski**,
4-(2-hydroksyetylo)morfoliniowe ciecze jonowe z anionem alkilokarboksylowym oraz sposób ich otrzymywania, PL. 215251, Data zgłoszenia: 2011-04-11. (Udzielenie patentu 29-11-2013 r.).

3. Patents applications

- 3.1. K. Fic, **B. Górska**, P. Bujewska, E. Frackowiak,
Kondensator elektrochemiczny pracujący w elektrolicie z cieczą jonową, Numer zgłoszenia: P – 419568, Data zgłoszenia: 21-11-2016.
- 3.2. Q. Abbas, F. Beguin, **B. Górska**,
Kondensator elektrochemiczny na bazie elektrolitu wodnego działający w szerokim zakresie temperatur, Numer zgłoszenia: P – 419355, Data zgłoszenia: 03-11-2016.
- 3.3. E. Frackowiak, K. Fic, **B. Górska**, P. Bujewska,
Kondensator elektrochemiczny, Numer zgłoszenia: P – 418770, Data zgłoszenia: 20-09-2016.
- 3.4. E. Frackowiak, K. Fic, **B. Górska**, P. Bujewska,
Kondensator elektrochemiczny, Numer zgłoszenia: P – 418570, Data zgłoszenia: 05-09-2016.
- 3.5. E. Frackowiak, K. Fic, **B. Górska**, P. Bujewska,
Kondensator elektrochemiczny, Numer zgłoszenia: P – 418569, Data zgłoszenia: 05-09-2016.
- 3.6. E. Frackowiak, K. Fic, **B. Górska**, P. Bujewska,
Kondensator elektrochemiczny, Numer zgłoszenia: P – 418568, Data zgłoszenia: 05-09-2016.
- 3.7. J. Pernak, F. Beguin, **B. Górska**,
Ciecze jonowe z kationem (2-bromoetylo)tri-metyloamoniowym, (3-bromo-propylo)trimetyloamoniowym oraz (2-bromoetylo)dietyloamoniowym oraz sposób ich otrzymywania, Numer zgłoszenia: P – 417533, Data zgłoszenia: 10-06-2016.
- 3.8. E. Frackowiak, K. Fic, **B. Górska**, P. Bujewska,
Kondensator elektrochemiczny, Numer zgłoszenia: P – 414196, Data zgłoszenia: 28-09-2015.
- 3.9. J. Pernak, F. Beguin, **B. Górska**, A. Kurzawska, K. Marcinkowska, T. Praczyk,
1-Alkilopiperdydniowe protonowe ciecze jonowe z anionem tiocyjanianowym oraz sposób ich otrzymywania; Numer zgłoszenia: P – 406107; Data zgłoszenia: 2013-11-18.
- 3.10. J. Pernak, A. Kurzawska, **B. Górska**, M. Niemczak, K. Marcinkowska, T. Praczyk,
Protonowe amoniowe ciecze jonowe z kationem (3-hydroksypropylo)di-

metyloamoniowym i anionem herbicydowym oraz sposób ich otrzymywania; Numer zgłoszenia: P – 404015; Data zgłoszenia: 2013-05-22.

4. Conferences

4.1. Oral presentations

- 4.1.1. Fic, **B. Górska**, P. Bujewska, F. Béguin, E. Frackowiak,
The 2016 MRS Fall Meeting, The Hynes Convention Center, Boston,
Massachusetts, November 27-December 2, 2016: Redox Activity of Pseudohalides
for Energy Enhancement and Overcharging Protection in Electrochemical
Capacitors (oral presentation).
- 4.1.2. K. Fic, **B. Górska**, P. Bujewska, F. Béguin, E. Frackowiak,
PRiME 2016, Honolulu, Hawaje, 2-7.10.2016: Pseudohalide-based electrolytes
for high-energy electrochemical capacitors(oral presentation).
- 4.1.3. K. Fic, **B. Gorska**, P. Bujewska, F. Béguin, E. Frackowiak,
5th International Conference on Advanced Capacitors, Otsu, Shiga, Japan,
23-27.06.2016: Pseudohalides as redox active electrolytes for supercapacitors (oral
presentation).
- 4.1.4. K. Fic, **B. Gorska**, P. Bujewska, F. Béguin, E. Frackowiak,
67th Annual Meeting of the International Society of Electrochemistry, Hague,
Netherlands, 21-26.08.2016: Pseudohalid-based electrolytes for high-energy
electrochemical capacitors (oral presentation).
- 4.1.5. **B. Górska**, J. Pernak, M. Anouti, F. Béguin,
Seminar: Last development in electrochemical capacitors, Tartu, Estonia,
16-18.12.2013:AC/AC supercapacitors using protic ionic liquids with chloroalkyl
substituted cations (oral presentation).
- 4.1.6. **B. Górska**, J. Pernak, M. Anouti, F. Béguin,
3rd International Symposium on Enhanced Electrochemical Capacitors, Taormina
03-07.06.2013: N-chloroalkyl substituted protic ionic liquids: novel electrolyte for
supercapacitors (oral presentation).

4.2. Poster presentations

- 4.2.1. F. Béguin, Q. Abbas, A. Laheäär, P. Ratajczak, **B. Górska**, P. Skowron, P.
Jeżowski, P. Przygocki, P. Babuchowska,

- Interdisciplinary FNP conference, Warszawa, Polska, 09-10.04.2015: Development of high performance and ecologically friendly supercapacitors for energy management – ECOLCAP project (poster presentation).
- 4.2.2. **B. Górska**, J. Pernak, M. Anouti, F. Béguin
2nd International Scientific Conference Oxygenalia 2014, Poznań, Poland, 07-08.11.2014: Influence of water content in protic ionic liquids on their electrochemical performance for activated carbon based supercapacitors (poster presentation).
- 4.2.3. **B. Górska**, J. Pernak, M. Anouti, F. Béguin,
3rd International Symposium on Enhanced Electrochemical Capacitors, Taormina 03-07.06.2013: Physicochemical properties of n-chloroalkyl substituted protic ionic liquids for supercapacitors.
- 4.2.4. **B. Górska**, J. Pernak, M. Anouti, F. Béguin
VII Sympozjum Czwartorzędowe Sole Amonioowe, Poznań 01-03.07.2013:
Synteza i właściwości fizykochemiczne nowych protonowych cieczy jonowych z kationem N-chloroalkiloamoniowym dla urządzeń elektrochemicznych.
- 4.2.5. **B. Górska**, J. Pernak, M. Anouti, F. Béguin,
VII Sympozjum Czwartorzędowe Sole Amonioowe, Poznań 01-03.07.2013:
Właściwości elektrochemiczne protonowych cieczy jonowych z kationem N-chloroalkiloamoniowym jako elektrolitów dla superkondensatorów.
- 4.2.6. A. Kurzawska, M. Niemczak, **B. Górska**, K. Marcinkowska
VII Sympozjum Czwartorzędowe Sole Amonioowe, Poznań 01-03.07.2013:
Herbicydowe protonowe cieczy jonowe z kationem(hydroksy-alkilo)dimetyloamoniowym.
- 4.2.7. **B. Górska**, M. Niemczak, J. Pernak, F. Béguin
7 Kongres Technologii Chemicznej, Kraków, 8-12 lipca 2012: Wybrane amoniowe cieczy jonowe jako elektrolity w superkondensatorach.
- 4.2.8. **B. Górska**, J. Pernak, F. Béguin,
7 Kongres Technologii Chemicznej, Kraków, 8-12 lipca 2012: Protonowe 1-alkiloimidazoliowe cieczy jonowe z anionem mrówczanowym jako elektrolity w superkondensatorach.

- 4.2.9. .Niemczak, **B. Górski**, P. Wenc, J. Pernak,
Kongres Technologii Chemicznej, Kraków, 8-12 lipca 2012: Zastosowanie protonowych cieczy jonowych jako katalizatorów w reakcji otrzymywania pianek poliuretanowych.
- 4.2.10. **B. Górski**, M. Kot, M. Szymkowiak, J. Pernak, E. Janus
54 Zjazd Polskiego Towarzystwa Chemicznego, Lublin, 18-22 września 2011:
Otrzymywanie i zastosowanie cieczy jonowych z kationem 4-(2-hydroksyetylo)morfoliniowym.
- 4.2.11. M. Kot, J. Pernak, **B. Górski**,
54 Zjazd Polskiego Towarzystwa Chemicznego, Lublin, 18-22 września 2011:
Desulfuryzacja ropy naftowej za pomocą cieczy jonowych.

5. Short scientific internships

Scientific stay at Physicochimie des Matériaux et Electrolytes pour l'énergie (PCM2E), Département de chimie, Université François Rabelais, Tours, France,

Dates of stay:

- 07.09.2012-21.09.2012.
- 04.03.2013-12.04.2013.

6. Participation in scientific projects

6.1. ECOLCAP

Project Development of high performance and ECOLogically friendly superCAPacitors for energy management realized in frame of the WELCOME program, funded by the Polish Foundation for Science (FNP) and European Union.

Project leader: Prof. François Béguin

- As a stipendee (PhD thesis): 1.11.2011-30.09.2015,
- As scientific-research assistant: 01.11.2015-31.12.2015.

6.2. Stypendia naukowe dla doktorantów kształcących się na kierunkach uznanych za szczególnie istotne z punktu widzenia rozwoju Województwa Lubuskiego

- As a stipendee (PhD thesis): 01.01.2014- 31.12.2014.

Abstract

Electrochemical capacitors (ECs) are energy storage devices performing with high power output. Their electrodes are generally constituted of carbonaceous materials, especially cost effective high surface area activated carbons (ACs). The performance of ECs, including their capacitance, maximum voltage and response time, depends considerably on the applied electrolyte. Accordingly, a significant body of work is dedicated to the development of electrolytes, i.e. modifying the properties of already existing ones as well as introducing completely novel compounds. Whereas some organic or aqueous electrolytes are already applied commercially, solvent-free ionic liquids (ILs) have been introduced as electrolytes for ECs only at the academic level. ILs are expected to provide significantly higher operation voltage than organic electrolytes, as well as they are thermally stable, nonvolatile, nonflammable, which is beneficial for the safety of the device. Likewise, during the exploration of new strategies, the application of the subclass of protic ionic liquids (PILs) has emerged as an interesting alternative to be investigated, expecting that they would combine a high operational voltage and good temperature stability, together with the activity of a protic medium promoting reversible faradaic contributions. Therefore, the objective of this dissertation is 1/ to optimize electrochemical performances using the most firmly established PIL in research work on ECs, e.g., triethylammonium bis[(trifluoromethyl)sulfonyl]imide, [HN₂₂₂][TFSI], especially paying attention to the low water content and to the relationship between carbon pore size and size of ions; 2/ to design novel [TFSI]⁻ based PILs displaying attractive properties for their applications in ECs, such as liquid state at room temperature, high electrochemical stability as well as good conductivity and low viscosity.

The first chapter presents the literature pertaining to the development of electrochemical capacitors and the present state-of-the-art. It starts with a general introduction, followed by the description of EC operation principles and their classification depending on the energy storage mechanism. The next section introduces the diversity of carbonaceous materials and specifies their potentiality for ECs advancement. Then, conventional - aqueous and organic - electrolytes are described in the context of their employment in ECs. In case of the aqueous ones, reversible hydrogen electrosorption is particularly discussed, as it has a crucial role in the performance of the negative electrode. Finally, the physicochemical and electrochemical properties of IL-electrolytes are presented, especially showing the attempts to apply them in ECs. A particular emphasis is laid on PILs and the promotion of pseudocapacitive phenomena owing to the labile hydrogen atom on the cation.

Chapter II aims at establishing the most advantageous composition of electrodes for [HN₂₂₂][TFSI]-based ECs by screening the influence of binder type and pore size distribution of the carbon material. Self-standing electrodes have been prepared by mixing a commercial activated carbon sold for ECs application (DLC Supra 30 from Norit, abbreviated as S30) with carbon black as conductivity additive and polyvinylidene fluoride (PVDF) or polytetrafluoroethylene (PTFE) binder. Whereas both types of bound electrodes display comparably good wettability, the pore volume of carbon is noticeably less reduced by implementing PTFE. Afterwards, three carbonaceous materials of differing porous texture (strictly microporous S30 activated carbon, bimodal xerogel carbon and activated carbon black) and bounded with PTFE have been implemented in two-electrode cells with [HN₂₂₂][TFSI] electrolyte to evaluate the impact of their specific surface area (SSA) and micro/mesopores volume ratio on the electrochemical performance. It has been proven that, regardless of comparable SSA of S30 and bimodal xerogel carbon (1725 vs. 1887 m²·g⁻¹, respectively), the latter one provides higher capacitance owing to the contribution of mesopores ensuring higher accessible surface area for bulk ions of PIL. Also, despite its slightly lower SSA, the activated carbon black turned out to be an effective electrode material owing to the impact of mesopores.

After selecting the most propitious composition of electrodes, namely bimodal xerogel carbon bounded with PTFE, chapter III focuses on the effect of water content (<20, 150, 1000 and 1000 ppm) in [HN₂₂₂][TFSI] on EC performance. It was expected that different amounts of water in PIL would affect the transport properties and also more importantly the performance of the negative electrode involving hydrogen electrosorption from the PIL. The process is discussed with reference to reports characterizing hydrogen storage from aqueous medium proven to be dependent on its acidity/alkalinity. During a cathodic scan, the intensity of the faradic current related with hydrogen electrosorption from the PIL increases with the water content in the PIL, evidencing enhanced hydrogen storage. It is reasoned as a difference in the hydrogen electrosorption mechanisms: 1/ in dry PIL, reduction of the protonated cations and hydrogen sorption onto the carbon electrode; 2/ in moisture containing PIL, hydrogen transfer (“hopping”) to water molecules and formation of hydronium cations, which are then reduced to generate nascent hydrogen sorbed in carbon. Likewise, during the anodic sweep, the desorption peak was shifted to lower potential values as the amount of water increased. It suggests lower sorption energy when hydrogen is stored from moisture containing PIL in comparison to “dry” PIL. Overall, the capacitors using [HN₂₂₂][TFSI] with

150 ppm of water demonstrated higher operational voltage, capacitance and stability. Therefore, all further investigations in this manuscript will be performed with PILs containing ca. 150 ppm of water.

Chapter IV aims at designing alternative PILs advantageous for their use in ECs, e.g., with good transport properties, high electrochemical stability as well as potentiality of faradaic contributions. Whereas, the [TFSI]⁻ anion is believed to be the most propitious for the formulation of electrochemically stable PILs, most of the reported PILs combining [TFSI]⁻ and small ammonium cations are solid at room temperature, except for the aforementioned [HN₂₂₂][TFSI]. In aim to provide room temperature PILs and to probe the effect of various cations on the performance of ECs, a series of PILs comprising the [TFSI]⁻ anion and N-chloroalkyl functionalized ammonium cations, both cyclic (morpholinium, piperidinium, pyrrolidinium) and aliphatic with different length of chain, was formulated. Such N-chloroalkyl functionalized cations have been selected owing to the prevalence and cost effectiveness of the starting materials as well as novelty of the obtained compounds. The physicochemical investigations showed lowered melting point of these PILs ($-8.5^{\circ}\text{C} < T_m < 34.1^{\circ}\text{C}$) as compared to their non-functionalized analogues, e.g., [HN_{2-Cl-22}][TFSI] with -8.5°C vs. [HN₂₂₂][TFSI] with 5.5°C . Since all these PILs were liquid at RT, their density, refractive index, viscosity and conductivity were measured. The alkylammonium and pyrrolidinium-based PILs: [HN_{2-Cl-22}][TFSI], [HN_{2-Cl-11}][TFSI], [HN_{3-Cl-11}][TFSI], [HC_{2-Cl}-Pyrr][TFSI] display reasonable conductivity ($1.23 \text{ mS}\cdot\text{cm}^{-1} < \sigma < 1.71 \text{ mS}\cdot\text{cm}^{-1}$), although their viscosity values are relatively high ($0.0665 \text{ Pa}\cdot\text{s} < \eta < 0.1093 \text{ Pa}\cdot\text{s}$).

Finally, chapter V illustrates the electrochemical applicability of the N-chloroalkyl functionalized PILs. Firstly, the electrochemical stability window was determined on glassy carbon (GC) electrode and proven to be wide for all PILs (4.1-5.1 V), alike the representative of non-chloro functionalized analogues, [HN₂₂₂][TFSI], with 4.3 V. These results were discussed in the light of HOMO/LUMO orbital theory serving as an electrochemical stability guide. Higher LUMO energy of the cations characterizes higher stability toward reduction, hence [HN_{2-Cl-22}]⁺ with its slightly lower value than [HN₂₂₂]⁺ was expected to be more susceptible for reduction; this prediction was warranted by practical measurements. However, a straightforward correlation was not valid within the series of N-chloroalkyl functionalized cations as a result of their considerably differentiated viscosity and or/impact of mutual cation-anion interactions. The next section focuses on the suitability of low-cost current collector materials such as stainless steel and aluminum for PIL electrolyte, conceived as

potential range of PIL stability on these materials. In both cases, the cathodic limits were similar for a given PIL, yet shifted toward higher potential values in comparison to GC, evidencing decrease of stability due to promoted hydrogen evolution. In contrast, the anodic behavior of stainless steel and aluminium differs significantly; the former one can be corroded if electrodecomposition products of the [TFSI]⁻ anion appear as opposed to aluminium, which is protected by formation of a passive layer; therefore the later has been selected for further studies. Then, the safe stability potential range of porous carbon electrodes made of the S30 AC in these PILs was established according to the Kötzt et al. reliable determination method of stability limits for electrical double-layer capacitors. The gathered information on safe potential limits allowed the performance of electrodes of symmetric ECs to be evaluated. At the same time, it was demonstrated that the performance of PIL-based ECs strongly depends on the cation type, meaning its structure itself as well as its pK_a value, which determines hydrogen lability and its electrosorption conditions. Finally, the operation of full cells in N-chloroalkyl functionalized PILs: [HC_{2-Cl}-Pyrr][TFSI] [HN_{2-Cl-22}][TFSI], [HN_{2-Cl-11}][TFSI], [HN_{3-Cl-11}][TFSI], which were selected based on their acceptable transport properties, were investigated and compared to cells implementing [HN₂₂₂][TFSI].

Streszczenie

Kondensatory elektrochemiczne (KE, ang. *Electrochemical capacitors*) to urządzenia do magazynowania energii charakteryzujące się wysokimi wartościami mocy wyjściowej. Zazwyczaj, ich elektrody wytwarza się z rozmaitych materiałów węglowych, w szczególności uzasadnionego ekonomicznie węgla aktywnego o wysokorozwiniętej powierzchni właściwej. Charakterystyka pracy kondensatorów elektrochemicznych, w tym pojemność, maksymalne napięcie pracy i czas odpowiedzi, znacząco zależy od zastosowanego elektrolitu. Dlatego też pokaźna część prac badawczych dotyczy rozwoju elektrolitów, czyli modyfikowania właściwości tych już istniejących jak i wprowadzania zupełnie nowych związków. Podczas gdy wybrane elektrolity zarówno organiczne jak i wodne stosuje się komercyjnie, to ciecze jonowe (ang. *Ionic liquids*) jako elektrolity dla KE są dopiero na etapie testów laboratoryjnych. Zastosowanie cieczy jonowych ma na celu znaczne zwiększenie napięcia pracy KE w porównaniu do tych na bazie klasycznych elektrolitów organicznych. Dodatkowo, ciecze jonowe są stabilne termicznie, mają niską prężność par i są najczęściej niepalne, co zwiększa bezpieczeństwo pracy takich urządzeń. Ponadto, w poszukiwaniu nowych strategii rozwoju zaproponowano wykorzystanie podgrupy protonowych cieczy jonowych (ang. *Protic ionic liquids*). Oczekiwano, iż elektrolity te pozwolą uzyskać wysokie napięcie pracy KE oraz dobrą stabilność termiczną, a jednocześnie przejawiać aktywność medium o charakterze protycznym, promującą udział odwracalnych reakcji faradajowskich. Dlatego celem niniejszej pracy doktorskiej jest 1/ optymalizacja pracy kondensatora elektrochemicznego, przy użyciu najczęściej stosowanej protonowej cieczy jonowej w badaniach nad elektrolitami dla KE bis(trifluorometylosulfonylo)imidku trietyloamoniowego, [HN₂₂₂][TFSI], zwracając szczególną uwagę na zawartość wody oraz kompatybilność pomiędzy wielkością porów węgla aktywnego, a wielkością jonów; 2/ zaprojektowanie nowych protonowych cieczy jonowych zawierających w swojej strukturze anion bis[(trifluorometylo)sulfonylo]imidkowy, [TFSI]⁻, i wykazujących atrakcyjne właściwości pod kątem ich zastosowania w KE, takie jak: ciekły stan skupienia w temperaturze pokojowej, wysoka stabilność elektrochemiczna, a także wysokie przewodnictwo właściwe oraz niska lepkość.

Pierwszy rozdział zawiera przegląd literaturowy na temat rozwoju kondensatorów elektrochemicznych, jak i obecny stan wiedzy w tej dziedzinie. Rozpoczyna się on od ogólnego wstępu o kondensatorach elektrochemicznych oraz opisuje zasadę działania tych urządzeń z wyszczególnieniem typowych mechanizmów magazynowania energii. W następnym podrozdziale przedstawione są różnorodne materiały węglowe ze wskazaniem

ich potencjału aplikacyjnego w KE. W dalszej kolejności opisuje się elektrolity konwencjonalne, organiczne i wodne, oraz ich praktyczne zastosowanie w KE. W odniesieniu do elektrolitów wodnych omawiany jest proces odwracalnej sorpcji wodoru, który ma decydujący wpływ na działanie elektrody ujemnej. W ostatniej części omawiane są właściwości fizykochemiczne cieczy jonowych oraz stan wiedzy na temat ich wykorzystania w KE. Szczególny nacisk kładziony jest na podgrupę protonowych cieczy jonowych zwłaszcza w kontekście promowania zjawisk pseudopojemnościowych przez medium o charakterze protycznym wynikających z oddziaływań z labilnym protonem kationu.

Rozdział drugi ma na celu wyznaczenie najkorzystniejszego składu elektrod stosowanych w kondensatorach elektrochemicznych (przy użyciu modelowej protonowej cieczy jonowej, [HN₂₂₂][TFSI], pełniącej rolę elektrolitu) poprzez zbadanie wpływu typu lepiszcza oraz znaczenia dystrybucji rozmiaru porów węgla aktywnego. Do tych badań przygotowano wolnostojące elektrody, wykonane z połączenia komercyjnego węgla aktywnego (DLC Supra 30, Norit, w skrócie S30) z sadzą jako dodatkiem podnoszącym przewodność elektrod oraz lepiszczem, poli(fluorkiem winylidenu) (PVDF) lub poli(tetrafluoroetylenem) (PTFE). Oba typy lepiszcza wykazały dobrą zwilżalność, jednak objętość porów węgla aktywnego była znacznie mniej zredukowana po zastosowaniu PTFE. W kolejnej części pracy trzy materiały węglowe różniące się teksturą porowatą (wyłącznie mikroporowaty węgiel aktywny S30, bimodalny kserożel oraz sadza) związane przy użyciu PTFE w wolnostojące elektrody zostały zastosowane w układach dwuelektrodowych (jako elektrolit także użyto [HN₂₂₂][TFSI]) do oceny wpływu ich powierzchni właściwej oraz udziału mikro- i mezoporów na charakterystykę pracy KE. Udowodniono, że bez względu na zbliżone wartości powierzchni właściwej węgla S30 i bimodalnego kserożelu (odpowiednio 1725 vs. 1887 m²·g⁻¹) ten drugi pozwala uzyskać znacznie wyższą pojemność KE dzięki udziałowi mezoporów zapewniających większą dostępną powierzchnię właściwą dla relatywnie dużych jonów elektrolitu. Ponadto, pomimo niższej powierzchni właściwej sadzy aktywowanej zastosowanie tego materiału okazało się być korzystne ze względu na udział mezoporów.

Po dokonaniu selekcji najkorzystniejszej kompozycji elektrod, czyli bimodalnego kserożelu związanego przy użyciu PTFE jako lepiszcza, rozdział III traktuje o wpływie ilości wody (<20, 150, 1000 i 1000 ppm) zawartej w protonowej cieczy jonowej, [HN₂₂₂][TFSI], na charakterystykę pracy KE. Oczekiwano, że różna zawartość H₂O będzie miała wpływ zarówno na właściwości transportowe tychże związków jak i, co ważniejsze, charakterystykę

pracy elektrody ujemnej wykorzystującej proces elektrosorpcji wodoru z protonowej cieczy jonowej. Sam proces elektrosorpcji jest omawiany w oparciu o doniesienia literaturowe na temat magazynowania wodoru z elektrolitów wodnych, wskazujących istotny wpływ kwasowości/zasadowości medium na jego przebieg. Stosując protonową ciecz jonową jako elektrolit, podczas skanowania elektrody do niższych potencjałów, intensywność prądu faradajowskiego związanego z elektrosorpcją wodoru rośnie wraz ze wzrostem zawartości wody w cieczy, co świadczy o nasileniu magazynowania wodoru. Zmiany te przypisuje się różnym mechanizmom procesu elektrosorpcji wodoru: 1/ w odwodnionej protonowej cieczy jonowej następuje redukcja protonowanych kationów i sorpcja wodoru na elektrodzie węglowej; 2/ w cieczy zawierającej wodę wodór jest przenoszony na cząsteczkę wody formując jon hydroniowy, który kolejno jest redukowany generując wodór cząsteczkowy sorbowany na węglu. Podobnie, po odwróceniu kierunku skanowania, pik świadczący o desorpcji wodoru występował przy niższych wartościach potencjału, gdy ilość wody w cieczy wzrastała. Sugeruje to, że energia sorpcji wodoru jest obniżona w przypadku próbek zawierających wodę w porównaniu do bezwodnej cieczy. Przeprowadzone badania wykazały, iż kondensator elektrochemiczny na bazie protonowej cieczy jonowej [HN₂₂₂][TFSI] zawierającej 150 ppm wody charakteryzował się najwyższym napięciem, pojemnością oraz stabilnością. W związku z tym dalsze prace badawcze przedstawione w niniejszej dysertacji przeprowadzono przy użyciu protonowych cieczy jonowych, których zawartość wody wyniosła około 150 ppm.

Rozdział IV poświęcony jest projektowaniu protonowych cieczy jonowych pod kątem ich zastosowania w KE, czyli związków charakteryzujących się wysokim przewodnictwem, niską lepkością oraz wysoką stabilnością elektrochemiczną, a także potencjalną możliwością uzyskania prądu faradajowskiego. Pomimo że zastosowanie anionu [TFSI]⁻ pozwala na wytworzenie stabilnych elektrochemicznie protonowych cieczy jonowych, większość opisanych w literaturze związków zawierających w swojej strukturze ten anion w połączeniu z kationami amoniowymi o niewielkich rozmiarach występuje w stanie stałym w temperaturze pokojowej. Wyjątek stanowi wspomniana uprzednio protonowa ciecz jonowa - [HN₂₂₂][TFSI]. Biorąc pod uwagę fakt że do badań potrzebne są związki ciekłe co najmniej w temperaturze pokojowej, a jednocześnie mając na celu zbadanie wpływu struktury kationu na charakterystykę pracy KE syntezowano serię protonowych cieczy jonowych, w których anion [TFSI]⁻ połączono z szeregiem kationów zawierających w swojej strukturze podstawnik alkilowy z chlorem jako grupą funkcyjną. Zastosowano zarówno kationy alicykliczne

(morfoliniowy, piperydyniowy, pirolidyniowy), jak i alifatyczne różniące się długością podstawników. Kationy te zostały wybrane ze względu na łatwą dostępność oraz niski koszt substratów, jak również literatura przedmiotu nie zawierała informacji na temat wykorzystania takich połączeń. Badania fizykochemiczne wykazały, iż protonowe ciecze jonowe zawierające w kationie podstawnik chloroalkilowy charakteryzują się znacznie niższymi temperaturami topnienia ($-8,5\text{ °C} < T_m < 34,1\text{ °C}$) niż ich niepodstawione analogi, np. $[\text{HN}_{2-\text{Cl}-22}][\text{TFSI}]$ o $T_m = -8,5\text{ °C}$ w porównaniu do $[\text{HN}_{222}][\text{TFSI}]$ o $T_m = 5,5\text{ °C}$. Jako że wszystkie te ciecze występowały w ciekłym stanie skupienia w temperaturze pokojowej zbadano ich gęstość, indeks refrakcji, lepkość oraz przewodnictwo. Ciecze o kationach amoniowych oraz pirolidyniowym odznaczają się zadowalającymi wartościami przewodnictwa właściwego ($1,23\text{ mS}\cdot\text{cm}^{-1} < \sigma < 1,71\text{ mS}\cdot\text{cm}^{-1}$) pomimo względnie wysokich wartości lepkości ($0,0665\text{ Pa}\cdot\text{s} < \eta < 0,1093\text{ Pa}\cdot\text{s}$).

Rozdział V prezentuje testy na protonowych cieczach jonowych zawierających w swojej strukturze podstawnik chloroalkilowy do celów elektrochemicznych. Na początku zbadano zakres ich stabilności elektrochemicznej (tzw. okno elektrochemiczne) na elektrodzie z węgla szklistego. Wartości te okazały się być wysokie dla wszystkich analizowanych cieczy (4,1-5,1 V) podobnie do ich niepodstawionego analogu $[\text{HN}_{222}][\text{TFSI}]$, którego stabilność elektrochemiczna wynosiła 4,3 V. Otrzymane wyniki omówiono w świetle teorii orbitalni granicznych HOMO/LUMO, których wartości służą jako wskazanie stabilności elektrochemicznej związków. Wyższa wartość energii LUMO kationu sugeruje wyższą stabilność przeciw redukcji elektrochemicznej, zatem spodziewano się, że kation $[\text{HN}_{2-\text{Cl}-22}]^+$ charakteryzujący się niższą wartością niż kation $[\text{HN}_{222}]^+$ będzie mniej stabilny, a predykcja ta została potwierdzona przeprowadzonymi badaniami. Jednak w przypadku serii cieczy o kationach z podstawnikiem chloroalkilowym nie uzyskano pełnej zgodności pomiędzy wartościami obliczonymi a zmierzonymi co przypisywane jest znacząco zróżnicowanej lepkości tych związków i/lub wpływowi wzajemnych oddziaływań kation-anion. W kolejnej części badana jest stabilność elektrochemiczna uzasadnionych ekonomicznie materiałów, z których wykonuje się kolektory prądowe, takich jak stal nierdzewna oraz aluminium, w kontakcie z badanymi protonowymi cieczami jonowymi. W przypadku obu materiałów stabilność elektrochemiczna przeciw redukcji była zbliżona, jednakże zaobserwowano zmniejszenie ich stabilności w porównaniu do wyników otrzymanych na elektrodzie szklistej, co przypisywane jest ułatwionemu wydzieleniu wodoru. W przypadku badań anodowych, właściwości stali nierdzewnej i aluminium bardzo się różniły. Wykazano, że stal nierdzewna

może ulec korozji, jeżeli w układzie pojawią się elektroaktywne produkty rozkładu anionu [TFSI]⁻ w odróżnieniu od aluminium, które chronione jest warstwą pasywacyjną. Dlatego też w dalszej części pracy zdecydowano się na zastosowanie kolektorów aluminiowych. Następnie, przeprowadzono badania stabilności omawianych protonowych cieczy jonowych na elektrodach porowatych wykonanych z komercyjnego węgla aktywnego zaprojektowanego do zastosowania w KE wykorzystując metodykę badawczą przeznaczoną do określania stabilności kondensatorów podwójnej warstwy elektrycznej rekomendowanej przez Kötz'a i współpracowników. Wyznaczone bezpieczne zakresy potencjałów zostały użyte do interpretacji stabilności symetrycznych KE z wykorzystaniem tychże cieczy jonowych. Jednocześnie przeprowadzone badania stabilnościowe wykazały znaczący wpływ właściwości kationu: jego struktury i wartości pK_a, które z kolei przekładają się na labilność wodoru i warunki jego elektrosorpcji przez co na wydajność pracy KE. Ostatnia część pracy przedstawia działanie układów badawczych na bazie wybranych protonowych cieczy jonowych, których kation zawiera podstawnik chloroalkilowy: [HC_{2-Cl}-Pyrr][TFSI], [HN_{2-Cl-22}][TFSI], [HN_{2-Cl-11}][TFSI], [HN_{3-Cl-11}][TFSI], gdzie kryterium wyboru stanowiły racjonalne wartości przewodnictwa i lepkości. Charakterystykę pracy takich układów porównano do działania KE na bazie [HN₂₂₂][TFSI].